Université catholique de Louvain

Institut de Recherche en
Mathématique et Physique

Entanglement and bipartite fidelity in low-dimensional quantum many-body systems

Gilles Parez

Thesis submitted in partial fulfilment of the requirements for
the degree of Docteur en Sciences

Dissertation committee

Prof. Jan Govaerts	*(President)*	UCLouvain
Prof. Christian Hagendorf	*(Supervisor)*	UCLouvain
Prof. Eric Ragoucy		LAPTh - CNRS
Prof. Philippe Ruelle	*(Secretary)*	UCLouvain
Dr. Jean-Marie Stéphan		Institut Camille Jordan - CNRS

October 2021

La montagna mi ha insegnato a non barare, a essere onesto con me stesso e con quello che facevo.

Walter Bonatti

Remerciements

Bien que de nature très différente, la rédaction d'une thèse en Physique et l'ascension d'un sommet vierge au bout du monde ont plus de points communs qu'il n'y parait. En particulier, dans les deux cas, l'accent est mis sur la réalisation finale (l'arrivée au sommet ou le manuscrit), ainsi que sur les protagonistes (les premiers ascensionnistes ou l'auteur de la thèse), mais il serait injuste d'oublier tous ceux qui, d'une manière ou d'une autre, ont contribué à la réalisation d'une telle entreprise.

Merci Christian pour ton soutien inébranlable. Depuis la troisième année du Bachelier tu m'as insufflé le goût de la recherche, motivé lorsque j'en avais besoin et donné beaucoup de liberté. Tu as été le guide dont chaque jeune alpiniste rêve, et je me réjouis à l'idée de continuer d'arpenter les sentiers de l'intégrabilité avec toi. Alexi, nous avons fait des boucles ensemble, mais sans jamais retourner sur nos pas (pour l'instant). Merci pour ta patience, ton enthousiasme et nos collaborations. Tu as énormément contribué à mon évolution scientifique, et je te pardonne pour PSTricks. Philippe, merci pour la bonne humeur et la détente que tu apportes au groupe. Je remercie aussi chaleureusement Jean-Marie, Éric et Jan d'avoir accepté de faire partie de mon jury de thèse. Merci pour vos commentaires et vos encouragements. Je tiens aussi à remercier le professeur André Nauts pour son fabuleux cours de Physique Statistique, sans lequel cette thèse n'aurait jamais vu le jour.

Merci aussi à tous les apprentis alpinistes qui ont partagé une partie de mon périple. Adrien, merci pour les magnifiques séances d'exercices. Jean, merci de m'avoir laissé de la place sur le tableau lorsque j'ai commencé mon mémoire. Bryan, tellement de chemin parcouru ! Félicitations pour ta belle thèse. Merci aussi Sandrine de m'avoir inclus aux pauses café. Le boss est tout à toi. Alexandre, merci pour ta bonne humeur, et pour les chouquettes ! Les amis mathématiciens, merci aussi ! Merci François et Élia pour nos aventures verticales. Vous êtes ceux avec qui la métaphore alpine dépasse la poésie. François, continue de voir le Verdon à moitié plein. Merci aussi à Florence, Corentin, Léo et tous ceux avec qui nous avons partagé d'interminables (mais bien méritées) pauses café et autres drinks de fin de thèse. Cathy, merci pour ton aide précieuse et nos nombreux moments d'échange. Je n'oublierai pas ces longs mois où nous étions les deux seuls résidents de la tour B. Merci à tous les membres de l'IRMP pour faire de cet institut ce qu'il est : un mélange de finesse scientifique et de convivialité. Mes quatre années de thèse furent heureuses, et c'est grâce à vous tous.

Cette thèse a aussi une grande composante italienne. Pasquale, merci de m'avoir accepté dans ton équipe durant mon séjour à Trieste. C'était une expérience formatrice pour moi, et je t'en suis grandement reconnaissant. Riccarda, amica mia, merci pour notre belle collaboration et tous ces moments partagés. Au plaisir de se revoir à San Candido ! Merci aussi à tous ceux qui ont croisé ma route à via Bonomea : Francesco, Gennaro, Alexandre, Stefano, Frederico, David, Sara, Giuseppe, Mario, Léo. Merci aussi aux grimpeurs de Trieste qui ont rendu mon séjour plus physique que la Physique : Mass, Nicolò, Carlotta, Simon. Daje !

Que serait une aventure en montagne sans les amis ? Merci aux bros de toujours, Nico, Rémi, Maître Hovine, vous allez me manquer les gars ! Shubidou, merci pour Freyr, le Colébi et les frayeurs. Bon voyage ! Le refuge des Marmottes, a.k.a le meilleur bar de Stockel, merci pour ces trois années de braséros, pan Golin et bêtises en tout genre. Marjo, c'était un plaisir de partager le long périple Wezembeek−LLN avec Supertramp à fond. Les gembloutois, restez comme vous êtes. Merci les Gitans pour tous les treks déjantés. Ced, Maumau, Jé, Guss, Sim, Guidosse, Guigui, keep climbing hard les gars. L'Aclo Team, merci pour les djotes et les carnavals ! Les amis du LSO, c'est avec un pincement

au cœur que j'écris ces lignes. Merci pour les bonnes guindailles. Le SCAP, merci pour les aventures étroites, vertigineuses ou mouillées ! Merci aussi à la communauté SWI pour les bières intégrables et les bons souvenirs aux Houches.

Un grimpeur n'est rien sans un bon assureur en qui il a une parfaite confiance. Mathilde, Papa, Maman, merci pour tous les bons moments et pour votre soutien tout au long de ces années. Marianne et JP, merci pour votre accueil et votre enthousiasme ! Bonne-Maman, Nanine, Léon, votre force m'inspire chaque jour, je suis fier d'être votre petit-fils.

Fif, merci pour la belle cordée que nous formons depuis maintenant presque dix ans.

À la douce mémoire de Bernard, à qui, j'en suis sûr, cette aventure aurait inspiré mille et une histoires.

List of publications

This thesis is based on the following publications:

- [1] G. Parez, R. Bonsignori, P. Calabrese, *Exact quench dynamics of symmetry resolved entanglement in a free fermion chain*, J. Stat. Mech. (2021) 093102.
- [2] G. Parez, R. Bonsignori, P. Calabrese, *Quasiparticle dynamics of symmetry-resolved entanglement after a quench: Examples of conformal field theories and free fermions*, Phys. Rev. B **103** (2021) L041104 .
- [3] A. Morin-Duchesne, G. Parez, J. Liénardy, *Bipartite fidelity for models with periodic boundary conditions*, J. Stat. Mech. (2021) 023101.
- [4] G. Parez, A. Morin-Duchesne, P. Ruelle, *Bipartite fidelity of critical dense polymers*, J. Stat. Mech. (2019) 103101.

The following publication (in preparation) is not discussed in the thesis:

- [5] C. Hagendorf, G. Parez, *On the logarithmic bipartite fidelity of the open XXZ spin chain at* $\Delta = -1/2$, in preparation (2021).

Contents

Introduction

Can quantum-mechanical description of physical reality be considered complete? This question is the title of a seminal paper published in 1935 by Einstein, Podolsky and Rosen [6], where they expressed their concerns about the Copenhagen formulation and interpretation of quantum mechanics. In particular, the authors imagined a *Gedankenexperiment*, that highlights what is now known as the *EPR paradox*. To illustrate the paradox, let us suppose that we have a system of two spins, labelled A and B, that are initially prepared in the singlet state

$$|\psi\rangle = \frac{1}{\sqrt{2}}(|\uparrow_A\downarrow_B\rangle - |\downarrow_A\uparrow_B\rangle). \tag{0.1}$$

The spins are then sent in opposite directions to distant observers, traditionally denoted Alice and Bob. If Alice observes that her spin is in the state $|\uparrow_A\rangle$, the axioms of quantum mechanics imply that the wave function has collapsed to the state $|\uparrow_A\downarrow_B\rangle$ and hence she *knows* that the outcome of Bob's measurement will be, or was, the state $|\downarrow_B\rangle$. Alice thus gained *information* on the state of Bob's spin *instantaneously* after measuring hers. The fact that this gain of information is instantaneous and independent of the physical distance between Alice and Bob seems to be in contradiction with the principles of Relativity and the finite velocity of light and information. The conclusion of the authors is that quantum mechanics has to be supplemented with local hidden variables in order to restore locality.

Using the idea of hidden variables as a postulate, John Bell discovered a set of inequalities, known as *Bell's inequalities* [7], that are maximally violated by the predictions of quantum machanics and respected by any local theory. Almost 20 years later, Alain Aspect and collaborators performed measurements on polarised photons and showed a maximal violation of Bell's inequalities, hence ruling out the theory of hidden variables [8–10]. Quantum mechanics is an intrinsic non-local theory, and the *spooky action at a distance*, as Einstein called it, is one of its fundamental features rather than a dismissing flaw. Non-locality in quantum mechanics is related to the notion of *quantum entanglement*. This concept is the focal point of this thesis.

We say that two quantum systems are entangled if performing a measurement on one influences the state of the other instantaneously and independently from their physical separation. Schrödinger understood that non-local correlations in quantum states are a direct consequence of the quantum-mechanical description of composite systems [11]. To illustrate that statement, let us consider a quantum system that is composed of two complementary subsystems A and B. The Hilbert space $\mathcal{H}$ of the whole system $A \cup B$ is the product of the local Hilbert spaces, $\mathcal{H} = \mathcal{H}_A \otimes \mathcal{H}_B$, where $\mathcal{H}_s$, $s = A, B$, is the Hilbert space of subsystem s. Using Schmidt's decomposition [12, 13], any state $|\psi\rangle$ of $\mathcal{H}$ can be written as

$$|\psi\rangle = \sum_{j=1}^{\chi} p_j \, |\phi_j^A\rangle \otimes |\phi_j^B\rangle \tag{0.2}$$

where $p_j > 0$ are the Schmidt coefficients, $\chi \leqslant \min(\dim \mathcal{H}_A, \dim \mathcal{H}_B)$ is the Schmidt number, and $\{|\phi_j^s\rangle\}$ is a set of basis vectors of $\mathcal{H}_s$. If the whole system is in a product state, namely $|\psi\rangle = |\phi_i^A\rangle \otimes |\phi_i^B\rangle$ for some i, then A and B are not entangled. On the contrary, A and B are entangled if there are at least two non-vanishing Schmidt's coefficients in the decomposition. In that case, it is not possible to assign a pure state to subsystem A. Instead, it is described by its reduced density matrix ρ_A, defined as the trace over the degrees of freedom of B of the total density matrix ρ,

$$\rho_A = \mathrm{Tr}_B \rho, \quad \rho = |\psi\rangle\langle\psi|. \tag{0.3}$$

Even though $|\psi\rangle$ provides us with perfect knowledge of the whole system, there is a *statistical* uncertainty on the state of A. This situation has no counterpart in classical mechanics.

To quantify the amount of entanglement between A and B, we need to measure how far the state $|\psi\rangle$ is from a product state, or equivalently how mixed the reduced density matrix ρ_A is. The most broadly studied entanglement measure is the so-called *entanglement entropy* [14]. It is defined as the von Neumann entropy [15] of the reduced density matrix,

$$S_1 = -\mathrm{Tr}(\rho_A \log \rho_A). \tag{0.4}$$

Here and throughout the thesis, we use the natural basis for the logarithm. In terms of the Schmidt coefficients, we have

$$S_1 = \sum_{j=1}^{\chi} -p_j^2 \log p_j^2. \tag{0.5}$$

This is precisely the so-called *Shannon entropy* [16] of the squares of the Schmidt coefficients, a central quantity in the theory of classical information. The entanglement entropy is interpreted as the amount of missing information regarding the state of A even though we know the state of whole system $A \cup B$.

The reduced density matrix satisfies $\mathrm{Tr}\rho_A = 1$, independently from its statistical mixture. In contrast, the trace $\mathrm{Tr}\rho_A^n$ for $n > 1$ is unity if and only if ρ_A corresponds to a pure state, namely $\rho_A = |\phi_i^A\rangle\langle\phi_i^A|$. For this reason, the following quantities also measure the entanglement between A and B,

$$S_n = \frac{1}{1-n} \log \mathrm{Tr}\rho_A^n, \tag{0.6}$$

where $n > 1$ is an integer. These quantities are the so-called *Rényi entropies* [17], and the limit $n \to 1$ in (0.6) yields the entanglement entropy.

The entanglement entropy measures the entanglement between a subsystem A and its complement B, independently from the topology of A. For instance, if $A = A_1 \cup A_2 \cup \cdots \cup A_m$, the entanglement entropy (0.4) still measures the entanglement between this collection of m disjoint subsystems and the rest of the system. In many cases, it is also relevant to investigate the entanglement between disjoint subsystems A_i and A_j

that are not complementary, or equivalently when the bipartite system $A_i \cup A_j$ is not in a pure state. In the case where A consists of two disjoint subsystems, $A = A_1 \cup A_2$, one often uses the so-called *mutual information*

$$I_1^{A_1:A_2} = S_1^{A_1} + S_1^{A_2} - S_1^{A_1 \cup A_2} \tag{0.7}$$

to quantify the quantum correlations between A_1 and A_2 [18]. In (0.7), S_1^s denotes the entanglement entropy that quantifies the entanglement between the system s and the rest of the system. The mutual information does not satisfy the information-theoretical definition of an entanglement measure [19], but it is nonetheless central in the study of mixed-state entanglement. Another measure that quantifies the entanglement between non-complementary subsystems is the entanglement negativity [20]. It shares many similarities with the mutual information, notably for nonequilibrium quantum many-body systems [21].

The systematic investigation of entanglement and entangled states was initiated within the quantum information community [22]. In this context, entanglement is seen as a resource needed to perform certain tasks and protocols that are not possible to execute with classical systems [23]. Examples include quantum teleportation [24], quantum cryptography [25], quantum error correction codes [26] and quantum computation [27]. An important challenge in the field is to exploit these theoretical ideas to build quantum computing devices of macroscopic size [28]. This goal is still far from being accomplished, but impressive progress has been made in recent years [29].

Over the last two decades, the interest in entanglement grew tremendously within other seemingly unrelated research areas, such as black hole [30] and condensed matter physics [31,32]. In the context of many-body systems, this interest stems from the observation that the entanglement entropy is an efficient tool to detect and characterise quantum critical points [33–35]. Many aspects of quantum critical systems in d dimensions are described by conformal field theories (CFTs) in $d+1$ dimensions [36], and the entanglement entropy in one-dimensional quantum critical models depends on the central charge of the underlying CFT [37, 38]. These results motivated an intense theoretical effort aimed at better understanding the universal behaviour of entanglement measures in the vicinity of a quantum phase transition [39–41].

Entanglement also plays a prominent role in our understanding of the nonequilibrium dynamics of quantum many-body systems [42–44]. Over the last decade, the evolution of entanglement after a so-called *quantum quench* [45–47], a paradigmatic protocol to drive a system out of equilibrium, received considerable attention [43, 44]. Notably, there is an important cross-fertilisation between theoretical ideas [21, 45–50] and groundbreaking cold-atom and ion-trap experiments, where it has been possible to measure the many-body entanglement of nonequilibrium states [51–54].

In this thesis, we study entanglement in the context of quantum many-body systems in low dimensions. In particular, we focus on so-called *integrable models* [55]. These are models whose rich mathematical structure allows one to perform exact calculations of physical quantities, such as the energy spectrum of the Hamiltonian [56], form factors [57] and correlation functions [58]. In addition, integrable models have a large number of conserved quantities that strongly constrain their nonequilibrium dynamics [59]. Among all quantum many-body systems, integrable models are the exception rather than the rule. However, they accurately describe a wide set of experimental results [60, 61] and strongly contribute to our modern understanding of quantum many-body physics. In the following, we investigate entanglement properties of integrable models at criticality and out of equilibrium separately. Accordingly, the manuscript is divided in two parts.

Part I: Bipartite fidelity of critical lattice models

In 2011, Dubail and Stéphan introduced the so-called *bipartite fidelity* [62,63]. It is not an entanglement measure in the quantum-informational sense [19], but nonetheless shares many properties with the entanglement entropy. In particular, it may also be used to detect and characterise quantum phase transitions. In the first part of the thesis, we investigate this quantity in the context of critical lattice models in low dimensions. Using tools from quantum integrability and CFT, we provide a variety of new exact lattice results that we compare with original CFT predictions. In Chapter 1, we first review the theory of critical phenomena and chosen aspects of CFT. Second, we discuss quantum phase transitions and explain how they are described by the same formalism as classical critical

systems. We then introduce the notion of quantum spin chains, paradigmatic examples of integrable models that exhibit critical behaviour. We also investigate the connection between entanglement and quantum criticality and conclude the chapter with the introduction of the bipartite fidelity and a detailed plan of the subsequent chapters of Part I. The original results from the papers [3, 4] are discussed in Chapters 2 to 4. We present general conclusions and outlooks in Chapter 5.

Keywords: Entanglement, bipartite fidelity, quantum spin chains, loop models, integrability, (logarithmic) conformal field theory.

Part II: Dynamics of symmetry-resolved entanglement

The investigation of the interplay between global symmetries and entanglement in the context of quantum many-body systems led to the concept of *symmetry-resolved entanglement* [64–66]. For systems out of equilibrium, understanding how the entanglement arises from the various symmetry sectors is necessary to better grasp the full many-body dynamics [52]. However, despite the recent considerable interest for the symmetry resolution of entanglement, there are only few results for systems out of equilibrium [52, 67–69]. In the second part of the thesis, we investigate the dynamics of symmetry-resolved entanglement measures after a global quantum quench in a one-dimensional free-fermion chain. In the quench protocol, an isolated quantum system is prepared in a pure state and evolves under the action of a Hamiltonian that does not commute with the initial density matrix. We find exact results for the symmetry-resolved entanglement dynamics for two distinct low-entangled initial states and provide conjectures for more generic initial states and interacting integrable models. In Chapter 6, we review chosen aspects of the entanglement dynamics after a quantum quench in an integrable model and define the symmetry-resolved entanglement entropies. Our original results from the papers [1, 2] are discussed in Chapters 7 and 8. Finally, we provide a series of concluding remarks and outlooks in Chapter 9.

Keywords: Symmetry-resolved entanglement, global quantum quench, quasiparticle picture, free-fermion models.

Part I

Bipartite fidelity of critical lattice models

1

Entanglement and quantum criticality

Many-body systems are central in physics. A general feature of such physical systems is that their complexity drastically increases with the number of constituents. For example, determining the trajectories of three (or more) point masses that interact gravitationally is a notoriously challenging problem, whereas the two-body problem is exactly solvable. Quantum mechanics is not exempt from such difficulties. In atomic physics, the spectrum of the hydrogen atom is obtained analytically, whereas for atoms with higher atomic numbers it is usually computed with numerical and perturbation methods. In condensed matter physics, and more generally in statistical mechanics, the aim is to understand macroscopic properties and collective behaviour of many-body systems with spatial extension based on microscopic interactions between the constituents. Phase transitions are a remarkable example of such collective behaviour, and play an invaluable role in our understanding of many-body systems.

A phase transition is characterised by a drastic change in the macroscopic properties of a system as a response to the variation of one or several parameters. The boiling point of water is a perfect example. At atmospheric pressure, as the temperature is increased from 373.14K to 373.16K, the density of water plummets as it undergoes a transition from liquid to vapour. Another notable example is the so-called *ferromagnetic transition*, where a magnet loses its spontaneous magnetisation as the

temperature reaches the so-called *Curie temperature* T_C. For example, the Curie temperature of iron is $T_C = 1044\text{K}$ [70].

The ferromagnetic and liquid-vapour phase transitions are examples where the temperature is the relevant parameter that drives the transition. There are also transitions that occur at zero temperature and hence are only caused by quantum effects. These *quantum phase transitions* [71] happen when the groundstate of a quantum Hamiltonian undergoes a drastic reorganisation as a global parameter is varied and crosses a critical value. This parameter can be an external magnetic field, an interaction strength or an anisotropy parameter, for example. Quantum phase transitions are central in our understanding of quantum many-body systems [71, 72]. They are associated with level-crossings, and hence the notion of quantum criticality is related to the properties of the spectral gap of quantum many-body Hamiltonians.

In this chapter, we review several aspects of quantum phase transitions and the connection between quantum criticality and entanglement. As we shall see, the formalism and tools used to describe quantum critical points are similar to those developed in the context of classical (as opposed to quantum) phase transitions. We start the chapter with chosen aspects of critical phenomena theory using the Ising model and the ferromagnetic transition as examples. We also discuss the universal properties of critical points and their description in terms of CFT. We then review the notion of quantum phase transitions and describe how entanglement may be used to diagnose and characterise quantum critical points. In this context, we discuss the bipartite fidelity. This quantity shall allow us to unveil new aspects of quantum phase transitions, and is the central object under consideration in this part of the thesis. We conclude with elements of context regarding the new results presented in the subsequent chapters and give the organisation of Part I.

1.1 Critical phenomena and lattice models

In the statistical description of a system at temperature T, the thermodynamic quantities are given in terms of derivatives of the free energy

$F = -k_B T \log Z$, where Z is the partition function and k_B is the Boltzmann constant. Mathematically, a phase transition occurs at a point of non-analyticity of the free energy or its derivatives with respect to the external parameters. In most physical models, F is a smooth function of these external parameters in finite size. Formally, phase transitions thus only arise in the thermodynamic limit, where the system size, or more generically the number of degrees of freedom, tends to infinity. However, the finite-size scaling of F yields strong insights into the nature of the transition.

A characteristic feature of a phase transition is its order. We say that a transition is of order n if it is the lowest order of a derivative of the free energy that diverges or is discontinuous at the transition point. This classification based on the degree of non-analyticity of the free energy is known as Ehrenfest's classification. In the modern theory of phase transitions, we only distinguish between first- and second-order transitions. For instance, the transition from liquid water to vapour at atmospheric pressure is a first-order phase transition. There is a discontinuity in the density of water at $T = 373.15$K related to latent heat absorbed by the system. Second-order phase transitions, on the other hand, do not involve latent heat and are thus sometimes referred to as continuous phase transitions. A point at which a second-order phase transition occurs is called a *critical point*. In the following we shall focus exclusively on the latter.

A way to investigate phase transitions is to consider simplified models that (i) reproduce the qualitative aspects of the system under consideration, but (ii) are simple enough to be handled with analytical (or affordable numerical) methods. The term solvable, or solved models, as Baxter prefers to put it [55], refers to models whose free energy is exactly known in finite size or in the thermodynamic limit. We focus on solvable lattice models that describe physical systems whose degrees of freedom reside on a discrete finite domain. We use the terminology *critical lattice model* for models that describe second-order phase transitions in the thermodynamic limit.

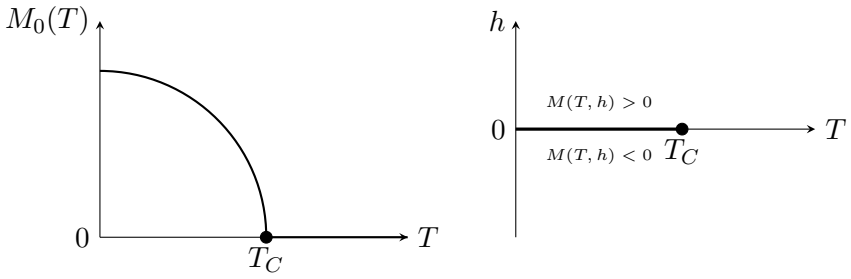

Figure 1.1: Typical behaviour of the spontaneous magnetisation $M_0(T)$ as a function of T (left) and the magnetisation $M(T,h)$ in the hT-plane (right).

1.1.1 Ising model and the ferromagnetic transition

In this section we discuss the ferromagnetic transition and its description by the Ising model, a paradigmatic example of critical lattice model [73].

Consider an iron bar at temperature T in an external magnetic field h. By convention, $h > 0$ corresponds to the field pointing in the direction that we denote by *up*, and $h < 0$ indicates a field pointing in the opposite direction, denoted *down*. The magnetisation $M(T,h)$ of the bar is a function of T and h, and indicates the average direction in which the spins of its atoms point to. A quantity of interest is the spontaneous magnetisation M_0, defined as the residual magnetisation of the bar as the external field is turned to zero from positive values,

$$M_0(T) = \lim_{h \to 0^+} M(T,h). \tag{1.1}$$

In a strong positive external magnetic field, all the spins are aligned in the direction of the field and we have $M(T,h) > 0$. At low temperatures, the thermal fluctuations do not break the magnetic order in the thermodynamic limit, and the residual magnetisation is non-zero: $M_0 > 0$. Conversely, when the temperature reaches the Curie temperature T_C, the magnetic order is broken and $M_0 = 0$. The typical behaviour of $M_0(T)$ is illustrated in the left panel of Figure 1.1.

To study the ferromagnetic transition, Lenz devised a simple model that is now known as the *Ising model* [74]. The model is named after his

student, Ernst Ising, who solved it in one dimension [75]. It is defined as follows. Let us consider a d-dimensional lattice $\mathbb{D} \subset \mathbb{Z}^d$ where each site is occupied by an atom. The atoms interact between nearest neighbours via the exchange interaction and there is a constant external magnetic field. To model this situation, each site $x_j \in \mathbb{D}$ of the lattice is assigned with a classical spin $\sigma_{x_j} = \pm 1$. For a given configuration of spins $\{\sigma_{x_j}\}$, the magnetic energy is

$$E(\{\sigma_{x_j}\}) = -J \sum_{\langle x_i, x_j \rangle} \sigma_{x_i} \sigma_{x_j} - h \sum_{x_j} \sigma_{x_j} \tag{1.2}$$

where the first sum runs over all pairs of neighbouring sites, $J > 0$ is the exchange interaction and h is the external magnetic field. The probability of a given configuration $\{\sigma_{x_j}\}$ at temperature T is

$$P(\{\sigma_{x_j}\}) = \frac{1}{Z} \mathrm{e}^{-E(\{\sigma_{x_j}\})/k_B T}, \quad Z = \sum_{\{\sigma_{x_j}\}} \mathrm{e}^{-E(\{\sigma_{x_j}\})/k_B T} \tag{1.3}$$

where Z is the partition function. The factor $\exp(-E(\{\sigma_{x_j}\})/k_B T)$ in the definition of the probability is often referred to as the *Boltzmann weight* of the configuration $\{\sigma_{x_j}\}$. These quantities allow us to compute correlation functions of lattice observables. For instance, the n-point correlation function of spin variables is

$$\langle \sigma_{x_1} \cdots \sigma_{x_n} \rangle_{\mathbb{D}} = \sum_{\{\sigma_{x_j}\}} \sigma_{x_1} \cdots \sigma_{x_n} P(\{\sigma_{x_j}\}). \tag{1.4}$$

In particular, the magnetisation is the sum over all the sites $x_j \in \mathbb{D}$ of the one-point functions,

$$M(T, h) = \sum_{x_j} \langle \sigma_{x_j} \rangle_{\mathbb{D}}, \tag{1.5}$$

and is obtained as the derivative of the free energy with respect to the magnetic field,

$$M(T, h) = -\frac{\partial F}{\partial h}, \quad F = -k_B T \log Z. \tag{1.6}$$

Ising showed that the model does not exhibit a phase transition in one dimension for $T > 0$, but then erroneously concluded to the absence of a

critical point in any dimension. However, Peierls proved that the model exhibits a phase transition at non-zero temperature in any dimension $d \geqslant 2$ [76]. The critical temperature of the two-dimensional model was computed by Kramers and Wannier [77], and reads

$$\tanh\left(\frac{2J}{k_B T_C}\right) = \frac{1}{\sqrt{2}}. \tag{1.7}$$

In 1944, Onsager found the exact expression for the free energy of the model in two dimensions without external magnetic field [78]. It is hard to overemphasise the importance of this result. This exact solution triggered an enormous amount of research in solvable lattice models and phase transitions [36, 55, 73]. Because of its exact solvability and rich phenomenology, the Ising model is a perfect theoretical laboratory to investigate collective and emergent behaviour in seemingly unrelated contexts, such as nonequilibrium physics [79, 80], machine learning [81] and sociology [82]. The solutions of the Ising model in two dimensions with an external field and in three dimensions are still open problems that go far beyond the scope of this dissertation.

To better understand the qualitative aspects of the ferromagnetic transition in the two-dimensional Ising model, it is useful to consider the behaviour of the magnetisation in the hT-plane, as illustrated in the right panel of Figure 1.1. In the region $h \neq 0$ and $T < T_C$, the magnetisation is non-zero and has the same sign as h. The region where $h = 0$ and $T < T_C$ corresponds to a line of discontinuity of the magnetisation. Indeed, as we approach the line from positive value of h, the magnetisation tends to $M_0 > 0$. Conversely, by symmetry, when we approach the line from negative values of h, we have $\lim_{h\to 0^-} M(T,h) = -M_0 < 0$. Since the magnetisation is the derivative of the free energy with respect to the magnetic field, the region $h = 0$ and $T < T_C$ is a continuous line of first-order critical points. For $T > T_C$, the magnetisation is continuous and vanishes smoothly as the external magnetic field is turned to zero. There are thus no transitions in that regime. At the extremity of the line of first-order transition, where $h = 0$ and $T = T_C$, the spontaneous magnetisation is vanishing and continuous, but its derivatives with respect to both h and T diverge. These quantities are the magnetic susceptibility $\chi(T,h)$ and specific heat $C(T,h)$, respectively. The point $h = 0$ and $T = T_C$ is thus a second-order critical point. In the vicinity of this

critical point, the behaviour of the various thermodynamic quantities is completely determined by a set of numbers called *critical exponents*. In terms of $t = (T - T_C)/T_C$, we have

$$C(T,0) \sim t^{-\alpha}, \qquad t \to 0^+, \tag{1.8a}$$
$$C(T,0) \sim (-t)^{-\alpha'}, \quad t \to 0^-, \tag{1.8b}$$
$$M_0(T) \sim (-t)^{\beta}, \qquad t \to 0^-, \tag{1.8c}$$
$$\chi(T,0) \sim t^{-\gamma}, \qquad t \to 0^+, \tag{1.8d}$$
$$\chi(T,0) \sim (-t)^{-\gamma'}, \quad t \to 0^-, \tag{1.8e}$$
$$M(T_C,h) \sim h^{1/\delta}, \qquad h \to 0^+, \tag{1.8f}$$

where the notation $X \sim Y$ indicates that the ratio X/Y is non-vanishing nor diverging in the thermodynamic limit. Another aspect of second-order critical points highlighted by the Ising model is the divergence of the correlation length in the thermodynamic limit. This quantity is denoted ξ, and characterises the exponential decay of the spin-spin correlation function away from the critical point. It is interpreted as the typical distance after which two spins cease to be correlated. The correlation length is a function of the temperature and the magnetic field, $\xi = \xi(T,h)$, and its divergence in the vicinity of the critical point defines two new critical exponents,

$$\xi(T,0) \sim t^{-\nu}, \qquad t \to 0^+. \tag{1.8g}$$
$$\xi(T,0) \sim (-t)^{-\nu'}, \quad t \to 0^-. \tag{1.8h}$$

For the two-dimensional Ising model, the critical exponents are [55]

$$\alpha = \alpha' = 0, \quad \beta = 1/8, \quad \gamma = \gamma' = 7/4, \quad \delta = 15, \quad \nu = \nu' = 1. \tag{1.9}$$

The exponents α and α' vanish because the divergence of the specific heat in the vicinity of the critical point is logarithmic, $C(T,0) \sim \log|t|$ as $t \to 0$.

Critical exponents encode universal properties about the transition they pertain to. They do not depend on the microscopic details of the model, but rather on global properties such as its symmetries, boundary conditions or dimensionality [55]. Two critical systems with the same critical exponents are said to belong to the same *universality class* and the transitions they describe are qualitatively the same, even if their microscopic

origin differ. For instance, it was observed experimentally that certain critical properties of fluids and magnetic materials are similar [83]. From a theoretical perspective, the investigation of phase transitions is strongly related to the classification and characterisation of universality classes.

1.1.2 Transfer matrix formalism

The solution of the two-dimensional Ising model by Onsager relies on the diagonalisation of the so-called transfer matrix. The idea of using transfer matrices to solve statistical models has since then been used in a vast class of models [84, 85].

Let us consider the two-dimensional Ising model defined on the square lattice of height $M+1$ and width N. For simplicity we assume periodic boundary conditions in the horizontal direction, as illustrated in Figure 1.2. In the vertical direction, we shall consider periodic, fixed and free boundary conditions. In the periodic case, the row $M+1$ is identified with the first one, and the whole lattice is a torus. On the other hand, fixed and free boundary conditions correspond to either fixing the spin variables on the bottom and top rows of the lattice, or letting them free to take any value. In both cases, the corresponding lattice is a cylinder.

In two dimensions, each site of the lattice is labelled by two integers (i, j), and we denote by $\sigma_{i,j} = \pm 1$ the associated spin variable. The energy of a configuration (1.2) only contains interactions between neighbouring sites, and it is possible to express it as a sum over terms that only depend on the configurations of successive rows:

$$E(\{\sigma_{i,j}\}) = \sum_{r=1}^{M} \boldsymbol{E}(\boldsymbol{S}_r, \boldsymbol{S}_{r+1}). \tag{1.10}$$

Here, $\boldsymbol{S}_r = (\sigma_{1,r}, \sigma_{2,r}, \dots, \sigma_{N,r})$ is the configuration of the row r. The function $\boldsymbol{E}(\boldsymbol{S}_r, \boldsymbol{S}_{r+1})$ contains the interaction terms within rows r and $r+1$ as well as the interactions between the two rows. The partition function is

$$Z = \sum_{\{\sigma_{i,j}\}} \mathrm{e}^{-\boldsymbol{E}(\boldsymbol{S}_1,\boldsymbol{S}_2)} \mathrm{e}^{-\boldsymbol{E}(\boldsymbol{S}_2,\boldsymbol{S}_3)} \cdots \mathrm{e}^{-\boldsymbol{E}(\boldsymbol{S}_{M-1},\boldsymbol{S}_M)} \mathrm{e}^{-\boldsymbol{E}(\boldsymbol{S}_M,\boldsymbol{S}_{M+1})} \tag{1.11}$$

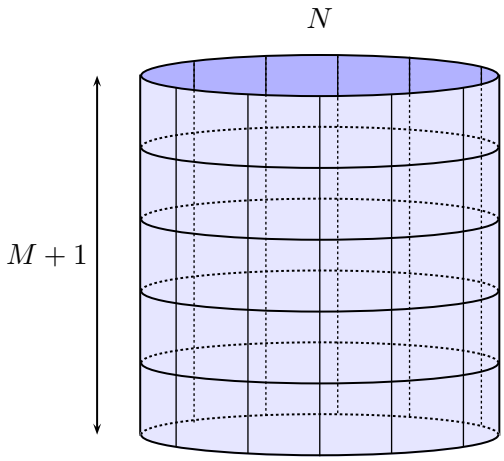

Figure 1.2: Illustration of a two-dimensional lattice of width N and height $M+1$ with periodic boundary conditions in the horizontal direction.

where the factor $(k_B T)^{-1}$ is absorbed in the definition of the energy. The form of Z suggests that it may be written in terms of a $2^N \times 2^N$ square matrix $\mathcal{T}$ whose components are labelled by the configurations of the rows:

$$\mathcal{T} = (\mathcal{T}_{\boldsymbol{S},\boldsymbol{S}'})_{\boldsymbol{S},\boldsymbol{S}' \in \{-1,+1\}^N}, \quad \mathcal{T}_{\boldsymbol{S},\boldsymbol{S}'} = \mathrm{e}^{-\boldsymbol{E}(\boldsymbol{S},\boldsymbol{S}')}. \tag{1.12}$$

The matrix $\mathcal{T}$ is the so-called *transfer matrix* and acts on the Hilbert space $\mathcal{H} = (\mathbb{C}^2)^{\otimes N}$ of dimension 2^N. Each row configuration $\boldsymbol{S}$ is associated with a basis vector of $\mathcal{H}$ that we denote by $|\boldsymbol{S}\rangle$. We use the canonical basis of $\mathbb{C}^2$,

$$|\uparrow\rangle = \begin{pmatrix} 1 \\ 0 \end{pmatrix}, \qquad |\downarrow\rangle = \begin{pmatrix} 0 \\ 1 \end{pmatrix}, \tag{1.13}$$

and a spin $\sigma_{i,j} = 1$ or $\sigma_{i,j} = -1$ is associated with $|\uparrow\rangle$ or $|\downarrow\rangle$, respectively. For example, the configuration $\boldsymbol{S} = (+,+,-,+,-)$ is associated with the vector $|\boldsymbol{S}\rangle = |\uparrow\uparrow\downarrow\uparrow\downarrow\rangle$, where $|ab\rangle = |a\rangle \otimes |b\rangle$.

The transfer matrix $\mathcal{T}$ of the two-dimensional Ising model is real and symmetric. It is has real eigenvalues λ_j with multiplicity $m_j > 0$, and

we use the convention $\lambda_0 > \lambda_1 > \dots$ to order them. In the case of periodic boundary conditions in the vertical direction, where the lattice is a torus, the partition function is

$$Z^{\text{torus}} = \text{Tr } \mathcal{T}^M = m_0 \lambda_0^M \Big(1 + \frac{m_1}{m_0}\Big(\frac{\lambda_1}{\lambda_0}\Big)^M + \dots\Big). \tag{1.14}$$

In particular, the largest eigenvalue λ_0 fully determines the partition function in the limit $M \to \infty$.

We now consider the case of fixed and free boundary conditions, where the lattice has the geometry of a cylinder. We denote by $|\boldsymbol{b}_1\rangle$ and $|\boldsymbol{b}_{M+1}\rangle$ the states of the first and top rows, respectively. In the case of fixed boundary conditions, $|\boldsymbol{b}_j\rangle = |\boldsymbol{S}_j\rangle$, $j = 1, M+1$, is a basis vector of the Hilbert space that corresponds to a given spin configuration $\boldsymbol{S}_j$ on row j. The state $|\boldsymbol{b}_j\rangle$ may also be a linear combination of basis vectors. In particular, free boundary conditions correspond to taking both $|\boldsymbol{b}_1\rangle$ and $|\boldsymbol{b}_{M+1}\rangle$ to be the linear combinations of all the basis vectors in the Hilbert space. In both cases, the partition function corresponds to the associated component of $\mathcal{T}^M$, namely

$$Z^{\text{cyl}} = \langle \boldsymbol{b}_{M+1} | \mathcal{T}^M | \boldsymbol{b}_1 \rangle. \tag{1.15}$$

Similarly to the periodic case, the largest eigenvalue of $\mathcal{T}$ determines the partition function and hence the free energy in the thermodynamic limit.

It is possible to define a transfer matrix for most planar models of statistical mechanics with local interactions. The Boltzmann weights are usually parametrised by an arbitrary parameter, traditionally denoted u, and the transfer matrix is $\mathcal{T}(u)$. A model is said to be *integrable* if the transfer matrices commute at different values of this parameter [55],

$$[\mathcal{T}(u), \mathcal{T}(v)] = 0. \tag{1.16}$$

In that case, u is referred to as the *spectral parameter*, since the eigenvectors of $\mathcal{T}(u)$ do not depend on u, whereas the eigenvalues do. The commutation relation (1.16) implies that the transfer matrix generates a family of commuting operators. The first order in the Taylor expansion of $\mathcal{T}(u)$ around $u = 0$ contains an operator that is usually identified as

the quantum Hamiltonian H of an underlying one-dimensional quantum model,

$$H \propto -\frac{\mathrm{d}\log \mathcal{T}(u)}{\mathrm{d}u}\Big|_{u=0}. \tag{1.17}$$

In particular, we have $[H, \mathcal{T}(u)] = 0$ and the eigenvectors of $\mathcal{T}(u)$ that correspond to its largest eigenvalue are groundstate vectors of H. We discuss explicit examples of the connection between two-dimensional statistical models and one-dimensional quantum Hamiltonians in subsequent chapters. This connection allows us to use the formalism and the field-theoretical description of two-dimensional critical models to investigate quantum phase transitions in one-dimensional quantum models.

1.1.3 Scaling limit of lattice models

In this section we discuss the continuous limit of critical lattice models.

Let us consider a generic two-dimensional lattice model defined on a finite square lattice $\mathbb{D}_{a,N} \subset (a\mathbb{Z})^2$ of size $N \times N$ where $a > 0$ is the lattice spacing. On the lattice, the sites are labelled with variables x_j that indicate their positions in terms of number of lattice sites. For instance, on the top left part of Figure 1.3, we have $x_1 = (1, 2)$ and $x_2 = (3, 3)$ if we place the origin on the bottom left corner of the lattice. The lattice $\mathbb{D}_{a,N}$ is embedded in a finite planar region $\mathcal{D} \subset \mathbb{R}^2$ such that each site $x_j \in \mathbb{D}_{a,N}$ is at position $\boldsymbol{r}(x_j) \in \mathcal{D}$. The distance between two lattice sites x_1 and x_2 is $\|\boldsymbol{r}(x_2) - \boldsymbol{r}(x_1)\|$, where $\|\bullet\|$ is the Euclidean norm in $\mathbb{R}^2$. Still on the top left part of Figure 1.3, we have $\boldsymbol{r}(x_1) = (a, 2a)$ and $\boldsymbol{r}(x_2) = (3a, 3a)$.

We denote by ϕ_j^{latt} local lattice quantities that take the value $\phi_j^{\mathrm{latt}}(x_j)$ on site $x_j \in \mathbb{D}_{a,N}$. On the lattice, a correlation function is defined as the average of a product of local quantities,

$$\langle \phi_1^{\mathrm{latt}}(x_1) \cdots \phi_n^{\mathrm{latt}}(x_n) \rangle_{\mathbb{D}_{a,N}} = \frac{1}{Z} \sum_{\{\phi_j^{\mathrm{latt}}\}} \phi_1^{\mathrm{latt}}(x_1) \cdots \phi_n^{\mathrm{latt}}(x_n)\ \mathrm{e}^{-E(\{\phi_j^{\mathrm{latt}}\})}, \tag{1.18}$$

where $E(\{\phi_j^{\mathrm{latt}}\})$ is the energy associated to a given configuration of the lattice observables, and Z is the partition function. The factor $(k_B T)^{-1}$

is absorbed in the definition of the energy. We also assume that the energy functional $E(\{\phi_j^{\rm latt}\})$ only contains short-ranged interactions. Away from criticality, the correlation length is much smaller than the typical size of the system, $a < \xi \ll N$, and the two-point functions are exponentially suppressed by a factor proportional to $\exp\left(-\|\boldsymbol{r}(x_2) - \boldsymbol{r}(x_1)\|/\xi\right)$ when $\|\boldsymbol{r}(x_1) - \boldsymbol{r}(x_2)\| \gg a$.

At the critical point, the correlation length is of the order of the system size, and all the points in the lattice are correlated. As a consequence, the correlation functions decay algebraically rather than exponentially, and the system becomes invariant under scale transformations [36]. The idea of such transformations is to increase the system size while reducing the lattice spacing, so that the Euclidean distances are kept constant. The new system size and lattice spacing are denoted N' and a', respectively, and they satisfy $N'a' = Na$. The corresponding lattice, denoted $\mathbb{D}_{a',N'}$, is closer to a continuous approximation of the domain $\mathcal{D}$. We give an example of a scale transformation in Figure 1.3 with $N' = 2N$ and $a' = a/2$. In particular, we illustrate how a pair of points $\{x_1, x_2\}$ of $\mathbb{D}_{a,N}$ is mapped onto $\{x_1', x_2'\} = \{2x_1, 2x_2\}$ in $\mathbb{D}_{a',N'}$, so that $\boldsymbol{r}(x_1) = \boldsymbol{r}(x_1')$ and $\boldsymbol{r}(x_2) = \boldsymbol{r}(x_2')$. The *scaling limit* corresponds to the simultaneous limits $N \to \infty$ and $a \to 0$ while the Euclidean distances are kept constant, as we illustrate in the bottom part of Figure 1.3. In this example, $\boldsymbol{r}_1 = \boldsymbol{r}(x_1) = \boldsymbol{r}(x_1')$ and $\boldsymbol{r}_2 = \boldsymbol{r}(x_2) = \boldsymbol{r}(x_2')$.

To discuss the implications of scale invariance in the scaling limit, we introduce the notation $\phi_j^{\rm latt}(\boldsymbol{r}_j)$ with $\boldsymbol{r}_j \in \mathcal{D}$. It denotes the lattice quantity $\phi_j^{\rm latt}$ evaluated on the lattice site $x_j \in \mathbb{D}_{a,N}$ with $\boldsymbol{r}(x_j) = \boldsymbol{r}_j$. If there are no sites at position $\boldsymbol{r}_j$, we evaluate $\phi_j^{\rm latt}$ on a site x_j such that $\|\boldsymbol{r}(x_j) - \boldsymbol{r}_j\| \leq \|\boldsymbol{r}(x_i) - \boldsymbol{r}_j\|$ for all $x_i \in \mathbb{D}_{a,N}$. The algebraic decay of the correlation functions at the critical point suggests that the limit

$$\lim_{\substack{a\to 0\\ N\to\infty\\ aN=\text{cst.}}} a^{-\sum_{j=1}^n Y_j} \langle \phi_1^{\rm latt}(\boldsymbol{r}_1) \cdots \phi_n^{\rm latt}(\boldsymbol{r}_n)\rangle_{\mathbb{D}_{a,N}} \tag{1.19}$$

exists for suitable combinations of local lattice observables and numbers Y_j. Since the scaling limit corresponds to a continuum limit of the lattice, we expect the scaled lattice correlation functions to correspond to correlation functions of fields $\phi_j(\boldsymbol{r})$ of an Euclidean quantum field

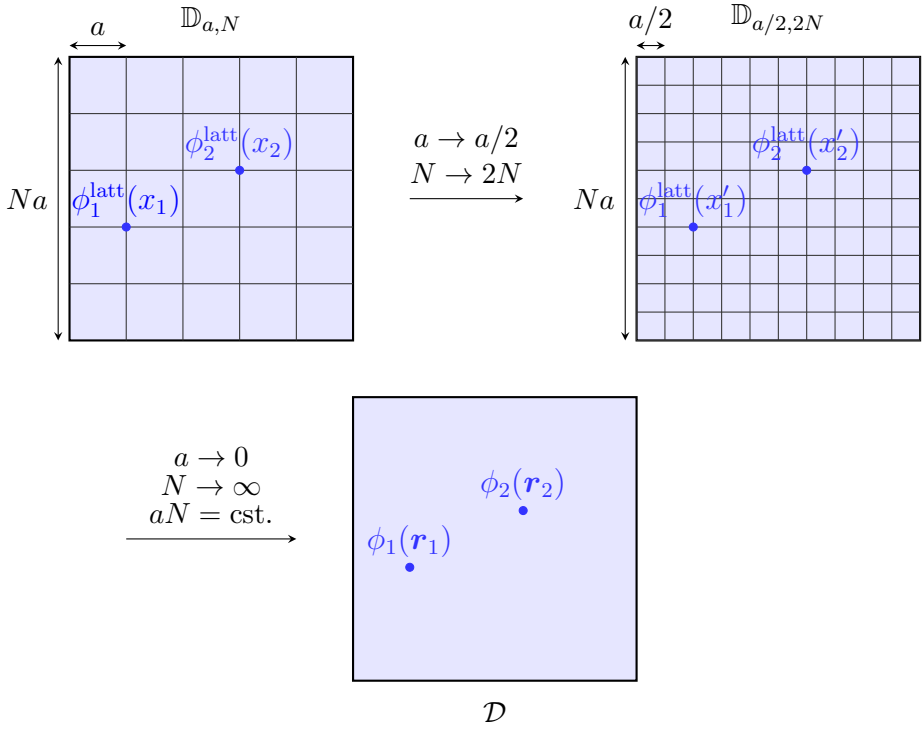

Figure 1.3: Illustration of a scale transformation and the scaling limit from a lattice of size $N \times N$ with lattice spacing $a > 0$.

theory (QFT) in two dimensions defined on the domain $\mathcal{D}$,

$$\lim_{\substack{a\to 0\\ N\to\infty\\ aN=\text{cst.}}} a^{-\sum_{j=1}^n Y_j} \langle \phi_1^{\text{latt}}(\boldsymbol{r}_1) \cdots \phi_n^{\text{latt}}(\boldsymbol{r}_n) \rangle_{\mathbb{D}_{a,N}} = \langle \phi_1(\boldsymbol{r}_1) \cdots \phi_n(\boldsymbol{r}_n) \rangle_{\mathcal{D}}. \tag{1.20}$$

The numbers Y_j are then interpreted as the so-called scaling dimensions of the fields $\phi_j(\boldsymbol{r})$.

In the scaling limit, many aspects of critical lattice models are described by CFTs, field theories whose action is invariant under conformal transformations. These transformations preserve the angles, and include translations, rotations, dilations and special conformal transformations. We illustrate a conformal transformation in Figure 1.4. An important aspect of CFTs is local conformal invariance, namely the correlation functions transform covariantly under coordinate transformations that

are conformal in the vicinity of the fields insertion points. In two dimensions, any analytical function is a local conformal map, whereas in higher dimensions, the group of conformal transformations is finite-dimensional. For that reason, CFTs in two dimensions play a special role, and in the following we exclusively focus on that case.

Proving the conformal invariance of a critical lattice model is a notoriously challenging task [86]. There are rigorous results regarding the conformal invariance of the model of critical site percolation on the triangular lattice [87] and the critical Ising model in two dimensions [88], but in most cases the conformal invariance of critical lattice models in the scaling limit is a conjecture. It is often argued that the scale invariance at second-order critical points in two dimensions implies conformal invariance, but it also requires a traceless stress-energy tensor [89]. In most critical models, both conditions are met, but there are counterexamples of systems with scale invariance that are not conformally invariant [90]. In the rest of the thesis, we use the correspondence between criticality and CFT as a working hypothesis that we test by comparing exact lattice results with CFT predictions. The calculations performed in the field theory do not depend on the microscopic details of the initial lattice model in finite size. For that reason, results that are obtained with CFT arguments are said to be *universal*. The problem of classifying different second-order phase transitions mainly reduces to determining the underlying CFT that describes the scaling limit of local lattice correlation functions. Different critical points described by the same CFT belong to the same universality class.

1.1.4 Aspects of $1 + 1d$ CFT

In this section, we discuss some chosen aspects of CFT in two dimensions. We refer to the vast literature on the subject for further discussions [36, 91, 92]. Planar CFTs are suited to describe two-dimensional critical model of statistical mechanics and one-dimensional quantum critical models. In the former case, the two dimensions are space dimensions, whereas in the latter one dimension corresponds to the physical space and the other is interpreted as the Euclidean time. For this reason, we often refer to planar CFTs as $1 + 1d$ CFTs.

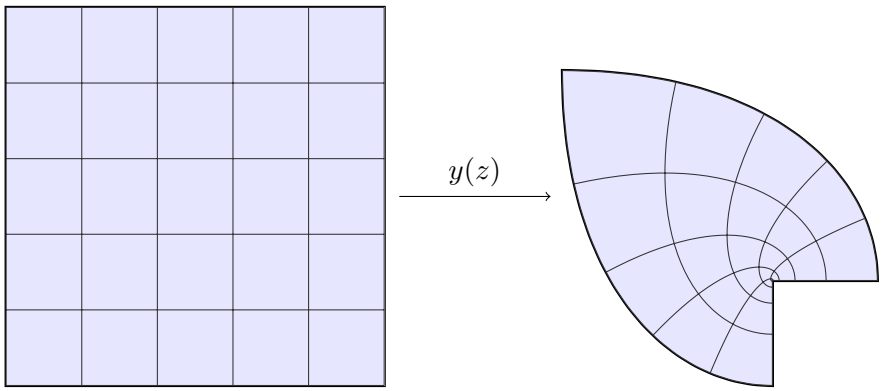

Figure 1.4: Illustration of the conformal transformation $y(z) = z^3$.

Primary fields

In two dimensions, it is common to work in the complex plane $\mathbb{C}$ with the complex coordinates z and $\bar{z}$. The coordinate $\bar{z}$ is often identified as the complex conjugate of z at the end of the developments. We say that a field $\phi(z, \bar{z})$ is *primary* if its transformation law under any conformal map $y = y(z)$ is

$$\phi(y, \bar{y}) = \Big(\frac{\mathrm{d}y}{\mathrm{d}z}\Big)^{-\Delta}\Big(\frac{\mathrm{d}\bar{y}}{\mathrm{d}\bar{z}}\Big)^{-\bar{\Delta}}\phi(z, \bar{z}) \tag{1.21}$$

where the numbers Δ and $\bar{\Delta}$ are the so-called holomorphic and anti-holomorphic conformal weights of ϕ. The combinations $Y = \Delta + \bar{\Delta}$ and $S = \Delta - \bar{\Delta}$ define the scaling dimension and the spin of the field, respectively.

The conformal invariance of the theory fixes the form of two-point functions of primary fields on the complex plane $\mathbb{C}$,

$$\langle \phi_1(z_1, \bar{z}_1)\phi_2(z_2, \bar{z}_2)\rangle_{\mathbb{C}} = \frac{\delta_{\Delta_1,\Delta_2}\delta_{\bar{\Delta}_1,\bar{\Delta}_2}C_{12}}{(z_2 - z_1)^{\Delta_1+\Delta_2}(\bar{z}_2 - \bar{z}_1)^{\bar{\Delta}_1+\bar{\Delta}_2}} \tag{1.22}$$

where $\delta_{i,j}$ is the Kronecker delta, Δ_j and $\bar{\Delta}_j$ are the conformal weights of the fields ϕ_j, $j = 1, 2$, and C_{12} is a constant. The fields are usually normalised such that $C_{12} = 1$ and we say that the two-point function is completely determined by conformal invariance. In general, the n-point functions of primary fields with $n > 2$ involve so-called *structure*

constants. These constants are not fixed by conformal invariance only, and their evaluation is typically a hard problem. For instance, the three-point function of spinless primary fields is

$$\langle \phi_1(z_1,\bar{z}_1)\phi_2(z_2,\bar{z}_2)\phi_3(z_3,\bar{z}_3)\rangle_{\mathbb{C}} = \frac{C_{123}}{z_{12}^{2(\Delta_1+\Delta_2-\Delta_3)} z_{13}^{2(\Delta_1+\Delta_3-\Delta_2)} z_{23}^{2(\Delta_2+\Delta_3-\Delta_1)}} \tag{1.23}$$

where $z_{ij} = |z_i - z_j|$ and C_{123} is an example of a structure constant.

The knowledge of the correlation functions of primary fields on the complex plane allows one to compute the correlation functions on any domain that can be mapped to $\mathbb{C}$ under a conformal transformation. However, the investigation of CFTs in domains that possess a boundary is also relevant for many problems in statistical mechanics [93]. The simplest domain with a boundary is the upper-half plane $\mathbb{H}$. Boundary fields only depend on one variable z, and in this case it is a real number. Under a conformal map $y = y(z)$, primary boundary fields transform as

$$\phi(y) = \left(\frac{\mathrm{d}y}{\mathrm{d}z}\right)^{-\Delta} \phi(z) \tag{1.24}$$

and their two-point function on the upper-half plane is

$$\langle \phi_1(z_1)\phi_2(z_2)\rangle_{\mathbb{H}} = \delta_{\Delta_1,\Delta_2} \frac{C_{12}}{(z_2 - z_1)^{\Delta_1+\Delta_2}}. \tag{1.25}$$

Virasoro algebra and radial quantisation

In CFT, there is a field-operator correspondence, where fields are associated with operators that act on the Hilbert space of the theory. The Hilbert space is infinite-dimensional, and its structure is closely related to the representation theory of the Virasoro algebra [94]. The generators of this algebra are denoted L_n and satisfy the commutation relation

$$[L_m, L_n] = (m-n)L_{m+n} + \frac{c}{12} m(m^2-1)\delta_{m+n,0} \tag{1.26}$$

where c is the so-called *central charge*. There is also an antiholomorphic copy of the algebra generated by operators $\bar{L}_n$ with central charge $\bar{c}$. In the cases we consider, we have $c = \bar{c}$ and only focus on the holomorphic copy. The operators L_n and $\bar{L}_n$ are the generators of the local conformal

transformations. In particular, the combination $L_0 + \bar{L}_0$ generates the dilations in the complex plane. Let us now consider the conformal map $y(z) = N/(2\pi) \log z$ that maps the complex plane punctured at the origin onto an infinite cylinder of circumference N. On the cylinder, the longitudinal direction is interpreted as time, whereas the periodic direction is space. In this setting, the operator that generates the time evolution is the Hamiltonian H_{cyl}. The dilations in the plane correspond to longitudinal translation on the cylinder, or time evolution, and H_{cyl} reads [95, 96]

$$H_{\text{cyl}} = \frac{2\pi}{N}(L_0 + \bar{L}_0) - \frac{\pi c}{6N}. \tag{1.27}$$

The central charge in this formula accounts for the introduction of the length-scale N in the system, and is sometimes called the *conformal anomaly* for that reason.

Let us now discuss the structure of the Hilbert space of a CFT. A first defining feature is the existence of a state, denoted $|0\rangle$, that is invariant under global conformal transformations. It is the vacuum of the theory, and satisfies

$$L_n|0\rangle = \bar{L}_n|0\rangle = 0, \quad n \geqslant -1. \tag{1.28}$$

In this operatorial approach, a spinless primary field ϕ with conformal weight Δ corresponds to an operator whose action on the vacuum yields a highest-weight vector $|\phi\rangle$ of the Hilbert space. It is defined as

$$|\phi\rangle = \lim_{z,\bar{z}\to 0} \phi(z,\bar{z})|0\rangle \tag{1.29}$$

and satisfies

$$\begin{aligned} L_0|\phi\rangle &= \bar{L}_0|\phi\rangle = \Delta|\phi\rangle, \\ L_n|\phi\rangle &= \bar{L}_n|\phi\rangle = 0, \quad n \geqslant 1. \end{aligned} \tag{1.30}$$

Moreover, the state $|\phi\rangle$ is an eigenstate of the Hamiltonian (1.27), with eigenvalue

$$E_\Delta = \frac{4\pi}{N}\Delta - \frac{\pi c}{6N}. \tag{1.31}$$

The action of the Virasoro generators L_n with $n < 0$ on the highest-weight vector $|\phi\rangle$ generates so-called descendent states. These states span an infinite-dimensional vector space, and the action of the Virasoro

algebra on this vector space defines a so-called *Verma module*. A basis of the descendant states is

$$L_{-k_1}L_{-k_2}\cdots L_{-k_n}|\phi\rangle, \quad 1 \leqslant k_1 \leqslant \cdots \leqslant k_n, \quad n \geqslant 1. \tag{1.32}$$

We define the dual basis of states with the relation $L_n^\dagger = L_{-n}$, and the dual state $\langle\phi| = |\phi\rangle^\dagger$ satisfies $\langle\phi|L_n = 0$ for $n < 0$. Moreover, we fix the normalisation such that $\langle\phi|\phi\rangle = 1$. The inner product between two states $|\{k_i\}\rangle = L_{-k_1}\cdots L_{-k_n}|\phi\rangle$ and $|\{\ell_j\}\rangle = L_{-\ell_1}\cdots L_{-\ell_m}|\phi\rangle$ is

$$\langle\{k_i\}|\{\ell_j\}\rangle = \langle\phi|L_{k_n}\cdots L_{k_1}L_{-\ell_1}\cdots L_{-\ell_m}|\phi\rangle. \tag{1.33}$$

As an example, let us compute the overlap $\langle\phi|L_nL_{-n}|\phi\rangle$ for $n \geqslant 1$. With the commutation relation (1.26), the properties of the highest-weight vector (1.30) and the normalisation $\langle\phi|\phi\rangle = 1$, we find

$$\begin{aligned}\langle\phi|L_nL_{-n}|\phi\rangle &= \langle\phi|L_{-n}L_n + 2nL_0 + \frac{c}{12}n(n^2-1)|\phi\rangle \\ &= 2n\Delta + \frac{c}{12}n(n^2-1).\end{aligned} \tag{1.34}$$

This simple example illustrates the fact that the inner product between a state and its dual depends on the conformal data of the CFT and is not necessarily positive. For instance, if $c < 0$ and $\Delta < 0$, we have $\langle\phi|L_nL_{-n}|\phi\rangle < 0$.

Unitary minimal models

We say that a representation of the Virasoro algebra is *unitary* if it contains no states $|\gamma\rangle$ such that $\langle\gamma|\gamma\rangle < 0$. As we saw, the definition of the inner product depends on the central charge c of the Virasoro algebra and the conformal weight Δ of the highest-weight vector of the representation. Hence, imposing the unitarity of a representation constrains the possible values of c and Δ. The investigation of the consequences of these constraints led to the notion of minimal models [97–99]. For $c \geqslant 1$, the unitarity of Verma modules is guaranteed provided $\Delta \geqslant 0$. For $c < 1$, the structure of the representations is more complex. Usually, the Verma modules are non-unitary, but there are values of the central charge and conformal weights such that quotients of Verma modules are

m	c	Δ	lattice model
2	0	0	/ (trivial)
3	$\frac{1}{2}$	$0, \frac{1}{16}, \frac{1}{2}$	Ising model
4	$\frac{7}{10}$	$0, \frac{3}{80}, \frac{1}{10}, \frac{7}{16}, \frac{3}{5}, \frac{3}{2}$	Tricritical Ising model
5	$\frac{4}{5}$	$0, \frac{1}{40}, \frac{1}{15}, \frac{1}{8}, \frac{2}{5}, \frac{21}{40}, \frac{2}{3}, \frac{7}{5}, \frac{13}{8}, 3$	3-state Potts model

Table 1.1: Conformal data of the first unitary minimal models and associated lattice models.

unitary. These values of the central charges and conformal weights are given by the Kac formula,

$$\begin{aligned} c &= 1 - \frac{6}{m(m+1)}, \quad m \geqslant 2, \\ \Delta = \Delta_{r,s} &= \frac{[r(m+1) - sm]^2 - 1}{4m(m+1)}, \quad 1 \leqslant s \leqslant r \leqslant m-1, \end{aligned} \tag{1.35}$$

where m, s, r are integers. The classification of unitary minimal models plays a major role in our understanding of critical models. Indeed, for most values of m, there are known critical lattice models whose scaling limits are described by the corresponding minimal models. In Table 1.1, we give the first minimal models with their conformal data and an associated lattice model.

In unitary CFTs, we always have $c \geqslant 0$ and $\Delta \geqslant 0$. As a consequence, the correlations decrease with the distance. In this case, the vacuum of the theory $|0\rangle$ is also the groundstate of the Hamiltonian (1.27) with eigenvalue

$$E_0 = -\frac{\pi c}{6N}. \tag{1.36}$$

Non-unitary CFTs

Imposing unitarity is not a necessary condition to describe proper physical systems. Examples of models described by non-unitary CFTs include disordered systems [100], quantum systems with $\mathcal{PT}$-symmetric

Hamiltonians [101] or statistical models with non-local degrees of freedom [102, 103]. In these models, the correlations are allowed to grow with the distance, and hence there may be fields with negative conformal weights in the CFT description. In this case, the groundstate is no longer the vacuum of the theory. Instead, it is the highest-weight vector associated to the minimal conformal weight of the theory $\Delta_{\min}$, which can be negative. The groundstate eigenvalue of the Hamiltonian (1.27) is thus

$$\begin{aligned} E_{\Delta_{\min}} &= \frac{4\pi}{N}\Delta_{\min} - \frac{\pi c}{6N} \\ &= -\frac{\pi c_{\text{eff}}}{6N} \end{aligned} \tag{1.37}$$

where $c_{\text{eff}} = c - 24\Delta_{\min}$ is interpreted as an effective central charge [104]. The finite-size scaling of the groundstate eigenvalue alone is no longer a sufficient measure of the central charge of the theory.

An important family of non-unitary CFTs are the so-called *logarithmic conformal field theories* (LCFTs) [105, 106]. In particular, the so-called logarithmic minimal models [102] are LCFTs labelled by two coprime integers p, p' with $0 < p < p'$ and denoted $\mathcal{LM}(p, p')$. The central charge is given by

$$c(p, p') = 1 - \frac{6(p - p')^2}{pp'} \tag{1.38}$$

and the conformal weights are

$$\Delta = \Delta_{r,s} = \frac{(p'r - ps)^2 - (p - p')^2}{4pp'}, \quad r, s = 1, 2, \ldots . \tag{1.39}$$

In particular, $\mathcal{LM}(m, m+1)$ is a generalisation of the unitary minimal model labelled by m that contains more fields and where the constraints on m, r, s in (1.35) are relaxed.

The defining feature of logarithmic CFTs is the appearance of Jordan blocks and indecomposable yet reducible representations of the Virasoro algebra. In that case, some eigenstates of L_0 have Jordan partners and are organised in a Jordan cell. The simplest case is a rank-two Jordan cell, where the eigenspace corresponding to an eigenvalue Δ of L_0 is two-dimensional and spanned by the states $|\varphi\rangle$ and $|\omega\rangle$. They satisfy

$$L_0|\varphi\rangle = \Delta|\varphi\rangle, \quad L_0|\omega\rangle = \Delta|\omega\rangle + 2\lambda_0|\varphi\rangle, \tag{1.40}$$

where λ_0 is a non-zero constant. In particular, the action of L_0 restricted the subspace spanned by these states has the form

$$L_0 = \begin{pmatrix} \Delta & 2\lambda_0 \\ 0 & \Delta \end{pmatrix} \tag{1.41}$$

and is not diagonalisable. The field $\varphi(z)$ associated with $|\varphi\rangle$ is a primary field with conformal weight Δ. Similarly, the field associated with $|\omega\rangle$, denoted $\omega(z)$, is its so-called logarithmic partner. We also say that $\omega(z)$ has the conformal weight Δ, even though it is not a primary field. In this context, the conformal weight refers to the eigenvalue of L_0 associated to the Jordan cell. In the context of CFT, the value of λ_0 can be adjusted by changing the normalisation of the field $\omega(z)$, so it is common to normalise it to $\lambda_0 = 1/2$. However, in cases where the fields arise from lattice calculations, they come with a natural normalisation, and it is more convenient to let λ_0 be a free parameter [107].

Under a conformal transformation $y = y(z)$, the fields satisfy [106]

$$\begin{aligned} \varphi(y) &= \left(\frac{\mathrm{d}y}{\mathrm{d}z}\right)^{-\Delta} \varphi(z), \\ \omega(y) &= \left(\frac{\mathrm{d}y}{\mathrm{d}z}\right)^{-\Delta} \left(\omega(z) - 2\lambda_0 \varphi(z) \log\left(\frac{\mathrm{d}y}{\mathrm{d}z}\right)\right), \end{aligned} \tag{1.42}$$

where we assumed that $\varphi(z)$ and $\omega(z)$ are boundary fields inserted on the real axis. On the upper-half plane, their correlation functions are

$$\begin{aligned} \langle \omega(z_0)\omega(z_1)\rangle_{\mathbb{H}} &= \frac{\lambda_1\lambda_2 - 4\lambda_0\lambda_1 \log(z_0 - z_1)}{(z_0 - z_1)^{2\Delta}}, \\ \langle \omega(z_0)\varphi(z_1)\rangle_{\mathbb{H}} &= \frac{\lambda_1}{(z_0 - z_1)^{2\Delta}}, \\ \langle \varphi(z_0)\varphi(z_1)\rangle_{\mathbb{H}} &= 0, \end{aligned} \tag{1.43}$$

where λ_1 and λ_2 are structure constants whose evaluation is typically a hard problem [107]. However, as we shall see, the exact values of these constants do not play any role in our forthcoming computations.

1.2 Quantum criticality

In this section we discuss some aspects of quantum phase transitions. Similarly to the classical case, we consider second-order transitions where the correlation length diverges.

1.2.1 Quantum criticality and universality

In quantum systems, relevant length-scales for the spatial extension of quantum correlations are related to the energy gap in the spectrum of the Hamiltonian. Let us consider a generic one-dimensional quantum system of length N with Hamiltonian H. The spectrum is $E_0 < E_1 < \dots$, where E_0 is the groundstate energy of H. The gaps are defined as $\delta_j = E_j - E_0$, and the correlation length behaves as $\xi \sim \delta_1^{-1}$. For critical systems that exhibit scale invariance and whose scaling limit is described by a CFT, the correlation length scales as the system size, namely

$$\xi \sim N. \tag{1.44}$$

Moreover, at criticality, the gaps δ_j of the leading excited states close as

$$\delta_j \sim N^{-1}. \tag{1.45}$$

In the scaling limit, these low-lying excitations form an infinity of states that is described by a $1+1d$ CFT. A way to access the conformal data of the underlying CFT is to investigate the finite-size scaling of the spectrum of H. For a system with open boundary conditions, the energies E_j of the leading excited states satisfy the large-N expansion [95, 96]

$$E_j = NE_{\text{bulk}} + E_{\text{bndr}} + \frac{\pi\nu_F}{N}\Big(\Delta_j - \frac{c}{24}\Big) + o(N^{-1}), \tag{1.46}$$

where E_{bulk} and E_{bndr} are two non-universal terms, c is the central charge, Δ_j is a conformal weight and ν_F is the so-called Fermi velocity. For free-fermion systems, the latter is defined as $\nu_F = \frac{\mathrm{d}\epsilon(k)}{\mathrm{d}k}|_{k=k_F}$ where $\epsilon(k)$ is the dispersion relation and k_F is the momentum of excitations at the Fermi level. The values of E_{bulk} and E_{bndr} do not depend on j, and hence we say that the Hamiltonian is gapless in the large-N limit.

1.2.2 Quantum spin chains

Spin chains are paradigmatic one-dimensional quantum many-body systems that exhibit critical behaviour. They describe spins located on a discrete lattice that interact between nearest neighbours via the exchange interaction. The first spin chain was introduced by Heinsenberg [108] in order to investigate the quantum origin of magnetism.

A model of considerable importance is the spin-1/2 XXZ quantum spin chain [55]. It is a quantum integrable model in one dimension that possesses a critical regime. The model was first diagonalised by means of the so-called *coordinate Bethe anzatz* [56,109]. In 1967, Lieb showed that the XXZ Hamiltonian commutes with the transfer matrix of the six-vertex model [84], an integrable lattice model in two dimensions originally introduced by Pauling to compute the residual entropy of ice. For a chain of length N with free boundary conditions, the Hamiltonian is

$$H = -\frac{1}{2}\sum_{j=1}^{N-1}\left(\sigma_j^x\sigma_{j+1}^x + \sigma_j^y\sigma_{j+1}^y + \Delta\sigma_j^z\sigma_{j+1}^z\right) \tag{1.47}$$

where Δ is the anisotropy parameter. The specialisation $\Delta = 1$ yields the Heisenberg Hamiltonian, and is now referred to as the spin-1/2 XXX quantum spin chain. In the following, we only consider spin-1/2 quantum spin chains. The Hamiltonian (1.47) acts on the Hilbert space $(\mathbb{C}^2)^{\otimes N}$ and we use the canonical basis (1.13) for $\mathbb{C}^2$. The notation σ_j^a denotes the operator that acts as the Pauli matrix σ^a, $a = x, y, z$, on site $j = 1, \ldots, N$ and trivially on the rest of the chain. It is defined as

$$\sigma_j^a = \underbrace{\mathbb{I}_2 \otimes \cdots \otimes \mathbb{I}_2}_{j-1} \otimes \sigma^a \otimes \underbrace{\mathbb{I}_2 \otimes \cdots \otimes \mathbb{I}_2}_{N-j}, \tag{1.48}$$

where $\mathbb{I}_2$ is the 2×2 identity matrix, and

$$\sigma^x = \begin{pmatrix} 0 & 1 \\ 1 & 0 \end{pmatrix}, \quad \sigma^y = \begin{pmatrix} 0 & -\mathrm{i} \\ \mathrm{i} & 0 \end{pmatrix}, \quad \sigma^z = \begin{pmatrix} 1 & 0 \\ 0 & -1 \end{pmatrix} \tag{1.49}$$

are the Pauli matrices. It is often useful to consider spin chains with periodic boundary conditions. In that case, the first sum in (1.47) runs up to $j = N$ and we impose $\sigma_{j+N}^a \equiv \sigma_j^a$. The two different boundary conditions are illustrated in Figure 1.5.

The XXZ spin chain is gapless in the regime $-1 < \Delta < 1$. In this critical regime, it is described by a free-boson CFT with central charge $c = 1$ [96]. Another paradigmatic critical spin chain is the so-called XY spin chain in an external magnetic field [110]. The Hamiltonian with free boundary conditions is

$$H = -\sum_{j=1}^{N-1}\left(\frac{1+\gamma}{2}\sigma_j^x\sigma_{j+1}^x + \frac{1-\gamma}{2}\sigma_j^y\sigma_{j+1}^y + h\sigma_j^z\right) \tag{1.50}$$

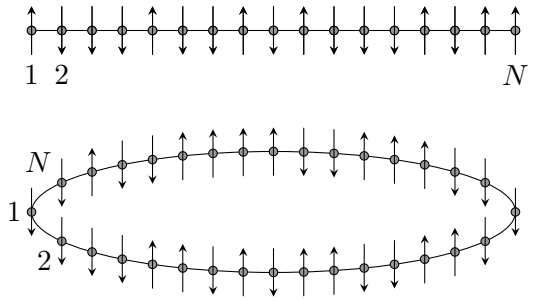

Figure 1.5: Illustration of spin chains with free boundary conditions (top) and periodic boundary conditions (bottom).

where h is the magnetic field and γ is the anisotropy of the spin-spin interaction in the xy-plane. There are two distinct critical regimes in this model [111]. First, for $|h| = 1$ and $|\gamma| \in (0, 1]$, the model is described by a free-fermion CFT with $c = 1/2$ and it is in the Ising universality class. Second, for $\gamma = 0$ and $|h| \in [0, 1]$, the model is described by a free-boson CFT with $c = 1$, similarly to the gapless XXZ spin chain. For other values of h and γ, the XY spin chain is not critical and is described by a massive QFT in the scaling limit.

Diagonalisation of the XX spin chain

The XY spin chain is a free-fermion model, because its diagonalisation implies a mapping from the spin chain onto a model of non-interacting lattice fermions [110]. For simplicity, we focus on the XY spin chain with $\gamma = h = 0$ (or equivalently the XXZ spin chain with $\Delta = 0$), also known as the XX spin chain. We consider a chain with free boundary conditions, but the periodic case is treated with similar techniques. The Hamiltonian is

$$H_f = -\frac{1}{2}\sum_{j=1}^{N-1}\left(\sigma_j^x\sigma_{j+1}^x + \sigma_j^y\sigma_{j+1}^y\right) \tag{1.51}$$

and commutes with the total magnetisation $S^z = \frac{1}{2}\sum_{j=1}^{N}\sigma_j^z$. We present the diagonalisation of this model for two reasons. First, we use the exact diagonalisation of the Hamiltonian to extract the conformal data

of the underlying CFT using (1.46), and hence provide a pedagogical example of the connection between one-dimensional quantum critical models and CFT. Second, we investigate various generalisations of the XX spin chain in forthcoming chapters (with boundary magnetic fields or periodic boundary conditions, for instance). We thus introduce the main technical tools that we use throughout the thesis.

To diagonalise the XX Hamiltonian (1.51), we use the so-called Jordan-Wigner transformation that maps spin operators to fermionic ones,

$$c_j = (-1)^{j-1}\left(\prod_{k=1}^{j-1}\sigma_k^z\right)\sigma_j^-, \qquad c_j^\dagger = (-1)^{j-1}\left(\prod_{k=1}^{j-1}\sigma_k^z\right)\sigma_j^+, \tag{1.52}$$

where $\sigma^\pm = (\sigma^x \pm \mathrm{i}\sigma^y)/2$. The operators c_j and $c_j^\dagger$ satisfy the canonical fermionic anticommutation relations

$$\{c_j, c_k^\dagger\} = \delta_{j,k}, \quad \{c_j, c_k\} = \{c_j^\dagger, c_k^\dagger\} = 0, \quad j,k = 1,\dots,N, \tag{1.53}$$

where $\{a,b\} \equiv ab + ba$. Moreover, the state $|0\rangle = |\downarrow\cdots\downarrow\rangle$ is annihilated by all the c_j operators. By means of the Jordan-Wigner transformation, we recast H_f as

$$\begin{aligned} H_f &= -\sum_{j=1}^{N-1}(c_j^\dagger c_{j+1} + c_{j+1}^\dagger c_j) \\ &= \sum_{i,j=1}^{N}\Lambda_{i,j}c_i^\dagger c_j \end{aligned} \tag{1.54}$$

with

$$\Lambda = \begin{pmatrix} 0 & -1 & 0 & \dots & 0 \\ -1 & 0 & -1 & \dots & 0 \\ 0 & \ddots & \ddots & \ddots & \vdots \\ \vdots & \dots & -1 & 0 & -1 \\ 0 & \dots & 0 & -1 & 0 \end{pmatrix}, \tag{1.55}$$

and the magnetisation operator takes the form $S^z = -\frac{N}{2} + \sum_{j=1}^N c_j^\dagger c_j$. The diagonalisation of Λ yields

$$\Lambda U_k = \epsilon_k U_k, \qquad k = 1,\dots,N, \tag{1.56}$$

with

$$[U_k]_j = \Big(\frac{2}{N+1}\Big)^{\frac{1}{2}} \sin\Big(\frac{kj\pi}{N+1}\Big), \qquad j,k = 1,\dots,N, \tag{1.57}$$

and

$$\epsilon_k = -2\cos\Big(\frac{k\pi}{N+1}\Big), \qquad k = 1,\dots,N. \tag{1.58}$$

The exact diagonalisation of Λ allows us to write H_f as

$$H_f = \sum_{k=1}^{N} \epsilon_k d_k^\dagger d_k \tag{1.59}$$

where we introduced the operators

$$\begin{aligned} d_k &= \Big(\frac{2}{N+1}\Big)^{\frac{1}{2}} \sum_{j=1}^{N} \sin\Big(\frac{kj\pi}{N+1}\Big) c_j, \\ d_k^\dagger &= \Big(\frac{2}{N+1}\Big)^{\frac{1}{2}} \sum_{j=1}^{N} \sin\Big(\frac{kj\pi}{N+1}\Big) c_j^\dagger. \end{aligned} \tag{1.60}$$

They satisfy the canonical fermionic anticommutation relations (1.53) and the operators d_k annihilate the vacuum $|0\rangle$. These properties and the diagonal form of H_f in (1.59) imply that its eigenstates are obtained by successive applications of the creation operators $d_k^\dagger$ on $|0\rangle$. They are given by

$$(d_1^\dagger)^{n_1} \cdots (d_N^\dagger)^{n_N} |0\rangle, \quad \{n_k\}_{k=1,\dots,N} \in \{0,1\}^N, \tag{1.61}$$

where n_k is the fermion occupation number of the mode k. These eigenstates satisfy

$$H_f \ (d_1^\dagger)^{n_1} \cdots (d_N^\dagger)^{n_N} |0\rangle = \Big(\sum_{k=1}^{N} n_k \epsilon_k\Big) (d_1^\dagger)^{n_1} \cdots (d_N^\dagger)^{n_N} |0\rangle \tag{1.62}$$

and have magnetisation $m = -N/2 + \sum_{k=1}^{N} n_k$. If N is an even number, the groundstate of H_f is

$$|x_0\rangle = d_1^\dagger \cdots d_{N/2}^\dagger |0\rangle \tag{1.63}$$

with energy

$$E_0 = \sum_{k=1}^{N/2} \epsilon_k = 1 - \csc\Big(\frac{\pi}{2N+2}\Big) \tag{1.64}$$

and magnetisation $m = 0$. The large-N expansion of E_0 yields

$$E_0 = -\frac{2N}{\pi} + 1 - \frac{2}{\pi} - \frac{\pi}{12N} + \mathcal{O}(N^{-2}). \tag{1.65}$$

If N is an odd number, we have $\epsilon_{(N+1)/2} = 0$ and the groundstate is doubly degenerate. The two groundstates belong to the magnetisation sectors $m = \pm 1/2$ and are given by

$$|x_{-1/2}\rangle = d_1^\dagger \cdots d_{(N-1)/2}^\dagger |0\rangle, \quad |x_{1/2}\rangle = d_1^\dagger \cdots d_{(N+1)/2}^\dagger |0\rangle. \tag{1.66}$$

Their energy is

$$E_{\pm 1/2} = 1 - \cot\left(\frac{\pi}{2N+2}\right) \tag{1.67}$$

and has the large-N expansion

$$E_{\pm 1/2} = -\frac{2N}{\pi} + 1 - \frac{2}{\pi} + \frac{\pi}{6N} + \mathcal{O}(N^{-2}). \tag{1.68}$$

In general, we denote by $|x_m\rangle$ and E_m the lowest-energy state in the magnetisation sector m and its associated energy, respectively. The magnetisation m is an integer if N is even, and half-integer if N is odd. The state $|x_m\rangle$ reads

$$|x_m\rangle = d_1^\dagger \cdots d_{(N+2m)/2}^\dagger |0\rangle \tag{1.69}$$

and the energy E_m has the large-N expansion [112]

$$E_m = -\frac{2N}{\pi} + 1 - \frac{2}{\pi} - \frac{\pi}{12N}(1 - 12m^2) + \mathcal{O}(N^{-2}). \tag{1.70}$$

Comparing this result with (1.46), we find $E_{\text{bulk}} = -\frac{2}{\pi}$ and $E_{\text{bndr}} = 1 - \frac{2}{\pi}$ for $m = -N/2, \ldots, N/2$, and conclude that the model is indeed gapless. The inspection of the terms of order $1/N$ yields

$$c - 24\Delta_m = 1 - 12m^2, \tag{1.71}$$

where we used $\nu_F = 2$ for the XX spin chain without external magnetic field [58].

This simple example highlights the fact that (1.46) is extremely useful to determine the conformal data of a CFT from lattice calculations, but is not enough. Here, we can only fix the combination $c - 24\Delta_m$, but

not c and Δ_m separately. The XX spin chain Hamiltonian (1.51) is Hermitian, and hence the underlying CFT is unitary. In particular, the central charge is $c = 1$ [96], so that the conformal weights in (1.71) are $\Delta_m = m^2/2$. As we discussed in Section 1.1.4, being able to discriminate between $c = 1$ or $c_{\text{eff}} = c - 24\Delta_{\text{min}} = 1$ is crucial in the case where we do not know if the underlying CFT is unitary, for instance. It is thus desirable to find other ways to extract the conformal data of a CFT from lattice calculations. In the forthcoming chapters, we investigate the bipartite fidelity, a quantity whose finite-size scaling yields different combinations of c and Δ [62, 63].

1.2.3 Entanglement and criticality

As we mentioned in the introduction, using techniques and tools from quantum information science in the context of quantum many-body systems strongly contributes to our modern understanding of a variety of many-body phenomena [31]. In this section, we review some aspects of entanglement in quantum many-body systems, and in particular the relation between entanglement and quantum criticality.

In the context of extended quantum many-body systems, we are interested in the entanglement between regions containing a large number of constituents. For instance, let us consider a bipartite quantum system $A \cup B$ in d dimensions, where A and B are two complementary subsystems. We give an illustration of a bipartition in two dimensions in Figure 1.6. If the whole system is in a pure state $|\psi\rangle$, the entanglement between A and B can be measured by the entanglement entropy (0.4), where we recall

$$S_1 = -\text{Tr}(\rho_A \log \rho_A) \tag{1.72}$$

and $\rho_A = \text{Tr}_B(|\psi\rangle\langle\psi|)$ is the reduced density matrix of subsystem A.

Entanglement is related to the presence of non-local correlations in the system, and is thus sensitive to the spatial extension of quantum correlations between A and B. In the case of a non-critical quantum system with a finite correlation length ξ, the correlations between A and B are extended over a region of size $\xi|\partial_{AB}|$, where $|\partial_{AB}|$ is the area of the boundary between the two subsystems. A schematic example is provided on the right panel of Figure 1.6. In that case, the groundstate

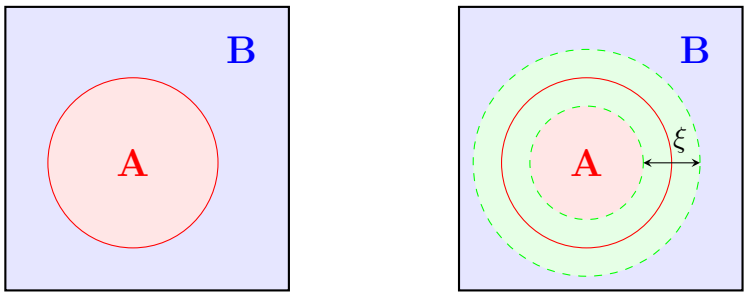

Figure 1.6: Example of a spatial bipartition in two dimensions. In the right panel, the green area corresponds to the spatial region over which A and B are correlated in the case of a non-critical model with finite correlation length ξ.

entanglement entropy typically obeys a so-called *area law* [18, 113–115] in the limit of large system size,

$$S_1 = \mathcal{O}(|\partial_{AB}|). \tag{1.73}$$

The notion of area law also has implications in black hole physics [30, 116–118] and classical simulations of quantum systems [119].

The entanglement entropy was initially investigated in the context of $1+1d$ CFT, where the subsystem A is an interval of length ℓ embedded in an infinitely long one-dimensional system [37]. The result is the celebrated formula

$$S_1 = \frac{c}{3}\log \ell + \mathcal{O}(1) \tag{1.74}$$

where c is the central charge and the term of order one is non-universal. This result corresponds to a logarithmic violation of the area law, and is related to the divergence of the correlation length at criticality. A decade later, Calabrese and Cardy re-derived this formula and generalised it in various contexts thanks to the so-called *replica trick* [38]. This powerful method allowed them to investigate the entanglement entropy of systems at finite temperature, in finite size and in the case where A consists of multiple disjoint intervals. Moreover, they showed that the entanglement entropy satisfies an area law away from criticality.

In the context of condensed matter systems, the observation that entanglement is an efficient tool to detect quantum critical points originated from the work of Osterloh and collaborators [33], and Osborne and Nielsen [34]. Their investigations focused on single-spin entropies [34] and two-spin correlations [33,34] in the XY spin chain. In a seminal paper of 2003 [35], Vidal and collaborators investigated the entanglement entropy of a block of ℓ contiguous spins in the groundstates of the XY and XXZ quantum spin chains. With numerical and analytical methods, they showed that the entanglement entropy saturates to a constant value away from criticality and diverges as $\log \ell$ at criticality. Their result reads

$$S_1 = \frac{c}{3} \log \ell + k + o(1) \tag{1.75}$$

where c depends on the critical regime under consideration, whereas k depends more strongly on the parameters of the Hamiltonians (1.47) and (1.50). In particular, they confirm $c = 1/2$ for the XY spin chain at $\gamma = h = 1$, and $c = 1$ for the XXZ chain with $-1 < \Delta < 1$. These lattice results are in perfect agreement with the CFT prediction (1.74) where c is the central charge and k a non-universal constant. The entanglement entropy is thus a powerful tool to detect and characterise quantum critical points. In particular, it provides a way to extract the central charge of the CFT underlying a quantum critical point.

Since the groundbreaking results (1.74) and (1.75), the investigation of entanglement measures in CFT and extended many-body systems has been an active research area [41], with applications in condensed matter [32,39,120] and in high energy physics [121,122]. In particular, an important amount of work is aimed at deriving exact formulas for entanglement measures in extended quantum systems [40,123]. Exact results are available for free fermions [48,124–126], but in general computing the entanglement entropy in a genuinely interacting model is a challenging problem.

In the context of non-unitary CFT and related lattice models, a natural question is whether the leading term of the groundstate entanglement entropy yields the central charge c of the theory, or rather the effective central charge $c_{\text{eff}} = c - 24\Delta_{\text{min}}$. It was initially argued that for such theories, S_1 only allows one to measure the effective central charge [127]. However, for non-unitary theories, the Hamiltonian H is not Hermitian

and its left-groundstate $\langle\psi_L|$ is not equal to the Hermitian conjugate of the right-groundstate $\langle\psi_R| = |\psi_R\rangle^\dagger$. This creates an ambiguity in the definition of the entanglement entropy, because the reduced density matrix can be defined as $\rho_A = \mathrm{Tr}_B(|\psi_R\rangle\langle\psi_L|)$ or $\rho_A = \mathrm{Tr}_B(|\psi_R\rangle\langle\psi_R|)$. It was later understood [128] that the leading coefficient in (1.75) is $c/3$ in the former case and $c_{\mathrm{eff}}/3$ in the latter.

1.3 Bipartite fidelity in extended systems

An observable that shares many features with the entanglement entropy is the *quantum fidelity* [129–134]. It is defined as the overlap between the groundstates of two Hamiltonians that differ by a perturbation. Let us consider a system described by a Hamiltonian $H(\lambda)$ that depends on a parameter λ and denote its groundstate by $|\psi_\lambda\rangle$. For simplicity we assume that the groundstate is not degenerate. The fidelity is

$$f(\lambda_1, \lambda_2) = \left| \frac{\langle\psi_{\lambda_1}|\psi_{\lambda_2}\rangle}{\sqrt{\langle\psi_{\lambda_1}|\psi_{\lambda_1}\rangle\,\langle\psi_{\lambda_2}|\psi_{\lambda_2}\rangle}} \right|. \tag{1.76}$$

As a particular example, we consider the situation where λ parametrises the interaction between two complementary subsystems A and B of an extended many-body system,

$$H(\lambda) = H^A + H^B + \lambda H^{\mathrm{int}}, \tag{1.77}$$

where H^A and H^B are the Hamiltonians of the subsystems A and B, respectively. The term H^{int} contains the interactions between the two subsystems. We denote by $|\psi^A\rangle$, $|\psi^B\rangle$ and $|\psi^{AB}\rangle$ the groundstates of H^A, H^B and $H^{AB} = H(1)$, respectively. The *logarithmic bipartite fidelity* [62, 63] is defined as

$$\mathcal{F} = -2\log \left| \frac{\langle\psi^A \otimes \psi^B|\psi^{AB}\rangle}{\sqrt{\langle\psi^A \otimes \psi^B|\psi^A \otimes \psi^B\rangle\,\langle\psi^{AB}|\psi^{AB}\rangle}} \right|, \tag{1.78}$$

with the notation $|\psi^A \otimes \psi^B\rangle \equiv |\psi^A\rangle \otimes |\psi^B\rangle$ for the groundstate of $H(0)$. Similarly to the entanglement entropy, this quantity vanishes when the groundstate of the whole system is the product state $|\psi^{AB}\rangle = |\psi^A \otimes \psi^B\rangle$, and is a positive number otherwise. However, there is a main conceptual difference between the entanglement entropy and the logarithmic

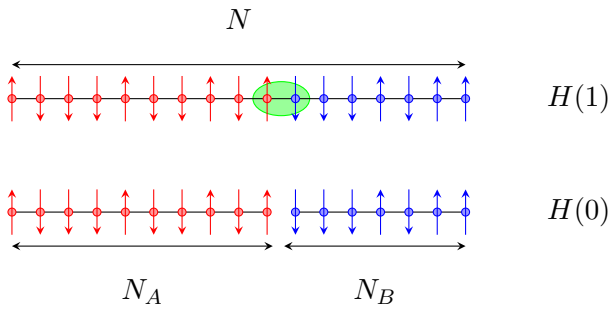

Figure 1.7: Illustration of the spin chains involved in the definition of the bipartite fidelity where the whole system and subsystems have free boundary conditions. The top panel represents the whole chain with Hamiltonian $H(1)$. The lower panel illustrates the chain cut in two non-interacting parts, with Hamiltonian $H(0)$.

bipartite fidelity. The former is well-defined for any pure state $|\psi^{AB}\rangle$, whereas the latter requires the knowledge of the underlying quantum Hamiltonian. Indeed, a state $|\psi^{AB}\rangle$ alone it is not enough to infer which states $|\psi^{A}\rangle$ and $|\psi^{B}\rangle$ one should use in the definition (1.78). For that reason, the logarithmic bipartite fidelity is not an entanglement measure in the information-theoretical sense, contrarily to the entanglement entropy [19]. It is nonetheless a powerful tool to investigate the ground-state entanglement properties of quantum many-body systems.

The normalised overlap inside the logarithm in the definition of $\mathcal{F}$ is the so-called *bipartite fidelity*. In terms of the definition (1.76), the bipartite fidelity corresponds to $f(0,1)$ with the Hamiltonian $H(\lambda)$ given in (1.77). For a quantum spin chain, the bipartite fidelity is the normalised overlap between the groundstate of the whole chain with the groundstate of the chain that has been cut in two parts. We illustrate this in Figure 1.7 in the case where the whole system and subsystems have free boundary conditions and respective lengths N, N_A and N_B, with $N = N_A + N_B$. In the following, we also consider the cases where the whole system is endowed with periodic boundary conditions, whereas the subsystems both have either periodic or free boundary conditions.

1.3.1 Bipartite fidelity of integrable models

For a quantum model in one dimension, the bipartite fidelity has an interpretation in terms of partition functions of the underlying two-dimensional statistical model. The partition functions are defined on lattices whose geometries depend on the boundary conditions in the quantum chain. For instance, in the case where the whole system and both subsystems have free boundary conditions, the overlap $\langle \psi^A \otimes \psi^B | \psi^{AB} \rangle$ is related to the partition function on the so-called *flat pants lattice*, denoted Z_f^{AB}. The lattice is equipped with a long vertical slit that extends halfway in the vertical direction, as illustrated in Figure 1.8. The height of the lattice is bM, where $b > 0$ is an even number that depends on the model and instance of the bipartite fidelity under consideration (in the following we encounter $b = 2$ and $b = 4$), whereas the top segment and the two lower ones separated by the slit have lengths N, N_A and N_B with $N = N_A + N_B$, respectively. Likewise, the scalar products in the denominator of (1.78) are tied to the partition functions Z_r^{AB}, Z_r^A and Z_r^B defined on rectangles of heights bM and widths N, N_A and N_B, respectively. The logarithmic bipartite fidelity on the flat pants lattice is

$$\mathcal{F}_f = \lim_{M\to\infty} -\log \left| \frac{\left(Z_f^{AB}\right)^2}{Z_r^A Z_r^B Z_r^{AB}} \right|. \tag{1.79a}$$

In the cases where the quantum system has periodic boundary conditions and the subsystems both have either periodic or free boundary conditions, the overlap $\langle \psi^A \otimes \psi^B | \psi^{AB} \rangle$ is related to the partition function of the two-dimensional model on the *periodic pants lattice* and the *skirt lattice*, respectively. These lattices are represented on Figure 1.9. Both lattices have height bM and their perimeter at the top is N. On the periodic pants lattice, the perimeters of the legs A and B are N_A and N_B with $N = N_A + N_B$. On the skirt lattice, the legs correspond to open segments of respective lengths N_A and N_B. This lattice is thus equipped with two long vertical slits that extend halfway in the vertical direction. The partition functions on the periodic pants and the skirt lattices are denoted Z_p^{AB} and Z_s^{AB}, respectively. The logarithmic

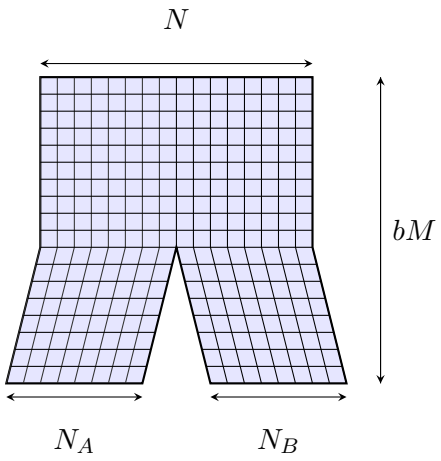

Figure 1.8: Illustration of the flat pants lattice.

bipartite fidelities are

$$\mathcal{F}_p = \lim_{M\to\infty} -\log\left|\frac{\left(Z_p^{AB}\right)^2}{Z_c^A Z_c^B Z_c^{AB}}\right| \tag{1.79b}$$

and

$$\mathcal{F}_s = \lim_{M\to\infty} -\log\left|\frac{\left(Z_s^{AB}\right)^2}{Z_r^A Z_r^B Z_c^{AB}}\right|. \tag{1.79c}$$

Here, Z_c^{AB}, Z_c^A and Z_c^B denote the partition functions on cylinders of heights bM and perimeters N, N_A and N_B, respectively. Clearly, the bipartite fidelities depend on the choices of boundary conditions assigned to the top and bottom of the lattices. For suitable choices of these boundary conditions, the partition functions are all non-zero and the limits $M \to \infty$ in (1.79) are well-defined.

The definitions of the bipartite fidelities in terms of quantum overlaps of groundstates and partition functions in two-dimensional models coincide for integrable models where the respective Hamiltonians and transfer matrices are related by (1.17). Let us denote by Λ_0^S and Γ_0^S the largest eigenvalues of the transfer matrices pertaining to the system $S = A, B, AB$, with free and periodic boundary conditions in the horizontal direction, respectively. Moreover, let us denote the respective

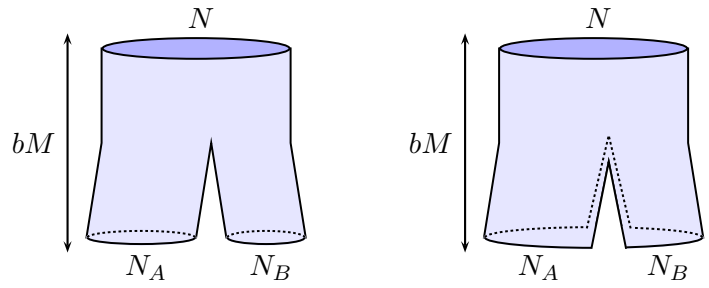

Figure 1.9: Illustration of the periodic pants lattice (left), and the skirt lattice (right).

eigenstates by $|x_0^S\rangle$ and $|X_0^S\rangle$. In the large-M limit, the partition functions Z_r^S and Z_c^S read

$$\begin{aligned} Z_r^S &\simeq (\Lambda_0^S)^{bM} \langle x_0^S | x_0^S \rangle, \\ Z_c^S &\simeq (\Gamma_0^S)^{bM} \langle X_0^S | X_0^S \rangle, \end{aligned} \tag{1.80a}$$

where the notation $\simeq$ indicates that subleading terms are omitted. Similarly, we have

$$\begin{aligned} Z_f^{AB} &\simeq (\Lambda_0^A \Lambda_0^B \Lambda_0^{AB})^{bM/2} \langle x_0^A \otimes x_0^B | x_0^{AB} \rangle, \\ Z_p^{AB} &\simeq (\Gamma_0^A \Gamma_0^B \Gamma_0^{AB})^{bM/2} \langle X_0^A \otimes X_0^B | X_0^{AB} \rangle, \\ Z_s^{AB} &\simeq (\Lambda_0^A \Lambda_0^B \Gamma_0^{AB})^{bM/2} \langle x_0^A \otimes x_0^B | X_0^{AB} \rangle. \end{aligned} \tag{1.80b}$$

When the relation (1.17) is satisfied, the states $|x_0^S\rangle$ and $|X_0^S\rangle$ correspond to the groundstates of the Hamiltonians for the system S with free and periodic boundary conditions, respectively. When we insert (1.80) into the definitions (1.79), the products of eigenvalues simplify between the numerators and the denominators, and the remaining ratios of overlaps correspond to the definition (1.78) adapted to the various boundary conditions. If the transfer matrices have Jordan blocks, the relations (1.80) are modified, and the definition of the dual states may depend on the instances of the bipartite fidelity under consideration. We relegate these discussions to the concrete examples presented in the forthcoming chapters.

1.3.2 Scaling limit and CFT predictions

Analogously to the entanglement entropy, the bipartite fidelity can also be used to detect quantum phase transitions. It satisfies an area law away from criticality and has extra logarithmic divergences at the critical point [62]. For critical lattice models in $1+1$ dimensions, Stéphan and Dubail [62, 63] investigated the universal behaviour of the logarithmic bipartite fidelity on the flat pants lattice using CFT arguments and obtained expressions for the leading terms in its large-N asymptotic expansion. Their results hold in the case where the CFT is unitary. In the simplest case where all the states correspond to the vacuum of the CFT, as in (1.78), their result is an application of the Cardy-Peschel formula [135] and the leading term is $c/8 \log N$, where c is the central charge. More generally, the bipartite fidelity can be defined, as in (1.78), in terms of three eigenstates $|\psi^{AB}\rangle$, $|\psi^{A}\rangle$ and $|\psi^{B}\rangle$ that do not correspond to the vacuum of the CFT in the scaling limit. The leading terms then depend on the weights Δ_i of four fields ϕ_i, $i = 1, 2, 3, 4$, that account for changes in the boundary conditions. The quantity $\mathcal{F}_f$ has an interpretation as a four-point function of these fields on the flat pants domain, that corresponds to the continuum limit of the flat pants lattice where M has been sent to infinity. The fields are inserted at infinity in each extremity of the flat pants domain, as well as on the endpoint of the slit, as illustrated on Figure 1.10. The lattice width N is taken to infinity with the aspect ratio $x = N_A/N$ kept fixed in the range $(0, 1)$. The resulting large-N expansion reads [63]

$$\mathcal{F}_f = \left(\frac{c}{8} + \Delta_2\right) \log N + g_f^{(1)}(x) + g_f^{(2)}(x) N^{-1} \log N + \mathcal{O}(N^{-1}), \quad (1.81)$$

where

$$\begin{aligned} g_f^{(1)}(x) = \Bigg[& \frac{c}{24}\left(2x - 1 + \frac{2}{x}\right) + \left(\frac{4}{3} - \frac{2}{x}\right)\Delta_1 \\ & + \frac{\Delta_2}{3} - \frac{2\Delta_3}{3} + \left(\frac{4}{3} - 2x\right)\Delta_4 \Bigg] \log(1-x) \\ & - \log \Upsilon(x) + \Big\{ x \to 1 - x; \Delta_1 \leftrightarrow \Delta_3 \Big\} + C_f \end{aligned} \quad (1.82)$$

and C_f is a non-universal constant that is independent of x. Here, $\Upsilon(x)$ is the function that appears in the four point function of the fields

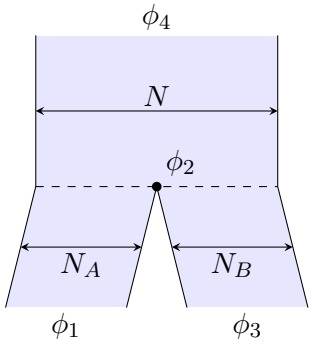

Figure 1.10: The flat pants domain and the fields insertion points in the CFT interpretation of $\mathcal{F}_f$.

$\phi_1, \ldots, \phi_4$ in the upper-half plane. It depends only on the anharmonic ratio ζ,

$$\left\langle \phi_1(z_1)\phi_2(z_2)\phi_3(z_3)\phi_4(z_4)\right\rangle_{\mathbb{H}} = \Upsilon(\zeta) \times \prod_{1\leqslant i<j\leqslant 4} z_{ij}^{\hat{\Delta}/3-\Delta_i-\Delta_j} \tag{1.83}$$

with

$$z_{ij} = z_i - z_j, \qquad \zeta = \frac{z_{12}z_{34}}{z_{13}z_{24}}, \qquad \hat{\Delta} = \Delta_1 + \Delta_2 + \Delta_3 + \Delta_4. \tag{1.84}$$

The notation $\{x \to 1-x; \Delta_1 \leftrightarrow \Delta_3\}$ in (1.82) indicates that the content of the first line must be duplicated but with x replaced by $1-x$ and Δ_1 exchanged with Δ_3. The function $g_f^{(2)}(x)$ in (1.81) is also given in [63] and takes the form of a universal function times a non-universal prefactor known as the *extrapolation length* Ξ:

$$g_f^{(2)}(x) = \Xi \times \left[\Delta_4 - \frac{c}{24} + \left(\frac{c}{24} - \Delta_1\right)\frac{1}{x} + \left(\frac{c}{24} - \Delta_3\right)\frac{1}{1-x}\right]. \tag{1.85}$$

The extrapolation length plays a prominent role in the study of surface critical phenomena [136]. In the context of CFT, it is a non-universal constant appearing in a perturbation of the stress-energy tensor that displaces the position of the boundary [63]. It also impacts the behaviour of one-point correlation functions near a corner.

In [62], Dubail and Stéphan also investigated the behaviour of the bipartite fidelity on the skirt domain, where the state $|\psi^{AB}\rangle$ used to compute

(1.78) in this case is the groundstate of the Hamiltonian with periodic boundary conditions, whereas $|\psi^A\rangle$ and $|\psi^B\rangle$ are the groundstates of the chains of the subsystems A and B with free boundary conditions. Their result covers the simplest case where no boundary condition changing fields are inserted. The resulting large-N expansion for the bipartite fidelity reads

$$\mathcal{F}_s = \frac{c}{4}\log N + \frac{c}{24}(G_s(x) + G_s(1-x)) + C_s + \mathcal{O}(N^{-1}\log N), \quad (1.86)$$

where C_s is a non-universal constant, and

$$G_s(x) = \frac{3 - 6x + 4x^2}{1-x}\log x. \quad (1.87)$$

1.4 Organisation of Part I

In the following chapters, we investigate the bipartite fidelity in various contexts, motivated by the following elements.

Up until now, there have been only few cases where the bipartite fidelity was computed explicitly via an exact lattice derivation. It was computed for the XX spin chain with free boundary conditions in [63] for the special case where the aspect ratio is $x = 1/2$ and the length of the chain is a multiple of four. It was also obtained [137] for the XXZ chain at the anisotropy $\Delta = -1/2$ with real magnetic fields at the endpoints. This last result holds for a single eigenstate, namely the special groundstate that has miraculous combinatorial properties. The bipartite fidelity was also computed by Weston [138, 139] for the XXZ chain in the infinite chain directly, for generic values of Δ in the range $-\infty < \Delta < -1$. In this case, the model is not critical and the result is a function of the correlation length ξ. From the CFT perspective, the current knowledge regarding the universal behaviour of the bipartite fidelity applies to models for which the underlying CFT is unitary. In particular, the conformal prediction (1.82) for $g_f^{(1)}(x)$ was obtained in [63] by assuming that the fields $\phi_1, \ldots, \phi_4$ are primary. Moreover, apart from the case of the bipartite fidelity on the skirt domain where all the states correspond to the vacuum of the CFT [62], there are no results for models with periodic boundary condition.

In Chapter 2 we investigate the bipartite fidelity in the model of critical dense polymers [103] on the flat pants lattice. This model is related to the simplest member of the family of logarithmic minimal models, and its underlying CFT description contains primary and logarithmic fields. Our first objective is to provide new exact lattice calculations of the bipartite fidelity in a critical model for arbitrary values of the aspect ratio x and systematically compare them with the CFT prediction (1.81) in the case where all the fields are primary. The second goal of this chapter is to provide a first calculation of the bipartite fidelity in the case where the fields inserted on the boundary are logarithmic, both with exact lattice and CFT calculations. We use the integrability of the model to achieve both objectives, and find a systematic perfect match between the asymptotic expansions of our lattice results and the CFT predictions, both for the known case of primary fields and our new prediction in the logarithmic case.

We investigate the bipartite fidelity for models with periodic boundary conditions in Chapters 3 and 4. In particular, we provide new CFT predictions and lattice computations of the bipartite fidelity on the periodic pants and skirt domains, respectively. To our knowledge, there are no previously known results for the bipartite fidelity on the periodic pants domain. For the skirt domain, we push further the investigation initiated in [62]. In particular, we consider the more general case where boundary condition changing fields are present in the CFT context, and derive the leading terms in (1.86) up to order $N^{-1}\log N$. In both cases, we test our new CFT predictions against exact and numerical lattice calculations in the XX spin chain and the model of critical dense polymers, and find a systematic perfect match.

We present concluding remarks and outlooks in Chapter 5.

2

Critical dense polymers on the flat pants lattice

In this chapter, we investigate several instances of the bipartite fidelity in the model of critical dense polymers [103] on the flat pants lattice. In the scaling limit, various properties of this model are described by the simplest member of the family of logarithmic minimal models, with the central charge and the conformal weights of the Kac table given by

$$c = -2, \qquad \Delta_{r,s} = \frac{(2r-s)^2 - 1}{8}. \tag{2.1}$$

The model of critical dense polymers model is a tiling model in two dimensions. Contrarily to the two-dimensional Ising model or the six-vertex model, where the degrees of freedom lie on the vertices and on the edges of the lattice, respectively, here the degrees of freedom lie on the faces. A given configuration of the model is a selection, for each face of the lattice, of one of these two tiles:

The observables in the model are the loops formed by these blue segments (and their numbers), which are non-local objects. This is the fundamental reason why the model of critical dense polymers is described by a logarithmic CFT rather than a unitary one. This is in stark contrast with the Ising model, where the degrees of freedom (the spins) and their correlation functions are entirely local in nature, and the corresponding underlying CFT is unitary.

As we discussed in Section 1.4, our aim is twofold. On the one hand we provide a new lattice derivation of the bipartite fidelity of a critical lattice model in finite-size and investigate its asymptotic behaviour. We achieve this for a family of boundary conditions labelled by a positive integer d, with the corresponding observables denoted by $\mathcal{F}_f^{(d)}$. On the other hand, we perform the first calculation of the bipartite fidelity in the case where the fields inserted on the boundary are logarithmic. We use the presence of logarithmic fields in the CFT description of the model in the scaling limit to define a second instance of the bipartite fidelity, denoted $\tilde{\mathcal{F}}_f^{(2)}$. Our derivations rely on the relation between the partition functions of the model and the Temperley-Lieb algebra. Moreover, the model of critical dense polymers can be mapped to the XX spin chain with the $U_q(s\ell_2)$-invariant boundary fields of Pasquier and Saleur [140] with $q = \mathrm{i}$ applied to the two endpoints. We exploit the integrability of the model and the known diagonalisation of its Hamiltonian and transfer matrix to derive exact lattice results for the relevant instances of the bipartite fidelity. We use the exact results for $\mathcal{F}_f^{(d)}$ and $\tilde{\mathcal{F}}_f^{(2)}$ to investigate their asymptotic behaviour. The scaling behaviour of $\mathcal{F}_f^{(d)}$ precisely matches the CFT prediction (1.81) with the known conformal data of the model of critical dense polymers. For the logarithmic case, we derive a new CFT prediction for the case where one field inserted on the domain is logarithmic and exactly recover the lattice result for $\tilde{\mathcal{F}}_f^{(2)}$. The results discussed in this chapter were initially presented in the publication [4].

2.1 Bipartite fidelity, partition functions and overlaps

We study the loop model of critical dense polymers on the flat pants lattice. In Figure 2.1, we depict this lattice as a $4M \times N$ rectangle with a vertical slit. The slit divides the lower segment in two subsegments A and B, of respective lengths N_A and N_B, and extends halfway across the rectangle.

The boundary condition consists of a collection of arcs connecting neighboring nodes called *simple arcs* and vertical loop segments called *defects*.

The left and right edges of the rectangle are decorated with simple arcs. The same applies to the interior of the slit. The top segment is made of a collection of d defects, which we choose to be adjacent and attached to the leftmost nodes, and $\frac{N-d}{2}$ arcs. On the bottom segment, the subsegment A is decorated with d defects, also attached to the leftmost nodes, and $\frac{N_A-d}{2}$ arcs. The subsegment B has only simple arcs.

The loop segments drawn on the tiles and on the boundary form loops. In a given configuration $\{\ell_i\}$ of loops, we assign a weight, or fugacity w_i, to each loop ℓ_i. The Boltzmann weight $W_f(\{\ell_i\})$ of a configuration is the product of the fugacities w_i of its loops: $W_f(\{\ell_i\}) = \prod_i w_i$. Some of the loops are closed and are referred to as *bulk loops*. The model of critical dense polymers is a special case of a so-called *dense loop model* where bulk loops have the fugacity $w_i = \beta = 0$ [103]. In general, dense loop models are a family of integrable models where bulk loops have an arbitrary fugacity β. Loop segments can also connect two defects from the boundary. We refer to this as a *boundary loop*. In defining the partition function on the flat pants lattice, we assign a fugacity $w_i = 1$ to a boundary loop if it connects the top and bottom segments, and a fugacity $w_i = 0$ if it connects two defects of the same segment. The partition function on the flat pants lattice, denoted $Z_f^{(d),AB}$, is

$$Z_f^{(d),AB} = \sum_{\{\ell_i\}} W_f(\{\ell_i\}). \tag{2.2}$$

We consider three more partition functions: $Z_r^{(d),AB}$, $Z_r^{(d),A}$ and $Z_r^{(2),B}$. We construct these partition functions with the same choices of fugacities for the bulk and boundary loops, but on lattices without slits, namely on the rectangular lattices given in Figure 2.2. The logarithmic bipartite fidelity is

$$\mathcal{F}_f^{(d)} = -\lim_{M\to\infty} \log \left| \frac{\left(Z_f^{(d),AB}\right)^2}{Z_r^{(d),AB} Z_r^{(d),A} Z_r^{(2),B}} \right|, \tag{2.3}$$

where the defect number d is taken to be greater or equal to one. This definition corresponds to (1.79a) adapted to the model of critical dense polymers. The choice to include $Z_r^{(2),B}$ in the denominator is justified as follows. We note that for the other dense loop models for which the fugacity of bulk loops β is non-zero, the natural choice is to write $Z_r^{(0),B}$ in the denominator instead of $Z_r^{(2),B}$. For the model of critical dense

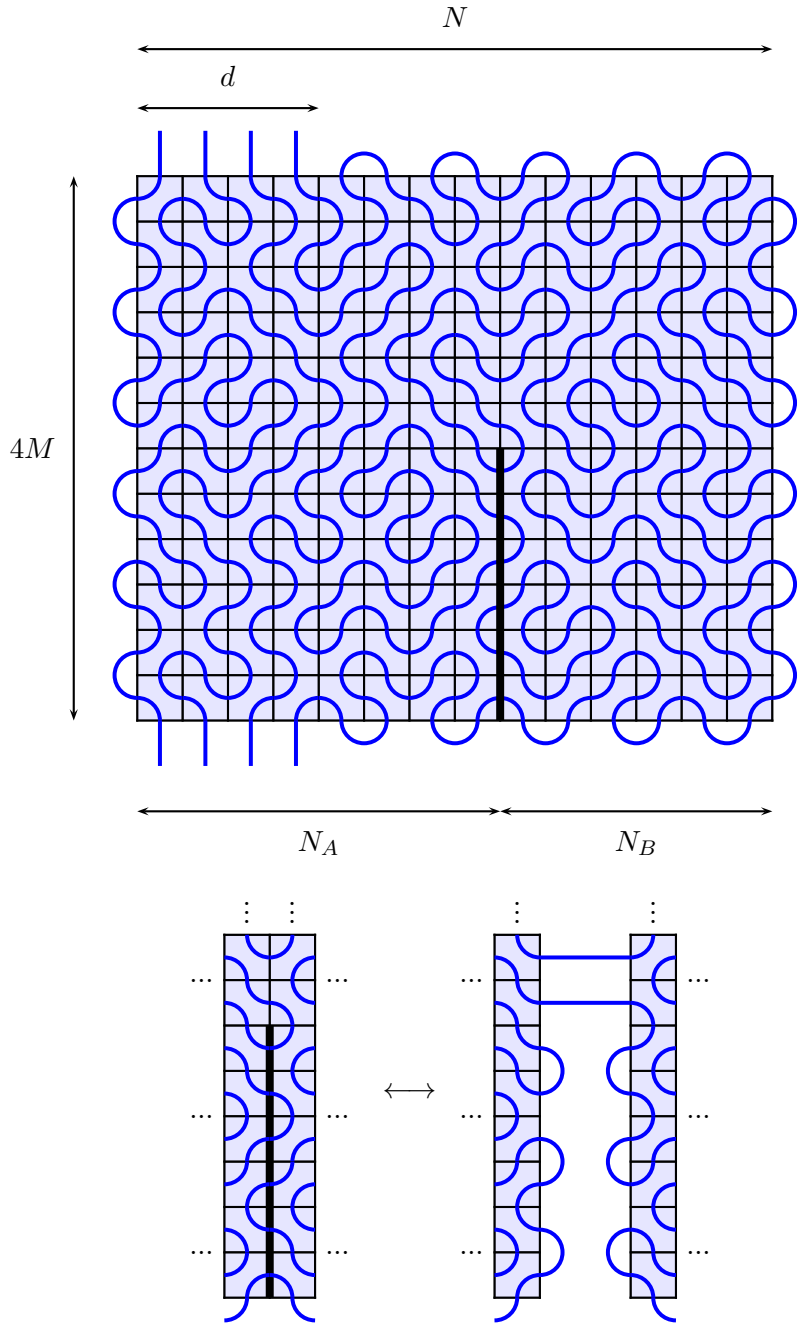

Figure 2.1: A configuration of the model of critical dense polymers on the flat pants lattice, with $M = 3$, $N = 14$, $N_A = 8$ and $N_B = 6$. The thick vertical line is the slit that separates the two lower parts of the lattice, as illustrated on the lower panel.

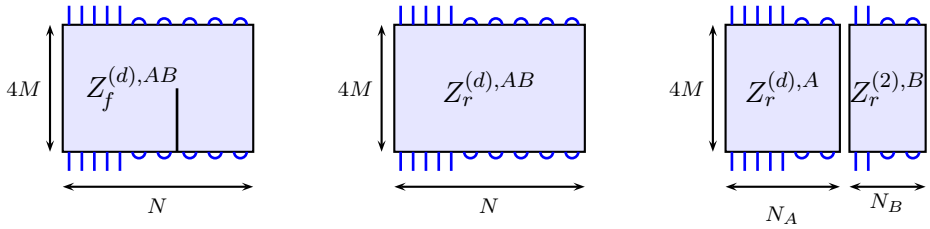

Figure 2.2: The lattices corresponding to the partition functions $Z_f^{(d),AB}$, $Z_r^{(d),AB}$, $Z_r^{(d),A}$ and $Z_r^{(2),B}$.

polymers, this partition function is $Z_r^{(0),B} = 0$. As argued in [141], the reference partition function in this case is instead $Z_r^{(2),B}$.

In this same paper [141], it was also underlined that the boundary condition consisting of two neighbouring defects forced to connect corresponds, from a CFT perspective, to a logarithmic field in a rank-two Jordan cell. Correlation functions involving this field are expected to have logarithmic behaviour. To investigate the effects of this logarithmic field on the bipartite fidelity, we study a second instance of the logarithmic bipartite fidelity for $d = 2$, denoted $\tilde{\mathcal{F}}_f^{(2)}$. We choose $\tilde{Z}_f^{(2),AB}$ to be the partition function on the flat pants lattice of Figure 2.1, but with different fugacities for the boundary loops. In computing the weights of configurations for $\tilde{Z}_f^{(2),AB}$, a boundary loop has a fugacity $w_i = 0$ if it connects a defect from the top segment to one of the bottom segment, and a fugacity $w_i = 1$ if it connects two defects of the same segment. Bulk loops still have zero fugacity. We similarly consider the partition functions $\tilde{Z}_r^{(2),AB}$ and $\tilde{Z}_r^{(2),A}$, with the same fugacities as for $\tilde{Z}_f^{(2),AB}$, but on the lattices of Figure 2.2. The second instance of the logarithmic bipartite fidelity is

$$\tilde{\mathcal{F}}_f^{(2)} = -\lim_{M\to\infty} \log \left| \frac{\left(\tilde{Z}_f^{(2),AB}\right)^2}{\tilde{Z}_r^{(2),AB}\tilde{Z}_r^{(2),A}Z_r^{(2),B}} \right|, \tag{2.4}$$

where we note that the last factor in the denominator is $Z_r^{(2),B}$ and not $\tilde{Z}_r^{(2),B}$.

2.1.1 The Temperley-Lieb algebra at $\beta = 0$

In this section, we express the various partition functions introduced in the previous paragraphs in the language of the Temperley-Lieb algebra $\mathsf{TL}_N(\beta = 0)$. The corresponding expressions involve the standard and projective modules over this algebra, the bilinear forms over these modules and the transfer tangle for the model of critical dense polymers.

The algebra $\mathsf{TL}_N(\beta)$. The Temperley-Lieb algebra [142–147] is a unital, associative algebra generated by the linear span of connectivities. A connectivity is a diagram drawn inside a rectangular box with N marked nodes on both its top and bottom segments. Inside the box, the nodes are connected pairwise by non-intersecting loop segments. A subset of the connectivities, namely the identity connectivity $\boldsymbol{I}$ and $N-1$ connectivities denoted by e_j, with $j = 1, \ldots, N-1$, generate this algebra. These connectivities are depicted as

$\boldsymbol{I} =$ 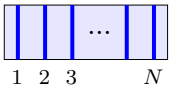

, $e_j =$ 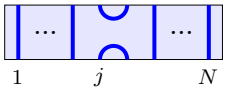

. (2.5)

The product $a_1 a_2$ of connectivities in $\mathsf{TL}_N(\beta)$ is obtained as follows: one stacks a_2 above a_1 and straightens the loop segments to obtain a new connectivity. Each loop created through this procedure is erased and replaced by a factor β. Here are some examples for $N = 4$:

$e_1 e_2 =$ 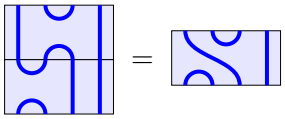 , (2.6)

$e_2 e_1 e_3 =$ 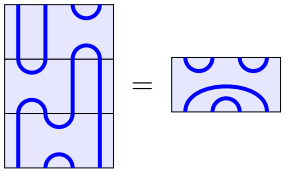 ,

$(e_1 e_2)(e_2 e_1 e_3)(e_1 e_2) =$ 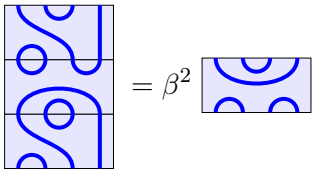 .

With products of the e_j generators, one can produce any connectivity in $\mathsf{TL}_N(\beta)$. The diagrammatic definition for the product of connectivities is equivalent to a set of relations satisfied by the generators:

$$(e_j)^2 = \beta\, e_j, \qquad e_j e_{j\pm1} e_j = e_j, \qquad e_j e_k = e_k e_j, \quad (|j-k|>1). \tag{2.7}$$

These are the defining relations of $\mathsf{TL}_N(\beta)$. The value of β pertaining to the model of critical dense polymers is $\beta = 0$. The algebra $\mathsf{TL}_N(0)$ is non-semisimple. Below, we describe the standard and projective modules over the Temperley-Lieb algebra, which will allow us to compute $\mathcal{F}_f^{(d)}$ and $\tilde{\mathcal{F}}_f^{(2)}$, respectively.

The standard modules $\mathsf{V}_{N,d}$. The standard modules $\mathsf{V}_{N,d}$ are built on the vector space generated by link states on N nodes with d defects. These are diagrams drawn above a segment with N marked nodes, wherein nodes are either connected pairwise or occupied by a defect that cannot be overarched. Here are the link states for the standard modules for $N = 4$:

$\mathsf{V}_{4,0}$:  , (2.8a)

$\mathsf{V}_{4,2}$:  , (2.8b)

$\mathsf{V}_{4,4}$: 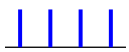 . (2.8c)

The action of a connectivity $a \in \mathsf{TL}_N(\beta)$ on a link state $v \in \mathsf{V}_{N,d}$, denoted $a\,v$, uses diagrammatic rules similar to those defined for the product of connectivities. One draws v above a, straightens the loop segments and reads the new link state produced at the bottom segment of a. If two defects connect, the result is set to zero. Otherwise the result of $a\,v$ is this new link state, with contractible loops replaced by multiplicative factors of β. For $\beta = 0$, this implies that if one or more contractible loops are formed, then $a\,v = 0$. Here are examples for $N = 4$:

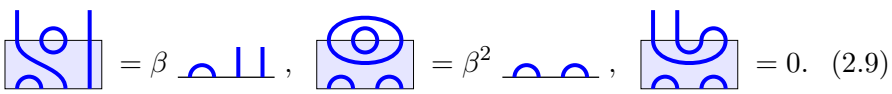 (2.9)

The projective modules $\mathsf{P}_{N,2}$. We define the modules $\mathsf{P}_{N,2}$ for $\mathsf{TL}_N(0)$ with even N. The vector space is spanned by link states with $d = 0$ and $d = 2$ defects. For example, for $N = 4$, $\mathsf{P}_{N,2}$ has dimension five and its link states are the first five states in (2.8).

The action of $a \in \mathsf{TL}_N(0)$ on $v \in \mathsf{P}_{N,2}$ also uses the diagrammatic construction. One draws v above a and reads the new link state from the diagram. If there are contractible loops in this diagram, the result is set to zero, as it is for the standard action for $\beta = 0$. However, in contrast with the standard action, if two defects connect, the result is *not* set to zero. For example, in $\mathsf{P}_{N,2}$, the calculations of (2.9) become

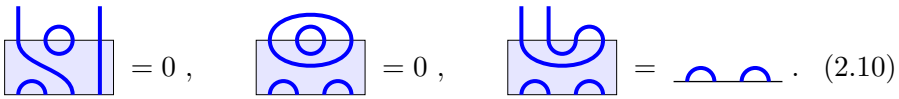

(2.10)

The third calculation gives a link state with weight one in $\mathsf{P}_{N,2}$, whereas this prefactor vanishes in $\mathsf{V}_{N,2}$. In contrast, the first two are in fact obtained identically in $\mathsf{P}_{N,2}$ and in $\mathsf{V}_{N,d}$, but here they vanish because $\beta = 0$.

In the modules $\mathsf{P}_{N,2}$, the number of defects is not a conserved quantity, as it may happen that the initial and final states respectively have $d = 2$ and $d = 0$ defects. Moreover, we note that $\mathsf{P}_{N,2}$ has a submodule isomorphic to $\mathsf{V}_{N,0}$. To distinguish between the actions in $\mathsf{V}_{N,d}$ and $\mathsf{P}_{N,2}$, in the following we indicate explicitly which module is involved, and write for instance $a\,v\big|_{\mathsf{V}_{N,d}}$ or $a\,v\big|_{\mathsf{P}_{N,2}}$.

Bilinear forms for $\mathsf{TL}_N(0)$. For the model of critical dense polymers, the Gram bilinear form is an invariant form on $\mathsf{V}_{N,d}$ defined as follows. Let v, v' be two link states in $\mathsf{V}_{N,d}$. Performing a vertical flip of v and connecting its nodes to those of v', we obtain a diagram where the loop segments form closed loops or connect defects together. The Gram product of v and v', denoted $v \cdot v'$, equals 1 if the number of closed loops is zero and all defects from v are connected to defects of v'. Otherwise, $v \cdot v' = 0$. To illustrate, for $v_1 =$ 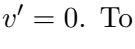 , $v_2 =$

and $v_3 =$  , we have

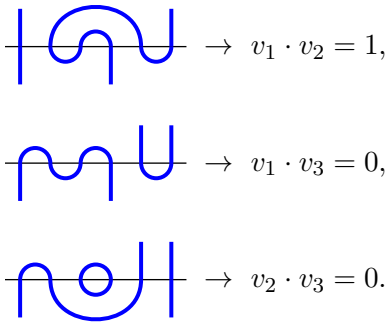

(2.11)

One can also check that $v_1 \cdot v_1 = v_2 \cdot v_2 = v_3 \cdot v_3 = 0$. We note that $v \cdot w = 0$ if $v, w \in \mathsf{V}_{N,0}$. The Gram bilinear forms used in the computations below involve $\mathsf{V}_{N,d}$ with $d \geqslant 1$.

We define a second bilinear form on the module $\mathsf{P}_{N,2}$. The link states in this module have either 0 or 2 defects. For two such link states v and v', we denote this second product by $v \odot v'$. As for the Gram product, we draw the diagram where v is flipped vertically and its nodes are attached to those of v'. If the number of closed loops is zero, the defects of v are connected among themselves, and likewise for those of v', then $v \odot v' = 1$. Otherwise, $v \odot v' = 0$. For the examples given above, we have

$$v_1 \odot v_2 = 0, \qquad v_1 \odot v_3 = 1, \qquad v_2 \odot v_3 = 0. \tag{2.12}$$

The transfer tangle. The double-row transfer tangle for the model of dense polymers is an element of $\mathsf{TL}_N(0)$ defined as [103]

$$\boldsymbol{D}(u) = \frac{1}{\sin 2u}$$

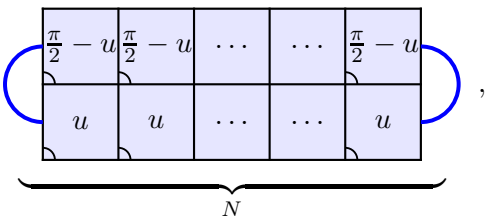

(2.13)

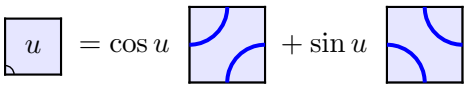

where u is the spectral parameter. We refer to the value $u = \frac{\pi}{4}$, for which both tiles have equal weights, as the *isotropic point*. Later, we

use the shorthand notation $\boldsymbol{D} = \boldsymbol{D}(\frac{\pi}{4})$. Indeed, the weight $W_f(\{\ell_i\})$ of a loop configuration assumes that the two tiles have the same weight.

The transfer tangle satisfies a number of identities: (i) it satisfies crossing symmetry, namely $\boldsymbol{D}(\frac{\pi}{2} - u) = \boldsymbol{D}(u)$, (ii) it satisfies the periodicity property $\boldsymbol{D}(u + \pi) = \boldsymbol{D}(u)$, (iii) it evaluates to the identity at $u = 0$: $\boldsymbol{D}(u = 0) = \boldsymbol{I}$. The transfer tangles also commute at different values of the spectral parameter, $[\boldsymbol{D}(u), \boldsymbol{D}(v)] = 0$, and therefore generate a family of commuting elements of $\mathsf{TL}_N(0)$. The Hamiltonian $\boldsymbol{H}_o$ of the model is related to the transfer tangle in the limit $u \to 0$ via the relation

$$\boldsymbol{D}(u) = \boldsymbol{I} - 2u\boldsymbol{H}_o + \mathcal{O}(u^2), \qquad \boldsymbol{H}_o = -\sum_{j=1}^{N-1} e_j, \tag{2.14}$$

and is also in this family of commuting elements. Finally, the transfer tangle satisfies an inversion identity [103]:

$$\boldsymbol{D}(u)\boldsymbol{D}(u + \tfrac{\pi}{2}) = \boldsymbol{I}\left(\frac{\cos^{2N} u - \sin^{2N} u}{\cos^2 u - \sin^2 u}\right)^2. \tag{2.15}$$

In particular, this relation implies that the eigenvalues $\Lambda(u)$ of $\boldsymbol{D}(u)$ are of the form

$$\Lambda(u) = \prod_{j=1}^{\lfloor \frac{N-1}{2} \rfloor} \Big(1 + \epsilon_j \sin 2u \, \sin t_j\Big)\Big(1 + \mu_j \sin 2u \, \sin t_j\Big),$$
$$t_j = \begin{cases} \frac{j\pi}{N} & \text{even } N, \\ \frac{(2j-1)\pi}{2N} & \text{odd } N, \end{cases} \tag{2.16}$$

where ϵ_j and μ_j are in $\{+1, -1\}$. Different eigenvalues then correspond to different choices of the signs ϵ_j and μ_j.

The partition functions. The various partition functions defined in the first paragraphs of Section 2.1 are written using the tools defined above. We assign the upper labels AB, A and B to the transfer tangles and link states to indicate which system or subsystem they pertain to. We find

$$Z_f^{(d),AB} = 2^{2MN}(v_d^A \otimes v_0^B)\cdot\big(\boldsymbol{D}^A \otimes \boldsymbol{D}^B\big)^M \big(\boldsymbol{D}^{AB}\big)^M v_d^{AB}\big|_{\mathsf{V}_{N,d}}\,, \tag{2.17a}$$

$$Z_r^{(d),AB} = 2^{2MN} v_d^{AB} \cdot (\boldsymbol{D}^{AB})^{2M} v_d^{AB}\big|_{\mathsf{V}_{N,d}} , \tag{2.17b}$$

$$Z_r^{(d),A} = 2^{2MN_A} v_d^{A} \cdot (\boldsymbol{D}^{A})^{2M} v_d^{A}\big|_{\mathsf{V}_{N_A,d}} , \tag{2.17c}$$

$$Z_r^{(2),B} = 2^{2MN_B} v_2^{B} \cdot (\boldsymbol{D}^{B})^{2M} v_2^{B}\big|_{\mathsf{V}_{N_B,2}} , \tag{2.17d}$$

and

$$\tilde{Z}_f^{(2),AB} = 2^{2MN} (v_2^A \otimes v_0^B) \odot \big(\boldsymbol{D}^A \otimes \boldsymbol{D}^B\big)^M \big(\boldsymbol{D}^{AB}\big)^M v_2^{AB}\Big|_{\mathsf{P}_{N,2}} , \tag{2.18a}$$

$$\tilde{Z}_r^{(2),AB} = 2^{2MN} v_2^{AB} \odot \big(\boldsymbol{D}^{AB}\big)^{2M} v_2^{AB}\Big|_{\mathsf{P}_{N,2}} , \tag{2.18b}$$

$$\tilde{Z}_r^{(2),A} = 2^{2MN_A} v_2^{A} \odot \big(\boldsymbol{D}^{A}\big)^{2M} v_2^{A}\Big|_{\mathsf{P}_{N_A,2}} , \tag{2.18c}$$

where

$v_d =$ 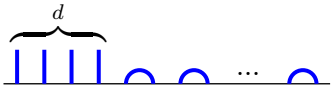

(2.19)

and $v \otimes w$ indicates that w is attached to the right of v. The powers of 2 ensure that each tile has weight 1 instead of $\frac{1}{\sqrt{2}}$ as it does in (2.13) for $u = \frac{\pi}{4}$.

2.1.2 Partition functions from the XX spin chain

The next step of the computation is to rewrite the formulas for the partition functions relevant for the bipartite fidelity in terms of matrix elements in the XX spin chain.

The XX representation. The XX representation of $\mathsf{TL}_N(0)$, which we denote by X_N, is defined on the vector space $(\mathbb{C}^2)^{\otimes N}$ where we use the canonical basis (1.13) for $\mathbb{C}^2$. This representation is linear, and the generators e_j are represented by the matrices [140]

$$\mathsf{X}_N(e_j) = \underbrace{\mathbb{I}_2 \otimes \cdots \otimes \mathbb{I}_2}_{j-1} \otimes \begin{pmatrix} 0 & 0 & 0 & 0 \\ 0 & \mathrm{i} & 1 & 0 \\ 0 & 1 & \mathrm{i}^{-1} & 0 \\ 0 & 0 & 0 & 0 \end{pmatrix} \otimes \underbrace{\mathbb{I}_2 \otimes \cdots \otimes \mathbb{I}_2}_{N-j-1} . \tag{2.20}$$

It is indeed not hard to check that these matrices satisfy the defining relations (2.7) of $\mathsf{TL}_N(0)$. The generators also commute with the total magnetisation $S^z = \frac{1}{2}\sum_{i=1}^{N}\sigma_i^z$. As a consequence, the representation X_N splits as a direct sum of smaller representations labelled by the eigenvalues m of S^z, given by $-\frac{N}{2}, -\frac{N-2}{2}, \ldots, \frac{N}{2}$.

In this representation, the Hamiltonian is the XX Hamiltonian with the $U_q(s\ell_2)$-invariant boundary magnetic fields of Pasquier and Saleur [140] and $q = \mathrm{i}$:

$$H_o = \mathsf{X}_N(\boldsymbol{H}_o) = -\frac{1}{2}\sum_{j=1}^{N-1}\left(\sigma_j^x\sigma_{j+1}^x + \sigma_j^y\sigma_{j+1}^y\right) - \frac{\mathrm{i}}{2}(\sigma_1^z - \sigma_N^z). \tag{2.21}$$

Likewise, the representative of $\boldsymbol{D}(u)$ in the XX representation, denoted $D(u)$, is the double-row transfer matrix of the six-vertex model. We use the notation $D = D(\frac{\pi}{4})$ for the transfer matrix at the isotropic point.

Embedding $\mathsf{V}_{N,d}$ in the XX representation. There exists a linear map from link states to spin states that intertwines the standard and spin-chain representations of $\mathsf{TL}_N(0)$. For a given link state $v \in \mathsf{V}_{N,d}$, we define its image in $(\mathbb{C}^2)^{\otimes N}$ under this map as $|v\rangle$. Locally, it is defined as

$$|\,\cap\,\rangle = \omega\,|{\uparrow\downarrow}\rangle + \omega^{-1}\,|{\downarrow\uparrow}\rangle, \qquad |\,\perp\,\rangle = |{\downarrow}\rangle, \qquad \omega = \mathrm{e}^{\mathrm{i}\pi/4}. \tag{2.22}$$

To obtain the spin state corresponding to a given link state, we repeatedly apply these local rules for each arc and each defect. For instance, for $N = 4$, we have

$$|\,\perp\perp\cap\,\rangle = \omega\,|{\downarrow\downarrow\uparrow\downarrow}\rangle + \omega^{-1}\,|{\downarrow\downarrow\downarrow\uparrow}\rangle, \tag{2.23a}$$

$$|\,\cap\cap\,\rangle = \omega^2\,|{\uparrow\downarrow\uparrow\downarrow}\rangle + |{\uparrow\downarrow\downarrow\uparrow}\rangle + |{\downarrow\uparrow\uparrow\downarrow}\rangle + \omega^{-2}\,|{\downarrow\uparrow\downarrow\uparrow}\rangle, \tag{2.23b}$$

$$|\,\cap\!\cap\,\rangle = \omega^2\,|{\uparrow\uparrow\downarrow\downarrow}\rangle + |{\uparrow\downarrow\uparrow\downarrow}\rangle + |{\downarrow\uparrow\downarrow\uparrow}\rangle + \omega^{-2}\,|{\downarrow\downarrow\uparrow\uparrow}\rangle. \tag{2.23c}$$

Link states in $\mathsf{V}_{N,d}$ are therefore mapped to spin states of magnetisation $m = -\frac{d}{2}$. The map is indeed a homomorphism, namely one can check that

$$\mathsf{X}_N(e_j)|v\rangle = \big|(e_j v|_{\mathsf{V}_{N,d}})\big\rangle \tag{2.24}$$

for $j = 1, \dots, N-1$ and $v \in \mathsf{V}_{N,d}$. This map also preserves the bilinear form for the standard modules. Indeed, with the notation $\langle\!\langle v| = |v\rangle^{\mathrm{t}}$, where the upper label $^{\mathrm{t}}$ stands for real transposition, we have $\langle\!\langle v|v'\rangle = v \cdot v'$, for each $v, v' \in \mathsf{V}_{N,d}$. For example,

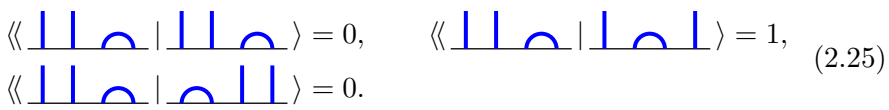

(2.25)

Clearly, if $v \in \mathsf{V}_{N,d}$ and $v' \in \mathsf{V}_{N,d'}$ with $d \neq d'$, then $\langle\!\langle v|v'\rangle = 0$.

Embedding $\mathsf{P}_{N,2}$ in the XX representation. There exists a similar map from link states to spin states for $\mathsf{P}_{N,2}$. For $v \in \mathsf{P}_{N,2}$, we denote its image under this map as $|\tilde{v}\rangle$. The local relations are

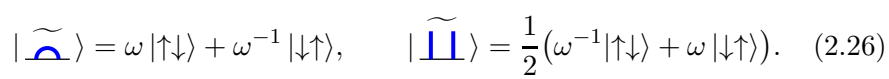

(2.26)

For a given $v \in \mathsf{P}_{N,2}$, these relations are applied locally to each arc and to the defects, to produce an element of $(\mathbb{C}^2)^{\otimes N}$. For example, for $N = 4$, we have

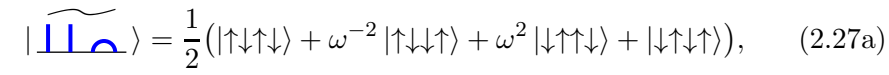

(2.27a)

which is not identical to (2.23a). The spin states corresponding to and  under this map coincide with those in (2.23b) and (2.23c). This map is a homomorphism of representations, namely

$$\mathsf{X}_N(e_j)|\tilde{v}\rangle = \big|\widetilde{(e_j v|_{\mathsf{P}_{N,2}})}\big\rangle. \tag{2.28}$$

It also preserves the bilinear form $\odot$ on $\mathsf{P}_{N,2}$: $\langle\!\langle \tilde{v}|\tilde{v}'\rangle = v \odot v'$ for $v, v' \in \mathsf{P}_{N,2}$. For instance, we have

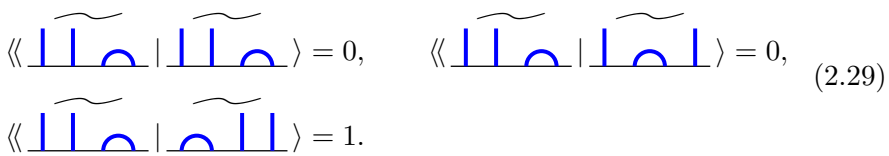

(2.29)

The partition functions. Because the maps introduced above are homomorphisms of $\mathsf{TL}_N(0)$ representations and preserve the bilinear

forms, we can translate the expressions (2.17) and (2.18) for the partition functions as matrix elements in the XX spin chain. We obtain:

$$Z_f^{(d),AB} = 2^{2MN} \langle\langle v_d^A \otimes v_0^B | \left(D^A \otimes D^B\right)^M \left(D^{AB}\right)^M | v_d^{AB} \rangle, \tag{2.30a}$$

$$Z_r^{(d),AB} = 2^{2MN} \langle\langle v_d^{AB} | (D^{AB})^{2M} | v_d^{AB} \rangle, \tag{2.30b}$$

$$Z_r^{(d),A} = 2^{2MN_A} \langle\langle v_d^A | (D^A)^{2M} | v_d^A \rangle, \tag{2.30c}$$

$$Z_r^{(2),B} = 2^{2MN_B} \langle\langle v_2^B | (D^B)^{2M} | v_2^B \rangle, \tag{2.30d}$$

and

$$\tilde{Z}_f^{(2),AB} = 2^{2MN} \langle\langle \tilde{v}_2^A \otimes \tilde{v}_0^B | \left(D^A \otimes D^B\right)^M \left(D^{AB}\right)^M | \tilde{v}_2^{AB} \rangle, \tag{2.31a}$$

$$\tilde{Z}_r^{(2),AB} = 2^{2MN} \langle\langle \tilde{v}_2^{AB} | \left(D^{AB}\right)^{2M} | \tilde{v}_2^{AB} \rangle, \tag{2.31b}$$

$$\tilde{Z}_r^{(2),A} = 2^{2MN_A} \langle\langle \tilde{v}_2^A | \left(D^A\right)^{2M} | \tilde{v}_2^A \rangle, \tag{2.31c}$$

where we recall that $\langle\langle v \otimes w| \equiv \langle\langle v| \otimes \langle\langle w|$.

2.1.3 Diagonalisation of the Hamiltonian

The diagonalisation procedure for the XX Hamiltonian (2.21) is similar to the one presented in Section 1.2.2. For the $U_q(s\ell_2)$-invariant chain at $q = \mathrm{i}$, it was studied in [148, 149]. The first step is to write H_o as

$$H_o = -\left(\sum_{j=1}^{N-1} c_{j+1}^\dagger c_j + c_j^\dagger c_{j+1} \right) - \mathrm{i} \left(c_1^\dagger c_1 - c_N^\dagger c_N \right) \tag{2.32}$$

where the c_j and $c_j^\dagger$ are the canonical fermionic operators (1.52) obtained with the Jordan-Wigner transformation. Recalling that $\omega = \mathrm{e}^{\mathrm{i}\pi/4}$, the second step is to perform a Fourier transform of these operators, by defining

$$\eta_k = \frac{1}{\kappa_k} \sum_{j=1}^{N-1} \sin(\tfrac{\pi k j}{N})\, a_j, \quad \eta_k^\dagger = \frac{1}{\kappa_k} \sum_{j=1}^{N-1} \sin(\tfrac{\pi k j}{N})\, a_j^\dagger, \tag{2.33}$$

where

$$\kappa_k = \sqrt{N \cos(\tfrac{\pi k}{N})} \tag{2.34}$$

and

$$a_j = \omega\, c_j + \omega^{-1} c_{j+1}, \qquad a_j^{\mathrm{t}} = \omega\, c_j^\dagger + \omega^{-1} c_{j+1}^\dagger. \tag{2.35}$$

These operators satisfy the anticommutation relations

$$\begin{aligned} &\{a_j, a_k^{\mathrm{t}}\} = \delta_{j,k-1} + \delta_{j,k+1}, \quad \{\eta_k, \eta_\ell^{\mathrm{t}}\} = \delta_{k,\ell}, \\ &\{a_j, a_k\} = \{a_j^{\mathrm{t}}, a_k^{\mathrm{t}}\} = \{\eta_k, \eta_\ell\} = \{\eta_k^{\mathrm{t}}, \eta_\ell^{\mathrm{t}}\} = 0. \end{aligned} \tag{2.36}$$

The Hamiltonian can be expressed in Jordan-normal form using these operators. We recall that we use the real transposition for the conjugation of fermionic operators, so that the overlaps computed in the spin chain correspond to partition functions in the loop model through the relations (2.30) and (2.31).

Results for odd N. For odd N, the resulting expression for the Hamiltonian is diagonal and takes the form

$$H_o = \sum_{k=1}^{N-1} \lambda_k \eta_k^{\mathrm{t}} \eta_k, \qquad \lambda_k = -2\cos(\tfrac{\pi k}{N}) \qquad (\text{odd } N). \tag{2.37}$$

The set of operators η_k and η_k^{t}, with $k = 1, \ldots, N-1$, is complemented with two extra operators,

$$\phi = \frac{1}{\kappa_\phi} \sum_{j=1}^{N} \mathrm{i}^{-(j-1)} c_j, \qquad \phi^{\mathrm{t}} = \frac{1}{\kappa_\phi} \sum_{j=1}^{N} \mathrm{i}^{-(j-1)} c_j^\dagger, \tag{2.38}$$

where

$$\kappa_\phi = 1 \qquad (\text{odd } N). \tag{2.39}$$

These operators satisfy the anticommutation relations

$$\begin{aligned} &\{\phi^{\mathrm{t}}, \phi\} = 1, \\ &\{\phi^{\mathrm{t}}, \eta_k\} = \{\phi, \eta_k^{\mathrm{t}}\} = \{\phi, \eta_k\} = \{\phi^{\mathrm{t}}, \eta_k^{\mathrm{t}}\} = 0. \end{aligned} \tag{2.40}$$

The full set thus consists of N creation operators and N annihilation operators. By acting with the N creation operators on the reference state $|0\rangle = |\downarrow \cdots \downarrow\rangle$, one obtains a basis for the 2^N eigenstates of H_o. In terms of these fermions, the magnetisation operator reads

$$S^z = -\frac{N}{2} + \phi^\dagger \phi + \sum_{k=1}^{N-1} \eta_k^\dagger \eta_k \qquad (\text{odd } N). \tag{2.41}$$

Results for even N. For even N, the set of operators η_k and η_k^{t}, with $k \in \{1, \ldots, \frac{N-2}{2}\} \cup \{\frac{N+2}{2}, \ldots, N-1\}$ is complemented with the operators

$$\begin{aligned} \chi &= -\omega\sqrt{\frac{2}{N}} \sum_{j=1}^{N} \mathrm{i}^{-(j-1)} \left(\lfloor \tfrac{j}{2} \rfloor - \tfrac{N}{4}\right) c_j, \\ \chi^{\mathrm{t}} &= -\omega\sqrt{\frac{2}{N}} \sum_{j=1}^{N} \mathrm{i}^{-(j-1)} \left(\lfloor \tfrac{j}{2} \rfloor - \tfrac{N}{4}\right) c_j^\dagger, \end{aligned} \tag{2.42}$$

as well as with the operators ϕ and ϕ^{t} in (2.38), with the constant κ_ϕ set to

$$\kappa_\phi = \omega\sqrt{\frac{N}{2}} \qquad \text{(even } N\text{)}. \tag{2.43}$$

The anticommutation relations in this case are

$$\begin{aligned} &\{\phi, \chi^{\mathrm{t}}\} = \{\phi^{\mathrm{t}}, \chi\} = 1, \\ &\{\phi^{\mathrm{t}}, \phi\} = \{\chi^{\mathrm{t}}, \chi\} = \{\phi, \chi\} = \{\phi^{\mathrm{t}}, \chi^{\mathrm{t}}\} = 0, \end{aligned} \tag{2.44}$$

and all the anticommutators involving the operators η_k and η_k^{t} and one of $\phi, \phi^{\mathrm{t}}, \chi$ and χ^{t} also vanish. In terms of these operators, the Hamiltonian takes the form

$$H_o = \phi^{\mathrm{t}}\phi + \sum_{\substack{k=1 \\ k\neq N/2}}^{N-1} \lambda_k \eta_k^{\mathrm{t}} \eta_k, \qquad \lambda_k = -2\cos(\tfrac{\pi k}{N}) \qquad \text{(even } N\text{)}. \tag{2.45}$$

The operators η_k^{t}, ϕ^{t} and χ^{t} form a set of N creation operators. Acting on the reference state $|0\rangle$ with these operators, one obtains a full basis of eigenstates and generalised eigenstates, of dimension 2^N. The magnetisation operator reads

$$S^z = -\frac{N}{2} + \phi^\dagger\chi + \chi^\dagger\phi + \sum_{\substack{k=1 \\ k\neq N/2}}^{N-1} \eta_k^\dagger \eta_k \qquad \text{(even } N\text{)}. \tag{2.46}$$

2.1.4 Groundstates

Except for the case of zero magnetisation, the groundstate eigenspace of H_o restricted to the sector of magnetisation m has dimension one. Recalling from Section 2.1.2 the relation $d = -2m$, we denote the groundstate

of magnetisation m by $|w_{-2m}\rangle = |w_d\rangle$ and the corresponding eigenvalue of the transfer matrix by $\Lambda_d(u)$. In terms of the fermions, this state takes the form

$$|w_d\rangle = \eta_1^{\mathrm{t}}\eta_2^{\mathrm{t}}\dots\eta_{(N-d)/2}^{\mathrm{t}}|0\rangle \qquad (d \neq 0). \tag{2.47}$$

For even N and $d = 0$, the eigenspace is two-dimensional,

$$|w_0\rangle = \phi^{\mathrm{t}}\eta_1^{\mathrm{t}}\eta_2^{\mathrm{t}}\dots\eta_{N/2-1}^{\mathrm{t}}|0\rangle, \qquad |\hat{w}_0\rangle = \chi^{\mathrm{t}}\eta_1^{\mathrm{t}}\eta_2^{\mathrm{t}}\dots\eta_{N/2-1}^{\mathrm{t}}|0\rangle, \tag{2.48}$$

and the states form a rank-two Jordan cell:

$$H_o|w_0\rangle = h_0|w_0\rangle, \quad H_o|\hat{w}_0\rangle = h_0|\hat{w}_0\rangle + |w_0\rangle, \quad h_0 = 1 - \cot(\tfrac{\pi}{2N}). \tag{2.49}$$

These states are also generalised eigenstates for the transfer matrix $D(u)$. The groundstate eigenvalue corresponds to a specific choice for the unfixed signs in (2.16) according to a *selection rule* [103, 148]. For the groundstate, these are given by $\epsilon_j = \mu_j = 1$ for $j = 1, \dots, \frac{N-2}{2}$. The eigenvalue reads

$$\Lambda_0(u) = \prod_{j=1}^{\frac{N-2}{2}} \left(1 + \sin 2u \, \sin t_j\right)^2. \tag{2.50}$$

The transfer tangle $D(u)$ mixes $|w_0\rangle$ and $|\hat{w}_0\rangle$ in a rank-two Jordan cell:

$$D(u)|w_0\rangle = \Lambda_0(u)|w_0\rangle, \qquad D(u)|\hat{w}_0\rangle = \Lambda_0(u)|\hat{w}_0\rangle + f(u)|w_0\rangle, \tag{2.51}$$

where $f(u)$ is a yet undetermined function of u. Using the inversion identity (2.15) and expanding $f(u)$ and $\Lambda_0(u)$ as centered Laurent polynomials in $\mathrm{e}^{\mathrm{i}u}$, we find [4]

$$f(u) = -\sin(2u)\Lambda_0(u). \tag{2.52}$$

2.2 Bipartite fidelity for primary fields

In this section, we apply Wick's theorem to derive closed-form expressions for the bipartite fidelity $\mathcal{F}_f^{(d)}$ for critical dense polymers. In the scaling limit, this lattice quantity is related to the correlation function of primary fields inserted on the flat pants domain.

2.2.1 Ratios of partition functions in the limit $M \to \infty$

To compute the bipartite fidelity, we extract the leading behaviour of the partition functions (2.30) as M tends to infinity. We start with (2.30a):

$$Z_f^{(d),AB} = 2^{2MN}\Big(\langle\langle v_d^A|(D^A)^M \otimes \langle\langle v_0^B|(D^B)^M\Big)\big(D^{AB}\big)^M|v_d^{AB}\rangle. \quad (2.53)$$

The state $|v_d\rangle$ can be written using the fermions a_j^{t} in (2.35) as

$$|v_d\rangle = a_{d+1}^{\mathrm{t}} a_{d+3}^{\mathrm{t}} a_{d+5}^{\mathrm{t}} \cdots a_{N-1}^{\mathrm{t}}|0\rangle. \quad (2.54)$$

The identity matrix restricted to the eigenspace of magnetisation $m = -d/2$ is of the form

$$\begin{aligned} \mathbb{I}\big|_{S^z=-d/2} &= |w_d\rangle\langle\langle w_d| + \dots \quad (d \neq 0), \\ \mathbb{I}\big|_{S^z=0} &= |\hat{w}_0\rangle\langle\langle w_0| + |w_0\rangle\langle\langle \hat{w}_0| + \dots \end{aligned} \quad (2.55)$$

where the next terms involve states that are not groundstates. We therefore have

$$(D^{AB})^M|v_d^{AB}\rangle \simeq (\Lambda_d^{AB})^M|w_d^{AB}\rangle\langle\langle w_d^{AB}|v_d^{AB}\rangle, \quad (2.56a)$$

$$\langle\langle v_d^A|(D^A)^M \simeq (\Lambda_d^A)^M\langle\langle v_d^A|w_d^A\rangle\langle\langle w_d^A|, \quad (2.56b)$$

$$\begin{aligned} \langle\langle v_0^B|(D^B)^M \simeq{}& (\Lambda_0^B)^M\langle\langle v_0^B|\hat{w}_0^B\rangle\langle\langle w_0^B| \\ &+ (\Lambda_0^B)^{M-1}\underbrace{\langle\langle v_0^B|w_0^B\rangle}_{=0}\Big(\Lambda_0^B\langle\langle \hat{w}_0^B| + Mf^B\langle\langle w_0^B|\Big), \end{aligned} \quad (2.56c)$$

where $\simeq$ denotes an equality up to terms that are exponentially small in M compared to the leading term. We use the notation $\Lambda_d = \Lambda_d(\frac{\pi}{4})$ and $f = f(\frac{\pi}{4})$. The overlap $\langle\langle v_0^B|w_0^B\rangle$ vanishes because the state $|w_0\rangle$ contains a fermion ϕ^{t} which anticommutes with a_j for each j and satisfies $\langle 0|\phi^{\mathrm{t}} = 0$, with $\langle 0| = |0\rangle^\dagger = |0\rangle^{\mathrm{t}}$. We thus find

$$\begin{aligned} Z_f^{(d),AB} \simeq (2^{2N}\Lambda_d^{AB}\Lambda_d^A\Lambda_0^B)^M &\langle\langle w_d^{AB}|v_d^{AB}\rangle \\ &\langle\langle v_d^A|w_d^A\rangle\,\langle\langle v_0^B|\hat{w}_0^B\rangle\,\langle\langle w_d^A \otimes w_0^B|w_d^{AB}\rangle. \end{aligned} \quad (2.57)$$

Repeating the same exercise for $Z_r^{(d),AB}$, $Z_r^{(d),A}$ and $Z_r^{(2),B}$, we find

$$\begin{aligned} Z_r^{(d),AB} &\simeq 2^{2MN}(\Lambda_d^{AB})^{2M}\langle\langle w_d^{AB}|v_d^{AB}\rangle^2, \\ Z_r^{(d),A} &\simeq 2^{2MN_A}(\Lambda_d^A)^{2M}\langle\langle v_d^A|w_d^A\rangle^2, \\ Z_r^{(2),B} &\simeq 2^{2MN_B}(\Lambda_2^B)^{2M}\langle\langle v_2^B|w_2^B\rangle^2. \end{aligned} \quad (2.58)$$

We also note that the eigenvalues of the sectors $d = 0$ and $d = 2$ are equal: $\Lambda_2 = \Lambda_0$. From (2.3), the bipartite fidelity $\mathcal{F}_f^{(d)}$ reads

$$\mathcal{F}_f^{(d)} = -\log\left(\frac{\langle\langle v_0^B|\hat{w}_0^B\rangle}{\langle\langle v_2^B|w_2^B\rangle}\langle\langle w_d^A \otimes w_0^B|w_d^{AB}\rangle\right)^2. \tag{2.59}$$

2.2.2 Fermionic operators in the different subsystems

In this subsection, we introduce the fermionic operators specific to the subsystems A and B and present the anticommutation relations that they satisfy with the fermions of the full system. We compute (2.59) with the states

$$\begin{aligned} |w_d^{AB}\rangle &= \eta_1^{\mathrm{t}} \cdots \eta_{\frac{N-d}{2}}^{\mathrm{t}} |0\rangle\,, \\ |w_d^A \otimes w_0^B\rangle &= \eta_1^{A,\mathrm{t}} \cdots \eta_{\frac{N_A-d}{2}}^{A,\mathrm{t}} \phi^{B,\mathrm{t}} \eta_1^{B,\mathrm{t}} \cdots \eta_{\frac{N_B-2}{2}}^{B,\mathrm{t}} |0\rangle \end{aligned} \tag{2.60}$$

where

$$\eta_k^A = \frac{1}{\kappa_k^A} \sum_{j=1}^{N_A-1} \sin(\tfrac{\pi k j}{N_A}) a_j, \qquad \kappa_k^A = \sqrt{N_A \cos(\tfrac{\pi k}{N_A})}, \tag{2.61a}$$

$$\eta_k^B = \frac{1}{\kappa_k^B} \sum_{j=N_A+1}^{N-1} \sin(\tfrac{\pi k (j-N_A)}{N_B}) a_j, \qquad \kappa_k^B = \sqrt{N_B \cos(\tfrac{\pi k}{N_B})}, \tag{2.61b}$$

$$\phi^B = \omega^{-1} \sqrt{\frac{2}{N_B}} \sum_{j=N_A+1}^{N} \mathrm{i}^{-(j-N_A-1)}\, c_j\,. \tag{2.61c}$$

The transpose of these fermions are denoted $\eta_k^{A,\mathrm{t}}$, $\eta_k^{B,\mathrm{t}}$ and $\phi^{B,\mathrm{t}}$.

In the following, we use Wick's theorem to express the various overlaps as determinants. Let θ_k and ϑ_ℓ, with $k, \ell = 1, \ldots, L$, be two sets of fermionic operators that annihilate the same vacuum state $|0\rangle$, namely $\theta_k|0\rangle = \vartheta_\ell|0\rangle = 0$ for $k, \ell = 1, \ldots, L$. Wick's theorem states that

$$\langle 0|\theta_L \ldots \theta_2 \theta_1 \vartheta_1^{\mathrm{t}} \vartheta_2^{\mathrm{t}} \ldots \vartheta_L^{\mathrm{t}}|0\rangle = \det_{k,\ell=1}^{L} \{\theta_k, \vartheta_\ell^{\mathrm{t}}\}. \tag{2.62}$$

We use this equality to compute the ratio $\langle\langle v_0^B|\hat{w}_0^B\rangle / \langle\langle v_2^B|w_2^B\rangle$. Both the numerator and the denominator are expressed as determinants, and

after a simple argument, we find

$$\frac{\langle\!\langle v_0^B|\hat{w}_0^B\rangle}{\langle\!\langle v_2^B|w_2^B\rangle} = \omega^2\sqrt{\frac{N_B}{2}}. \tag{2.63}$$

The other overlaps involve fermions of both the full system and the subsystems A and B. To compute them, we introduce the rescaled operators

$$\tilde{\eta}_k = \sum_{j=1}^{N-1} \sin(\tfrac{\pi kj}{N})\, a_j, \qquad k = 1, \dots, N-1, \tag{2.64}$$

and likewise for $\tilde{\eta}_k^A$ and $\tilde{\eta}_k^B$, by removing the constants κ_k^A and κ_k^B in (2.61). These operators have the advantage of being well defined for $k = N/2$. All the fermionic operators appearing in $\langle\!\langle w_d^A \otimes w_0^B|w_d^{AB}\rangle$ can in fact be written in terms of the $\tilde{\eta}_k$. Indeed, we have $\tilde{\eta}_k = \kappa_k \eta_k$ and, for even N, $\tilde{\eta}_{\frac{N}{2}} = (\omega\kappa_\phi)\phi$. The same holds for the operators of the subsystems A and B. With this convention, Wick's theorem yields

$$\frac{\langle\!\langle v_0^B|\hat{w}_0^B\rangle}{\langle\!\langle v_2^B|w_2^B\rangle}\langle\!\langle w_d^A \otimes w_0^B|w_d^{AB}\rangle = \left(\prod_{k=1}^{(N_A-d)/2} \kappa_k^A \prod_{k'=1}^{(N_B-2)/2} \kappa_{k'}^B \prod_{\ell=1}^{(N-d)/2} \kappa_\ell\right)^{-1} \det \mathcal{M}_d \tag{2.65}$$

where

$$[\mathcal{M}_d]_{k,\ell} = \begin{cases} \{\tilde{\eta}_k^A, \tilde{\eta}_\ell^t\} & k = 1, \dots, \frac{N_A-d}{2}, \\ \{\tilde{\eta}^B_{k-\frac{N_A-d}{2}}, \tilde{\eta}_\ell^t\} & k = \frac{N_A-d}{2}+1, \dots, \frac{N-d}{2}, \end{cases} \tag{2.66}$$

with $\ell = 1, \dots, \frac{N-d}{2}$. The anticommutators in this matrix are

$$\begin{aligned} \{\tilde{\eta}_k^A, \tilde{\eta}_\ell^t\} &= (-1)^k \frac{\cos(\frac{\pi\ell}{N})\sin\left(\frac{\pi k}{N_A}\right)\sin(\pi\ell x)}{\cos\left(\frac{\pi k}{N_A}\right) - \cos(\frac{\pi\ell}{N})}, \\ \{\tilde{\eta}_k^B, \tilde{\eta}_\ell^t\} &= -\frac{\cos(\frac{\pi\ell}{N})\sin\left(\frac{\pi k}{N_B}\right)\sin(\pi\ell x)}{\cos\left(\frac{\pi k}{N_B}\right) - \cos(\frac{\pi\ell}{N})}, \end{aligned} \tag{2.67}$$

where $x = N_A/N$ is the aspect ratio.

2.2.3 Closed form for the overlaps

In computing the determinant of $\mathcal{M}_d$, we find that all the trigonometric functions appearing in the numerators in (2.67) factor out. Because $\mathcal{M}_d$ is defined in two parts, this is a non-trivial result. It stems from the fact that the ℓ-dependent factors in the numerators are identical. In contrast, the same factorisation does not occur for the XX spin chain with free boundary conditions. Exact asymptotics in this case were only obtained for $x = 1/2$ in [63]. The ratio of overlaps in (2.65) becomes

$$\frac{\langle\langle v_0^B|\hat{w}_0^B\rangle}{\langle\langle v_2^B|w_2^B\rangle}\langle w_d^A\otimes w_0^B|w_d^{AB}\rangle = \prod_{k=1}^{\frac{N_A-d}{2}}\frac{\sin\left(\frac{\pi k}{N_A}\right)}{\kappa_k^A}\prod_{k=1}^{\frac{N_B-2}{2}}\frac{\sin\left(\frac{\pi k}{N_B}\right)}{\kappa_k^B}\prod_{\ell=1}^{\frac{N-d}{2}}\frac{\cos(\frac{\pi\ell}{N})\sin(\pi\ell x)}{\kappa_\ell}\times\det\mathcal{C}_d \quad (2.68)$$

where

$$[\mathcal{C}_d]_{k,\ell} = \begin{cases} \left[\cos\left(\frac{\pi k}{N_A}\right)-\cos(\frac{\pi\ell}{N})\right]^{-1} & k=1,\dots,\frac{N_A-d}{2}, \\ \left[\cos\left(\frac{\pi(k-(N_A-d)/2)}{N_B}\right)-\cos(\frac{\pi\ell}{N})\right]^{-1} & k=\frac{N_A-d+2}{2},\dots,\frac{N-d}{2}, \end{cases} \quad (2.69)$$

and $\ell = 1,\dots,\frac{N-d}{2}$. The determinant is evaluated using Cauchy's identity:

$$\det_{k,\ell=1}^{L}\left(\frac{1}{w_k-z_\ell}\right) = \frac{\prod_{1\leqslant k<\ell\leqslant L}(w_\ell-w_k)(z_k-z_\ell)}{\prod_{k,\ell=1}^{L}(w_k-z_\ell)}. \quad (2.70)$$

The result is

$$\begin{aligned}\det\mathcal{C}_d = &\prod_{1\leqslant k<k'\leqslant\frac{N_A-d}{2}}\left(\cos\left(\tfrac{\pi k'}{N_A}\right)-\cos\left(\tfrac{\pi k}{N_A}\right)\right)\prod_{1\leqslant k<k'\leqslant\frac{N_B}{2}}\left(\cos\left(\tfrac{\pi k'}{N_B}\right)-\cos\left(\tfrac{\pi k}{N_B}\right)\right)\\ &\times\prod_{k=1}^{\frac{N_A-d}{2}}\prod_{k'=1}^{\frac{N_B}{2}}\left(\cos\left(\tfrac{\pi k'}{N_B}\right)-\cos\left(\tfrac{\pi k}{N_A}\right)\right)\prod_{1\leqslant\ell<\ell'\leqslant\frac{N-d}{2}}\left(\cos\left(\tfrac{\pi\ell}{N}\right)-\cos\left(\tfrac{\pi\ell'}{N}\right)\right)\\ &\times\prod_{k=1}^{\frac{N_A-d}{2}}\prod_{\ell=1}^{\frac{N-d}{2}}\left(\cos\left(\tfrac{\pi k}{N_A}\right)-\cos\left(\tfrac{\pi\ell}{N}\right)\right)^{-1}\prod_{k=1}^{\frac{N_B}{2}}\prod_{\ell=1}^{\frac{N-d}{2}}\left(\cos\left(\tfrac{\pi k}{N_B}\right)-\cos\left(\tfrac{\pi\ell}{N}\right)\right)^{-1}.\end{aligned} \quad (2.71)$$

We note that the equalities (2.68) and (2.71) hold in the case where $\gcd(N_A, N) = 1$ for odd N, and $\gcd(\frac{N_A}{2}, \frac{N}{2}) = 1$ for even N. If these conditions are not met, some factors in the numerator and denominator may vanish. When this happens, the number of zeros in the numerator and denominator are always equal and the correct finite result is obtained by taking a limit on N_A in the generic expressions. In fact, our asymptotic analysis in Section 2.4 presupposes that N_A and N satisfy these coprimality conditions. The resulting functions are continuous in x, and we can approach any value $x \in (0, 1)$ in the scaling limit with these conditions.

2.2.4 Asymptotic expansion

With the closed-form formulas (2.68) and (2.71), we derive the asymptotic expansion of $\mathcal{F}_f^{(d)}$ in the limit of large N where the aspect ratio x is set to a constant in the interval $(0, 1)$. We find

$$\begin{aligned}\mathcal{F}_f^{(d)} = &-\frac{2}{8}\log N - 2\log \Upsilon_d(x) + \Big[-\frac{1}{12}\left(2x - 1 + \frac{2}{x}\right) \\ &+ \left(\frac{4}{3} - \frac{2}{x}\right)\Delta_{1,d+1} + \left(\frac{4}{3} - 2x\right)\Delta_{1,d+1}\Big]\log(1-x) \\ &+ \Big[-\frac{1}{12}\left(2(1-x) - 1 + \frac{2}{1-x}\right) - \frac{2}{3}\Delta_{1,d+1} \\ &+ \left(\frac{4}{3} - 2(1-x)\right)\Delta_{1,d+1}\Big]\log x \\ &+ 3\log A - \frac{1}{4}\left[1 + \log\left(\frac{\pi}{8}\right)\right] + \mathcal{O}\left(N^{-1}\right) \end{aligned} \tag{2.72}$$

where

$$\Upsilon_d(x) = (1-x)^{-\frac{2}{3}\Delta_{1,d+1}} x^{\frac{1}{3}\Delta_{1,d+1}}, \qquad \Delta_{r,s} = \frac{(2r-s)^2 - 1}{8}, \tag{2.73}$$

and $A = 1.282427...$ is the Glaisher-Kinkelin constant. We give the proof of this result in Section 2.4.

The formula (2.72) exactly matches the CFT prediction (1.81) of Stéphan and Dubail [63] for the logarithmic bipartite fidelity in the case where primary fields are inserted on the flat pants domain. First, the coefficient of the leading $\log N$ term is consistent with the known value $c = -2$ for

the central charge of the model and the conformal weight $\Delta_2 = 0$ of the field inserted at the end of the slit. It is indeed clear that, in the two-dimensional model defined on the flat pants geometry (see Figure 2.1), there is no change of boundary conditions at the end of the slit, and the weight of the identity field indeed vanishes.

Second, the constant term in (2.72) has the form of $g_f^{(1)}(x)$ given in (1.82) for a two-point function of primary fields. The fields ϕ_1 and ϕ_4 have the dimension $\Delta_1 = \Delta_4 = \Delta_{1,d+1}$, which is the known value for the boundary changing operator that accounts for the insertion of d defects on a boundary [141, 150]. The two other fields are identity fields, with $\Delta_2 = \Delta_3 = 0$. The function $\Upsilon_d(x)$ has the correct form that ensures that the four-point function (1.83) reduces to the usual power-law formula for the two-point function. The non-universal constant in (1.82) is given by

$$C_f = 3\log A - \frac{1}{4}\left(1 + \log\left(\frac{\pi}{8}\right)\right) = -3\zeta'(-1) - \frac{1}{4}\log\left(\frac{\pi}{8}\right), \qquad (2.74)$$

where $\zeta(z)$ is the Riemann zeta function.

Finally, we also note that $\mathcal{F}_f^{(d)}$ has no term proportional to $N^{-1}\log N$. Comparing with the predicted form (1.85) of the function $g_f^{(2)}(x)$, we deduce that the extrapolation length Ξ vanishes in the present case. For the XX chain on the flat pants lattice with no boundary magnetic fields, Dubail and Stéphan computed the $N^{-1}\log N$ contribution to the bipartite fidelity and found $\Xi = 1$ [63]. In this case, the momenta of the fermions are of the form $\frac{\pi j}{N+1}$. In contrast, the fermionic momenta for the model investigated in this chapter are of the form $\frac{\pi j}{N}$, leading to a vanishing extrapolation length. It is then tempting to conjecture that, for momenta of the form $\frac{\pi j}{N+\delta}$, the quantity $N + \delta$ is an effective length for the system from which the extrapolation length can be read directly. We note that a similar vanishing of the $N^{-1}\log N$ term was previously observed in [137] for the XXZ spin chain at the combinatorial point. In this case, the authors argue that the central charge and the conformal weights are such that the expression inside the bracket in (1.85) vanishes, thus preventing a measure of the extrapolation length.

2.3 Bipartite fidelity for logarithmic fields

In this section, we calculate the bipartite fidelity $\tilde{\mathcal{F}}_f^{(2)}$ with lattice and field theoretical approaches. In the scaling limit, this second instance of the bipartite fidelity is related to the correlation function of a primary field and his logarithmic partner in a rank-two Jordan cell on the flat pants domain. In the following, N, N_A and N_B are all even integers.

2.3.1 Ratios of partition functions in the limit $M \to \infty$

We start from (2.4) and (2.31) and apply the ideas used in Section 2.2.1 to the computation of $\tilde{\mathcal{F}}_f^{(2)}$. For $\tilde{Z}_f^{(2),AB}$, we have:

$$\tilde{Z}_f^{(2),AB} = 2^{2MN}\Big(\langle\!\langle \tilde{v}_2^A|(D^A)^M \otimes \langle\!\langle \tilde{v}_0^B|(D^B)^M\Big)\big(D^{AB}\big)^M|\tilde{v}_2^{AB}\rangle. \quad (2.75)$$

In this case, $\langle\!\langle \tilde{v}_2^A|$, $\langle\!\langle \tilde{v}_0^B|$ and $|\tilde{v}_2^{AB}\rangle$ all have zero magnetisation. We find

$$\begin{aligned}(D^{AB})^M|\tilde{v}_2^{AB}\rangle &\simeq (\Lambda_0^{AB})^M|w_0^{AB}\rangle\langle\!\langle \hat{w}_0^{AB}|\tilde{v}_2^{AB}\rangle \\ &\quad + (\Lambda_0^{AB})^{M-1}\Big(\Lambda_0^{AB}|\hat{w}_0^{AB}\rangle + Mf^{AB}|w_0^{AB}\rangle\Big)\langle\!\langle w_0^{AB}|\tilde{v}_2^{AB}\rangle, \quad (2.76a)\end{aligned}$$

$$\begin{aligned}\langle\!\langle \tilde{v}_2^A|(D^A)^M &\simeq (\Lambda_0^A)^M\langle\!\langle \tilde{v}_2^A|\hat{w}_0^A\rangle\langle\!\langle w_0^A| \\ &\quad + (\Lambda_0^A)^{M-1}\langle\!\langle \tilde{v}_2^A|w_0^A\rangle\Big(\Lambda_0^A\langle\!\langle \hat{w}_0^A| + Mf^A\langle\!\langle w_0^A|\Big), \quad (2.76b)\end{aligned}$$

$$\langle\!\langle \tilde{v}_0^B|(D^B)^M \simeq (\Lambda_0^B)^M\langle\!\langle \tilde{v}_0^B|\hat{w}_0^B\rangle\langle\!\langle w_0^B|, \quad (2.76c)$$

where $\langle\!\langle w_0^{AB}|\tilde{v}_2^{AB}\rangle$ and $\langle\!\langle \tilde{v}_2^A|w_0^A\rangle$ are non-zero, in contrast with the previous calculation. In computing $\tilde{Z}_f^{(2),AB}$, the leading-order term in the large-M expansion vanishes because $\langle\!\langle w_0^A \otimes w_0^B|w_0^{AB}\rangle = 0$. This occurs because $\langle\!\langle w_0^A \otimes w_0^B|\phi^{\mathrm{t}} = 0$. We therefore compute the next term in the large-M expansion and find

$$\begin{aligned}\tilde{Z}_f^{(2),AB} &\simeq 2^{2MN}M(\Lambda_0^{AB}\Lambda_0^A\Lambda_0^B)^M\langle\!\langle w_0^{AB}|\tilde{v}_2^{AB}\rangle\langle\!\langle \tilde{v}_2^A|w_0^A\rangle\langle\!\langle \tilde{v}_0^B|\hat{w}_0^B\rangle \\ &\quad \times\Big(\frac{f^{AB}}{\Lambda_0^{AB}}\langle\!\langle \hat{w}_0^A \otimes w_0^B|w_0^{AB}\rangle + \frac{f^A}{\Lambda_0^A}\langle\!\langle w_0^A \otimes w_0^B|\hat{w}_0^{AB}\rangle\Big). \quad (2.77)\end{aligned}$$

Repeating the derivations for $\tilde{Z}_r^{(2),AB}$ and $\tilde{Z}_r^{(2),A}$, we find

$$\begin{aligned}\tilde{Z}_r^{(2),AB} &\simeq 2^{2MN}(2M)(\Lambda_0^{AB})^{2M-1}f^{AB}\langle\!\langle w_0^{AB}|\tilde{v}_2^{AB}\rangle^2, \\ \tilde{Z}_r^{(2),A} &\simeq 2^{2MN_A}(2M)(\Lambda_0^A)^{2M-1}f^A\langle\!\langle \tilde{v}_2^A|w_0^A\rangle^2.\end{aligned} \quad (2.78)$$

The function $f(u)$ is given in (2.52), and we have $f(\frac{\pi}{4})/\Lambda_0(\frac{\pi}{4}) = -1$. Recalling that the denominator in (2.4) involves $Z_r^{(2),B}$ which we compute in (2.58), we find the following expression for $\tilde{\mathcal{F}}_f^{(2)}$:

$$\tilde{\mathcal{F}}_f^{(2)} = \\ -\log\left(\frac{1}{2}\frac{\langle\!\langle v_0^B|\hat{w}_0^B\rangle}{\langle\!\langle v_2^B|w_2^B\rangle}\big(\langle\!\langle \hat{w}_0^A\otimes w_0^B|w_0^{AB}\rangle + \langle\!\langle w_0^A\otimes w_0^B|\hat{w}_0^{AB}\rangle\big)\right)^2. \quad (2.79)$$

We note that, had $\tilde{\mathcal{F}}_f^{(2)}$ been defined with $\tilde{Z}_r^{(2),B}$ in the denominator instead of $Z_r^{(2),B}$, the argument of the logarithm in (2.4) would have vanished trivially in the limit.

2.3.2 Closed form for the overlaps

To obtain a closed-form expression for $\tilde{\mathcal{F}}_f^{(2)}$, it is easier to compare with (2.59) and compute the difference $\tilde{\mathcal{F}}_f^{(2)} - \mathcal{F}_f^{(2)}$:

$$\tilde{\mathcal{F}}_f^{(2)} - \mathcal{F}_f^{(2)} = -2\log\left(\frac{1}{2}\frac{\langle\!\langle \hat{w}_0^A\otimes w_0^B|w_0^{AB}\rangle + \langle\!\langle w_0^A\otimes w_0^B|\hat{w}_0^{AB}\rangle}{\langle\!\langle w_2^A\otimes w_0^B|w_2^{AB}\rangle}\right). \quad (2.80)$$

We express the three overlaps in the right side in terms of the fermionic operators,

$$\langle\!\langle \hat{w}_0^A\otimes w_0^B|w_0^{AB}\rangle = \\ \langle 0|\eta^B_{\frac{N_B}{2}-1}\cdots\eta_1^B\phi^B\eta^A_{\frac{N_A}{2}-1}\cdots\eta_1^A\chi^A\ \phi^{\mathrm{t}}\eta_1^{\mathrm{t}}\cdots\eta^{\mathrm{t}}_{\frac{N}{2}-1}|0\rangle, \quad (2.81a)$$

$$\langle\!\langle w_0^A\otimes w_0^B|\hat{w}_0^{AB}\rangle = \\ \langle 0|\eta^B_{\frac{N_B}{2}-1}\cdots\eta_1^B\phi^B\eta^A_{\frac{N_A}{2}-1}\cdots\eta_1^A\phi^A\ \chi^{\mathrm{t}}\eta_1^{\mathrm{t}}\cdots\eta^{\mathrm{t}}_{\frac{N}{2}-1}|0\rangle, \quad (2.81b)$$

$$\langle\!\langle w_2^A\otimes w_0^B|w_2^{AB}\rangle = \\ \langle 0|\eta^B_{\frac{N_B}{2}-1}\cdots\eta_1^B\phi^B\eta^A_{\frac{N_A}{2}-1}\cdots\eta_1^A\eta_1^{\mathrm{t}}\cdots\eta^{\mathrm{t}}_{\frac{N}{2}-1}|0\rangle, \quad (2.81c)$$

with

$$\phi^A = \omega^{-1}\sqrt{\frac{2}{N_A}}\sum_{j=1}^{N_A}\mathrm{i}^{-(j-1)}\,c_j\,, \\ \chi^A = -\omega\sqrt{\frac{2}{N_A}}\sum_{j=1}^{N_A}\mathrm{i}^{-(j-1)}\big(\lfloor\tfrac{j}{2}\rfloor - \tfrac{N_A}{4}\big)\,c_j. \quad (2.82)$$

The other fermionic operators for the subsystems A and B are defined in (2.61). We have the anticommutation relations

$$\begin{aligned} &\{\eta_j^A, \phi^{\mathrm{t}}\} = 0, \quad \{\chi^A, \phi^{\mathrm{t}}\} = \sqrt{x}, \\ &\{\eta_k^B, \phi^{\mathrm{t}}\} = 0, \quad \{\phi^B, \phi^{\mathrm{t}}\} = 0, \end{aligned} \tag{2.83a}$$

$$\begin{aligned} &\{\eta_j^A, \chi^{\mathrm{t}}\} = 0, \quad \{\phi^A, \chi^{\mathrm{t}}\} = \sqrt{x}, \\ &\{\eta_k^B, \chi^{\mathrm{t}}\} = 0, \quad \{\phi^B, \chi^{\mathrm{t}}\} = (-1)^{\frac{N_A}{2}} \sqrt{1-x}. \end{aligned} \tag{2.83b}$$

Recalling that N_A is even, we use these anticommutation relations to rewrite the first two overlaps in (2.81) as

$$\begin{aligned} &\langle\!\langle \hat{w}_0^A \otimes w_0^B | w_0^{AB} \rangle = \\ &\qquad \sqrt{x}\ \langle 0 | \eta^B_{\frac{N_B}{2}-1} \cdots \eta_1^B \phi^B \eta^A_{\frac{N_A}{2}-1} \cdots \eta_1^A\ \eta_1^{\mathrm{t}} \cdots \eta^{\mathrm{t}}_{\frac{N}{2}-1} | 0 \rangle, \end{aligned} \tag{2.84a}$$

$$\begin{aligned} \langle\!\langle w_0^A \otimes w_0^B | \hat{w}_0^{AB} \rangle &= \sqrt{x}\ \langle 0 | \eta^B_{\frac{N_B}{2}-1} \cdots \eta_1^B \phi^B \eta^A_{\frac{N_A}{2}-1} \cdots \eta_1^A\ \eta_1^{\mathrm{t}} \cdots \eta^{\mathrm{t}}_{\frac{N}{2}-1} | 0 \rangle \\ &+ \sqrt{1-x}\ \langle 0 | \eta^B_{\frac{N_B}{2}-1} \cdots \eta_1^B \eta^A_{\frac{N_A}{2}-1} \cdots \eta_1^A \phi^A\ \eta_1^{\mathrm{t}} \cdots \eta^{\mathrm{t}}_{\frac{N}{2}-1} | 0 \rangle, \end{aligned} \tag{2.84b}$$

and therefore

$$\frac{\langle\!\langle \hat{w}_0^A \otimes w_0^B | w_0^{AB} \rangle}{\langle\!\langle w_2^A \otimes w_0^B | w_2^{AB} \rangle} = \sqrt{x}, \tag{2.85a}$$

$$\begin{aligned} \frac{\langle\!\langle w_0^A \otimes w_0^B | \hat{w}_0^{AB} \rangle}{\langle\!\langle w_2^A \otimes w_0^B | w_2^{AB} \rangle} &= \sqrt{x} \\ + (-1)^{\frac{N}{2}} \frac{(1-x)}{\sqrt{x}} &\frac{\langle 0 | \tilde{\eta}^B_{\frac{N_B}{2}-1} \cdots \tilde{\eta}_1^B \tilde{\eta}^A_{\frac{N_A}{2}} \cdots \tilde{\eta}_1^A\ \tilde{\eta}_1^{\mathrm{t}} \cdots \tilde{\eta}^{\mathrm{t}}_{\frac{N}{2}-1} | 0 \rangle}{\langle 0 | \tilde{\eta}^B_{\frac{N_B}{2}} \cdots \tilde{\eta}_1^B \tilde{\eta}^A_{\frac{N_A}{2}-1} \cdots \tilde{\eta}_1^A\ \tilde{\eta}_1^{\mathrm{t}} \cdots \tilde{\eta}^{\mathrm{t}}_{\frac{N}{2}-1} | 0 \rangle}. \end{aligned} \tag{2.85b}$$

The right side of this last equality is written in terms of the rescaled operators $\tilde{\eta}_k$ defined in (2.64). To evaluate the remaining ratio, we use the identity

$$\tilde{\eta}^A_{\frac{N_A}{2}} = \tilde{\eta}_{\frac{N}{2}} - (-1)^{\frac{N_A}{2}} \tilde{\eta}^B_{\frac{N_B}{2}} \tag{2.86}$$

in the numerator. The first term with $\tilde{\eta}_{N/2}$ vanishes because this operator anticommutes with all the other operators. For the second term, by anticommuting $\tilde{\eta}^B_{N_B/2}$ towards the left across the operators $\tilde{\eta}^B_k$, we find

that the numerator is proportional to the denominator, with the overall factor $(-1)^{N/2}$. The result is

$$\frac{\langle\langle w_0^A \otimes w_0^B | \hat{w}_0^{AB}\rangle}{\langle\langle w_2^A \otimes w_0^B | w_2^{AB}\rangle} = \sqrt{x} + \frac{(1-x)}{\sqrt{x}} = \frac{1}{\sqrt{x}}. \tag{2.87}$$

Putting the results together, we conclude that the bipartite fidelity $\tilde{\mathcal{F}}_f^{(2)}$ satisfies the relation

$$\tilde{\mathcal{F}}_f^{(2)} - \mathcal{F}_f^{(2)} = -2\log\left(\frac{1+x}{2\sqrt{x}}\right). \tag{2.88}$$

Interestingly, this result holds for finite values of N.

2.3.3 CFT derivation of the universal behaviour

In this subsection, we derive the CFT prediction for the bipartite fidelity of logarithmic fields. We consider a logarithmic CFT at an arbitrary value c of the central charge that includes a pair $(\varphi(z), \omega(z))$ of boundary fields with conformal weight Δ in a rank-two Jordan cell, where $\varphi(z)$ is primary and $\omega(z)$ is its Jordan partner. Their transformation laws under a conformal transformation $y = y(z)$, as well as their two-point correlation functions on the upper-half plane are given in (1.42) and (1.43), respectively. For the sake of completeness, we recall

$$\begin{aligned} \varphi(y) &= \left(\frac{\mathrm{d}y}{\mathrm{d}z}\right)^{-\Delta} \varphi(z), \\ \omega(y) &= \left(\frac{\mathrm{d}y}{\mathrm{d}z}\right)^{-\Delta} \left(\omega(z) - 2\lambda_0 \varphi(z) \log\left(\frac{\mathrm{d}y}{\mathrm{d}z}\right)\right), \end{aligned} \tag{2.89}$$

and

$$\begin{aligned} \langle\omega(z_0)\omega(z_1)\rangle_{\mathbb{H}} &= \frac{\lambda_1\lambda_2 - 4\lambda_0\lambda_1\log(z_0-z_1)}{(z_0-z_1)^{2\Delta}}, \\ \langle\omega(z_0)\varphi(z_1)\rangle_{\mathbb{H}} &= \frac{\lambda_1}{(z_0-z_1)^{2\Delta}}, \\ \langle\varphi(z_0)\varphi(z_1)\rangle_{\mathbb{H}} &= 0. \end{aligned} \tag{2.90}$$

For the model of critical dense polymers, the central charge is $c = -2$. In [141], it is argued that the boundary field that accounts for the insertion of two adjacent defects forced to connect together is a logarithmic

field $\omega(z)$ of conformal weight $\Delta = 0$. In contrast, the field that inserts a simple arc on the boundary is identified with the identity field $\varphi(z)$. It also has weight $\Delta = 0$. The lattice calculations considered in Sections 2.3.1 and 2.3.2 correspond to computing a ratio of two-point correlation functions of these fields.

In the context of logarithmic CFT, we define the bipartite fidelities $\mathcal{F}_f^\Delta$ and $\tilde{\mathcal{F}}_f^\Delta$ similarly to their lattice analogs of (2.3) and (2.4). They are expressed in terms of partition functions defined on four domains $\mathcal{D}_{AB}$, $\mathcal{D}_{A\cup B}$, $\mathcal{D}_A$ and $\mathcal{D}_B$, each with specific fields inserted at two ends of the domains. The domains $\mathcal{D}_{A\cup B}$, $\mathcal{D}_A$ and $\mathcal{D}_B$ are infinite horizontal strips where the lower edge is the real axis and the upper edge corresponds to the line with imaginary parts N, Nx and $N(1-x)$ respectively. The domain $\mathcal{D}_{AB}$ is the flat pants domain. It has the same upper and lower edges as $\mathcal{D}_{A\cup B}$ but has an extra separation between the subsystems A and B in the form of a half-line from $\mathrm{i}N(1-x)$ to $-\infty + \mathrm{i}N(1-x)$. The domains $\mathcal{D}_{AB}$, $\mathcal{D}_{A\cup B}$, $\mathcal{D}_A$ are depicted in Figure 2.3, along with the upper-half plane that serves as the reference domain for the calculation.

The bipartite fidelities $\mathcal{F}_f^\Delta$ and $\tilde{\mathcal{F}}_f^\Delta$ are defined as

$$\mathcal{F}_f^\Delta = -\log\left|\frac{\left(Z^\Delta_{\mathcal{D}_{AB}}\right)^2}{Z^\Delta_{\mathcal{D}_{A\cup B}} Z^\Delta_{\mathcal{D}_A} Z^\Delta_{\mathcal{D}_B}}\right|, \quad \tilde{\mathcal{F}}_f^\Delta = -\log\left|\frac{\left(\tilde{Z}^\Delta_{\mathcal{D}_{AB}}\right)^2}{\tilde{Z}^\Delta_{\mathcal{D}_{A\cup B}} \tilde{Z}^\Delta_{\mathcal{D}_A} Z^\Delta_{\mathcal{D}_B}}\right|. \tag{2.91}$$

In these expressions, $Z^\Delta_{\mathcal{D}}$ corresponds to a two-point function of the primary field with its logarithmic partner on domain $\mathcal{D}$, $\langle\varphi(y_0)\omega(y_1)\rangle_{\mathcal{D}}$, whereas $\tilde{Z}^\Delta_{\mathcal{D}}$ is the correlation function of the logarithmic field with itself, $\langle\omega(y_0)\omega(y_1)\rangle_{\mathcal{D}}$. In each case, the points y_0 and y_1 are assigned to the top boundary of the strip, namely

$$\mathrm{Im}(y_0) = \mathrm{Im}(y_1) = \begin{cases} N & \text{on } \mathcal{D}_{AB} \text{ and } \mathcal{D}_{A\cup B}, \\ Nx & \text{on } \mathcal{D}_A, \\ N(1-x) & \text{on } \mathcal{D}_B. \end{cases} \tag{2.92}$$

The real parts of y_0 and y_1 are set to $-m$ and $+m$ and are sent to $-\infty$ and $+\infty$ in the limit. The corresponding expressions are expected to be well-behaved as $m \to \infty$ and to reproduce the results obtained from the lattice.

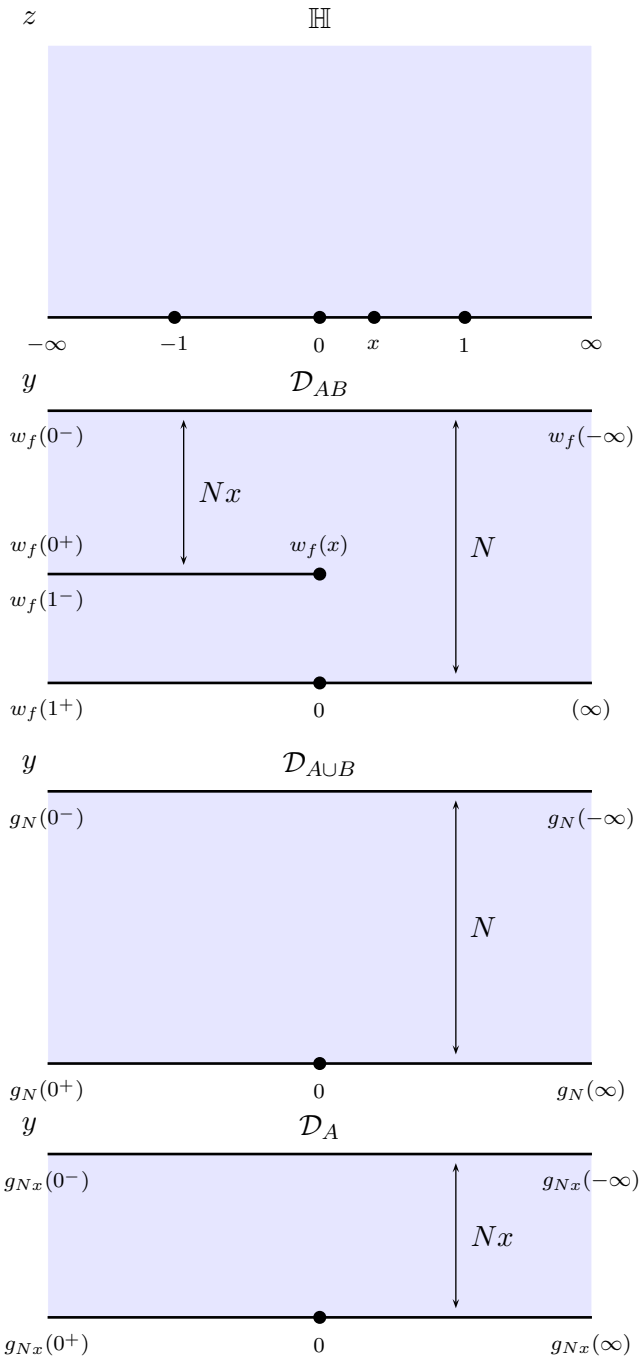

Figure 2.3: The upper-half plane $\mathbb{H}$ is mapped to the three domains $\mathcal{D}_{AB}$, $\mathcal{D}_{A\cup B}$ and $\mathcal{D}_A$ via the transformations $y = w_f(z)$, $y = g_N(z)$ and $y = g_{Nx}(z)$.

To reproduce the results of Section 2.3.2, we investigate the difference $\tilde{\mathcal{F}}_f^\Delta - \mathcal{F}_f^\Delta$. Its explicit expression in terms of two-point correlation functions is independent of the choice of reference partition function on the domain $\mathcal{D}_B$, and reads

$$\tilde{\mathcal{F}}_f^\Delta - \mathcal{F}_f^\Delta = -2\log|\Gamma_\Delta|, \tag{2.93a}$$

$$\Gamma_\Delta = \lim_{m\to\infty} \frac{\langle\omega(-m+\mathrm{i}N)\omega(m+\mathrm{i}N)\rangle_{\mathcal{D}_{AB}}}{\langle\omega(-m+\mathrm{i}N)\varphi(m+\mathrm{i}N)\rangle_{\mathcal{D}_{AB}}} \times \left(\frac{\langle\omega(-m+\mathrm{i}Nx)\varphi(m+\mathrm{i}Nx)\rangle_{\mathcal{D}_A}}{\langle\omega(-m+\mathrm{i}Nx)\omega(m+\mathrm{i}Nx)\rangle_{\mathcal{D}_A}} \frac{\langle\omega(-m+\mathrm{i}N)\varphi(m+\mathrm{i}N)\rangle_{\mathcal{D}_{A\cup B}}}{\langle\omega(-m+\mathrm{i}N)\omega(m+\mathrm{i}N)\rangle_{\mathcal{D}_{A\cup B}}}\right)^{1/2}. \tag{2.93b}$$

The map that sends $\mathbb{H}$ to a horizontal strip of height h is

$$g_h(z) = \frac{h}{\pi}\log z. \tag{2.94}$$

Likewise, the map that sends $\mathbb{H}$ to $\mathcal{D}_{AB}$ is [62]

$$w_f(z) = \frac{N}{\pi}\big(x\log z + (1-x)\log(z-1)\big) - \frac{N}{\pi}\big(x\log x + (1-x)\log(1-x)\big). \tag{2.95}$$

Together with the transformation laws (1.42) and the known correlation functions (1.43) on $\mathbb{H}$, these maps allow us to compute the two-point functions on $\mathcal{D}_{AB}$, $\mathcal{D}_{A\cup B}$ and $\mathcal{D}_A$.

Correlation functions on the horizontal strips. We start by computing the correlation functions on $\mathcal{D}_A$. With $y = g_{Nx}(z)$ and $y' = \frac{Nx}{\pi z}$, we find

$$\begin{aligned}\langle\omega(y_0)\varphi(y_1)\rangle_{\mathcal{D}_A} &= \big(g'_{Nx}(z_0)\big)^{-\Delta}\big(g'_{Nx}(z_1)\big)^{-\Delta}\langle\omega(z_0)\varphi(z_1)\rangle_{\mathbb{H}} \\ &= \left(\frac{z_0 z_1 \pi^2}{N^2x^2}\right)^{\Delta}\frac{\lambda_1}{(z_0-z_1)^{2\Delta}}\end{aligned} \tag{2.96}$$

and similarly

$$\langle\omega(y_0)\omega(y_1)\rangle_{\mathcal{D}_A} = \langle\omega(y_0)\varphi(y_1)\rangle_{\mathcal{D}_A} \times \Big(-4\lambda_0\log\big(\mathrm{e}^{\frac{\pi y_0}{Nx}} - \mathrm{e}^{\frac{\pi y_1}{Nx}}\big) + \lambda_2$$

$$- 4\lambda_0 \log\Big(\frac{Nx}{\pi}\Big) + 2\lambda_0 \frac{\pi}{Nx}(y_0 + y_1)\Big). \quad (2.97)$$

Hence, the ratio is

$$\frac{\langle\omega(-m+\mathrm{i}Nx)\omega(m+\mathrm{i}Nx)\rangle_{\mathcal{D}_A}}{\langle\omega(-m+\mathrm{i}Nx)\varphi(m+\mathrm{i}Nx)\rangle_{\mathcal{D}_A}} = - 4\lambda_0 \log\Big(2\sinh\Big(\frac{\pi m}{Nx}\Big)\Big) + \lambda_2 - 4\lambda_0 \log\Big(\frac{Nx}{\pi}\Big). \quad (2.98)$$

We obtain the analogous ratio of correlation functions on $\mathcal{D}_{A\cup B}$ by setting $x = 1$ in (2.98):

$$\frac{\langle\omega(-m+\mathrm{i}N)\omega(m+\mathrm{i}N)\rangle_{\mathcal{D}_{A\cup B}}}{\langle\omega(-m+\mathrm{i}N)\varphi(m+\mathrm{i}N)\rangle_{\mathcal{D}_{A\cup B}}} = - 4\lambda_0 \log\Big(2\sinh\Big(\frac{\pi m}{N}\Big)\Big) + \lambda_2 - 4\lambda_0 \log\Big(\frac{N}{\pi}\Big). \quad (2.99)$$

The leading-order terms in the limit $m \to \infty$ are linear:

$$\frac{\langle\omega(-m+\mathrm{i}Nx)\omega(m+\mathrm{i}Nx)\rangle_{\mathcal{D}_A}}{\langle\omega(-m+\mathrm{i}Nx)\varphi(m+\mathrm{i}Nx)\rangle_{\mathcal{D}_A}} = -4\lambda_0 \frac{\pi m}{Nx} + \mathcal{O}(1), \quad (2.100a)$$

$$\frac{\langle\omega(-m+\mathrm{i}Nx)\omega(m+\mathrm{i}Nx)\rangle_{\mathcal{D}_{A\cup B}}}{\langle\omega(-m+\mathrm{i}Nx)\varphi(m+\mathrm{i}Nx)\rangle_{\mathcal{D}_{A\cup B}}} = -4\lambda_0 \frac{\pi m}{N} + \mathcal{O}(1). \quad (2.100b)$$

Correlation functions on the pants domain. We perform the same calculations on the domain $\mathcal{D}_{AB}$. With $y = w_f(z)$ and $y' = \frac{N}{\pi}\big(\frac{z-x}{z(z-1)}\big)$, we find

$$\langle\omega(y_0)\varphi(y_1)\rangle_{\mathcal{D}_{AB}} = w_f'(z_0)^{-\Delta} w_f'(z_1)^{-\Delta} \langle\omega(z_0)\varphi(z_1)\rangle_{\mathbb{H}} = \left(\frac{\pi^2}{N^2}\frac{z_0(z_0-1)}{z_0-x}\frac{z_1(z_1-1)}{z_1-x}\right)^{\Delta} \frac{\lambda_1}{(z_0-z_1)^{2\Delta}}. \quad (2.101)$$

A calculation similar to the one for the strip domains gives

$$\frac{\langle\omega(y_0)\omega(y_1)\rangle_{\mathcal{D}_{AB}}}{\langle\omega(y_0)\varphi(y_1)\rangle_{\mathcal{D}_{AB}}} = -4\lambda_0 \log(z_0 - z_1) + \lambda_2 - 4\lambda_0 \log\Big(\frac{N}{\pi}\Big) - 2\lambda_0 \log\Big(\frac{z_0-x}{z_0(z_0-1)}\frac{z_1-x}{z_1(z_1-1)}\Big). \quad (2.102)$$

The next step is to express the right side in terms of $y_0 = -m + \mathrm{i}N$ and $y_1 = m + \mathrm{i}N$. Obtaining a closed-form expression for $z(y)$ is not possible,

and we instead resort to series expansions for large m. In this regime, the points z_0 and z_1 approach the values 0^- and $-\infty$ respectively. We find

$$z_0 = -\mathrm{e}^{-\frac{\pi(m+2K_x)}{Nx}} + \Big(\frac{1-x}{x}\Big)\mathrm{e}^{-\frac{2\pi(m+2K_x)}{Nx}} + \mathcal{O}\Big(\mathrm{e}^{-\frac{3\pi(m+2K_x)}{Nx}}\Big), \quad (2.103a)$$

$$z_1 = -\mathrm{e}^{\frac{\pi(m-2K_x)}{N}} + (x-1) + \mathcal{O}\Big(\mathrm{e}^{-\frac{\pi(m-2K_x)}{N}}\Big), \quad (2.103b)$$

where

$$K_x = -\frac{N}{2\pi}\big(x\log x + (1-x)\log(1-x)\big) \quad (2.104)$$

is half of the additive constant appearing in (2.95). It turns out that computing $\tilde{\mathcal{F}}_2 - \mathcal{F}_2$ only requires the leading-order terms in (2.103). Inserting the series expansions for z_0 and z_1 in (2.102), we again find a leading term that is linear in m,

$$\frac{\langle\omega(-m+\mathrm{i}N)\omega(m+\mathrm{i}N)\rangle_{\mathcal{D}_{AB}}}{\langle\omega(-m+\mathrm{i}N)\varphi(m+\mathrm{i}N)\rangle_{\mathcal{D}_{AB}}} = -2\lambda_0\frac{\pi m}{N}\Big(\frac{1+x}{x}\Big) + \mathcal{O}(1). \quad (2.105)$$

Final result. We combine (2.93), (2.100) and (2.105) and find

$$\tilde{\mathcal{F}}_f^{\Delta} - \mathcal{F}_f^{\Delta} = -2\log\left(\frac{1+x}{2\sqrt{x}}\right). \quad (2.106)$$

This expression is identical to the lattice result (2.88). Remarkably, the final expression for this difference is independent of the value of the central charge c and of the conformal weight Δ of the two fields. It also does not depend on the constants λ_0, λ_1 and λ_2 that appear in the two-point functions.

2.4 Asymptotic calculations

In this section, we give the computational details needed to obtain the asymptotic expansion (2.72) of the logarithmic bipartite fidelity from the closed formulas (2.59), (2.68) and (2.71). The main ingredients we use are

(i) the Euler-Maclaurin formula

$$\sum_{i=a}^{b} f(i) = \int_a^b f(x)\mathrm{d}x + \frac{f(a)+f(b)}{2} + \sum_{k=1}^{\infty} \frac{B_{2k}}{(2k)!}(f^{(2k-1)}(b) - f^{(2k-1)}(a)), \quad (2.107)$$

where the B_k are the Bernoulli numbers and $f(x)$ is a smooth function,

(ii) the integral formula for the $\log\Gamma(z)$ function for $\mathrm{Re}(z) > 0$,

$$\log\Gamma(z) = \int_0^\infty \frac{\mathrm{d}t}{t}\Big\{(z-1)\mathrm{e}^{-t} - \frac{\mathrm{e}^{-t}-\mathrm{e}^{-zt}}{1-\mathrm{e}^{-t}}\Big\}, \quad (2.108)$$

(iii) the exact product formula

$$\prod_{\ell=1}^{\frac{n-2}{2}} \sin\left(\tfrac{\pi\ell}{n}\right) = \prod_{\ell=1}^{\frac{n-2}{2}} \cos\left(\tfrac{\pi\ell}{n}\right) = \frac{n^{\frac{1}{2}}}{2^{\frac{n-1}{2}}} \qquad (\text{even } n). \quad (2.109)$$

The lattice dimensions N_A and N are assumed to satisfy $\gcd(N_A, N) = 1$ for odd N and $\gcd(\frac{N_A}{2}, \frac{N}{2}) = 1$ for even N.

2.4.1 Closed forms

With (2.68) and (2.71), we write (2.59) as

$$\begin{aligned}\mathcal{F}_f^{(d)} = -2\Big(&\log\big|P_0(N,x,d)\big| - \log\big|P_1(N,x,d)\big| - \log\big|P_2(N,1-x,d)\big| \\ &+ \log\big|P_2\big(Nx, \tfrac{1-x}{x}, d\big)\big| + \log\big|P_3(N,x,d)\big| \\ &+ \log\big|P_3(N,1-x,0)\big| + \log\big|P_3(N,1,d)\big|\Big)\end{aligned} \quad (2.110)$$

where

$$P_0(N,x,d) = \prod_{k=1}^{\frac{Nx-d}{2}} \frac{\sin\left(\frac{\pi k}{Nx}\right)}{\sqrt{Nx\cos\left(\frac{\pi k}{Nx}\right)}} \prod_{\ell=1}^{\frac{N-d}{2}} \frac{\cos(\frac{\pi\ell}{N})\sin(\pi\ell x)}{\sqrt{N\cos\left(\frac{\pi\ell}{N}\right)}} \times \prod_{k=1}^{\frac{N(1-x)-2}{2}} \frac{\sin\left(\frac{\pi k}{N(1-x)}\right)}{\sqrt{N(1-x)\cos\left(\frac{\pi k}{N(1-x)}\right)}}, \quad (2.111a)$$

$$P_1(N,x,d) = \prod_{k=1}^{\frac{Nx-d}{2}} \prod_{\ell=1}^{\frac{N-d}{2}} \Big(\cos\left(\tfrac{\pi k}{Nx}\right) - \cos\left(\tfrac{\pi \ell}{N}\right) \Big), \tag{2.111b}$$

$$P_2(N,x,d) = \prod_{k=1}^{\frac{Nx}{2}} \prod_{\ell=1}^{\frac{N-d}{2}} \Big(\cos\left(\tfrac{\pi k}{Nx}\right) - \cos\left(\tfrac{\pi \ell}{N}\right) \Big), \tag{2.111c}$$

$$P_3(N,x,d) = \prod_{1 \leqslant k < k' \leqslant \frac{Nx-d}{2}} \Big(\cos\left(\tfrac{\pi k'}{Nx}\right) - \cos\left(\tfrac{\pi k}{Nx}\right) \Big). \tag{2.111d}$$

We recall that $N_B = N(1-x)$ is even and N, Nx and d have the same parity, so that $N-d$ and $Nx-d$ are even numbers too.

In the following, we derive the large-N expansion of the logarithm of each product in (2.111a). For $P_0(N,x,d)$, we use (2.109) with $n = N_B$. We express the other products in terms of the cardinal sine function $s[x] = \sin(x)/x$ by transforming the differences of cosines into products of sines. We find

$$\begin{aligned} P_0(N,x,d) &= N^{-\frac{2N-2d-3}{4}} x^{-\frac{Nx-d}{4}} (1-x)^{-\frac{N(1-x)-3}{4}} 2^{-\frac{N(1-x)-1}{4}} \\ &\quad \times \prod_{k=1}^{\frac{Nx-d}{2}} \frac{\sin\left(\frac{\pi k}{Nx}\right)}{\sqrt{\cos\left(\frac{\pi k}{Nx}\right)}} \prod_{\ell=1}^{\frac{N-d}{2}} \sqrt{\cos\left(\tfrac{\pi \ell}{N}\right)} \sin(\pi \ell x), \end{aligned} \tag{2.112a}$$

$$\begin{aligned} \log|P_1(N,x,d)| &= \Big(\frac{Nx-d}{2}\Big)\Big(\frac{N-d}{2}\Big)(-2\log N + 2\log\pi - \log 2) \\ &+ g(N,x,d,d) + h(N,x,d,d) + Y_+\Big(N,x,d\Big) + Y_-\Big(N,x,d\Big) \\ &- 2X\Big(\frac{1}{4},N,x,d\Big) - 2X\Big(\frac{1}{4},N,1,d\Big), \end{aligned} \tag{2.112b}$$

$$\begin{aligned} \log|P_2(N,x,d)| &= \frac{Nx}{2}\Big(\frac{N-d}{2}\Big)(-2\log N + 2\log\pi - \log 2) \\ &+ g(N,x,d,2) + h(N,x,d,2) + \log\Gamma\Big(N - \frac{d}{2} + 1\Big) - \log N \\ &+ \log 2 - \log\Gamma\Big(\frac{d}{2}\Big) + \tilde{Y}_+\Big(N,x,d\Big) + \tilde{Y}_-\Big(N,x,d\Big) \\ &- 2X\Big(\frac{1}{4},N,x,0\Big) - 2X\Big(\frac{1}{4},N,1,d\Big), \end{aligned} \tag{2.112c}$$

$$\log|P_3(N,x,d)| = \frac{(Nx-d)(Nx-d-2)}{4}\Big(- \log Nx - \log\pi - \frac{1}{2}\log 2\Big)$$

$$+ i\Big(\frac{Nx-d}{2}+1\Big) + \frac{1}{2}Y_+\Big(Nx,1,d\Big) + \frac{1}{2}Y_-\Big(Nx,1,d\Big) \qquad (2.112d)$$
$$- 2X\Big(\frac{1}{4},N,x,d\Big) - \frac{1}{2}X\Big(\frac{1}{2},N,x,d\Big),$$

where

$$X(a,N,x,m) = \sum_{k=0}^{\frac{Nx-m}{2}} \log s\left[\frac{2\pi a}{N}\Big(\frac{k}{x}\Big)\right], \qquad (2.113a)$$

$$Y_\pm(N,x,m) = \sum_{k=0}^{\frac{Nx-m}{2}}\sum_{\ell=0}^{\frac{N-m}{2}} \log s\left[\frac{\pi}{2N}\Big(\frac{k}{x}\pm\ell\Big)\right], \qquad (2.113b)$$

$$\tilde{Y}_\pm(N,x,m) = \sum_{k=0}^{\frac{Nx}{2}}\sum_{\ell=0}^{\frac{N-m}{2}} \log s\left[\frac{\pi}{2N}\Big(\frac{k}{x}\pm\ell\Big)\right], \qquad (2.113c)$$

$$g(N,x,d,m) = \sum_{k=1}^{\frac{Nx-m}{2}}\sum_{\ell=1}^{\frac{N-d}{2}} \log\Big(\frac{k}{x}+\ell\Big), \qquad (2.113d)$$

$$h(N,x,d,m) = \sum_{k=1}^{\frac{Nx-m}{2}}\sum_{\ell=1}^{\frac{N-d}{2}} \log\Big|\frac{k}{x}-\ell\Big|, \qquad (2.113e)$$

$$i(N) = \sum_{k=1}^{N-2}\sum_{\ell=k+1}^{N-1} \log(\ell+k)+\log(\ell-k). \qquad (2.113f)$$

2.4.2 Asymptotic behaviour of $P_0(N,x,d)$

In order to access the asymptotic expansion of $P_0(N,x,d)$, we need to simplify the trigonometric products in (2.112a). For that matter, we introduce the following identities:

$$\prod_{\ell=1}^{\frac{n-2}{2}} \big|\sin(\tfrac{\pi\ell m}{n})\big| = \frac{n}{2^{\frac{n}{2}}} \qquad (m,\text{even } n,\ \gcd(\tfrac{m}{2},\tfrac{n}{2})=1), \qquad (2.114a)$$

$$\prod_{\ell=1}^{\frac{n-1}{2}} \big|\sin(\tfrac{\pi\ell m}{n})\big| = \frac{n^{\frac{1}{2}}}{2^{\frac{n-1}{2}}} \qquad (\text{odd } n,\ \gcd(m,n)=1), \qquad (2.114b)$$

$$\prod_{\ell=1}^{\frac{n-1}{2}} \cos(\tfrac{\pi\ell}{n}) = \frac{1}{2^{\frac{n-1}{2}}} \qquad (\text{odd } n). \qquad (2.114c)$$

We use (2.109) together with (2.114c) to find the intermediate results

$$\log \prod_{\ell=1}^{\frac{N-d}{2}} \cos\left(\tfrac{\pi\ell}{N}\right) = \frac{d-1}{2}\log N - \frac{N-1}{2}\log 2 - \frac{d-2}{2}\log\pi - \log\Gamma\Big(\frac{d}{2}\Big) + \mathcal{O}\big(N^{-2}\big), \tag{2.115}$$

$$\log \prod_{\ell=1}^{\frac{N-d}{2}} \sin\left(\tfrac{\pi\ell}{N}\right) = \frac{1}{2}\log N - \frac{N-1}{2}\log 2 + \mathcal{O}\big(N^{-2}\big), \tag{2.116}$$

for both parities of N. We use (2.114a) and (2.114b) to derive an exact expression for the term $\prod_{\ell=1}^{(N-d)/2}\sin(\pi\ell x)$ in (2.112a). We find

$$\log \prod_{\ell=1}^{\frac{n-d}{2}} \Big|\sin\left(\tfrac{\pi\ell m}{n}\right)\Big| = \begin{cases} \log n - \frac{n}{2}\log 2 - \sum_{\ell=1}^{\frac{d}{2}-1} \log\big|\sin(\frac{\pi\ell m}{n})\big| & \left(\begin{smallmatrix} m, \text{even } n \\ \gcd(\frac{m}{2},\frac{n}{2}) = 1 \end{smallmatrix}\right), \\ \frac{1}{2}\log n - \frac{n-1}{2}\log 2 - \sum_{\ell=1}^{\frac{d-1}{2}} \log\Big|\cos\Big(\frac{\pi m}{n}(\ell - \frac{d}{2})\Big)\Big| & \left(\begin{smallmatrix} m, n \text{ odd} \\ \gcd(m,n) = 1 \end{smallmatrix}\right), \\ \frac{1}{2}\log n - \frac{n-1}{2}\log 2 - \sum_{\ell=1}^{\frac{d-1}{2}} \log\Big|\sin\Big(\frac{\pi m}{n}(\ell - \frac{d}{2})\Big)\Big| & \left(\begin{smallmatrix} \text{even } m, \text{ odd } n \\ \gcd(m,n) = 1 \end{smallmatrix}\right). \end{cases} \tag{2.117}$$

The identities (2.115) and (2.117) applied in (2.112a) yield

$$\log P_0(N,x,d) = \frac{N}{4}(-2\log N - (1-x)\log(1-x) - x\log x - 4\log 2) + \frac{1}{4}\big((2d+9)\log N + 3\log(1-x) + 3\log x + 5\log 2\big) - \begin{cases} \frac{1}{2}\log 2 + \sum_{j=1}^{\frac{d}{2}-1}\log|\sin(\pi j x)| + \mathcal{O}\big(N^{-2}\big) & (N,d \text{ even}), \\ \frac{1}{2}\log N + \sum_{j=1}^{\frac{d-1}{2}}\log\Big|\cos\Big(\pi x(j-\frac{d}{2})\Big)\Big| + \mathcal{O}\big(N^{-2}\big) & (N,d \text{ odd}). \end{cases} \tag{2.118}$$

2.4.3 Asymptotic behaviour of $P_j(N, x, d)$

In order to compute the asymptotic behaviour of $P_1(N, x, d)$, $P_2(N, x, d)$ and $P_3(N, x, d)$ in (2.112), we need to investigate the asymptotics of the functions X, $Y_\pm$,$\tilde{Y}_\pm$, g, h and i in (2.113).

The functions X, $Y_\pm$ and $\tilde{Y}_\pm$. We define the integrals

$$\mathcal{I}_0(a) = \int_0^1 \log s\,[\pi a z]\,\mathrm{d}z, \tag{2.119a}$$

$$\mathcal{I}_\pm(x) = \int_0^x \log s\left[\frac{\pi(z \pm x)}{4x}\right]\mathrm{d}z, \tag{2.119b}$$

$$\mathcal{J}_\pm(x) = \int_0^x \int_0^x \log s\left[\frac{\pi(y \pm z)}{4x}\right]\mathrm{d}y\;\mathrm{d}z, \tag{2.119c}$$

where we recall $s[x] = \sin(x)/x$. We make repeated use of Euler-Maclaurin formula (2.107) and obtain the expansions

$$X(a, N, x, m) = \frac{Nx}{2}\mathcal{I}_0(a) + \frac{1-m}{2}\log s[\pi a] + \mathcal{O}\big(N^{-1}\big), \tag{2.120a}$$

$$\begin{aligned} Y_+(N, x, m) &= \frac{N^2}{4x}\mathcal{J}_+(x) + \frac{Nx}{2}\Big(\frac{1}{2x} + \frac{1}{2}\Big)\mathcal{I}_0\Big(\frac{1}{4}\Big) \\ &+ \frac{N}{2}\Big(\frac{1}{2x} + \frac{1}{2} - \frac{m}{2}\Big(1 + \frac{1}{x}\Big)\Big)\mathcal{I}_+(x) \\ &- \frac{4 - 6m(x-1)^2 + 4x(-3+x) + 3m^2(1+x^2)}{24x}\log s\Big[\frac{\pi}{4}\Big] \\ &+ \frac{2 - 6m(1+x)^2 + 3m^2(1+x)^2 + 2x(3+x)}{24x}\log s\Big[\frac{\pi}{2}\Big] \\ &+ \mathcal{O}\big(N^{-1}\big), \end{aligned} \tag{2.120b}$$

$$\begin{aligned} Y_-(N, x, m) &= \frac{N^2}{4x}\mathcal{J}_-(x) + \frac{Nx}{2}\Big(\frac{1}{2x} + \frac{1}{2}\Big)\mathcal{I}_0\Big(\frac{1}{4}\Big) \\ &+ \frac{N}{2}\Big(\frac{1}{2x} + \frac{1}{2} - \frac{m}{2}\Big(1 + \frac{1}{x}\Big)\Big)\mathcal{I}_-(x) \\ &+ \frac{4 - 6m(x+1)^2 + 4x(3+x) + 3m^2(1+x^2)}{24x}\log s\Big[\frac{\pi}{4}\Big] \\ &+ \mathcal{O}\big(N^{-1}\big), \end{aligned} \tag{2.120c}$$

$$\tilde{Y}_+(N, x, m) = \frac{N^2}{4x}\mathcal{J}_+(x) + \frac{Nx}{2}\Big(\frac{1}{2x} + \frac{1}{2}\Big)\mathcal{I}_0\Big(\frac{1}{4}\Big)$$

$$
\begin{aligned}
&+\frac{N}{2}\Big(\frac{1}{2x}+\frac{1}{2}-\frac{m}{2}\Big)\mathcal{I}_+(x)\\
&-\frac{4+4x(-3+x)+3mx(2+(-2+m)x)}{24x}\log s\Big[\frac{\pi}{4}\Big]\\
&+\frac{2+2x(3+x)+3mx(-2+(-2+m)x)}{24x}\log s\Big[\frac{\pi}{2}\Big]\\
&+\mathcal{O}\big(N^{-1}\big),
\end{aligned}
\tag{2.120d}
$$

$$
\begin{aligned}
\tilde{Y}_-(N,x,m)&=\frac{N^2}{4x}\mathcal{J}_-(x)+\frac{Nx}{2}\Big(\frac{1}{2x}+\frac{1}{2}\Big)\mathcal{I}_0\Big(\frac{1}{4}\Big)\\
&+\frac{N}{2}\Big(\frac{1}{2x}+\frac{1}{2}-\frac{m}{2}\Big)\mathcal{I}_-(x)\\
&+\frac{4+4x(3+x)+3mx(-2+(-2+m)x)}{24x}\log s\Big[\frac{\pi}{4}\Big]\\
&+\mathcal{O}\big(N^{-1}\big).
\end{aligned}
\tag{2.120e}
$$

Remarkably, all the terms in (2.120) that contain the integrals defined in (2.119) identically cancel in the combination (2.110).

The function $i(N)$. We express $i(N)$ in (2.113) in terms of the Gamma function and Barnes' G-function:

$$
\Gamma(z+1)=z\,\Gamma(z),\qquad G(z+1)=\Gamma(z)G(z).
\tag{2.121}
$$

Indeed, using the duplication formula for the Gamma function,

$$
\Gamma(2k)=\frac{2^{2k-1}}{\sqrt{\pi}}\Gamma(k)\Gamma\Big(k+\frac{1}{2}\Big),
\tag{2.122}
$$

we obtain

$$
\begin{aligned}
i(N)=&-(N-2)(N-1)\log 2+\frac{N-2}{2}\log\pi+\log G(2N-1)\\
&-\log G(N+1)-\log G\Big(N-\frac{1}{2}\Big)+\log G\Big(\frac{3}{2}\Big).
\end{aligned}
\tag{2.123}
$$

The asymptotic behaviour of the Barnes' G-function in the limit $z\to\infty$ is known,

$$
\begin{aligned}
&\log G(z)=\\
&\qquad\Big(\frac{(z-1)^2}{2}-\frac{1}{12}\Big)\log(z-1)-\frac{3(z-1)^2}{4}+\frac{z-1}{2}\log(2\pi)
\end{aligned}
$$

$$+\frac{1}{12}-\log A+\mathcal{O}\big(z^{-1}\big), \quad (2.124)$$

where we recall that $A = 1.282427...$ is the Glaisher-Kinkelin constant. We insert this expansion in (2.123) and find

$$i(N) = N^2\Big(\log N-\frac{3}{2}+\log 2\Big)+\frac{N}{2}\Big(-5\log N+5+\log\Big(\frac{\pi}{4}\Big)\Big)$$
$$-\log\pi+\frac{1}{24}(-12\log A+23\log N+1-7\log 2)+\mathcal{O}\big(N^{-1}\big). \quad (2.125)$$

The functions $g(N,x,d,m)$ and $h(N,x,d,m)$. The first step is to rewrite the functions $g(N,x,d,m)$ and $h(N,x,d,m)$ as integrals with the integral representation of $\log\Gamma(z)$ given in (2.108). In doing so, we obtain sums of integrals which are separately divergent. We regularise the integrals by restricting the domain of integration to $[\epsilon,+\infty)$ and compute the first terms in an expansion in ϵ at order $\mathcal{O}(\epsilon)$. All terms that are divergent as $\epsilon\to 0$ eventually cancel out in the sum. We denote the regularised functions by $g_\epsilon(N,x,d,m)$ and $h_\epsilon(N,x,d,m)$.

With the identity $z=\Gamma(z+1)/\Gamma(z)$, the summation over ℓ in $g(N,x,d,m)$ is telescopic and yields

$$g(N,x,d,m)=\sum_{k=1}^{\frac{Nx-m}{2}}\Big[\log\Gamma\big(\tfrac{k}{x}+1+\tfrac{N-d}{2}\big)-\log\Gamma\big(\tfrac{k}{x}+1\big)\Big]. \quad (2.126)$$

With (2.108), the summation over k leads to

$$g_\epsilon(N,x,d,m)=\frac{(Nx-m)(N-d)}{4}\int_\epsilon^\infty\frac{\mathrm{d}t}{t}\mathrm{e}^{-t}$$
$$-\int_\epsilon^\infty\frac{\mathrm{d}t}{t}\frac{1-\mathrm{e}^{-(N-d)t/2}}{\mathrm{e}^t-1}\cdot\frac{1-\mathrm{e}^{-(Nx-m)t/2x}}{\mathrm{e}^{t/x}-1}. \quad (2.127)$$

For the function $h(N,x,d,m)$, we treat the cases where $m=d$ and $m=2$ separately. For $m=d$, the summation over ℓ in the function $h(N,x,d,m)$ yields

$$h(N,x,d,d)=\sum_{k=1}^{\frac{Nx-d}{2}}\Big[\log\Gamma\big(\tfrac{k}{x}\big)-\log\big|\Gamma\big(\tfrac{d}{2}+\tfrac{2-d}{2x}-\tfrac{k}{x}\big)\big|\Big], \quad (2.128)$$

where we used the change of variable $k \to \frac{Nx-d}{2} + 1 - k$. With the identity $\Gamma(z)\Gamma(1-z) = \frac{\pi}{\sin \pi z}$ and the integral representation of $\log \Gamma(z)$, we obtain

$$h(N,x,d,d) = \sum_{k=1}^{\frac{Nx-d}{2}} \log \Big| \frac{\sin\big(\pi(\frac{k}{x} + \frac{(2-d)(x-1)}{2x})\big)}{\pi} \Big| + \sum_{k=1}^{\frac{Nx-d}{2}} \big[\log \Gamma(\tfrac{k}{x}) + \log \Gamma(\tfrac{k}{x} + \tfrac{(2-d)(x-1)}{2x}) \big], \quad (2.129)$$

and subsequently

$$\begin{aligned} h_\epsilon(N,x,d,d) = {} & \sum_{k=1}^{\frac{Nx-d}{2}} \log \Big| \frac{\sin\big(\pi(\frac{k}{x} + \frac{(2-d)(x-1)}{2x})\big)}{\pi} \Big| \\ & + \tfrac{(Nx-d)(N-d-2)}{4} \int_\epsilon^\infty \frac{\mathrm{d}t}{t}\, \mathrm{e}^{-t} - (Nx-d) \int_\epsilon^\infty \frac{\mathrm{d}t}{t} \frac{1}{\mathrm{e}^t - 1} \\ & + \int_\epsilon^\infty \frac{\mathrm{d}t}{t}\, \frac{1 + \mathrm{e}^{-(d-2)(1-x)t/2x}}{1 - \mathrm{e}^{-t}} \cdot \frac{1 - \mathrm{e}^{-(Nx-d)t/2x}}{\mathrm{e}^{t/x} - 1}. \end{aligned} \quad (2.130)$$

For $m = 2$, the same procedure would involve the integral representation of $\log \Gamma(z)$ for $\mathrm{Re}(z) < 0$. Instead we carry out the summation over k first. The other steps are similar and yield

$$h(N,x,d,2) = -\tfrac{(Nx-2)(N-d)}{4} \log x + \sum_{\ell=1}^{\frac{N-d}{2}} \log \Big| \frac{\sin(\pi \ell x)}{\pi} \Big| + \sum_{\ell=1}^{\frac{N-d}{2}} \big[\log \Gamma(\ell x) + \log \Gamma\big((\ell + \tfrac{d}{2} - 1)x\big) \big] \quad (2.131)$$

and

$$\begin{aligned} h_\epsilon(N,x,d,2) = {} & \sum_{\ell=1}^{\frac{N-d}{2}} \log \Big| \frac{\sin(\pi \ell x)}{\pi} \Big| - \tfrac{(Nx-2)(N-d)}{4} \log x \\ & + \tfrac{(Nx-4)(N-d)}{4} \int_\epsilon^\infty \frac{\mathrm{d}t}{t}\, \mathrm{e}^{-t} - (N-d) \int_\epsilon^\infty \frac{\mathrm{d}t}{t} \frac{1}{\mathrm{e}^t - 1} \\ & + \int_\epsilon^\infty \frac{\mathrm{d}t}{t}\, \frac{1 + \mathrm{e}^{-(d-2)xt/2}}{1 - \mathrm{e}^{-t}} \cdot \frac{1 - \mathrm{e}^{-(N-d)xt/2}}{\mathrm{e}^{xt} - 1}. \end{aligned} \quad (2.132)$$

In the above expressions for g_ϵ and h_ϵ, one can distinguish two types of integrals: those for which the integrand decays exponentially fast with N (because they contain a factor e^{-aNt}), and those which do not depend on N. We start with the first category, bearing in mind that we are interested in the asymptotic value of the integrals to order $N^{-1}\log N$. All terms of order N^{-1} or smaller will be neglected.

The integrals we have to evaluate are of the form $\int_\epsilon^\infty \mathrm{e}^{-aNt}F(t)$ where the function $F(t)$ decays exponentially fast at infinity but generically has a pole at the origin of finite order (smaller or equal to 3 in all cases). Expanding $F(t)$ in a Laurent series around the singularity $t=0$, the positive power part of the expansion can be neglected since a power of t^k, upon integration, contributes a finite term proportional to N^{-k-1}. In particular, no term proportional to $N^{-1}\log N$ can be produced. For the negative powers of t, we use the following results [151], valid for any positive n:

$$\int_\epsilon^\infty \frac{\mathrm{d}t}{t}\mathrm{e}^{-nt} = -\log\epsilon - \log n - \gamma + \mathcal{O}(\epsilon), \tag{2.133a}$$

$$\int_\epsilon^\infty \frac{\mathrm{d}t}{t^2}\mathrm{e}^{-nt} = \frac{1}{\epsilon} + n\log\epsilon + n\log n + n(\gamma-1) + \mathcal{O}(\epsilon), \tag{2.133b}$$

$$\int_\epsilon^\infty \frac{\mathrm{d}t}{t^3}\mathrm{e}^{-nt} = \frac{1}{2\epsilon^2} - \frac{n}{\epsilon} - \frac{n^2}{2}\log\epsilon - \frac{n^2}{2}\Big(\log n - \frac{3}{2} + \gamma\Big) + \mathcal{O}(\epsilon) \tag{2.133c}$$

where $\gamma = 0.57722...$ is the Euler constant. For some of the integrals which do not depend on N, we also use the following integral [151] valid for $\alpha > 0$:

$$\int_\epsilon^\infty \frac{\mathrm{d}t}{t}\frac{1}{\mathrm{e}^{\alpha t}-1} = \frac{1}{\alpha\epsilon} + \frac{1}{2}\log\epsilon + \frac{1}{2}\log\alpha + \frac{\gamma}{2} - \frac{1}{2}\log(2\pi) + \mathcal{O}(\epsilon). \tag{2.134}$$

An inspection of (2.112b) and (2.112c) shows that the two functions $g(N,x,d,m)$ and $h(N,x,d,m)$ only appear through their sum, which we denote by $gh(N,x,d,m)$. When computing $gh(N,x,d,m)$, we are free to regularise the functions g_ϵ and $h_{\epsilon'}$ with two parameters ϵ and ϵ' that can differ. The convenient choice turns out to be $\epsilon = \epsilon'$ for $m = d$ and

$\epsilon = x\epsilon'$ for $m = 2$. For instance, we combine an integral from (2.127) with a second integral from (2.132) and find

$$-\int_{\epsilon}^{\infty} \frac{\mathrm{d}t}{t} \frac{1}{\mathrm{e}^{t}-1} \cdot \frac{1}{\mathrm{e}^{t/x}-1} + \int_{\epsilon'}^{\infty} \frac{\mathrm{d}t}{t} \frac{1}{1-\mathrm{e}^{-t}} \cdot \frac{1}{\mathrm{e}^{xt}-1} = \int_{\epsilon}^{\infty} \frac{\mathrm{d}t}{t} \frac{1}{\mathrm{e}^{t}-1} \tag{2.135}$$

and the resulting integral is of the form (2.134) with $\alpha = 1$. We then encounter only two integrals that are not expressible as the integrals in (2.133) and (2.134). Both are independent of N. They read, respectively for $m = d$ and $m = 2$,

$$\int_{\epsilon}^{\infty} \frac{\mathrm{d}t}{t} \frac{\mathrm{e}^{-(\frac{d}{2}-1)(1-x)t/x}}{(1-\mathrm{e}^{-t})(\mathrm{e}^{t/x}-1)} \quad \text{and} \quad \int_{\epsilon}^{\infty} \frac{\mathrm{d}t}{t} \frac{\mathrm{e}^{-(\frac{d}{2}-1)xt}}{(1-\mathrm{e}^{-t})(\mathrm{e}^{xt}-1)}. \tag{2.136}$$

By subtracting counterterms, their ϵ-expansion can be expressed in terms of the following two convergent integrals $I_1(x)$ and $I_2(x)$,

$$I_1(x) = \int_0^{\infty} \frac{\mathrm{d}t}{t} \Big\{ \frac{\mathrm{e}^{-(\frac{d}{2}-1)(1-x)t/x}}{(1-\mathrm{e}^{-t})(\mathrm{e}^{t/x}-1)} - A(t;x)\, \mathrm{e}^{-t(1+x)/(2x)} \Big\} \tag{2.137a}$$

with

$$A(t;x) = \Big[\frac{x}{t^2} + \frac{1-\frac{d}{2}(1-x)}{t} + \frac{11-12d+3d^2+6xd(2-d)+x^2(3d^2-1)}{24x} \Big], \tag{2.137b}$$

and

$$I_2(x) = \int_0^{\infty} \frac{\mathrm{d}t}{t} \Big\{ \frac{\mathrm{e}^{-(\frac{d}{2}-1)xt}}{(1-\mathrm{e}^{-t})(\mathrm{e}^{xt}-1)} - B(t;x)\, \mathrm{e}^{-t(1+x)/2} \Big\}, \tag{2.137c}$$

with

$$B(t;x) = \Big[\frac{1}{xt^2} + \frac{1-\frac{d}{2}+\frac{1}{x}}{t} + \frac{11+12x(2-d)+x^2(11-12d+3d^2)}{24x} \Big], \tag{2.137d}$$

to which must be added the divergent integrals of the counterterms, well under control by using (2.133).

Putting all together, we obtain the following expression of $gh(N,x,d,m)$ for $m=d$,

$$\begin{aligned}
gh(N,x,d,d) &= \frac{N^2 x}{2}\big(\log N - \tfrac{3}{2}\big)\\
&+\frac{N}{2}\big[d(x+1)+\log 2 + x\log(4\pi) - d(x+1)\log N\big]\\
&+\frac{(1-3d+\frac{3}{2}d^2)(1+x^2)-3x(3-2d-d^2)}{12x}\Big(\log N - \log\Big(\frac{1+x}{2x}\Big)\Big)\\
&+\frac{d^2-1}{2}\,\log\Big(\frac{1+x}{2x}\Big) + (1-d)\log 2 - \frac{d+1}{2}\log(2\pi)\\
&-\frac{1}{2}\log x - \frac{(x+1)(5-3x+4d(x-1))}{16x} + I_1(x)\\
&+\sum_{k=1}^{\frac{Nx-d}{2}} \log\Big|\frac{\sin\big(\pi(\frac{k}{x}+\frac{(2-d)(x-1)}{2x})\big)}{\pi}\Big| + \mathcal{O}\big(N^{-1}\big),
\end{aligned} \tag{2.138a}$$

and for $m=2$,

$$\begin{aligned}
gh(N,x,d,2) &= \frac{N^2 x}{2}\big(\log N - \tfrac{3}{2}\big)\\
&+\frac{N}{2}\big[(dx+2)+(x+1)\log 2 + \log(2\pi) - (dx+2)\log N\big]\\
&+\frac{1-3x(1-3d)+x^2(1-3d+\frac{3}{2}d^2)}{12x}\Big(\log N - \log\Big(\frac{1+x}{2x}\Big)\Big)\\
&+(d-\tfrac{1}{2})\,\log\Big(\frac{1+x}{2x}\Big) - \frac{d}{2}\log 2 - \frac{d+1}{2}\log(2\pi)\\
&+\frac{(x+1)(4dx-5(x+1))}{16x} + I_2(x)\\
&+\sum_{\ell=1}^{\frac{N-d}{2}} \log\Big|\frac{\sin(\pi\ell x)}{\pi}\Big| + \mathcal{O}\big(N^{-1}\big).
\end{aligned} \tag{2.138b}$$

In the final expression (2.110), we only need the following combination of $gh(N,x,d,m)$:

$$C_{gh}(N,x,d) \equiv$$
$$2\Big(gh(N,x,d,d) + gh(N,1-x,d,2) - gh(Nx,\tfrac{1-x}{x},d,2)\Big). \quad (2.139)$$

In order to evaluate this combination, we need to compute the sum $I_1(x)+I_2(1-x)-I_2(\frac{1-x}{x})$. Since both I_1 and I_2 are convergent, we can make the change of variable $t \to xt$ in the first term, $I_1(x)$, and in the third one, $I_2(\frac{1-x}{x})$. Doing this yields

$$\begin{aligned} I_1(x) + I_2(1-x) - I_2(\tfrac{1-x}{x}) = \\ \int_0^\infty \frac{\mathrm{d}t}{t}\Bigg\{ & \frac{\mathrm{e}^{-(\frac{d}{2}-1)(1-x)t}}{1-\mathrm{e}^{-t}}\Big[\frac{\mathrm{e}^{-t}}{1-\mathrm{e}^{-xt}} + \frac{1}{\mathrm{e}^{(1-x)t}-1}\Big] \\ & - \frac{\mathrm{e}^{-(\frac{d}{2}-1)(1-x)t}}{(1-\mathrm{e}^{-xt})(\mathrm{e}^{(1-x)t}-1)} - A(xt;x)\,\mathrm{e}^{-t(1+x)/2} \\ & - B(t;1-x)\,\mathrm{e}^{-t(2-x)/2} + B(xt;\tfrac{1-x}{x})\,\mathrm{e}^{-t/2}\Bigg\}. \quad (2.140) \end{aligned}$$

The three first terms on the right-hand side miraculously cancel out, leaving the integral of the three last terms. It is easily carried out by using the formulas (2.133),

$$\begin{aligned} I_1(x) + I_2(1-x) - I_2(\tfrac{1-x}{x}) = \frac{17}{16} - \frac{x}{2} + \frac{d}{2}(x-1) \\ + \frac{5-6d+\frac{3}{2}d^2 - x(5-9d+3d^2) + x^2(1-3d+\frac{3}{2}d^2)}{12(1-x)}\log(2-x) \\ + \frac{(1-3d+\frac{3}{2}d^2)(1+x^2) - 3x(1-d)^2}{12x}\log(1+x). \quad (2.141) \end{aligned}$$

The function $C_{gh}(N,x,d)$ may then be computed. We simplify the sum of logarithms of trigonometric functions in (2.138b) with (2.117). A similar identity is used for (2.138a). The result reads

$$\begin{aligned} C_{gh}(N,x,d) = {} & N^2\Big((1-x+x^2)(\log N - \tfrac{3}{2}) + x(x-1)x\log x\Big) \\ & + N\Big((2-2x+d+dx)(1-\log N) + (d+2x-dx)\log x + 2\log 2\Big) \\ & + d^2\log N + \frac{2x-(2-6d+3d^2)(1-x)^2}{12x}\log(1-x) - \log\Big(\frac{\pi}{2}\Big) \\ & - \frac{10-10x+2x^2+6d(2-x-x^2)+3d^2(1-x)^2}{12(1-x)}\log x - 3d\log 2 \end{aligned}$$

$$+\begin{cases} \log N - 2\sum_{j=1}^{\frac{d}{2}-1} \log|\sin(\pi j x)| + \mathcal{O}\big(N^{-1}\big) & (N, d \text{ even}), \\ \log 2 - 2\sum_{j=1}^{\frac{d-1}{2}} \log\left|\cos\left(\pi x(j-\frac{d}{2})\right)\right| + \mathcal{O}\big(N^{-1}\big) & (N, d \text{ odd}). \end{cases} \tag{2.142}$$

In computing (2.110), we find that the sums of logarithms of trigonometric functions from (2.142) simplify with those in (2.118). Combining (2.110), (2.112b) to (2.112d), (2.118), (2.120), (2.125) and (2.142), we obtain (2.72) for both parities of N and d, hence ending the proof. As noted earlier, the final result contains no $N^{-1}\log N$ term.

2.5 Summary of the main results

In the present chapter, we defined and investigated two instances of the bipartite fidelity for the model of critical dense polymers on the flat pants lattice: $\mathcal{F}_f^{(d)}$ and $\tilde{\mathcal{F}}_f^{(2)}$. We obtained closed-form expressions at finite lattice size N and computed the leading terms of their large-N asymptotic expansions as a function of the aspect ratio $x = N_A/N$. In both cases, the leading term is $\frac{(-2)}{8}\log N$, which is consistent with the known value $c = -2$ of the central charge for the model of critical dense polymers. The next leading term is constant with respect to N. For $\mathcal{F}_f^{(d)}$, we found that it has precisely the form (1.82) predicted by Stéphan and Dubail, with the conformal weights of the field that accounts for the insertion of d defects on the boundary equal to $\Delta_{1,d+1} = \frac{d(d-2)}{8}$. This is consistent with earlier known results for the weights of these fields [141, 150]. We also computed the constant term for $\tilde{\mathcal{F}}_f^{(2)}$, and it differs from the value of the same constant for $\mathcal{F}_f^{(2)}$ by the simple factor $-2\log((1+x)/(2\sqrt{x}))$. This lattice result was confirmed by a LCFT argument, with the simple factor understood to be universal. In particular, we found that this universal factor is independent on the conformal data of the underlying LCFT. To our knowledge, this is the first result regarding the bipartite fidelity in the context of non-unitary CFT. Finally, the next-leading term predicted by Stéphan and Dubail, proportional to $N^{-1}\log N$, is zero for both $\mathcal{F}_f^{(d)}$ and $\tilde{\mathcal{F}}_f^{(2)}$, indicating that the (non-universal) extrapolation length Ξ in (1.85) vanishes.

Few observables allow one to measure directly the central charge c of a conformally invariant model. As we discussed in Chapter 1, the finite-size scaling of the eigenvalues of the Hamiltonian (or equivalently the transfer matrix), in particular, only allow for a measurement of the effective central charge, $c_{\text{eff}} = c - 24\Delta_{\text{min}}$, where Δ_{min} is the smallest conformal weight in the subsector of the theory corresponding to the boundary conditions that are considered. For the model of critical dense polymers, the effective central charge is $c_{\text{eff}} = c = -2$ for even N, and $c_{\text{eff}} = 1$ for odd N. In the former case, the groundstate has the conformal weight $\Delta_{1,1} = 0$, whereas in the latter, the conformal weight is $\Delta_{1,2} = -1/8$. All our results are compatible with $c = -2$, even in the case where N is an odd number. Our investigations thus suggest that the bipartite fidelity allows one to measure c and not just c_{eff}. In our calculations, we computed $\mathcal{F}_f^{(d)}$ and $\tilde{\mathcal{F}}_f^{(2)}$ using overlaps of the form $\langle\langle v|w\rangle$ with the definition $\langle\langle v| = |v\rangle^{\text{t}}$ for the dual states, in such a way that these overlaps are equal to the corresponding bilinear forms $v \cdot w$ and $v \odot w$, respectively. This definition for the dual states originated from our choice to define the bipartite fidelities in terms of partition functions in the loop model. In the spin chain, the left-eigenstates of the non-Hermitian Hamiltonian H_o have the form $\langle\langle v| = |v\rangle^{\text{t}}$, where $|v\rangle$ is a right-eigenstate. As we discussed in Section 1.2.3, the definition of the dual state influences whether the leading coefficient is $c/3$ or $c_{\text{eff}}/3$ for the entanglement entropy. Presumably, by repeating our derivation but with the definition $\langle v| = |v\rangle^{\dagger}$ instead of $\langle\langle v|$ for the dual states, we would find a large-N expansion for the logarithmic bipartite fidelity with the first term proportional to the effective central charge.

3

Bipartite fidelity on the periodic pants geometry

In this chapter, we investigate the logarithmic bipartite fidelity $\mathcal{F}_p$ on the periodic pants geometry in the context of CFT and critical lattice models. We recall that for quantum spin chains, $\mathcal{F}_p$ is given by the definition (1.78) where each system A, B and AB has periodic boundary conditions, whereas it is defined in (1.79b) for two-dimensional lattice models. In Section 3.1, we give the CFT predictions for the leading terms of the large-N expansion of the logarithmic bipartite fidelity. In Sections 3.2 and 3.3, we compute $\mathcal{F}_p$ for the XX spin chain and for the model of critical dense polymers. Finally, we compare the asymptotic behaviour of the lattice results with the CFT predictions in Section 3.4. The results discussed in this chapter were initially presented in the publication [3].

3.1 Predictions of conformal field theory

In this section, we give the CFT predictions for the bipartite fidelity on the periodic pants domain. The details of the calculations are similar to those used by Dubail and Stéphan in their initial investigation of the bipartite fidelity on the flat pants lattice [62, 63], and are given in the Appendix A of [3]. These calculations are not reproduced here. We consider the asymptotic behaviour of $\mathcal{F}_p$ in the limit where N and N_A are sent to infinity such that the aspect ratio $x = N_A/N$ converges to a constant in the interval $(0, 1)$. The logarithmic bipartite fidelity $\mathcal{F}_p$ has

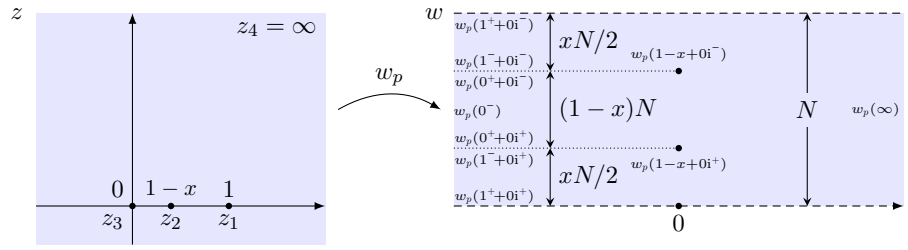

Figure 3.1: The function $w_p(z)$ maps the complex plane onto the periodic pants domain. On the right part of the figure, the dashed and dotted lines are identified pairwise.

the large-N expansion

$$\mathcal{F}_p = g_p^{(0)} \log N + g_p^{(1)}(x) + g_p^{(2)}(x) N^{-1} \log N + \mathcal{O}(N^{-1}). \tag{3.1}$$

In the CFT framework, the periodic pants domain is an infinite horizontal strip of width N drawn in the complex plane. The strip is decorated with two slits that divide its left half into two strips of width Nx and $N(1-x)$. The boundary conditions are periodic along the strip's edges and along the slits. This geometry is topologically equivalent of the one displayed on left panel of Figure 1.9 in the limit of large M. In particular, due to the periodicity, the two endpoints of the slits are identified as a unique point in the domain. We refer to this point as the *crotch point*. The mapping from the complex plane to the periodic pants domain is

$$\begin{aligned} w_p(z) &= \frac{N}{2\pi}\big(x \log(z-1) + (1-x)\log z\big) + K_x, \\ K_x &= -\frac{N}{2\pi}\big(x \log x + (1-x)\log(1-x)\big). \end{aligned} \tag{3.2}$$

This map is illustrated in Figure 3.1.

In a general setting, we consider the situation where four bulk fields are inserted on the periodic pants domain. A field ϕ_1 is inserted at $-\infty$ in the leg A, a field ϕ_2 is inserted on the crotch point, a field ϕ_3 is inserted at $-\infty$ in the leg B, and a field ϕ_4 is inserted at $+\infty$. We denote by $w_p(z_i)$ the corresponding positions on the periodic pants domain, where z_i are the corresponding positions in the complex plane. For simplicity, we assume that each field ϕ_i is spinless with conformal weight $\Delta_i = \bar{\Delta}_i$. We illustrate this setting and the fields insertion points in Figure 3.2.

We obtain the first term $g_p^{(0)}$ in the expansion (3.1) as a direct application of the Cardy-Peschel formula [135] for conical singularities. Indeed, the crotch point in the periodic pants domain corresponds to a single conical singularity of angle 4π, as we can see from the expansion of $w_p(z)$ about the point $z = z_2$. The resulting expression for $g_p^{(0)}$ depends on the dimension of the field ϕ_2 and on the central charge:

$$g_p^{(0)} = \frac{c}{4} + 2\Delta_2. \tag{3.3}$$

The next term $g_p^{(1)}(x)$ depends on the aspect ratio x and on the dimensions Δ_i of the four fields. In the case where the four fields are non-trivial primary fields, $g_p^{(1)}(x)$ also depends on the four-point function of the fields ϕ_1, ϕ_2, ϕ_3 and ϕ_4. We give the result in two cases: (i) no field is inserted on the crotch point and the fields ϕ_1, ϕ_3 and ϕ_4 are primary, and (ii) the four fields ϕ_i are vertex operators with charges $q_i = \bar{q}_i$ and conformal weights $\Delta_i = \bar{\Delta}_i = q_i^2/2$ in a free-boson CFT with central charge $c = 1$. Vertex operators are primary fields whose n-point function on the complex plane reads

$$\left\langle \prod_{i=1}^{n} \phi_i(z_i, \bar{z}_i) \right\rangle_{\mathbb{C}} = \prod_{1 \leqslant i < j \leqslant n} |z_i - z_j|^{2q_i q_j}, \qquad \sum_{i=1}^{n} q_i = 0. \tag{3.4}$$

For case (i), we use the known form of the three-point functions and find

$$g_p^{(1)}(x) = 4\Big(\Delta_4 - \frac{\Delta_1}{x} - \frac{\Delta_3}{1-x}\Big)\big(x \log x + (1-x)\log(1-x)\big) + \frac{c}{12}\big(G_p(x) + G_p(1-x)\big) + C_p \tag{3.5}$$

where

$$G_p(x) = \frac{3 - 3x + 2x^2}{1-x} \log x \tag{3.6}$$

and C_p is a non-universal constant with respect to N and x. However, this quantity depends on the structure constant C_{134} that appears in the three-point function (1.23) of the fields ϕ_1, ϕ_3 and ϕ_4. If we write $C_p = C_p(\phi_1, \phi_3, \phi_4)$ to stress the dependence on the fields, we have

$$C_p(\phi_1, \phi_3, \phi_4) - C_p(\phi_1', \phi_3', \phi_4') = -2 \log\Big(\frac{C_{134}}{C_{134}'}\Big) \tag{3.7}$$

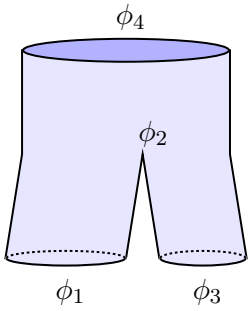

Figure 3.2: Illustration of the fields insertion points on the periodic pants domain. The top part, bottom left and bottom right legs have perimeters N, N_A and N_B, respectively.

where C'_{134} is the structure constant of the three-point function of three other primary fields ϕ'_1, ϕ'_3 and ϕ'_4.

For case (ii), the function $g_p^{(1)}(x)$ reads

$$g_p^{(1)}(x) = 2\left[q_1^2\Big(1-\frac{1}{x}\Big) - q_3^2 - 2q_3q_2 - \frac{q_2^2}{2} + q_4^2(1-x)\right]\log(1-x) + \{q_1 \leftrightarrow q_3, x \to 1-x\} + \frac{c}{12}\big(G_p(x) + G_p(1-x)\big) + C'_p \quad (3.8)$$

where C'_p is a non-universal constant. On the second line of (3.8), the first contribution, marked by a bracket, indicates that the first line must be copied but with the substitutions indicated inside this bracket.

Finally, we find that the prefactor $g_p^{(2)}(x)$ of the $N^{-1}\log N$ term is

$$g_p^{(2)}(x) = 2\,\Xi \times \left(\frac{c\,(1-x+x^2)}{24x(1-x)} + \Delta_4 - \frac{\Delta_1}{x} - \frac{\Delta_3}{1-x}\right) \quad (3.9)$$

for both cases (i) and (ii). We recall that the extrapolation length Ξ is a non-universal constant. As a remark, we note that the conformal predictions for $g_p^{(0)}$, $g_p^{(1)}(x)$ and $g_p^{(2)}(x)$ are twice the same functions obtained by Dubail and Stéphan for the asymptotic expansion of $\mathcal{F}_f$ on the flat pants domain. This property stems from the relation $w_f(z) = 2w_p(z)|_{x\to 1-x}$ for $z \in \mathbb{H}$, where $w_f(z)$ is the map (2.95) to the flat pants domain.

3.2 Lattice calculation for the XX spin chain

We compute the bipartite fidelity of the periodic XX spin chain with twisted boundary conditions. For a chain of length N and twist angle ϕ, the Hamiltonian is

$$H_p = -\sum_{j=1}^{N-1} \left(\sigma_j^+\sigma_{j+1}^- + \sigma_j^-\sigma_{j+1}^+\right) - \mathrm{e}^{\mathrm{i}\phi}\sigma_N^+\sigma_1^- - \mathrm{e}^{-\mathrm{i}\phi}\sigma_N^-\sigma_1^+ \tag{3.10}$$

where we use the notations and conventions of Section 1.2.2. We restrict our investigations to the case where N is an even number. The Hamiltonian commutes with the total magnetisation $S^z = \frac{1}{2}\sum_{j=1}^N \sigma_j^z$.

We also consider two smaller periodic chains of lengths N_A and N_B with respective twist angles are ϕ_A and ϕ_B. The three twist angles ϕ, ϕ_A and ϕ_B are three free parameters. We impose that both lengths are even numbers that satisfy $N_A + N_B = N$. We denote by H_p^{AB}, H_p^A and H_p^B the Hamiltonians of the chains of lengths N, N_A and N_B, and their respective groundstates are $|X_0^{AB}\rangle$, $|X_0^A\rangle$ and $|X_0^B\rangle$. The subscript 0 indicates that these states belong to the subspaces of zero magnetisation. We define the dual states as

$$\langle v| = |v\rangle^\dagger, \tag{3.11}$$

and the states $\langle X_0^{AB}|$, $\langle X_0^A|$ and $\langle X_0^B|$ are the left-groundstates of the Hamiltonians H_p^{AB}, H_p^A and H_p^B. The logarithmic bipartite fidelity for the XX spin chain on the periodic pants lattice is

$$\mathcal{F}_p^{XX} = -\log\left|\langle X_0^A \otimes X_0^B | X_0^{AB}\rangle\right|^2, \tag{3.12}$$

where $|X_0^{AB}\rangle$, $|X_0^A\rangle$ and $|X_0^B\rangle$ are assumed to have unit norms.

3.2.1 Diagonalisation of the Hamiltonian

The diagonalisation of H_p is very similar to the diagonalisation of H_f presented in Section 1.2.2. It also uses the Jordan-Wigner transformation (1.52) and a Fourier transform. The result is

$$H_p = -\sum_{k=1}^{N} 2\cos(\theta_k)\mu_k^\dagger\mu_k, \tag{3.13}$$

where

$$\mu_k = \frac{1}{\sqrt{N}} \sum_{j=1}^{N} \mathrm{e}^{\mathrm{i}j\theta_k} c_j, \qquad \mu_k^\dagger = \frac{1}{\sqrt{N}} \sum_{j=1}^{N} \mathrm{e}^{-\mathrm{i}j\theta_k} c_j^\dagger,$$
$$\theta_k = \begin{cases} \frac{2\pi k - \phi}{N} & \frac{N}{2} + S^z \text{ odd}, \\ \frac{2\pi(k-\frac{1}{2}) - \phi}{N} & \frac{N}{2} + S^z \text{ even}. \end{cases} \tag{3.14}$$

The operators μ_k and $\mu_\ell^\dagger$ satisfy the usual fermionic anticommutation rules

$$\{\mu_k, \mu_\ell^\dagger\} = \delta_{k,\ell}, \qquad \{\mu_k, \mu_\ell\} = \{\mu_k^\dagger, \mu_\ell^\dagger\} = 0. \tag{3.15}$$

With k in the set $\{1, \ldots, N\}$, we have a full set of fermionic operators. It is however useful to extend the range of k to negative values using the periodicity properties $\mu_{k+N} = \mu_k$ and $\mu_{k+N}^\dagger = \mu_k^\dagger$.

For $\phi \in (-\pi, \pi)$, the groundstate eigenvalue of H_p is non-degenerate. The groundstate vector lies in the magnetisation sector $S^z = 0$ and reads

$$|X_0\rangle = \begin{cases} \mu_{(4-N)/4}^\dagger \cdots \mu_{N/4}^\dagger |0\rangle & \frac{N}{2} \text{ even}, \\ \mu_{(2-N)/4}^\dagger \cdots \mu_{(N-2)/4}^\dagger |0\rangle & \frac{N}{2} \text{ odd}. \end{cases} \tag{3.16}$$

Due to the anticommutation relations of the operators μ_k and $\mu_\ell^\dagger$, the groundstate has norm one, namely $\langle X_0 | X_0 \rangle = 1$, where

$$\langle X_0| = \begin{cases} \langle 0|\mu_{N/4} \cdots \mu_{(4-N)/4} & \frac{N}{2} \text{ even}, \\ \langle 0|\mu_{(N-2)/4} \cdots \mu_{(2-N)/4} & \frac{N}{2} \text{ odd}, \end{cases} \tag{3.17}$$

is the left-groundstate of H_p.

For $\phi = \pm\pi$, the groundstate eigenvalue is doubly degenerate because there is a value $k_0 \in \{1, \ldots, N\}$ which depends on the parity of $N/2 + S^z$ such that $\cos(\theta_{k_0}) = 0$. For ϕ outside of the range $(-\pi, \pi)$, the state defined in (3.16) is still an eigenstate of the Hamiltonian, but it corresponds to an excited state. In the following, unless stated otherwise, our results for the bipartite fidelity hold for arbitrary values of the twist angles ϕ, ϕ_A, ϕ_B, but they should be interpreted in terms of overlaps of groundstates only for $\phi, \phi_A, \phi_B \in (-\pi, \pi)$.

3.2.2 Bipartite fidelity

To compute the bipartite fidelity, we introduce the fermion operators for the subsystems A and B:

$$\mu_k^A = \frac{1}{\sqrt{N_A}} \sum_{j=1}^{N_A} \mathrm{e}^{\mathrm{i}j\theta_k^A} c_j, \qquad (\mu_k^A)^\dagger = \frac{1}{\sqrt{N_A}} \sum_{j=1}^{N_A} \mathrm{e}^{-\mathrm{i}j\theta_k^A} c_j^\dagger, \tag{3.18a}$$

$$\mu_k^B = \frac{1}{\sqrt{N_B}} \sum_{j=N_A+1}^{N} \mathrm{e}^{\mathrm{i}(j-N_A)\theta_k^B} c_j, \quad (\mu_k^B)^\dagger = \frac{1}{\sqrt{N_B}} \sum_{j=N_A+1}^{N} \mathrm{e}^{-\mathrm{i}(j-N_A)\theta_k^B} c_j^\dagger, \tag{3.18b}$$

with

$$\theta_k^A = \begin{cases} \frac{2\pi k-\phi_A}{N_A} & \frac{N_A}{2} + (S^z)^A \text{ odd}, \\ \frac{2\pi(k-\frac{1}{2})-\phi_A}{N_A} & \frac{N_A}{2} + (S^z)^A \text{ even}, \end{cases} \tag{3.18c}$$

$$\theta_k^B = \begin{cases} \frac{2\pi k-\phi_B}{N_B} & \frac{N_B}{2} + (S^z)^B \text{ odd}, \\ \frac{2\pi(k-\frac{1}{2})-\phi_B}{N_B} & \frac{N_B}{2} + (S^z)^B \text{ even}, \end{cases} \tag{3.18d}$$

where $(S^z)^A = \frac{1}{2}\sum_{j=1}^{N_A} \sigma_j^z$ and $(S^z)^B = S^z - (S^z)^A$. The three ground-states $|X_0^{AB}\rangle$, $|X_0^A\rangle$ and $|X_0^B\rangle$ have unit norms. Using Wick's theorem, we evaluate the overlap in (3.12) as a determinant. The corresponding matrix contains the anticommutators of the operators $\mu_{k'}^\dagger$ and μ_k^A or μ_k^B. After simplification, the result is

$$\big|\langle X_0^A \otimes X_0^B | X_0^{AB}\rangle\big| = 2^{-N/2} N^{-N/2} \\ x^{-Nx/4}(1-x)^{-N(1-x)/4} \big|\det \mathcal{A}\big|, \tag{3.19}$$

with

$$\mathcal{A}_{k,k'} = \begin{cases} \dfrac{1+\mathrm{e}^{-\mathrm{i}\pi x(2k'-1)}\mathrm{e}^{-\mathrm{i}(\phi_A - x\phi)}}{\sin\left[\frac{\pi(2k-1)}{2Nx} - \frac{\pi(2k'-1)}{2N} - \frac{\phi_A - x\phi}{2Nx}\right]} & k = 1, \ldots, \frac{Nx}{2}, \\ \dfrac{1+\mathrm{e}^{-\mathrm{i}(\phi-\phi_B)}\mathrm{e}^{\mathrm{i}\pi(1-x)(2k'-1)}\mathrm{e}^{\mathrm{i}x\phi}}{\sin\left[\frac{\pi(2k-Nx-1)}{2N(1-x)} - \frac{\pi(2k'-1)}{2N} - \frac{\phi_B-(1-x)\phi}{2N(1-x)}\right]} & k = \frac{Nx+2}{2}, \ldots, \frac{N}{2}, \end{cases} \tag{3.20}$$

and $k' = 1, \ldots, \frac{N}{2}$. This holds for all parities of $N/2$, $N_A/2$ and $N_B/2$. For generic twist angles, we do not know how to evaluate this determinant in closed form. This is due to the numerators in (3.20) which are

different in the two parts of the matrix $\mathcal{A}$. We can however evaluate the determinant if the twist parameters ϕ, ϕ_A and ϕ_B are such that

$$1+\mathrm{e}^{-\mathrm{i}\pi x(2k'-1)}\mathrm{e}^{-\mathrm{i}(\phi_A-x\phi)}=1+\mathrm{e}^{-\mathrm{i}(\phi-\phi_B)}\mathrm{e}^{\mathrm{i}\pi(1-x)(2k'-1)}\mathrm{e}^{\mathrm{i}x\phi}. \tag{3.21}$$

The solutions are

$$\phi=\phi_A+\phi_B-\pi+2\pi\ell, \qquad \ell\in\mathbb{Z}. \tag{3.22}$$

In the following, we focus on the case $\ell=0$. Under this specialisation, we are able to simplify the determinant and obtain a closed-form formula. Indeed, we find

$$\begin{aligned}|\langle X_0^A\otimes X_0^B|X_0^{AB}\rangle| &= N^{-N/2}x^{-Nx/4}(1-x)^{-N(1-x)/4}\\ &\quad\times\left|\prod_{k'=1}^{N/2}\cos\left[\pi xk'-\tfrac{\phi_A(x-1)+x\phi_B}{2}\right]\right||\det\mathcal{M}|\end{aligned} \tag{3.23}$$

where

$$\mathcal{M}_{k,k'}=\begin{cases}\sin\left[\frac{\pi(2k-1)-\phi_A}{2Nx}-\frac{\pi(2k'-1)-\phi}{2N}\right]^{-1} & k=1,\dots,\frac{Nx}{2},\\ \sin\left[\frac{\pi(2k-Nx-1)-\phi_B}{2N(1-x)}-\frac{\pi(2k'-1)-\phi}{2N}\right]^{-1} & k=\frac{Nx}{2}+1,\dots,\frac{N}{2},\end{cases} \tag{3.24}$$

and $k'=1,\dots,\frac{N}{2}$. We use the sine version of the Cauchy identity,

$$\det_{k,\ell=1}^{L}\frac{1}{\sin(w_k-z_\ell)}=\frac{\prod_{1\leqslant k<\ell\leqslant L}\sin(w_\ell-w_k)\sin(z_k-z_\ell)}{\prod_{k,\ell=1}^{L}\sin(w_k-z_\ell)}, \tag{3.25}$$

and find

$$\begin{aligned}\det \mathcal{M} = &\prod_{1\le k<k'\le Nx/2} \sin\Big[\frac{\pi}{Nx}(k-k')\Big] \times \prod_{1\le k<k'\le N/2} \sin\Big[\frac{\pi}{N}(k'-k)\Big] \\ &\times \prod_{1\le k<k'\le N(1-x)/2} \sin\Big[\frac{\pi}{N(1-x)}(k-k')\Big] \\ &\times \prod_{k=1}^{Nx/2}\prod_{k'=1}^{N(1-x)/2} \sin\Big[\frac{\pi(2k-1)-\phi_A}{2Nx} - \frac{\pi(2k'-1)-\phi_B}{2N(1-x)}\Big] \\ &\times \left(\prod_{k=1}^{Nx/2}\prod_{k'=1}^{N/2} \sin\Big[\frac{\pi(2k-1)-\phi_A}{2Nx} - \frac{\pi(2k'-1)-\phi}{2N}\Big]\right)^{-1} \\ &\times \left(\prod_{k=1}^{N(1-x)/2}\prod_{k'=1}^{N/2} \sin\Big[\frac{\pi(2k-1)-\phi_B}{2N(1-x)} - \frac{\pi(2k'-1)-\phi}{2N}\Big]\right)^{-1}.\end{aligned} \tag{3.26}$$

Many of these products have a similar structure. We define two generic products R_1 and R_2,

$$R_1(N) = \prod_{1\le k<k'\le N/2} \Big|\sin\Big[\frac{\pi}{N}(k-k')\Big]\Big|, \tag{3.27a}$$

$$R_2(N_1,N_2,\phi_1,\phi_2) = \prod_{k=1}^{N_1/2}\prod_{k'=1}^{N_2/2} \Big|\sin\Big[\frac{\pi k}{N_1} - \frac{\pi k'}{N_2} - \frac{\pi+\phi_1}{2N_1} + \frac{\pi+\phi_2}{2N_2}\Big]\Big|, \tag{3.27b}$$

and recast the overlap $|\langle X_0^A \otimes X_0^B | X_0^{AB}\rangle|$ as

$$\begin{aligned}\mathrm{e}^{-\frac{1}{2}\mathcal{F}_p^{XX}}\big|_{\phi=\phi_A+\phi_B-\pi} &= N^{-N/2} x^{-Nx/4}(1-x)^{-N(1-x)/4} \\ &\quad\times \Big|\prod_{k'=1}^{N/2} \cos\Big[\pi x k' - \tfrac{\phi_A(x-1)+x\phi_B}{2}\Big]\Big| \\ &\times \frac{R_1(N)\,R_1(Nx)\,R_1(N(1-x))\,R_2(Nx,N(1-x),\phi_A,\phi_B)}{R_2(Nx,N,\phi_A,\phi_A+\phi_B-\pi)\,R_2(N(1-x),N,\phi_B,\phi_A+\phi_B-\pi)}.\end{aligned} \tag{3.28}$$

3.2.3 Other instances of the bipartite fidelity

The CFT predictions of Section 3.1 cover cases where fields are inserted in the legs and on the crotch point. In order to investigate these cases further, we consider modified instances of the bipartite fidelity for the XX spin chain on the periodic pants lattice. We do this by relaxing the condition tying N, N_A and N_B, and define

$$\mathcal{F}_p^{XX}(n) = -\log \left| \langle X_0^A \otimes X_0^B \otimes \underbrace{\uparrow\downarrow \otimes \cdots \otimes \uparrow\downarrow}_{n/2 \text{ times}} | X_0^{AB} \rangle \right|^2, \tag{3.29}$$

where n is an even integer. The spin state $|\uparrow\downarrow \cdots \uparrow\downarrow\rangle$ is known as a *Néel state* of length n. The new constraint on the lengths is $N = N_A + N_B + n$. In the scalar product (3.29), the magnetisation of the dual state vanishes, and the corresponding overlap is non-zero. Following the arguments presented in Section 3.2.2 for $\mathcal{F}_p^{XX}$, we obtain a determinant expression for this overlap similar to (3.19), which we do not reproduce here. We are unable to evaluate it in product form. We analyse $\mathcal{F}_p^{XX}(n)$ for small values of n in Section 3.4 using the numerical evaluation of these determinants. The case $n = 0$ corresponds to the standard definition (3.12) of $\mathcal{F}_p^{XX}$.

3.3 Lattice calculation for critical dense polymers

The second lattice model for which we compute the bipartite fidelity on the periodic pants lattice is the model of critical dense polymers. The lattice is divided into three parts, as illustrated in the example of Figure 2.1. The top part is an $M \times N$ rectangular array of tiles, with even N. The boundary conditions on this rectangle are periodic in the horizontal direction, so that the left and right segments of this rectangle are identified as the same segment. The bottom part is divided into two smaller arrays of tiles of respective sizes $M \times N_A$ and $M \times N_B$, with N_A and N_B both even and satisfying $N_A + N_B = N$. Each of these smaller arrays also has periodic horizontal boundary conditions. The tops of these two arrays are placed side-by-side and attached to the bottom segment of the $M \times N$ rectangle. The three free ends of

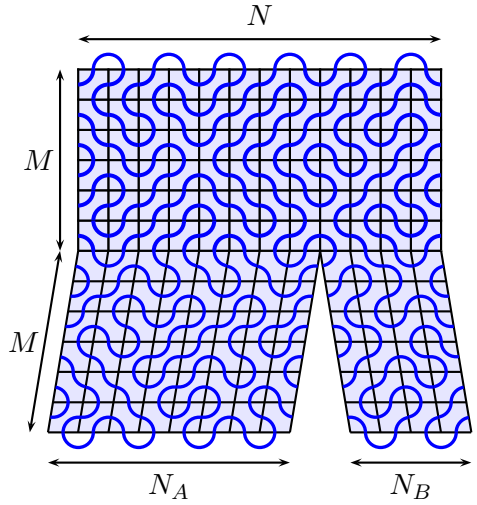

Figure 3.3: A configuration of the model of critical dense polymers on the periodic pants lattice, with $M = 6$, $N = 12$, $N_A = 8$ and $N_B = 4$. It contains four non-contractible loops and therefore has a weight α^4.

the periodic pants lattice, one at the top and two at the bottom of the lattice, are decorated by simple arcs that connect each tile to one of its neighbours. Put together, the loop segments drawn on the tiles and on the boundary arcs form a set of loops. The contractible loops, namely those that can be continuously deformed to a point, are given a weight $\beta = 0$. Non-contractible loops are divided into three families. They can (i) wrap around leg A, (ii) wrap around leg B, or (iii) wrap around the waist of the pants (or equivalently around both legs A and B). We choose to assign a weight $\alpha \in \mathbb{R}$ to non-contractible loops in the families (i) and (iii), but a weight zero to those in the family (ii). The Boltzmann weight of a configuration $\{\ell_i\}$ is

$$W_p(\{\ell_i\}) = \alpha^{n_A+n_{AB}} \delta_{n_\beta,0} \delta_{n_B,0} \tag{3.30}$$

where n_β is the number of contractible loops, and n_A, n_B and n_{AB} are the numbers of non-contractible loops in families (i), (ii) and (iii), respectively. The partition function on the periodic pants lattice, denoted

Z_p^{AB}, is

$$Z_p^{AB} = \sum_{\{\ell_i\}} W_p(\{\ell_i\}). \tag{3.31}$$

We also consider Z_c^{AB} and Z_c^A, the partition functions for the model of dense polymers on cylinders of dimensions $2M \times N$ and $2M \times N_A$, respectively. On these cylinders, the bottom and top ends are also decorated with simple arcs. The contractible and non-contractible loops have the fugacities 0 and α, respectively. Finally, we define Z_c^B, a partition function defined on a cylinder of size $2M \times N_B$. It is different from the other partition functions, in that the only configurations with non-zero weights are those with exactly one loop. This loop can be contractible or non-contractible. The boundary conditions are as before, with both ends of the cylinder decorated with simple arcs. Each of the contributing configurations has a weight 1, and Z_c^B is simply the number of such configurations. As argued in [141], one way to implement this without taking a limit on the fugacity of the loops is to replace one of the arcs at the top edge by two defects, and likewise at the bottom of the cylinder. One then imposes that the defects at the top connect with those at the bottom, with weight 1. For convenience, we choose that the last arc, on both the top and bottom segments, is the one replaced by a pair of defects. The lattices corresponding to the different partition functions are depicted in Figure 3.4.

The logarithmic bipartite fidelity of the model of critical dense polymers on the periodic pants lattice is

$$\mathcal{F}_p^{CDP} = -\lim_{M\to\infty} \log\left(\frac{\left(Z_p^{AB}\right)^2}{Z_c^{AB} Z_c^A Z_c^B}\right). \tag{3.32}$$

As we shall see, the ratio in the parenthesis has a well-defined limit.

3.3.1 The enlarged periodic Temperley-Lieb algebra

As in Chapter 2, our goal is to express the partition functions defined in the previous paragraphs in terms of the Temperley-Lieb algebra. Because of the periodic boundary conditions, our calculation of $\mathcal{F}_p^{CDP}$ requires the periodic incarnation of the algebra. This algebra was first introduced [152] by Levy in 1991 and was subsequently studied [153–156]

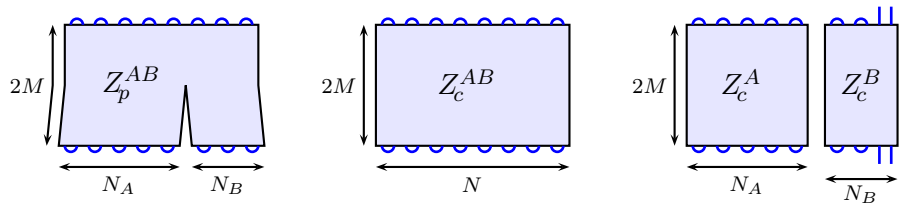

Figure 3.4: The lattices and boundary conditions corresponding to Z_p^{AB}, Z_c^{AB}, Z_c^A and Z_c^B. The boundary conditions are periodic in the horizontal direction so that the corresponding lattices from left to right are the periodic pants lattice and cylinders of perimeter N, N_A and N_B.

by both physicists and mathematicians. Certain details in the definition of this algebra vary from one paper to the next, and here we work with the *enlarged periodic Temperley-Lieb algebra* $\mathcal{E}\mathsf{PTL}_N(\alpha,\beta)$, as defined in [157]. The standard Temperley-Lieb algebra $\mathsf{TL}_N(\beta)$ is a subalgebra of $\mathcal{E}\mathsf{PTL}_N(\alpha,\beta)$, $\mathsf{TL}_N(\beta) \subset \mathcal{E}\mathsf{PTL}_N(\alpha,\beta)$. Hence, the definitions and concepts that we introduce here generalise those we discussed in Section 2.1.1.

Definition of the algebra. The enlarged periodic Temperley-Lieb algebra $\mathcal{E}\mathsf{PTL}_N(\alpha,\beta)$ is the linear span of connectivity diagrams where the boundary conditions are periodic in the horizontal direction. The loop segments can therefore cross the vertical edges of the box, in which case we say that they travel via the back of the cylinder. The product $a_1 a_2$ of two connectivity diagrams in $\mathcal{E}\mathsf{PTL}_N(\alpha,\beta)$ is done by vertical concatenation: one draws a_1 below a_2 and obtains the new connectivity from the connection of the top and bottom nodes. Each loop formed in the process is removed and replaced by a factor α or β, depending on its contractibility. Here are two examples of products of connectivity diagrams for $N = 4$:

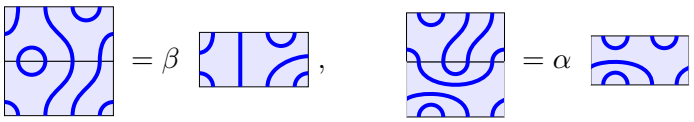

(3.33)

This algebra is generated by $N+2$ connectivity diagrams: Ω, Ω^{-1}, and e_j with $j = 1, \ldots, N$. The generators e_j with $j = 1, \ldots, N-1$ are given in (2.5), whereas the remaining ones are depicted as

$\Omega =$ 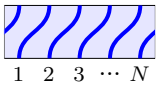

, $\Omega^{-1} =$ 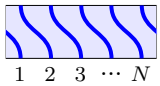

, (3.34a)

and

$e_N =$ 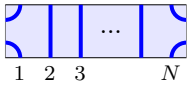

. (3.34b)

Finally, the identity $\boldsymbol{I}$ for this algebra is the element

$\boldsymbol{I} = \Omega^{-1}\Omega = \Omega\Omega^{-1} =$ 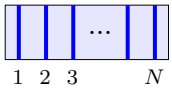

. (3.35)

The diagrammatic rule that describes the product in this algebra can be translated into relations satisfied by the generators. These are given for instance in [157]. The value of β pertaining to the model of critical dense polymers is $\beta = 0$. In our calculations below, we keep α as free parameter and set N to an even integer.

The transfer tangle and the Hamiltonian. The transfer tangle for the model of critical dense polymers with periodic boundary conditions $\boldsymbol{T}(u)$ is an element of $\mathcal{E}\mathsf{PTL}_N(\alpha, 0)$,

$\boldsymbol{T}(u) =$ 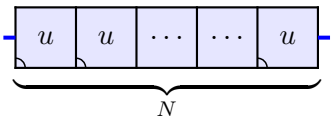

,

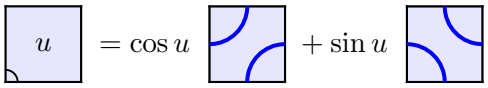

. (3.36)

It is a linear combination of 2^N connectivity diagrams. As in the case of free boundary conditions discussed in the previous chapter, the isotropic value is $u = \frac{\pi}{4}$, and we use the short-hand notation $\boldsymbol{T} = \boldsymbol{T}(\frac{\pi}{4})$. This transfer tangle commutes for different values of the spectral parameter: $[\boldsymbol{T}(u), \boldsymbol{T}(v)] = 0$. Expanding $\boldsymbol{T}(u)$ in a Taylor series in u in the limit $u \to 0$, we obtain

$$\boldsymbol{T}(u) = \Omega(\boldsymbol{I} - u\boldsymbol{H}_p) + \mathcal{O}(u^2), \qquad \boldsymbol{H}_p = -\sum_{j=1}^{N} e_j, \tag{3.37}$$

where $\boldsymbol{H}_p$ is the Hamiltonian. It commutes with the transfer tangle: $[\boldsymbol{H}_p, \boldsymbol{T}(u)] = 0$.

The standard modules $\mathsf{W}_{N,0}$ and $\mathsf{W}_{N,2}$. The algebra $\mathcal{E}\mathsf{PTL}_N(\alpha,\beta)$ possesses a family of standard modules $\mathsf{W}_{N,d}$ labelled by an integer number d of defects. Our calculation of $\mathcal{F}_p^{CDP}$ requires two standard modules: $\mathsf{W}_{N,0}$ and $\mathsf{W}_{N,2}$. These are respectively defined on the vector spaces generated by link states with zero and two defects. The boundary conditions are periodic in the horizontal direction. For example, here are the link states for $N = 4$:

$\mathsf{W}_{4,0}$:

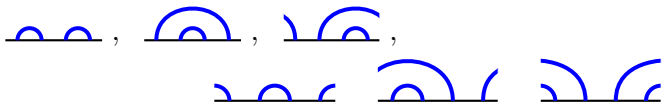

(3.38a)

$\mathsf{W}_{4,2}$:

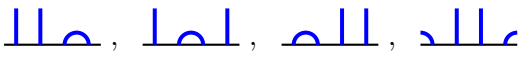

(3.38b)

The action of a connectivity in $\mathcal{E}\mathsf{PTL}_N(\alpha,\beta)$ on a link state w in $\mathsf{W}_{N,0}$ is similar to the action of $\mathcal{E}\mathsf{PTL}_N(\alpha,\beta)$ on itself. One draws the link state w on top of the connectivity and reads the resulting new link state from the bottom nodes. If this procedure creates non-contractible or contractible loops, they are removed and replaced by a multiplicative factor of α or β, respectively. Moreover, for $\mathsf{W}_{N,2}$, the result is zero if the two defects are connected. Here are examples of this standard action:

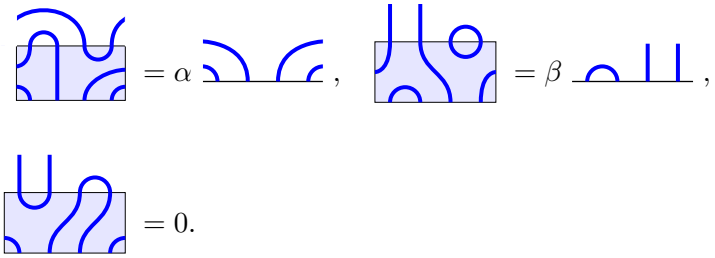

(3.39)

A link state module with identified connectivities. In the special case where $\alpha = \beta$, there exists another representation defined on link states with zero defects, with so-called *identified connectivities* [157]. We denote it by $\widehat{\mathsf{W}}_{N,0}$. Its vector space is spanned by the link states with zero

defects in $\mathsf{W}_{N,0}$ that have no arcs travelling via the back of the cylinder. These are in fact the same link states that span the standard module $\mathsf{V}_{N,0}$ with zero defects of the usual Temperley-Lieb algebra $\mathsf{TL}_N(\beta)$. For $N = 4$, these link states are:

$\widehat{\mathsf{W}}_{4,0}$: 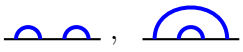 . (3.40)

The action of connectivity diagrams on link states in $\widehat{\mathsf{W}}_{N,0}$ is defined using the same construction as for standard modules. One draws the link state above the connectivity diagram, reads the new link state from the bottom edge of the diagram, and includes factors of β for each closed loop, both contractible and non-contractible. Crucially, in reading off the resulting link state, there is no distinction between arcs travelling via the front or back of the cylinder. Any arc travelling around the back of the cylinder is transformed into an arc travelling in the front of the cylinder. Here are two examples of this action for $N = 4$:

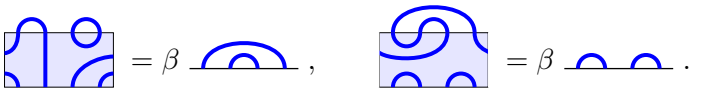 (3.41)

The XX representation. We extend the XX representation X_N of $\mathsf{TL}_N(0)$ discussed in Section 2.1.2 to $\mathcal{E}\mathsf{PTL}_N(\alpha, 0)$. The generators e_j with $j = 1, \ldots, N-1$ are represented by the matrices given in (2.20). Likewise, the generators $\Omega^{\pm 1}$ and e_N are represented by

$$\mathsf{X}_N(\Omega^{\pm 1}) = t^{\pm 1} \mathrm{e}^{\pm \mathrm{i}\phi\sigma_1^z/2}, \qquad \mathsf{X}_N(e_N) = \mathsf{X}_N(\Omega)\mathsf{X}_N(e_1)\mathsf{X}_N(\Omega^{-1}), \tag{3.42}$$

where ϕ is the twist angle and t is the translation operator:

$$t\big(|v_1\rangle \otimes |v_2\rangle \otimes \cdots \otimes |v_N\rangle\big) = |v_2\rangle \otimes \cdots \otimes |v_N\rangle \otimes |v_1\rangle. \tag{3.43}$$

The matrices $\mathsf{X}_N(e_j)$ and $\mathsf{X}_N(\Omega^{\pm 1})$ realise a representation of the enlarged periodic Temperley-Lieb algebra $\mathcal{E}\mathsf{PTL}_N(\alpha, 0)$ for

$$\alpha = 2\cos\Big(\frac{\phi}{2}\Big). \tag{3.44}$$

They also commute with the total magnetisation $S^z = \frac{1}{2}\sum_{i=1}^N \sigma_i^z$. As a consequence, the representation X_N splits as a direct sum of smaller

representations labelled by the eigenvalues m of S^z, which take the values $m = -\frac{N}{2}, -\frac{N-2}{2}, \ldots, \frac{N}{2}$.

In this representation, the Hamiltonian $\boldsymbol{H}_p$ is the twisted XX Hamiltonian (3.10):

$$H_p = \mathsf{X}_N(\boldsymbol{H}_p) = -\sum_{j=1}^{N-1} \left(\sigma_j^+\sigma_{j+1}^- + \sigma_j^-\sigma_{j+1}^+\right) - \mathrm{e}^{\mathrm{i}\phi}\sigma_N^+\sigma_1^- - \mathrm{e}^{-\mathrm{i}\phi}\sigma_N^-\sigma_1^+. \tag{3.45}$$

Likewise, the transfer matrix is defined as $T(u) = \mathsf{X}_N(\boldsymbol{T}(u))$. It is the transfer matrix of the six-vertex model at the anisotropy $\Delta = 0$, with periodic boundary conditions and a diagonal twist. We use the notation $T = T(\frac{\pi}{4})$ for this transfer matrix at the isotropic point.

Homomorphisms. Similarly to the case of free boundary conditions from Section 2.1.2, we discuss the map from link states to spin states that intertwines the standard and spin-chain representations of $\mathcal{E}\mathsf{PTL}_N(\alpha, 0)$. For a given link state w in $\mathsf{W}_{N,0}$, $\mathsf{W}_{N,2}$ or $\widehat{\mathsf{W}}_{N,0}$, we write its image in $(\mathbb{C}^2)^{\otimes N}$ under this map as $|w\rangle$. It is defined from the following local maps:

$$|\,\cap\,\rangle = \omega\,|{\uparrow\downarrow}\rangle + \omega^{-1}\,|{\downarrow\uparrow}\rangle, \qquad |\,\perp\,\rangle = |{\downarrow}\rangle,$$
$$|\,\curvearrowright\,\rangle = \omega^{-1}\mathrm{e}^{-\frac{\mathrm{i}\phi}{2}}\,|{\uparrow\downarrow}\rangle + \omega\,\mathrm{e}^{\frac{\mathrm{i}\phi}{2}}\,|{\downarrow\uparrow}\rangle, \tag{3.46}$$

where we recall $\omega = \mathrm{e}^{\mathrm{i}\pi/4}$. For a given link state, these local rules are applied to each arc and each defect. For $w \in \mathsf{W}_{N,0}$, $\mathsf{W}_{N,2}$ and $\widehat{\mathsf{W}}_{N,0}$, the resulting state $|w\rangle$ has the magnetisation $m = 0, -1$ and 0, respectively. The homomorphism property then reads

$$\mathsf{X}_N(e_j)|w\rangle = |e_j w\rangle, \quad \mathsf{X}_N(\Omega^{\pm 1})|w\rangle = |\Omega^{\pm 1} w\rangle, \quad j = 1, \ldots, N, \tag{3.47}$$

and is satisfied for each link state w. This holds for $\mathsf{W}_{N,0}$, $\widehat{\mathsf{W}}_{N,0}$ and $\mathsf{W}_{N,2}$, with the action of the generators on the right sides of the equations adapted accordingly, for each case. For $\mathsf{W}_{N,0}$, the homomorphism with the spin-chain representation holds for α fixed as a function of ϕ as in (3.44). For $\widehat{\mathsf{W}}_{N,0}$, non-contractible loops have the weight β and the homomorphism holds provided that ϕ is fixed to $\pm\pi$. In that case, $|\,\cap\,\rangle$ and $|\,\curvearrowright\,\rangle$ are equal up to a sign. For $\mathsf{W}_{N,2}$, the map (3.46) is

a homomorphism for the special value $\phi = 0$. This is consistent with the fact that our definition of this module was given without including a parameter that keeps track of the winding of the defects.

3.3.2 Bilinear forms and partition functions

In this section, we extend the Gram bilinear form for critical dense polymers introduced in Section 2.1.1 to the modules $\mathsf{W}_{N,0}$ and $\mathsf{W}_{N,2}$, and define a new bilinear form on the periodic pants lattice. These definitions allow us to express the partition functions used in the definition (3.32) of the logarithmic bipartite fidelity in terms of the enlarged periodic Temperley-Lieb algebra. We use the XX representation of the algebra to recast the partition functions as overlaps in the spin chain.

Bilinear forms for link states. The Gram bilinear form is an invariant form on the standard modules. For critical dense polymers with periodic boundary conditions, it is defined as follows. Let w, w' be two link states in $\mathsf{W}_{N,0}$ or $\mathsf{W}_{N,2}$. Performing a vertical flip of w and connecting its nodes to those of w', we obtain a diagram where the loop segments form loops, that can be contractible or non-contractible loops. For $\mathsf{W}_{N,0}$, the Gram product of w and w', denoted $w \cdot w'$, is defined as $\alpha^{n_\alpha}\delta_{n_\beta,0}$, where n_α and n_β count the non-contractible and the contractible loops. It is therefore non-zero only if the number of contractible loops is zero.

For $\mathsf{W}_{N,2}$, the same diagram constructed from w and w' involves loops as before, but also finds the defects connected pairwise. If both defects of w are connected to defects of w' and there are no loops, then $w \cdot w' = 1$. Otherwise, $w \cdot w' = 0$. To illustrate, for $N = 4$, the matrices encoding the Gram products between the link states in the bases (3.38) are

$$\begin{pmatrix} 0 & 0 & 0 & \alpha & 0 & 0 \\ 0 & 0 & \alpha & 0 & \alpha & \alpha^2 \\ 0 & \alpha & 0 & 0 & \alpha^2 & \alpha \\ \alpha & 0 & 0 & 0 & 0 & 0 \\ 0 & \alpha & \alpha^2 & 0 & 0 & \alpha \\ 0 & \alpha^2 & \alpha & 0 & \alpha & 0 \end{pmatrix}, \qquad \begin{pmatrix} 0 & 1 & 0 & 1 \\ 1 & 0 & 1 & 0 \\ 0 & 1 & 0 & 1 \\ 1 & 0 & 1 & 0 \end{pmatrix}. \tag{3.48}$$

These bilinear forms allow us to express the partition functions Z_c^{AB}, Z_c^A and Z_c^B in terms of Gram products:

$$Z_c^{AB} = 2^{MN} v_0^{AB} \cdot (\boldsymbol{T}^{AB})^{2M} v_0^{AB}\big|_{\mathsf{W}_{N,0}} , \tag{3.49a}$$

$$Z_c^{A} = 2^{MN_A} v_0^{A} \cdot (\boldsymbol{T}^{A})^{2M} v_0^{A}\big|_{\mathsf{W}_{N_A,0}} , \tag{3.49b}$$

$$Z_c^{B} = 2^{MN_B} v_2^{B} \cdot (\boldsymbol{T}^{B})^{2M} v_2^{B}\big|_{\mathsf{W}_{N_B,2}} , \tag{3.49c}$$

where the boundary states are

$v_0 =$ 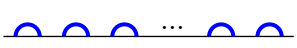 , $\quad v_2 =$ 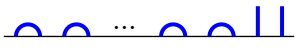 . (3.50)

There appears to be a difference between v_2 in (3.50) and v_d for $d = 2$ in (2.19), namely the pair of defects is not located on the same position. However, since we consider systems with periodic boundary conditions, the position of the pair of defect in v_2 is irrelevant and does not affect our final results. The superscripts AB, A and B for $\boldsymbol{T}$ in (3.49) serve as a reminder that the corresponding objects are elements of the enlarged periodic Temperley-Lieb algebra with N, N_A and N_B nodes, respectively. We have also indicated by subscripts on the right side which action is used. Finally, we note that the powers of 2 ensure that each tile has a weight 1 instead of $\frac{1}{\sqrt{2}}$ as it does in (3.36) for $u = \frac{\pi}{4}$.

Gram products on the periodic pants geometry. We define a new Gram product, denoted $(w_1 \times w_2) \cdot w_3$, that is needed to compute Z_p^{AB}. In this product, the states w_1, w_2 and w_3 belong to $\mathsf{W}_{N_A,0}$, $\widehat{\mathsf{W}}_{N_B,0}$ and $\mathsf{W}_{N,0}$ respectively, with $N = N_A + N_B$. The result of this product is obtained as follows. One flips w_1 and w_2 vertically, draws them on the legs A and B of the periodic pants lattice, and connects the nodes to those of w_3 drawn on the top part of the pants lattice. Then $(w_1 \times w_2) \cdot w_3$ equals $\alpha^{n_A + n_{AB}} \delta_{n_\beta,0} \delta_{n_B,0}$, where n_β counts the number of contractible loops, and the numbers n_A, n_B and n_{AB} count the non-contractible loops in the three families, as explained in the beginning of Section 3.3. Here are two examples to illustrate this definition:

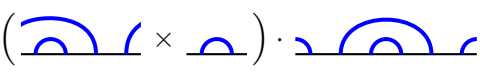 $= \alpha^2$, (3.51a)

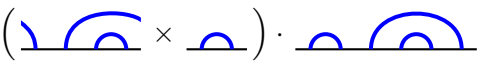 $= 0$. (3.51b)

In terms of this Gram product, the partition function Z_p^{AB} reads

$$Z_p^{AB} = 2^{MN}\Big((\boldsymbol{T}^A)^M v_0^A \times (\boldsymbol{T}^B)^M v_0^B\Big) \cdot (\boldsymbol{T}^{AB})^M v_0^{AB}. \tag{3.52}$$

In this expression, the transfer tangles $\boldsymbol{T}^A$ and $\boldsymbol{T}^{AB}$ act on the boundary states v_0^A and v_0^{AB} under the standard actions of $\mathsf{W}_{N_A,0}$ and $\mathsf{W}_{N,0}$ respectively (where α is a free parameter). In contrast, $(\boldsymbol{T}^B)^M$ acts on v_0^B under the module action of $\widehat{\mathsf{W}}_{N_B,0}$ (where $\alpha = 0$).

We note that one can define more generally a Gram product on the periodic pants geometry where the result of the product is $\alpha_1^{n_A}\alpha_2^{n_B}\alpha_3^{n_{AB}}\delta_{n_\beta,0}$ and thus depends on three free parameters, one for each family of non-contractible loops. Our choice to set $\alpha_2 = 0$ and $\alpha_1 = \alpha_3 = \alpha$ however allows for an important simplification. Indeed, in this case, the connectivity of link states in leg B can be described using the module $\widehat{\mathsf{W}}_{N_B,0}$, and the Gram products on the periodic pants geometry can be computed using the Gram product on the cylinder, for $\mathsf{W}_{N,0}$. Our construction above achieves this by using the natural embedding from $\mathsf{W}_{N_A,0} \times \widehat{\mathsf{W}}_{N_B,0}$ into $\mathsf{W}_{N,0}$, where the two link states w_1 and w_2 are simply drawn side by side, and the loop segments of w_1 that travel via the back of the cylinder (if any) are extended to travel via the back of the larger cylinder. For instance,

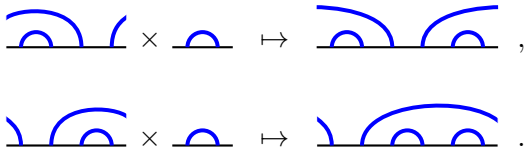

(3.53)

The same embedding in $\mathsf{W}_{N,0}$ does not naturally extended to $\mathsf{W}_{N_A,0} \times \mathsf{W}_{N_B,0}$. For example, we cannot embed  in $\mathsf{W}_{N,0}$ in the same way as in (3.53).

Thus, for the case $\alpha_2 = 0$, any Gram product on the periodic pants geometry can be computed using the same product on the cylinder. In the spin-chain language, the resulting embedding translates simply to

$$|w_1 \times w_2\rangle = |w_1\rangle \otimes |w_2\rangle. \tag{3.54}$$

Overlaps in the XX chain. At the end of Section 3.3.1, we defined a map $w \mapsto |w\rangle$ that intertwines the link state and spin-chain representations of $\mathcal{E}\mathsf{PTL}_N(\alpha, 0)$. For each link state w, we define the dual state

$\langle\!\langle w|$ as

$$\langle\!\langle w| = |w\rangle^{\mathrm{t}}\Big|_{\phi\to-\phi} \tag{3.55}$$

where the superscript $^{\mathrm{t}}$ stands for real transposition. Let us note that in the absence of a twist ($\phi = 0$), the definition of the dual state reduces to $\langle\!\langle w| = |w\rangle^{\mathrm{t}}$. The relation (3.55) is thus a generalisation compatible with the notion of dual state that we used in Chapter 2 for the model of critical dense polymers on the flat pants lattice. The Gram product between two link states w_1 and w_2 can then be computed from the spin-chain representation [158]:

$$w_1 \cdot w_2 = \langle\!\langle w_1|w_2\rangle. \tag{3.56}$$

In the spin-chain language, the partition functions read

$$Z_c^{AB} = 2^{MN}\langle\!\langle v_0^{AB}|(T^{AB})^{2M}|v_0^{AB}\rangle, \tag{3.57a}$$

$$Z_c^{A} = 2^{MN_A}\langle\!\langle v_0^{A}|(T^{A})^{2M}|v_0^{A}\rangle, \tag{3.57b}$$

$$Z_c^{B} = 2^{MN_B}\langle\!\langle v_2^{B}|(T^{B})^{2M}|v_2^{B}\rangle, \tag{3.57c}$$

$$Z_p^{AB} = 2^{MN}\langle\!\langle v_0^{A}\otimes v_0^{B}|\big((T^{A})^{M}\otimes(\widehat{T}^{B})^{M}\big)(T^{AB})^{M}|v_0^{AB}\rangle. \tag{3.57d}$$

Here, T^{AB} and T^{A} are the transfer matrices of the six-vertex model with a twist ϕ for system sizes N and N_A respectively, whereas T^B and $\widehat{T}^B$ are the transfer matrices for the system size N_B with the twists $\phi = 0$ and $\phi = \pi$, respectively.

3.3.3 Bipartite fidelity

In this section, we use the known diagonalisation of H_p to derive a closed-form expression for $\mathcal{F}_p^{CDP}$.

Diagonalisation of the Hamiltonian. The diagonalisation of H_p is given in Section 3.2.1. We recall that for $\phi \in (-\pi, \pi)$, the groundstate of H_p is unique, belongs to the magnetisation sector $S^z = 0$ and is

$$|X_0\rangle = \begin{cases} \mu^\dagger_{(4-N)/4}\cdots\mu^\dagger_{N/4}|0\rangle & \frac{N}{2} \text{ even}, \\ \mu^\dagger_{(2-N)/4}\cdots\mu^\dagger_{(N-2)/4}|0\rangle & \frac{N}{2} \text{ odd}. \end{cases} \tag{3.58}$$

Likewise, in the sector $S^z = -1$, the lowest-energy state of H_p for $\phi = 0$ is unique and given by

$$|X_{-1}\rangle = \begin{cases} \mu^\dagger_{(4-N)/4} \cdots \mu^\dagger_{(N-4)/4}|0\rangle\big|_{\phi=0} & \frac{N}{2} \text{ even}, \\ \mu^\dagger_{(6-N)/4} \cdots \mu^\dagger_{(N-2)/4}|0\rangle\big|_{\phi=0} & \frac{N}{2} \text{ odd}. \end{cases} \tag{3.59}$$

The transfer matrix and Hamiltonian commute, and we have

$$T|X_0\rangle = \Gamma_0|X_0\rangle, \qquad (T|_{\phi=0})|X_{-1}\rangle = \Gamma_{-1}|X_{-1}\rangle. \tag{3.60}$$

The eigenvalues are [157, 159]

$$\Gamma_0 = \frac{\cos(\frac{\phi}{2})}{2^{N-1}} \prod_{j=1}^{N/2} (1 + \tan x_j) \prod_{j=(N+2)/2}^{N} (1 - \tan x_j) \tag{3.61a}$$

with $x_j = \frac{\pi(j-\frac{1}{2})-\frac{\phi}{2}}{N}$, and

$$\Gamma_{-1} = \frac{N}{2^{N-1}} \prod_{j=1}^{(N-2)/2} \big(1 + \tan(\tfrac{\pi j}{N})\big)^2. \tag{3.61b}$$

These are the largest eigenvalues in the sectors $S^z = 0$ and $S^z = -1$, respectively. We note in particular that $\Gamma_{-1} = \lim_{\phi\to\pi} \Gamma_0$.

In the representations $\mathsf{W}_{N,0}$ and $\mathsf{W}_{N,2}$, the transfer tangle $\boldsymbol{T}$ has the right-eigenstates X_0 and X_{-1} with respective eigenvalues Γ_0 and Γ_{-1}, and $|X_0\rangle$ and $|X_{-1}\rangle$ are their images under the homomorphism map. Their duals $\langle\langle X_0|$ and $\langle\langle X_{-1}|$ are obtained from the definition (3.55). Because

$$\mu^{\mathrm{t}}_k\big|_{\phi\to-\phi} = \begin{cases} \mu^\dagger_{-k} & \frac{N}{2} + S^z \text{ odd}, \\ \mu^\dagger_{1-k} & \frac{N}{2} + S^z \text{ even}, \end{cases} \tag{3.62}$$

we have

$$\langle\langle X_0| = (-1)^{N(N-2)/8}\langle X_0|, \quad \langle\langle X_{-1}| = (-1)^{(N-2)(N-4)/8}\langle X_{-1}|, \tag{3.63}$$

where $\langle X_0| = |X_0\rangle^\dagger$ and $\langle X_{-1}| = |X_{-1}\rangle^\dagger$. The state $\langle X_0|$ is given in (3.17) and is the left-groundstate of H_p in the sector $S^z = 0$. Likewise, $\langle X_{-1}|$ is the left-groundstate in the sector $S^z = -1$. Because of the fermionic relations (3.15), the groundstates have unit norms, and therefore we have

$$\langle\langle X_0|X_0\rangle = (-1)^{N(N-2)/8}, \qquad \langle\langle X_{-1}|X_{-1}\rangle = (-1)^{(N-2)(N-4)/8}. \tag{3.64}$$

Ratios of overlaps. We now adapt the calculations of Section 2.2.1 and extract the leading behaviour of the partition functions (3.49) and (3.52) as M tends to infinity. We start with Z_p^{AB} and assign the extra labels AB, A and B to the groundstates over $(\mathbb{C}^2)^{\otimes N}$, $(\mathbb{C}^2)^{\otimes N_A}$ and $(\mathbb{C}^2)^{\otimes N_B}$, respectively. From (3.64), we deduce that the identity matrix over $(\mathbb{C}^2)^{\otimes N}$ in the sector of zero magnetisation has a contribution along the groundstate of the form

$$\mathbb{I}\big|_{S^z=0} = (-1)^{N(N-2)/8}|X_0^{AB}\rangle\langle\langle X_0^{AB}| + \dots \tag{3.65}$$

where the next terms involve states that are not groundstates. Likewise, for $(\mathbb{C}^2)^{\otimes N_A}$ and $(\mathbb{C}^2)^{\otimes N_B}$, we have

$$\mathbb{I}\big|_{S^z=0} = (-1)^{N_A(N_A-2)/8}|X_0^{A}\rangle\langle\langle X_0^{A}| + \dots\ , \tag{3.66a}$$

$$\mathbb{I}\big|_{S^z=0} = (-1)^{N_B(N_B-2)/8}|X_0^{B}\rangle\langle\langle X_0^{B}| + \dots\ . \tag{3.66b}$$

We then have

$$(T^{AB})^M|v_0^{AB}\rangle \simeq (-1)^{N(N-2)/8}(\Gamma_0^{AB})^M|X_0^{AB}\rangle\langle\langle X_0^{AB}|v_0^{AB}\rangle, \tag{3.67a}$$

$$\langle\langle v_0^{A}|(T^{A})^M \simeq (-1)^{N_A(N_A-2)/8}(\Gamma_0^{A})^M\langle\langle v_0^{A}|X_0^{A}\rangle\langle\langle X_0^{A}|\,, \tag{3.67b}$$

$$\langle\langle v_0^{B}|(\widehat{T}^{B})^M \simeq (-1)^{N_B(N_B-2)/8}(\Gamma_0^{B})^M\langle\langle v_0^{B}|X_0^{B}\rangle\langle\langle X_0^{B}|, \tag{3.67c}$$

where Γ_0^{AB}, Γ_0^{A} and Γ_0^{B} are the eigenvalues of T^{AB}, T^{A} and $\widehat{T}^{B}$ in the zero magnetization sector. The symbol $\simeq$ indicates that the smaller contributions coming from excited states have been omitted. We thus find

$$\begin{aligned} Z_p^{AB} \simeq \epsilon\, 2^{MN}(\Gamma_0^{AB}\Gamma_0^{A}\Gamma_0^{B})^M\langle\langle v_0^{A}|X_0^{A}\rangle\langle\langle v_0^{B}|X_0^{B}\rangle \\ \times\langle\langle X_0^{A}\otimes X_0^{B}|X_0^{AB}\rangle\langle\langle X_0^{AB}|v_0^{AB}\rangle, \end{aligned} \tag{3.68}$$

where ϵ is a sign that will be irrelevant for our computation of $\mathcal{F}_p^{CDP}$. We repeat the same argument for the other partition functions and find

$$Z_c^{AB} \simeq 2^{MN}(\Gamma_0^{AB})^{2M}\langle\langle v_0^{AB}|X_0^{AB}\rangle\langle\langle X_0^{AB}|X_0^{AB}\rangle\langle\langle X_0^{AB}|v_0^{AB}\rangle, \tag{3.69a}$$

$$Z_c^{A} \simeq 2^{MN_A}(\Gamma_0^{A})^{2M}\langle\langle v_0^{A}|X_0^{A}\rangle\langle\langle X_0^{A}|X_0^{A}\rangle\langle\langle X_0^{A}|v_0^{A}\rangle, \tag{3.69b}$$

$$Z_c^{B} \simeq 2^{MN_B}(\Gamma_{-1}^{B})^{2M}\langle\langle v_2^{B}|X_{-1}^{B}\rangle\langle\langle X_{-1}^{B}|X_{-1}^{B}\rangle\langle\langle X_{-1}^{B}|v_2^{B}\rangle, \tag{3.69c}$$

where Γ^B_{-1} is the groundstate eigenvalue of T^B in the sector $S^z = -1$. Using (3.64) and $\Gamma^B_0 = \Gamma^B_{-1}$, we find

$$\mathcal{F}_p^{CDP} = -\log\Bigg(\sigma\,\langle\!\langle X_0^A \otimes X_0^B | X_0^{AB}\rangle\!\rangle^2 \times \frac{\langle\!\langle X_0^{AB}|v_0^{AB}\rangle\!\rangle}{\langle\!\langle v_0^{AB}|X_0^{AB}\rangle\!\rangle}\frac{\langle\!\langle v_0^A|X_0^A\rangle\!\rangle}{\langle\!\langle X_0^A|v_0^A\rangle\!\rangle}\frac{\langle\!\langle v_0^B|X_0^B\rangle\!\rangle^2}{\langle\!\langle v_2^B|X_{-1}^B\rangle\!\rangle\langle\!\langle X_{-1}^B|v_2^B\rangle\!\rangle}\Bigg) \tag{3.70a}$$

with

$$\sigma = (-1)^{\frac{N(N-2)}{8}}(-1)^{\frac{N_A(N_A-2)}{8}}(-1)^{\frac{(N_B-2)(N_B-4)}{8}}. \tag{3.70b}$$

Product expressions for the overlaps involving boundary states. We use Wick's theorem to evaluate the various overlaps in (3.70a). To start, we express the boundary states $\langle\!\langle v_0|$ and $\langle\!\langle v_2|$ in terms of the fermionic operators a_j defined in (2.35) as

$$\begin{aligned}\langle\!\langle v_0| &= \langle 0|a_{N-1}a_{N-3}\cdots a_5 a_3 a_1,\\ \langle\!\langle v_2| &= \langle 0|a_{N-3}a_{N-5}\cdots a_5 a_3 a_1.\end{aligned} \tag{3.71}$$

With the anticommutation relation

$$\{a_{2\ell-1}, \mu_k^\dagger\} = \frac{\mathrm{e}^{-2\mathrm{i}\ell\theta_k}}{\sqrt{N}}\big(\omega\,\mathrm{e}^{\mathrm{i}\theta_k} + \omega^{-1}\big) \tag{3.72}$$

and Wick's theorem, we write the overlaps $\langle\!\langle X_0|v_0\rangle\!\rangle$ and $\langle\!\langle X_{-1}|v_2\rangle\!\rangle$ as

$$\begin{aligned}\langle\!\langle v_0|X_0\rangle\!\rangle &= \det_{\substack{k\in K_0\\ \ell=1,\ldots,N/2}}\{a_{2\ell-1},\mu_k^\dagger\},\\ \langle\!\langle v_2|X_{-1}\rangle\!\rangle &= \det_{\substack{k\in K_{-1}\\ \ell=1,\ldots,(N-2)/2}}\{a_{2\ell-1},\mu_k^\dagger\}\big|_{\phi=0},\end{aligned} \tag{3.73}$$

where

$$\begin{aligned}K_0 &= \begin{cases}\{\frac{4-N}{4},\cdots,\frac{N}{4}\} & \frac{N}{2}\text{ even},\\ \{\frac{2-N}{4},\cdots,\frac{N-2}{4}\} & \frac{N}{2}\text{ odd},\end{cases}\\ K_{-1} &= \begin{cases}\{\frac{4-N}{4},\cdots,\frac{N-4}{4}\} & \frac{N}{2}\text{ even},\\ \{\frac{6-N}{4},\cdots,\frac{N-2}{4}\} & \frac{N}{2}\text{ odd}.\end{cases}\end{aligned} \tag{3.74}$$

We factorise the terms that only depend on k in (3.72), and evaluate the remaining determinants in terms of a product using the Vandermonde identity. We simplify the result with the identities

$$\prod_{j=1}^{N/2} \sin\left(\tfrac{\pi j}{N}\right) = \frac{N^{1/2}}{2^{(N-1)/2}}, \qquad \prod_{j=1}^{N/2}\prod_{k=j+1}^{N/2} \sin\left(\tfrac{2\pi(k-j)}{N}\right) = \frac{N^{N/4}}{2^{N^2/8}}, \tag{3.75}$$

and find

$$\langle\!\langle v_0|X_0\rangle = 2^{N/4}\mathrm{e}^{\mathrm{i}\phi(N+1)/4}\mathrm{e}^{-\mathrm{i}\pi N(N-2)/16}\prod_{j=1}^{N/2}\sin\left(\tfrac{(2j-1)\pi+\phi}{2N}\right), \tag{3.76a}$$

$$\langle\!\langle v_0|X_0\rangle\big|_{\phi=\pi} = \frac{N^{1/2}}{2^{(N-2)/4}}\mathrm{e}^{-\mathrm{i}\pi(N^2-6N-4)/16}, \tag{3.76b}$$

$$\langle\!\langle v_2|X_{-1}\rangle = \frac{\mathrm{e}^{-\mathrm{i}\pi(N-2)(N-4)/16}}{2^{(N-2)/4}}. \tag{3.76c}$$

It also follows from the definition (3.55) of dual states that

$$\langle\!\langle X_0|v_0\rangle = \langle\!\langle v_0|X_0\rangle\big|_{\phi\to-\phi}, \qquad \langle\!\langle X_{-1}|v_2\rangle = \langle\!\langle v_2|X_{-1}\rangle. \tag{3.77}$$

Putting these results together, we obtain

$$\frac{\langle\!\langle X_0^{AB}|v_0^{AB}\rangle}{\langle\!\langle v_0^{AB}|X_0^{AB}\rangle} = \mathrm{e}^{-\mathrm{i}\phi(N+1)/2}\prod_{j=1}^{N/2}\frac{\sin\left(\frac{(2j-1)\pi-\phi}{2N}\right)}{\sin\left(\frac{(2j-1)\pi+\phi}{2N}\right)}, \tag{3.78a}$$

$$\frac{\langle\!\langle v_0^{A}|X_0^{A}\rangle}{\langle\!\langle X_0^{A}|v_0^{A}\rangle} = \mathrm{e}^{\mathrm{i}\phi(N_A+1)/2}\prod_{j=1}^{N_A/2}\frac{\sin\left(\frac{(2j-1)\pi+\phi}{2N_A}\right)}{\sin\left(\frac{(2j-1)\pi-\phi}{2N_A}\right)}, \tag{3.78b}$$

$$\frac{\langle\!\langle v_0^{B}|X_0^{B}\rangle^2}{\langle\!\langle v_2^{B}|X_{-1}^{B}\rangle\langle\!\langle X_{-1}^{B}|v_2^{B}\rangle} = -\mathrm{i}N_B. \tag{3.78c}$$

Exact expression for the bipartite fidelity. It remains to compute the overlap $\langle\!\langle X_0^A \otimes X_0^B|X_0^{AB}\rangle$. Up to unimportant signs that come from (3.64), the overlap is exactly the one that we consider in (3.19), with the specialisations $\phi_A = \phi$ and $\phi_B = \pi$. We note that these specialisations are compatible with (3.22) for $\ell = 0$, for which we were able to obtain closed-form formula (3.28). From (3.70a) and (3.78) we find

$$\mathcal{F}_p^{CDP} = \mathcal{F}_p^{XX}\big|_{\substack{\phi_A=\phi\\ \phi_B=\pi}} - Q(N,\phi) + Q(Nx,\phi) - \log\big(N(1-x)\big) \tag{3.79}$$

where

$$Q(N,\phi)=\sum_{j=1}^{N/2}\log\left|\frac{\sin\left(\frac{(2j-1)\pi-\phi}{2N}\right)}{\sin\left(\frac{(2j-1)\pi+\phi}{2N}\right)}\right|. \tag{3.80}$$

The closed-form expression for $\mathcal{F}_p^{XX}\big|_{\substack{\phi_A=\phi\\ \phi_B=\pi}}$ is read from (3.28).

3.4 Asymptotic results

In this section, we study the large-N asymptotics of the bipartite fidelity for the XX chain and the model of critical dense polymers on the periodic pants lattice, and compare the results with the CFT predictions of Section 3.1.

3.4.1 XX spin chain

Exact results for $\mathcal{F}_p^{XX}$ with $\phi=\phi_A+\phi_B-\pi$. The calculation of the first terms in the large-N asymptotics of (3.28) is a long yet straightforward calculation. The details are similar to the asymptotic calculations presented in Section 2.4. We find

$$\begin{aligned}\mathcal{F}_p^{XX}\big|_{\phi=\phi_A+\phi_B-\pi}&=\frac{1}{2}\log N\\ &-\frac{\pi^2(-1-x+2x^2)-6\pi x\Big((-1+x)\phi_A+x\phi_B\Big)}{6\pi^2 x}\log(1-x)\\ &+\frac{\pi^2(3x-2x^2)+6\pi(-1+x)\Big((-1+x)\phi_A+x\phi_B\Big)}{6\pi^2(1-x)}\log x\\ &-\frac{\Big((-1+x)\phi_A+x\phi_B\Big)^2}{2\pi^2(1-x)}\log x-\frac{\Big((-1+x)\phi_A+x\phi_B\Big)^2}{2\pi^2 x}\log(1-x)\\ &-\frac{1}{2}-\frac{1}{2}\log\pi+6\log A+\mathcal{O}\big(N^{-1}\big)\end{aligned} \tag{3.81}$$

where $A=1.282427...$ is the Glaisher-Kinkelin constant. As expected, $\mathcal{F}_p^{XX}$ is symmetric under the simultaneous transformations $x\to 1-x$ and $\phi_A\leftrightarrow\phi_B$. This result is identical to the CFT prediction (3.1) for case (ii) where $g_p^{(0)}$ and $g_p^{(1)}(x)$ are given in (3.3) and (3.8) with the

central charge $c = 1$, the charges

$$q_1 = \frac{\phi_A}{2\pi}, \quad q_2 = -\frac{1}{2}, \quad q_3 = \frac{\phi_B}{2\pi}, \quad q_4 = -\frac{\phi_A + \phi_B - \pi}{2\pi}, \tag{3.82}$$

and the non-universal constant

$$C'_p = -\frac{1}{2} - \frac{1}{2}\log\pi + 6\log A = 0.420162... \ . \tag{3.83}$$

The result (3.81) holds for arbitrary values of the twist angles ϕ_A and ϕ_B. However, as we discussed at the end of Section 3.2.1, $\mathcal{F}_p^{XX}$ corresponds to an overlap of groundstates when ϕ_A and ϕ_B are in the interval $(-\pi, \pi)$ and are such that $\phi = \phi_A + \phi_B - \pi \in (-\pi, \pi)$ too. Finally, we remark that there is no term proportional to $N^{-1}\log N$ in (3.81). Comparing with (3.9), we observe that the content of the large parenthesis in this equation does not vanish in general. We therefore deduce that the extrapolation length Ξ vanishes in this case.

Numerical results for $\mathcal{F}_p^{XX}(n)$. We now study the large-N behaviour of the bipartite fidelities in the case where the three twists angles ϕ, ϕ_A and ϕ_B are arbitrary. We consider the standard bipartite fidelity (3.12) as well as the modified instances $\mathcal{F}_p^{XX}(n)$ defined in (3.29). Since we do not have an exact product formula, we instead use the determinant expression (3.19), and very similar formulas for the modified instances, to study the large-N behaviour of these quantities numerically. To get precise numerical estimates, we follow the strategy of [62] and fit $\mathcal{F}_p^{XX}(n)$ as

$$\begin{aligned}\mathcal{F}_p^{XX}(n) = g_p^{(0)}\log N + g_p^{(1)}(x) + g_p^{(2)}(x)N^{-1}\log N + \gamma_3\frac{1}{N} \\ + \gamma_4\frac{\log N}{N^2} + \gamma_5\frac{1}{N^2} + \gamma_6\frac{\log N}{N^3} + \gamma_7\frac{1}{N^3}.\end{aligned} \tag{3.84}$$

In the following, we consider that a fitted value g^{fit} matches a theoretical prediction g^{th} if the error is smaller than $10^{-5}\%$:

$$\left|\frac{g^{\text{th}} - g^{\text{fit}}}{g^{\text{th}}}\right| < 10^{-5}. \tag{3.85}$$

From our numerical explorations, we find that the leading terms in the asymptotic expansion (3.84) match the CFT prediction of Section 3.1, which in this case reads

$$\mathcal{F}_p^{XX}(n) = \left(\frac{1}{4} + \frac{1}{4}\Big(\frac{\phi - \phi_A - \phi_B}{\pi}\Big)^2\right) \log N + g_p^{(1)}(x) + g_p^{(2)}(x) N^{-1} \log N + \mathcal{O}\big(N^{-1}\big), \quad (3.86)$$

where $g_p^{(1)}(x)$ is given by the formula (3.8) for vertex operators, with $c = 1$ and

$$q_1 = \frac{\phi_A}{2\pi}, \quad q_2 = \frac{\phi - \phi_A - \phi_B}{2\pi}, \quad q_3 = \frac{\phi_B}{2\pi}, \quad q_4 = -\frac{\phi}{2\pi}. \quad (3.87)$$

The constant C_p' is unknown and obtained from a fit in our analysis.

Likewise, $g_p^{(2)}(x)$ is given by (3.9) with the conformal weights $\Delta_i = q_i^2/2$, the charges q_i in (3.87), and the extrapolation length

$$\Xi = -n. \quad (3.88)$$

In particular, we have $\Xi = 0$ for the standard bipartite fidelity. This result supports the interpretation proposed in the previous chapter, namely that the extrapolation length is related to the effective length of the system. In this case, this effective length is modified by the insertion of a spin state on the crotch point.

In Figure 3.5, we plot (3.86) and compare it with numerical values obtained from the determinant formula (3.19), as a function of x and N. The analogous plots for $\mathcal{F}_p^{XX}(n)$ with $n = 2, 4, 6$ are very similar, and the match is again convincing in the sense of (3.85). Finally, in Figure 3.6 we plot the CFT prediction for function the $g_p^{(2)}(x)$ with $n = 2, 4$, and compare it with our fitted values. The function $g_p^{(2)}(x)$ depends on the spin state inserted at the crotch point only via the extrapolation length (3.88). The match between our numerical results and the CFT prediction is again convincing.

Conformal interpretation. Let us now discuss how our results fit with previously known results about the conformal interpretation of the XX chain. It is well-known that the XX chain (and more generally the XXZ chain) is described by a CFT with central charge $c = 1$ [96]. In this context, the presence of a twist line ϕ between two points z_1 and z_2 is accounted for by the insertion of two fields $\varphi(z_1)$ and $\varphi(z_2)$. The field φ is a so-called *electric operator* [160]. Its multi-point functions

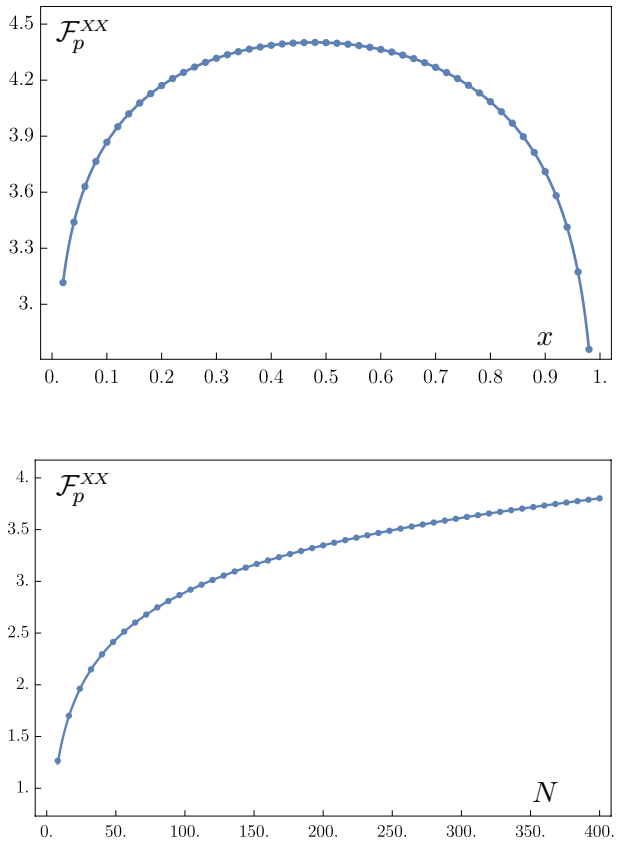

Figure 3.5: The bipartite fidelity $\mathcal{F}_p^{XX}$ as a function of x for $N = 800$ (top panel), and N for $x = \frac{1}{4}$ (bottom panel). The symbols are the numerical data obtained from the evaluation of the determinant expression (3.19), and the solid lines are (3.86) with (3.87), $\Xi = 0$ and $C_p' = 0.447447$. In all panels, the twist angles are $\phi = 1$, $\phi_A = 2$ and $\phi_B = 3$.

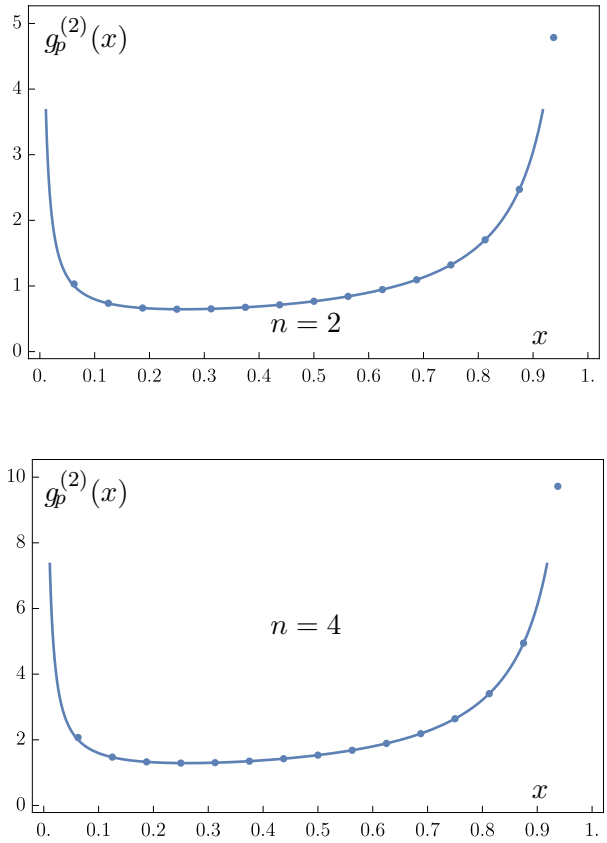

Figure 3.6: The function $g_p^{(2)}(x)$ for the XX spin chain with $\phi = 1$, $\phi_A = 2$ and $\phi_B = 3$ for $n = 2$ and $n = 4$. The symbols are obtained from the numerical evaluation of determinants similar to (3.19). The solid lines correspond to the CFT prediction (3.9) with the conformal data (3.87) and Ξ given in (3.88).

are known to have the form (3.4), and our analysis in this subsection confirms this. It is also a spinless field. Its conformal weight $\Delta_\phi^{XX} = \bar{\Delta}_\phi^{XX}$ can be computed from the $1/N$ finite-size correction term of the largest eigenvalue of the periodic transfer matrix T with a diagonal twist. Indeed, this finite-size correction can be obtained either via the Bethe ansatz [161] or with the method of functional relations [162], and it allows one to compute the difference $c - 24\Delta$ explicitly:

$$c - 24\Delta = 1 - \frac{3\phi^2}{\pi^2}. \tag{3.89}$$

With $c = 1$, the resulting conformal weight is

$$\Delta_\phi^{XX} = \frac{\phi^2}{8\pi^2}. \tag{3.90}$$

This conformal weight is consistent with the known values $q = \bar{q} = \frac{\phi}{2\pi}$ for the charges of electric operators, and the values $\Delta_i = q_i^2/2$ obtained in (3.82) and (3.87). Comparing (3.3) and (3.86), we see that (3.90) also produces the correct value for $g_p^{(0)}$. We note that the field inserted on the crotch point is special, as it lies at the intersection of three twist lines. Accordingly, its conformal weight is obtained from (3.90) with ϕ replaced by the difference $\phi - \phi_A - \phi_B$ of the twists at this intersection. The insertion of a Néel state of size n on the crotch point does not modify this conformal weight.

3.4.2 Critical dense polymers

The large-N expansion for $\mathcal{F}_p^{CDP}$ follows directly from the expansion (3.81) for $\mathcal{F}_p^{XX}$ at the special point $\phi = \phi_A$ and $\phi_B = \pi$, and the large-N expansion of the function $Q(N, \phi)$ defined in (3.80). This asymptotic calculation is straightforward and yields

$$Q(N,\phi) = -\frac{\phi}{\pi}\log\frac{N}{\pi} + \log\frac{\Gamma\left(\frac{1}{2}+\frac{\phi}{2\pi}\right)}{\Gamma\left(\frac{1}{2}-\frac{\phi}{2\pi}\right)} + \mathcal{O}\left(N^{-1}\right). \tag{3.91}$$

We insert these results in (3.79) and find

$$\mathcal{F}_p^{CDP} = -\frac{1}{2}\log N - \frac{1}{6}(G_p(x) + G_p(1-x))$$

$$-\frac{1}{2}\Big(\frac{\phi^2}{\pi^2}-1\Big)\Big((1-x)\log x+\frac{(1-x)^2}{x}\log(1-x)\Big)$$
$$-\frac{1}{2}-\frac{1}{2}\log\pi+6\log A+\mathcal{O}\big(N^{-1}\big) \quad (3.92)$$

where $G_p(x)$ is defined in (3.6). This large-N expansion exactly corresponds to the CFT prediction for case (i) with

$$c=-2, \qquad \Delta_1=\Delta_4=\frac{1}{8}\Big(\frac{\phi^2}{\pi^2}-1\Big), \qquad \Delta_3=0, \quad (3.93)$$

and the non-universal constants are

$$C_p=-\frac{1}{2}-\frac{1}{2}\log\pi+6\log A, \qquad \Xi=0. \quad (3.94)$$

Our results fit with the conformal interpretation of the model of critical dense polymers. The central charge of the model is known to be $c=-2$ [103, 157]. In this context, for the model defined on an infinite cylinder, assigning a fugacity $\alpha\neq\beta$ to the non-contractible loops amounts to inserting two copies of a conformal field $\rho(z)$ at the top and bottom of the cylinder. The properties of this field were investigated in detail in [107]. The conformal weights Δ_ϕ^{CDP} and $\bar{\Delta}_\phi^{CDP}$ of $\rho(z)$ are equal and can be obtained from the $1/N$ finite-size correction term for the groundstate eigenvalue of the periodic transfer matrix. The spectrum of the transfer matrix for the six-vertex model and for the model of critical dense polymers are identical for $\alpha=2\cos(\frac{\phi}{2})$. As a result, the difference $c-24\Delta$ for critical dense polymers is also given by (3.89). Setting $c=-2$ and solving for the conformal weight yields

$$\Delta_\phi^{CDP}=\frac{1}{8}\Big(\frac{\phi^2}{\pi^2}-1\Big). \quad (3.95)$$

We obtained this value for the conformal weights of Δ_1 and Δ_4 in (3.93). It is also the value previously known from Coulomb gas calculations [163].

3.5 Summary of the main results

In this chapter, we investigated the bipartite fidelity on the periodic pants geometry. In the context of CFT, this quantity is related to the

four-point function of bulk fields inserted on the periodic pants domain. We adapted CFT arguments initially developed by Dubail and Stéphan and obtained predictions for the leading terms in the large-N expansions of $\mathcal{F}_p$ up to order $N^{-1}\log N$ in two distinct cases. In the first case, no field is inserted on the crotch point, and the three bulk fields inserted in both legs and at infinity are spinless primary fields. In the second case, the four fields are vertex operators. We compared these predictions with exact and numerical lattice calculations and found a precise match for two lattice models: the XX spin chain and the model of critical dense polymers. These models are known to be described by CFTs with central charges $c = 1$ and $c = -2$, respectively.

In the XX spin chain, we defined the quantity $\mathcal{F}_p^{XX}(n)$. It is related to the overlap between the groundstate of the whole system with the product of the groundstates of the subsystems A and B where each system is endowed with periodic boundary conditions and a Néel state of length n is inserted on the crotch point. The logarithmic bipartite fidelity $\mathcal{F}_p^{XX}(n)$ also depends on the twist angles ϕ, ϕ_A and ϕ_B. We found a closed-form expression for the bipartite fidelity when $n = 0$ and the twist angles satisfy $\phi = \phi_A + \phi_B - \pi$. For arbitrary values of n and the twist angles, we expressed $\mathcal{F}_p^{XX}(n)$ as a determinant that we are unable to simplify but whose numerical evaluation is simple. Using both analytical and numerical results, we investigated the large-N behaviour of $\mathcal{F}_p^{XX}(n)$ with fixed aspect ratio. In the CFT, the presence of twist lines connecting certain points of the domain correspond to the insertions of electric operators whose n-point functions are given by the simple formula (3.4), and our analysis of $\mathcal{F}_p^{XX}(n)$ confirms this. The charges of the electric operator are $q = \bar{q} = \frac{\phi}{2\pi}$, and the conformal weights are $\Delta_\phi^{XX} = \bar{\Delta}_\phi^{XX} = \frac{q^2}{2}$. If a field marks a transition between two twist lines ϕ and ϕ_A, then its charge is $q = \frac{\phi-\phi_A}{2\pi}$. We also investigated the case of an intersection point between three twist lines of twists ϕ, ϕ_A and ϕ_B, and found that the corresponding charge is $q = \frac{\phi-\phi_A-\phi_B}{2\pi}$. Our numerical investigations of the term of order $N^{-1}\log N$ suggests that the extrapolation lengths depends linearly on the length n of the Néel state via the relation $\Xi = -n$.

Finally, we investigated the logarithmic bipartite fidelity $\mathcal{F}_p^{CDP}$ of the model of critical polymers on the periodic pants lattice. We fixed the

fugacity of non-contractible loops that wrap around the waist of the periodic pants lattice and those that wrap around leg A to $\alpha = 2\cos(\frac{\phi}{2})$. In the CFT description, this amounts to inserting a bulk operator with conformal weight $\Delta_\phi^{CDP} = \frac{1}{8}\big(\frac{\phi^2}{\pi^2} - 1\big)$. We also set the fugacities of non-contractible loops that wrap around leg B and contractible loops to $\alpha = \beta = 0$. We expressed $\mathcal{F}_p^{CDP}$ in closed form and investigated its asymptotic behaviour for large N and fixed aspect ratio. Our results are in perfect agreement with our CFT prediction for the first case, where no field is inserted on the crotch point and the other fields are primary. Similarly to what we observed on the flat pants lattice, we find that the extrapolation length vanishes.

4 Bipartite fidelity on the skirt geometry

In this chapter, we use the various tools and concepts that we introduced in Chapters 2 and 3 to investigate the logarithmic bipartite fidelity $\mathcal{F}_s$ on the skirt domain. Similarly to the previous chapter, we study $\mathcal{F}_s$ in the context of CFT, the XX spin chain and the model of critical dense polymers. We recall that for quantum spin chains, $\mathcal{F}_s$ is given by the definition (1.78) where the whole system has periodic boundary conditions and the subsystems have free boundary conditions, whereas $\mathcal{F}_s$ is defined in (1.79c) for two-dimensional lattice models. In Section 4.1, we give the CFT predictions for the leading terms in the large-N expansion of the logarithmic bipartite fidelity. In Sections 4.2 and 4.3, we compute $\mathcal{F}_s$ for the XX spin chain and for the model of critical dense polymers. Finally, we compare the asymptotic behaviour of the lattice results with the predictions of conformal field theory in Section 4.4. The results discussed in this chapter were initially presented in the publication [3].

4.1 Predictions of conformal field theory

This section gives the CFT predictions for the bipartite fidelity on the skirt domain. As in Section 3.1, the details of the calculations are given in the Appendix A of [3] and are not reproduced here. We consider the asymptotic behaviour of $\mathcal{F}_s$ in the limit where N and N_A are sent to infinity such that the aspect ratio $x = N_A/N$ converges to a constant

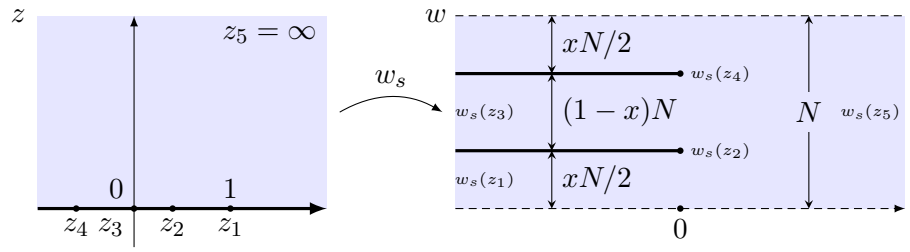

Figure 4.1: The function $w_s(z)$ maps the upper half-plane onto the skirt domain. The positions z_2 and z_4 that are the preimages of the slits' endpoints are $z_2 = (\sqrt{x-x^2}+x-1)/(2x-1)$ and $z_4 = (-\sqrt{x-x^2}+x-1)/(2x-1)$. The bold lines are the boundaries of the domains. On the right part of the figure, the dashed lines are identified.

in the interval $(0,1)$. The logarithmic bipartite fidelity has the large-N expansion

$$\mathcal{F}_s = g_s^{(0)} \log N + g_s^{(1)}(x) + g_s^{(2)}(x) N^{-1} \log N + \mathcal{O}(N^{-1}). \tag{4.1}$$

In the CFT framework, the skirt domain is described as an infinite horizontal strip of width N drawn in the complex plane. The boundary conditions are periodic along the strip's edges, so that two points with respective imaginary parts 0 and N with the same real parts are identified. The strip is decorated with two slits that divide the left half into two strips of width Nx and $N(1-x)$. In contrast with the periodic pants domain, the two slits are not identified, and the skirt domain really has two distinct slit endpoints. The map from the upper half-plane to the skirt domain is

$$w_s(z) = \frac{N}{2\pi}\big(x \log\left(-(z-1)^2\right) + (1-x)\log z^2 - \log(z^2+(z-1)^2)\big) + K_x, \tag{4.2}$$

where K_x is given in (3.2). This map is illustrated in Figure 4.1. It can be understood as the composition $w_s = w_p \circ v$ of the function $w_p(z)$ given in (3.2) and the function $v(z) = z^2/(2z^2-2z+1)$. The latter maps the upper half-plane into the complex plane with a cut along the segment $[0,1]$. Hence the boundary of the upper half-plane is mapped to the two slits of the skirt domain.

We consider the situation where five fields are inserted in the skirt domain. A field ϕ_1 is inserted at $-\infty$ in the leg A, a field ϕ_2 is inserted on the first slit's endpoint, a field ϕ_3 is inserted at $-\infty$ in the leg B, a field ϕ_4 is inserted on the second slit's endpoint, and a field ϕ_5 is inserted at $+\infty$. We denote by $w_s(z_i)$ their positions in the skirt domain, and by z_i the corresponding positions in the complex plane. The fields ϕ_i with $i = 1, 2, 3, 4$ are boundary fields that depend on a single variable and have the conformal weight Δ_i. In contrast, ϕ_5 is a bulk field that depends on two variables in the complex plane. For simplicity, we assume that ϕ_5 is spinless. It has the conformal weights $\Delta_5 = \bar{\Delta}_5$. We illustrate this setting and the fields insertion points in Figure 4.2.

The first function $g_s^{(0)}$ in the expansion (4.1) is obtained as a direct application of the Cardy-Peschel formula [135] for domains with corners. Indeed, the skirt domain has two corners of angles 2π. The resulting expression for $g_s^{(0)}$ depends on the dimensions of the field ϕ_2 and ϕ_4 and on the central charge:

$$g_s^{(0)} = \frac{c}{4} + \Delta_2 + \Delta_4. \tag{4.3}$$

The next-leading terms $g_s^{(1)}(x)$ and $g_s^{(2)}(x)$ depend non-trivially on the aspect ratio x. In a general setting where the five fields are primary fields, the function $g_s^{(1)}(x)$ also depends on the non-trivial functions of the cross-ratios that arise in the five-point function of these fields in the upper half-plane. Because ϕ_5 is a bulk field, from Cardy's method of images [93], we know that this correlator is in fact a six-point function in the full complex plane. Here we restrict our focus to the following special cases: (i) only one non-trivial primary field is present, namely the bulk field ϕ_5, and (ii) each of the fields ϕ_i is a vertex operator in a free-boson CFT with central charge $c = 1$. In this case, the fields ϕ_i with $i = 1, \ldots, 4$ are boundary fields with charges q_i and conformal weight $\Delta_i = q_i^2/2$. In contrast, the field ϕ_5 is a bulk field with the charges $q_5 = \bar{q}_5$ and conformal weights $\Delta_5 = \bar{\Delta}_5 = q_5^2/2$.

The results are as follows. For case (i), we have

$$\begin{aligned} g_s^{(1)}(x) = \frac{c}{24}(G_s(x) + G_s(1-x)) \\ + 4\Delta_5(x\log x + (1-x)\log(1-x) + 2\log 2) + C_s \end{aligned} \tag{4.4}$$

where we recall that

$$G_s(x) = \frac{3 - 6x + 4x^2}{1 - x} \log x \tag{4.5}$$

is given in (1.87), and C_s is a constant. For case (ii), we have

$$\begin{aligned} g_s^{(1)}(x) = \frac{c}{24}\left(G_s(x) + G_s(1-x)\right) - \frac{\Delta_1}{x}\log(1-x) - \frac{\Delta_3}{1-x}\log x \\ + 4\Delta_5\left(x\log x + (1-x)\log(1-x) + 2\log 2\right) \\ + (\Delta_2 + \Delta_4)\log(x - x^2) + C_s' \end{aligned} \tag{4.6}$$

where C_s' is a constant. As expected, the functions $g_s^{(0)}$ and $g_s^{(1)}(x)$ reduce to the prediction (1.86) obtained in [62] for the special case where all the conformal weights are zero.

To proceed, we compute the function $g_s^{(2)}(x)$ using the arguments of Stéphan and Dubail [63]. As we shall see in Section 4.4, a correct CFT interpretation of our lattice results requires a generalisation of their derivation to cases where each slit is assigned its own extrapolation length. We denote them by Ξ_2 and Ξ_4, and they correspond to the corners situated at $w_s(z_2)$ and $w_s(z_4)$, respectively. For case (i), we obtain

$$g_s^{(2)}(x) = (\Xi_2 + \Xi_4) \times \left(\frac{c\,(1-2x)^2}{48x(1-x)} + 2\Delta_5\right). \tag{4.7}$$

For the case (ii), the expression for $g_s^{(2)}(x)$ instead reads

$$\begin{aligned} g_s^{(2)}(x) = \Xi_2 \times \Big[\frac{c(1-2x)^2}{48(1-x)x} + \frac{q_2^2 - q_4^2}{16x(1-x)} \\ - \frac{q_1\,(q_1 - q_2 + q_4)}{4x} - \frac{q_3\,(q_3 - q_2 + q_4)}{4(1-x)} + q_5^2\Big] \\ + \{\Xi_2 \to \Xi_4, q_2 \leftrightarrow q_4\}. \end{aligned} \tag{4.8}$$

On the last line of (4.8), the contribution marked by a bracket indicates that the previous lines must be copied but with the substitutions indicated inside this bracket. We note that (4.8) greatly simplifies for $\Xi_2 = \Xi_4$, and becomes independent of the charges q_2 and q_4 of the fields inserted at the endpoints of the slits. The function $g_s^{(2)}(x)$ also simplifies for $q_2 = q_4$. In that case, it only depends on the sum $\Xi_2 + \Xi_4$, as in (4.7), and can be written in terms of the dimensions $\Delta_i = q_i^2/2$:

$$g_s^{(2)}(x)\big|_{q_2=q_4} = (\Xi_2 + \Xi_4) \times \left(\frac{c\,(1-2x)^2}{48x(1-x)} + 2\Delta_5 - \frac{\Delta_1}{2x} - \frac{\Delta_3}{2(1-x)}\right). \tag{4.9}$$

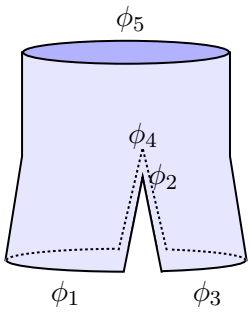

Figure 4.2: Illustration of the fields insertion points on the skirt domain. The top part has perimeter N, whereas the left and right bottom subsegments have respective lengths N_A and N_B.

4.2 Lattice calculation for the XX spin chain

The first model for which we compute the bipartite fidelity on the skirt lattice is the XX chain. In this case, the system AB is a periodic chain of length N. Its Hamiltonian H_p is given in (3.10) and depends on the twist angle ϕ. The subsystems A and B are instead chains of lengths N_A and N_B with free boundary conditions. Their Hamiltonian is H_f from (1.51) with N_A and N_B sites, respectively. We denote by $\langle x_0^A|$ and $\langle x_0^B|$ the left-groundstates of H_f with N_A and N_B sites in their zero-magnetisation sectors. As before, $N_A + N_B = N$ and all three lengths are even numbers. The logarithmic bipartite fidelity is

$$\mathcal{F}_s^{XX} = -\log \left| \langle x_0^A \otimes x_0^B | X_0^{AB} \rangle \right|^2 \tag{4.10}$$

where $|X_0^{AB}\rangle$ is the groundstate of H_p given in (3.16). The states $|x_0^A\rangle$ and $|x_0^B\rangle$, like $|X_0^{AB}\rangle$, are assumed to have unit norms.

4.2.1 Bipartite fidelity

The diagonalisation of H_f is detailed in Section 1.2.2. We adapt the result from that section to the case of a bipartite chain where two subsystems A and B are described by H_f with N_A and N_B sites, and do not interact. The tensor product of the left-groundstates is

$$\langle x_0^A \otimes x_0^B | = \langle 0 | \, d_{N_B/2}^B \cdots d_1^B d_{N_A/2}^A \cdots d_1^A \tag{4.11}$$

where

$$d_k^A = \Big(\frac{2}{N_A+1}\Big)^{1/2} \sum_{j=1}^{N_A} \sin\Big(\frac{\pi k j}{N_A+1}\Big) c_j, \tag{4.12a}$$

$$d_k^B = \Big(\frac{2}{N_B+1}\Big)^{1/2} \sum_{j=N_A+1}^{N} \sin\Big(\frac{\pi k (j-N_A)}{N_B+1}\Big) c_j. \tag{4.12b}$$

The operators c_j are the fermionic operators in (1.52). With the choice of normalisation in (4.12), both $\langle x_0^A|$ and $\langle x_0^B|$ have unit norms. To compute (4.10), we use Wick's theorem and find

$$\big|\langle x_0^A \otimes x_0^B | X_0^{AB}\rangle\big| = 2^{-3N/4} N^{-N/4} (N_A+1)^{-(N_A-2)/4} \times (N_B+1)^{-(N_B-2)/4} \, |\det \mathcal{D}| \tag{4.13a}$$

where

$$\mathcal{D}_{k,k'} = \begin{cases} \dfrac{1-(-1)^k \mathrm{e}^{-\mathrm{i}(N_A+1)\vartheta_{k'}}}{\cos\big(\frac{\pi k}{N_A+1}\big) - \cos\vartheta_{k'}} & k = 1, \dots, \frac{N_A}{2}, \\[2ex] \mathrm{e}^{-\mathrm{i}N_A\vartheta_{k'}} \dfrac{1-(-1)^{k-N_A/2}\, \mathrm{e}^{-\mathrm{i}(N_B+1)\vartheta_{k'}}}{\cos\big(\frac{\pi(k-N_A/2)}{N_B+1}\big) - \cos\vartheta_{k'}} & k = \frac{N_A}{2}+1, \dots, \frac{N}{2}, \end{cases} \tag{4.13b}$$

with $k' = 1, \dots, \frac{N}{2}$, and

$$\vartheta_k = \frac{2\pi(k - \frac{1}{2} - \frac{N}{4}) - \phi}{N}. \tag{4.13c}$$

This holds for both parities of $N/2$. Sadly, we have been unable to push the calculation further and evaluate this determinant in product form with the methods we developed in the previous chapters, even for special values of x and ϕ.

4.2.2 Other instances of the bipartite fidelity

The CFT predictions of Section 4.1 covers cases where fields are inserted in the legs and on the slits' endpoints. In order to investigate these cases on the lattice, we consider various modified instances of the bipartite fidelity on the skirt lattice. In each case, the state $|X_0^{AB}\rangle$ is

kept unchanged in the overlap, whereas the state $\langle x_0^A \otimes x_0^B|$ is replaced by a state of the form

$$\langle x_{m_A}^A \otimes s_2 \otimes x_{m_B}^B \otimes s_4|. \tag{4.14}$$

Here $\langle x_m^S|$ is the left-groundstate of the XX spin chain for the system S with free boundary conditions in the magnetisation sector m, and s_2, s_4 are spin states that we impose on the corners situated at $w_s(z_2)$ and $w_s(z_4)$ on the skirt domain, respectively. We select these states from the set $\{\emptyset, \uparrow, \downarrow, \uparrow\downarrow, \uparrow\uparrow, \uparrow\uparrow\uparrow\}$. The condition on the even parity of N_A and N_B is relaxed and the relation tying them to N is $N = N_A + n_2 + N_B + n_4$, where n_2 and n_4 are the lengths of the states $|s_2\rangle$ and $|s_4\rangle$. Table 4.1 gives an overview of the thirteen cases that we consider. In particular, case 1 corresponds to the standard bipartite fidelity, as defined in (4.10) with the overlap (4.13). In the other cases, N_A is chosen to be even if m_A is an integer and odd if m_A is a half-integer, and likewise for N_B in terms of m_B. In each case, the magnetisation of the state (4.14) vanishes, and the corresponding overlap $\left|\langle x_{m_A}^A \otimes s_2 \otimes x_{m_B}^B \otimes s_4|X_0^{AB}\rangle\right|$ is non-zero. We obtain a determinant expression for each of these overlaps similar to (4.13), which we do not reproduce here. We are unable to evaluate these determinants in product form. Our analysis in Section 4.4.1 of the asymptotics of $\mathcal{F}_s^{XX}$ thus relies on the numerical evaluations of these determinants.

4.3 Lattice calculation for critical dense polymers

We study the model of dense polymers on the skirt lattice. The lattice is a cylinder of height $4M$ and width N, which we choose to be even. There are two vertical slits that extend halfway across the cylinder. They divide the lower edge into two open segments of lengths N_A and N_B, which are even numbers too.

The top circular edge, the bottom segments as well as the interior of the two slits are decorated with simple arcs. The situation is similar to the example of Figure 2.1, with the following differences: (i) the total height of the lattice is $4M$ instead of $2M$, and (ii) the four diagonal edges in the

Case	m_A	s_2	m_B	s_4
1	0	$\emptyset$	0	$\emptyset$
2	$-1/2$	$\emptyset$	$+1/2$	$\emptyset$
3	-1	$\emptyset$	$+1$	$\emptyset$
4	$-3/2$	$\emptyset$	$+3/2$	$\emptyset$
5	-2	$\emptyset$	2	$\emptyset$
6	0	$\uparrow$	0	$\downarrow$
7	$-1/2$	$\uparrow$	$+1/2$	$\downarrow$
8	$+1/2$	$\downarrow$	$+1/2$	$\downarrow$
9	0	$\emptyset$	0	$\uparrow\downarrow$
10	$-1/2$	$\emptyset$	$-1/2$	$\uparrow\uparrow$
11	$-1/2$	$\emptyset$	0	$\uparrow$
12	-1	$\emptyset$	0	$\uparrow\uparrow$
13	$-3/2$	$\emptyset$	0	$\uparrow\uparrow\uparrow$

Table 4.1: The thirteen cases we consider for the XX chain on the skirt lattice.

diagram's lower-half are decorated with simple arcs. The contractible loops have a fugacity $\beta = 0$, whereas the non-contractible loops have a fugacity α. The Boltzmann weight of a configuration $\{\ell_i\}$ is $W_s(\{\ell_i\}) = \alpha^{n_\alpha}\delta_{n_\beta,0}$, where n_α and n_β are the numbers of non-contractible and contractible loops in the configuration. The partition function on the skirt lattice, denoted Z_s^{AB}, is

$$Z_s^{AB} = \sum_{\{\ell_i\}} W_s(\{\ell_i\}). \tag{4.15}$$

To proceed, we consider three more partition functions. The first, Z_c^{AB}, is the partition function on the cylinder of height $4M$ and perimeter N where the top and bottom segments are decorated with simple arcs. It corresponds to the example in the central panel of Figure 3.4, but with height $4M$ instead of $2M$. The other two partition functions, $Z_r^{(2),A}$ and $Z_r^{(2),B}$, are defined on rectangular lattices of respective dimensions $4M \times N_A$ and $4M \times N_B$. These partition functions correspond to the partition functions $Z_r^{(d),S}$ with $S = A, B$ and $d = 2$ that we introduced in Section 2.1. In particular, we saw that the partition function $Z_r^{(2),S}$

with a pair of defects that connect the top and bottom segments with weight 1 it is the reference partition function on the rectangle [141].

With these various partition functions, the logarithmic bipartite fidelity of the model of critical dense polymers on the skirt lattice is

$$\mathcal{F}_s^{CDP} = -\lim_{M\to\infty} \log\left(\frac{\left(Z_s^{AB}\right)^2}{\alpha\, Z_c^{AB} Z_r^{(2),A} Z_r^{(2),B}}\right). \tag{4.16}$$

As we shall see, the limit $M \to \infty$ of the ratio (4.16) is well-defined. Moreover, the factor α in the denominator ensures that $\mathcal{F}_s^{CDP}$ is also well-defined in the limit $\alpha \to 0$. Indeed, Z_s^{AB} and Z_c^{AB} both vanish linearly in α as it tends to zero. With this convention for $\mathcal{F}_s^{CDP}$, the leading powers of α coincide between the numerator and the denominator.

4.3.1 Partition functions

Our lattice calculations exploit the tools and methods that we introduced in the two previous chapters. As before, we first express the partition functions that appear in (4.16) in the context of the Temperley-Lieb algebra. We already computed the partitions function Z_c^{AB} in (3.49) with $2M$ instead of $4M$, and the partition functions $Z_r^{(2),A}$ and $Z_r^{(2),B}$ are given in (2.17). We use the results from Sections 2.1.1 and 3.3.2 to derive a similar expression for Z_s^{AB} and find

$$Z_s^{AB} = 2^{2MN}(v_0^A \otimes v_0^B)\cdot\left(\boldsymbol{D}^A \otimes \boldsymbol{D}^B\right)^M \left(\boldsymbol{T}^{AB}\right)^{2M} v_0^{AB}\big|_{\mathsf{W}_{N,0}}, \tag{4.17a}$$

$$Z_c^{AB} = 2^{2MN} v_0^{AB}\cdot(\boldsymbol{T}^{AB})^{4M} v_0^{AB}\big|_{\mathsf{W}_{N,0}}, \tag{4.17b}$$

$$Z_r^{(2),A} = 2^{2MN_A} v_2^A \cdot (\boldsymbol{D}^A)^{2M} v_2^A\big|_{\mathsf{V}_{N_A,2}}, \tag{4.17c}$$

$$Z_r^{(2),B} = 2^{2MN_B} v_2^B \cdot (\boldsymbol{D}^B)^{2M} v_2^B\big|_{\mathsf{V}_{N_B,2}}. \tag{4.17d}$$

Second, we follow Sections 2.1.2 and 3.3.2 and express the partition functions as overlaps in the XX spin chain. We find

$$Z_s^{AB} = 2^{2MN}\langle\!\langle v_0^A \otimes v_0^B | \left(D^A \otimes D^B\right)^M \left(T^{AB}\right)^{2M} | v_0^{AB}\rangle, \tag{4.18a}$$

$$Z_c^{AB} = 2^{2MN}\langle\!\langle v_0^{AB} | (T^{AB})^{4M} | v_0^{AB}\rangle, \tag{4.18b}$$

$$Z_r^{(2),A} = 2^{2MN_A} \langle\langle v_2^A | (D^A)^{2M} | v_2^A \rangle, \tag{4.18c}$$

$$Z_r^{(2),B} = 2^{2MN_B} \langle\langle v_2^B | (D^B)^{2M} | v_2^B \rangle, \tag{4.18d}$$

where $\langle\langle v_0|$ and $\langle\langle v_2|$ are defined in (3.71). We note that all the states that appear as dual states do not depend on the twist parameter ϕ, so in this case (3.55) simply becomes $\langle\langle w| = |w\rangle^{\mathrm{t}}$.

Following the same steps and logic as in Sections 2.2.1 and 3.3.3, we finally extract the leading behaviour of the overlaps (4.18) in the limit $M \to \infty$. The result is

$$\mathcal{F}_s^{CDP} = -\log \left(\frac{\langle\langle w_0^A \otimes w_0^B | X_0^{AB} \rangle^2}{\alpha} \times \frac{\langle\langle v_0^A | \hat{w}_0^A \rangle^2}{\langle\langle v_2^A | w_2^A \rangle^2} \frac{\langle\langle v_0^B | \hat{w}_0^B \rangle^2}{\langle\langle v_2^B | w_2^B \rangle^2} \frac{\langle\langle X_0^{AB} | v_0^{AB} \rangle}{\langle\langle v_0^{AB} | X_0^{AB} \rangle} \right). \tag{4.19}$$

4.3.2 Closed-form expressions for the bipartite fidelity

After a long but straightforward calculation that uses free-fermion techniques similar to those of Sections 2.2.2, 2.2.3, 2.3.2 and 3.3.3, we find

$$\mathrm{e}^{-\mathcal{F}_s^{CDP}} = N^{-\frac{N}{2}} (Nx)^{-\frac{Nx}{2}+\frac{3}{2}} (N(1-x))^{-\frac{N(1-x)}{2}+\frac{3}{2}} \times 2^{-\frac{N}{2}+1} (\det \mathcal{C})^2 \tag{4.20}$$

where

$$\mathcal{C}_{k,k'} = \begin{cases} \sin\left(\frac{Nx\vartheta_{k'}}{2} - \frac{\pi k}{2}\right) \left(\cos\vartheta_{k'} - \cos\left(\frac{\pi k}{Nx}\right) \right)^{-1}, \\ (-1)^{k'} \sin\left(\frac{N(1-x)\vartheta_{k'}}{2} - \frac{\pi(k-\frac{Nx}{2})}{2}\right) \left(\cos\vartheta_{k'} - \cos\left(\frac{\pi(k-\frac{Nx}{2})}{N(1-x)}\right) \right)^{-1} \end{cases} \tag{4.21}$$

with $k = 1, \ldots, \frac{Nx}{2}$ and $k = \frac{Nx}{2}+1, \ldots, \frac{N}{2}$ for the top and bottom entries, respectively, and $k' = 1, \ldots, \frac{N}{2}$. For arbitrary values of x and ϕ, we are unable to evaluate the determinant in closed form using the Cauchy determinant formula (2.70) or (3.25). We are however able to compute the determinant for two specialisations of x and ϕ: (i) $x = 1/2$ with arbitrary ϕ and (ii) $\phi = 0$ with arbitrary x. For simplicity, we give our results for these two cases when N is a multiple of four.

Specialisation (i): $x = 1/2$ and arbitrary ϕ. For $x = 1/2$, $N \equiv 0 \bmod 4$ and arbitrary values of ϕ, after some simplifications, we find

$$|\det \mathcal{C}| = \cos(\tfrac{\phi}{2})^{N/4} \Big| \det_{k,k'=1}^{N/4} \Big(\cos\vartheta_{2k'} - \cos\big(\tfrac{\pi k}{N}\big)\Big)^{-1} \Big| \times \Big| \det_{k,k'=1}^{N/4} \Big(\cos\vartheta_{2k'-1} - \cos\big(\tfrac{\pi k}{N}\big)\Big)^{-1} \Big|. \quad (4.22)$$

In this case, we apply (3.25) to evaluate both determinants.

Specialisation (ii): $\phi = 0$ and arbitrary x. For $\phi = 0$, $N \equiv 0 \bmod 4$ and arbitrary values of x, we find

$$|\det \mathcal{C}| = 2^{N/4} \Big| \det \mathcal{C}^1 \det \mathcal{C}^2 \Big| \times \Big| \prod_{k=1}^{N/4} \cos\Big(\tfrac{Nx\vartheta_k}{2}\Big) \prod_{k=N/4+1}^{N/2} \sin\Big(\tfrac{Nx\vartheta_k}{2}\Big) \Big| \quad (4.23a)$$

with

$$\mathcal{C}^1_{k,k'} = \begin{cases} \Big(\cos\vartheta_{k'} - \cos\big(\frac{\pi(2k-1)}{Nx}\big)\Big)^{-1} & k = 1, \dots, \frac{Nx}{4}, \\ \Big(\cos\vartheta_{k'} - \cos\big(\frac{\pi(2k-\frac{Nx}{2})}{N(1-x)}\big)\Big)^{-1} & k = \frac{Nx}{4}+1, \dots, \frac{N}{4}, \end{cases} \quad (4.23b)$$

where $k' = 1, \dots, \frac{N}{4}$, and

$$\mathcal{C}^2_{k,k'} = \begin{cases} \Big(\cos\vartheta_{k'} - \cos\big(\frac{\pi 2k}{Nx}\big)\Big)^{-1} & k = 1, \dots, \frac{Nx}{4}, \\ \Big(\cos\vartheta_{k'} - \cos\big(\frac{\pi(2k-\frac{Nx}{2}-1)}{N(1-x)}\big)\Big)^{-1} & k = \frac{Nx}{4}+1, \dots, \frac{N}{4}, \end{cases} \quad (4.23c)$$

where $k' = \frac{N}{4}+1, \dots, \frac{N}{2}$. In this case too we evaluate both determinants with (3.25).

4.4 Asymptotics

In this section, we study the large-N asymptotics of the bipartite fidelity for the XX chain and the model of critical dense polymers on the skirt lattice. We compare these results with the CFT predictions of Section 4.1.

Case	$\boldsymbol{\Delta_1}$	$\boldsymbol{\Delta_2}$	$\boldsymbol{\Delta_3}$	$\boldsymbol{\Delta_4}$	$\boldsymbol{\Delta_5}$	$\boldsymbol{C_s'}$	$\boldsymbol{\Xi_2}$	$\boldsymbol{\Xi_4}$
1	0	0	0	0	Δ_ϕ^{XX}	0.03669	1	1
2	1/8	0	1/8	0	Δ_ϕ^{XX}	0.03669	1	1
3	1/2	0	1/2	0	Δ_ϕ^{XX}	0.03669	1	1
4	9/8	0	9/8	0	Δ_ϕ^{XX}	0.03669	1	1
5	2	0	2	0	Δ_ϕ^{XX}	0.03669	1	1
6	0	1/8	0	1/8	Δ_ϕ^{XX}	1.11331	0	0
7	1/8	1/8	1/8	1/8	Δ_ϕ^{XX}	1.11331	0	0
8	1/8	1/8	1/8	1/8	Δ_ϕ^{XX}	0.42016	0	0
9	0	0	0	0	Δ_ϕ^{XX}	0.96639	1	−1
10	1/8	0	1/8	1/2	Δ_ϕ^{XX}	0.78562	1	−1
11	1/8	0	0	1/8	Δ_ϕ^{XX}	0.40172	1	0
12	1/2	0	0	1/2	Δ_ϕ^{XX}	0.78562	1	−1
13	9/8	0	0	9/8	Δ_ϕ^{XX}	1.06794	1	−2

Table 4.2: The conformal weights, the constant C_s' and the extrapolation lengths for each of the thirteen cases, with Δ_ϕ^{XX} defined in (3.90).

4.4.1 XX spin chain

We study the asymptotic behaviour of the bipartite fidelity for the XX chain numerically, for each case in Table 4.1. We obtained the data points by evaluating the determinants numerically, namely the expression (4.13) for case 1 and similar determinant expressions for the other cases. As in Section 3.4.1, we compare these numerical values with a fit of the form

$$\mathcal{F}_s^{XX} = g_s^{(0)} \log N + g_s^{(1)}(x) + g_s^{(2)} N^{-1} \log N + \gamma_3 \frac{1}{N} + \gamma_4 \frac{\log N}{N^2} + \gamma_5 \frac{1}{N^2} + \gamma_6 \frac{\log N}{N^3} + \gamma_7 \frac{1}{N^3} \quad (4.24)$$

and we consider that the numerical results and CFT predictions match when the criteria (3.85) is satisfied. From this analysis, we find that the asymptotic behaviour of $\mathcal{F}_s^{XX}$ is correctly predicted by the CFT formula (4.1) for case (ii), with the functions $g_s^{(0)}$, $g_s^{(1)}(x)$ and $g_s^{(2)}(x)$ given in (4.3), (4.6) and (4.8). These are specialised to the value $c = 1$ of the central charge and to values of the conformal weights Δ_i and of the

constant C_s' that depend on the case considered. We give these values in Table 4.2. In Figure 4.3, we plot the numerical data and the curve $g_s^{(0)} \log N + g_s^{(1)}(x)$, for the cases 8 and 12 and find a good agreement. We find a similar agreement for all other eleven cases.

The conformal weights in Table 4.2 are consistent with known results for the CFT description of the XX spin chain and the six-vertex model. The field inserted at $z = z_5$ accounts for the presence of the twist ϕ in the model. As discussed in Section 3.4.1, this electric operator has the conformal weights $\Delta_\phi^{XX} = \bar{\Delta}_\phi^{XX}$ given in (3.90). The other fields in the positions z_i with $i = 1, \dots, 4$ are called *magnetic operators* [160]. These are primary fields that account for the presence of spin states of fixed magnetisation m. Here they are inserted on the boundary and thus depend on a single variable. Their conformal weight Δ_m depends only on the magnetisation m of the state inserted at $z = z_i$. As we discussed in Section 1.2.2, this dimension can be computed from the finite-size correction of the groundstate energy of the Hamiltonian H_f defined in (1.51). We recall that the difference $c - 24\Delta_m$ reads

$$c - 24\Delta_m = 1 - 12m^2, \tag{4.25}$$

see (1.71), and setting $c = 1$ yields

$$\Delta_m = \frac{m^2}{2}. \tag{4.26}$$

The values of Δ_1, Δ_2, Δ_3 and Δ_4 in Table 4.2 are precisely given by (4.26) with the corresponding values for $m \in \{0, \pm\frac{1}{2}, \pm 1, \pm\frac{3}{2}, \pm 2\}$. Regarding the non-universal additive constant C_s', we observe that it is independent of ϕ and only depends on the fields inserted on the endpoints of the slits, corresponding to the states s_2 and s_4 in (4.14).

We plot our numerical data for $g_s^{(2)}(x)$ in Figure 4.4 for the cases 3 and 13. This data appears alongside the CFT prediction for $g_s^{(2)}(x)$, with the suitably chosen values of the extrapolation lengths Ξ_2 and Ξ_4, given in Table 4.2. Once again, we do not plot the eleven other cases but find similar agreement.

The original derivation of the $N^{-1} \log N$ term in [63] is based on a perturbative calculation. By varying the position of a boundary near a corner by a distance Ξ, one obtains the variation of the free energy as

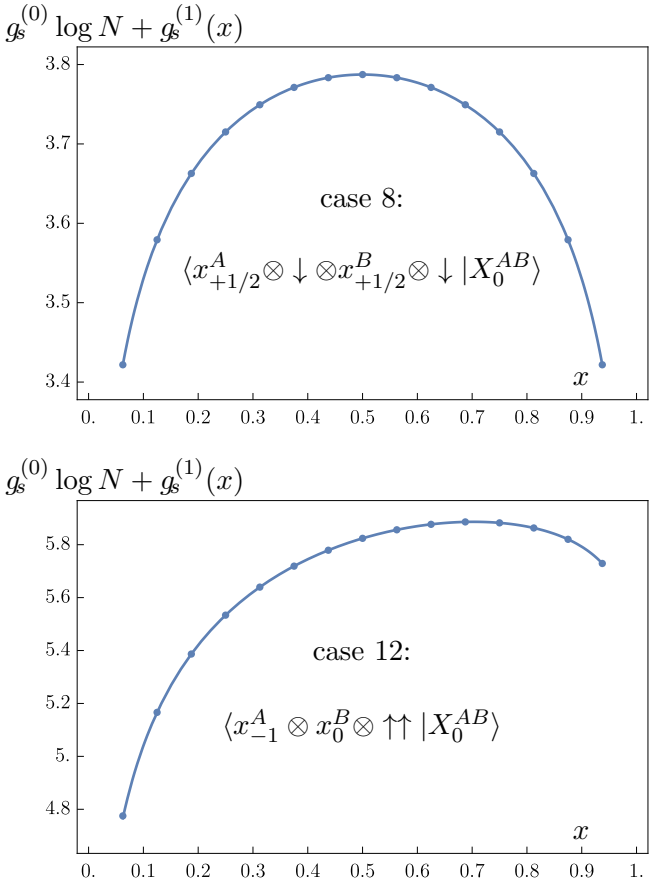

Figure 4.3: The function $g_s^{(0)} \log N + g_s^{(1)}(x)$ as a function of x for $N = 800$ and $\phi = 2$ for the cases 8 and 12. For the data points, $g_s^{(0)}$ and $g_s^{(1)}(x)$ are obtained by fitting (4.24), whereas the solid curve is the CFT prediction for these two functions with the data of Table 4.2.

a function of the perturbation, and then integrates it to obtain $g_s^{(2)}(x)$. On the skirt domain, there are two corners, each of internal angle 2π, and in this case, one can perform two separate perturbations near those corners. One can then assign an extrapolation length to each of the two slits, denoted Ξ_2 and Ξ_4. This generalised result with two distinct extrapolation lengths is necessary to correctly reproduce the data for the cases 9 to 13, for which $\Xi_2 \neq \Xi_4$. In the general case, our numerics

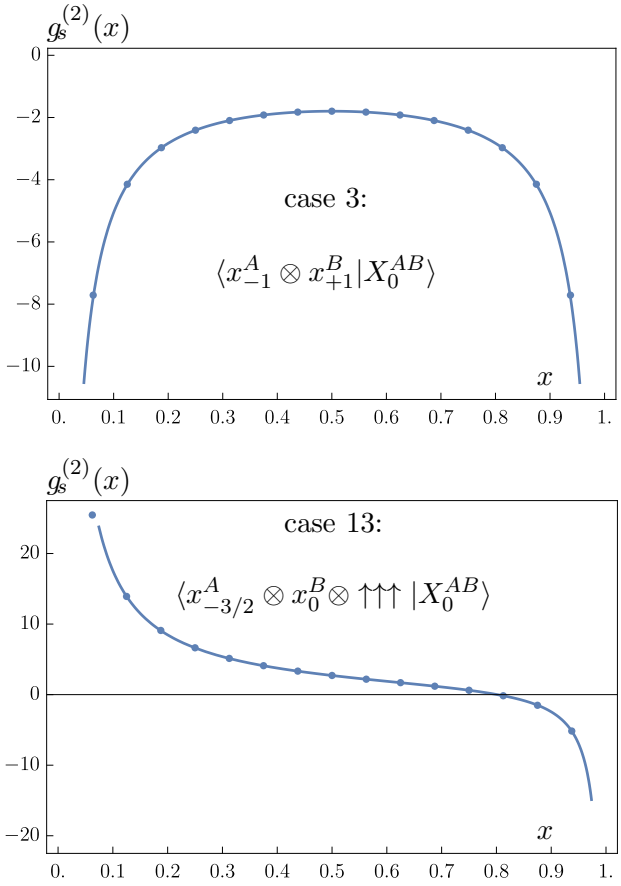

Figure 4.4: The function $g_s^{(2)}(x)$ for the XX spin chain for $\phi = 2$ for the cases 3 and 13. The data points are obtained by fitting (4.24), whereas the solid lines are the CFT predictions with the conformal weights and extrapolation lengths fixed as in Table 4.2.

reveal that the extrapolation lengths are

$$\Xi_2 = 1 - n_2, \qquad \Xi_4 = 1 - n_4, \tag{4.27}$$

where n_i, with $i = 2, 4$, is the length of the spin state s_i defined in Section 4.2.2 inserted on the corner i. Similarly to the previous chapter, we interpret this result in terms of the effective length of the system, which depends on spin states inserted on the corners and on the boundary conditions.

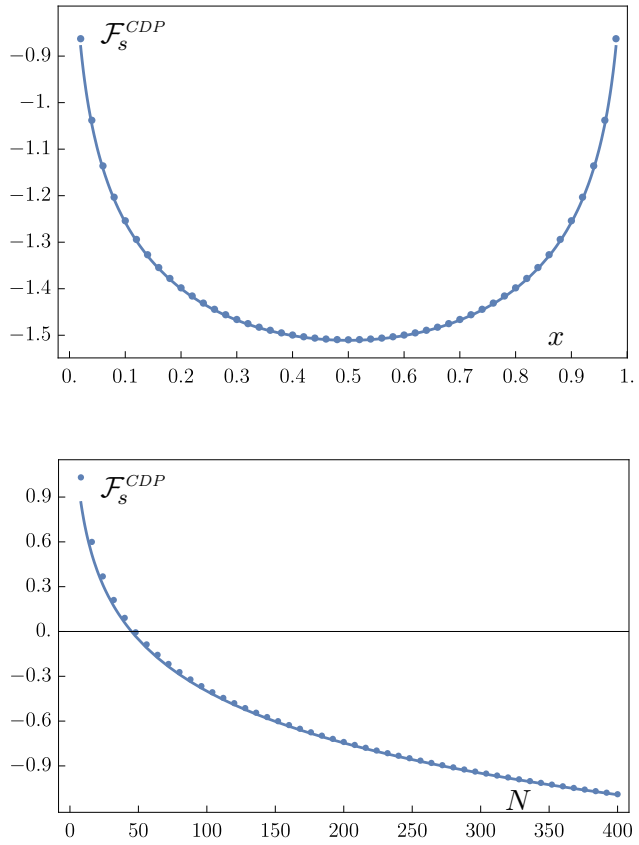

Figure 4.5: The bipartite fidelity $\mathcal{F}_s^{CDP}$ as a function of x for $N = 800$ (top panel) and as a function of N for $x = \frac{1}{4}$ (bottom panel). In both cases, the fugacity is set to $\alpha = 2\cos(\frac{\phi}{2})$ with $\phi = 2$. The data points are computed from the determinant (4.20), whereas the solid line is (4.28c).

4.4.2 Critical dense polymers

We now study the large-N expansion for the bipartite fidelity for the model of dense polymers on the skirt lattice. In Section 4.3.1, we obtained closed-form expressions for $\mathcal{F}_s^{CDP}$ for two specialisations: (i) $x = 1/2$ with arbitrary ϕ, and (ii) $\phi = 0$ with arbitrary x. We extract the asymptotic behaviour in these two cases using arguments that are similar to those presented in Section 2.4. We obtain

$$\mathcal{F}_s^{CDP}\big|_{x=\frac{1}{2}} = -\frac{1}{2}\log N + \frac{\log 2}{3} + 4\Delta_\phi^{CDP}\log 2$$

$$+\frac{1}{2}(-1+12\log A-\log\pi+4\log 2)+\mathcal{O}(N^{-1}) \quad (4.28a)$$

and

$$\begin{aligned}\mathcal{F}_s^{CDP}\big|_{\phi=0} &= -\frac{1}{2}\log N-\frac{1}{12}(G_s(x)+G_s(1-x))\\ &\quad -\frac{1}{2}(x\log x+(1-x)\log(1-x)+2\log 2)\\ &\quad +\frac{1}{2}(-1+12\log A-\log\pi+4\log 2)+\mathcal{O}(N^{-1}),\end{aligned} \quad (4.28b)$$

where we recall that $G_s(x)$ and Δ_ϕ^{CDP} are defined in (1.87) and (3.95), respectively.

We performed numerical evaluations of the determinant expression (4.20) for values of x and ϕ that do not enter the specialisations (i) and (ii). In Figure 4.5, we plot the results for the value $\phi = 2$. From the exact results (4.28) and our numerical experiments, we conjecture that the general formula is

$$\begin{aligned}\mathcal{F}_s^{CDP} &= -\frac{1}{2}\log N-\frac{1}{12}(G_s(x)+G_s(1-x))\\ &\quad +4\Delta_\phi^{CDP}\big(x\log x+(1-x)\log(1-x)+2\log 2\big)\\ &\quad +\frac{1}{2}(-1+12\log A-\log\pi+4\log 2)+\mathcal{O}(N^{-1}).\end{aligned} \quad (4.28c)$$

This conjecture reproduces the numerical results with good precision, in the sense of (3.85). Moreover, it also coincides with the CFT prediction (4.1) for case (i), with $g_s^{(0)}$ given in (4.3), $g_s^{(1)}(x)$ in (4.4), $g_s^{(2)}(x)$ in (4.7), the conformal data specified to

$$c=-2, \qquad \Delta_5=\Delta_\phi^{CDP}, \quad (4.28d)$$

the non-universal constant taking the value

$$C_s'=\frac{1}{2}(-1+12\log A-\log\pi+4\log 2), \quad (4.28e)$$

and with vanishing extrapolation lengths: $\Xi_2 = \Xi_4 = 0$. Indeed, since the conditions at the two slits' endpoints are identical, we must have $\Xi_2 = \Xi_4$. From the exact results (4.28) and the numerical evaluations, we find that the term proportional to $N^{-1}\log N$ vanishes, namely

$g_s^{(2)}(x) = 0$. A glance at (4.8) indicates that this is only possible if both extrapolation lengths vanish.

The values (4.28d) are precisely those expected in the conformal description of the model of dense polymers. Indeed, there is no change of boundary condition at the endpoints of the slits. Moreover, the boundary conditions in the legs A and B are known to correspond to the groundstate of the model. Both of these features correspond to identity fields with the dimension $\Delta = 0$. Similarly to what is discussed in Section 3.4.2, the bulk field at $z = z_5$ assigns weights $\alpha \neq 0$ to the non-contractible loops and has the conformal weight Δ_ϕ^{CDP}.

4.5 Summary of the main results

In this chapter, we investigated the bipartite fidelity on the skirt geometry. In the context of CFT, this quantity is related to the five-point function of fields inserted on the skirt domain. We obtained new predictions for the leading terms in the asymptotic large-N expansions of $\mathcal{F}_s$ up to order $N^{-1} \log N$ in two distinct cases, and hence generalise an earlier result of Dubail and Stéphan. In the first case, the only non-trivial field is the spinless primary bulk field inserted at infinity. In the second case, the five fields are vertex operators. We compared these predictions with exact and numerical lattice calculations and found a precise match for the XX spin chain and the model of critical dense polymers.

In the XX spin chain, we investigated thirteen instances of the bipartite fidelity. We considered various overlaps between the groundstate of the whole periodic system in the zero magnetisation sector, the groundstates of the subsystems A and B with free boundary conditions in the magnetisation sectors m_A and m_B, and fixed spin states s_2 and s_4 on both slits endpoints. We expressed these instances of the bipartite fidelity as determinants that we investigated with numerical evaluations. In the CFT, the insertion of spin states with fixed magnetisation m corresponds to inserting magnetic operators, whereas the presence of twist lines ϕ connecting certain points of the domain correspond to inserting electric operators. Hence, our investigation of the bipartite fidelity on the skirt geometry is related to correlators that mix electric and magnetic

operators. Our numerical analysis reveals that these mixed correlators take the simple form (3.4) for vertex operators. This factorisation of the n-point functions is the expected result for a free CFT [36], however it is interesting to recover this property from the scaling limit of lattice calculations. We found that the charges of the magnetic operators are $q = m$ and their conformal weights are $\Delta_m = m^2/2$, whereas the conformal weight of the electric operator related to the twist ϕ is Δ_ϕ^{XX}. These are the known conformal data of the XX spin chain. Our numerical investigations of the term of order $N^{-1}\log N$ suggests that we must assign an independent extrapolation length Ξ_i, $i = 2, 4$, to each corner. We found that the extrapolation lengths depend linearly on the lengths n_i of the spin states inserted on each corner via the relation $\Xi_i = 1 - n_i$.

Finally, we investigated the bipartite fidelity $\mathcal{F}_s^{CDP}$ in the model of critical dense polymers on the skirt lattice. On this geometry there is only one family of non-contractible loops with fugacity $\alpha = 2\cos(\frac{\phi}{2})$, whereas contractible loops have the fugacity $\beta = 0$. The CFT interpretation is the same as on the periodic pants geometry, namely this choice for the loop fugacities amounts to inserting a bulk operator with conformal weight $\Delta_\phi^{CDP} = \frac{1}{8}\big(\frac{\phi^2}{\pi^2} - 1\big)$. We expressed $\mathcal{F}_s^{CDP}$ in closed form for two specific combinations of the aspect ratio and the twist angle, and investigated its asymptotic behaviour for large N and fixed aspect ratio. We used numerical evaluations of determinants for other arbitrary values of x and ϕ. Our results are in agreement with our CFT prediction for the first case, where there is only one non-trivial field inserted as infinity. Moreover, we found that the extrapolation lengths associated to both corners vanish.

5

Conclusion and outlooks of Part I

In the first part of the thesis, we investigated the bipartite fidelity in the context of CFT and related critical lattice models in low dimensions. We provided original results in the context of non-unitary CFT and systems with periodic boundary conditions, with the systematic aim of comparing the asymptotic limit of exact or numerical lattice results with new or existing CFT predictions. For the lattice calculations, we focused on two critical lattice models: the XX spin chain and the model of critical dense polymers. In all the cases we considered, we found a systematic match between the CFT and lattice results.

To conclude, we mention a selection of future developments and generalisations of our work that we believe are worthy of investigation. The lattice derivations that we presented in the previous chapters use the exact diagonalisation of free-fermion Hamiltonians and related free-fermion techniques, such as Wick's theorem. An important development would be to repeat our calculations for genuinely interacting models, such as the XXZ spin chain with anisotropy $\Delta \neq 0$, or dense loop models where bulk loops have a fugacigy $\beta \neq 0$. Exact results and conjectures exist for the bipartite fidelity of the XXZ spin chain at $\Delta = -1/2$ with diagonal boundary magnetic fields [5, 137, 164]. These results rely on the extraordinary structure of the groundstate of the XXZ spin chain at its so-called *combinatorial point* [165–173]. We expect that similar arguments will allow us to investigate the bipartite fidelity of the XXZ spin chain at the combinatorial point on other geometries, such as the

periodic pants lattice. However, the case of arbitrary Δ remains elusive. A main challenge is to understand whether the tools developed in the context of the algebraic Bethe ansatz [58], and most notably the celebrated Slavnov formula for the overlap of Bethe states [174], can be adapted to evaluate the bipartite fidelity of interacting integrable systems. Another interesting avenue would be to use the framework of the quantum separation of variables [175, 176] and understand whether the bipartite fidelity takes a simple form in the separated basis. In his doctoral dissertation, Liénardy derived a plethora of explicit expressions and conjectures for multipartite fidelities in the XXZ spin chain at the combinatorial point [177]. These quantities generalise the bipartite fidelity when there are more than two subsystems. We believe that, as for the bipartite fidelity, it would be a major achievement to generalise these results for other integrable models by means of Bethe ansatz techniques or the quantum separation of variables.

An important result of this thesis concerns the bipartite fidelity on the flat pants geometry in the case where logarithmic fields are inserted on the domain. From the LCFT perspective, our calculation corresponds to the simplest case where two logarithmic fields from a rank-two Jordan cell are inserted on the flat pants domain. In this case, we observed that the difference between the LCFT result and the equivalent CFT result for primary fields only differs by a universal constant that is independent on the conformal data of the theory. A natural question is whether this result remains valid for generic settings of the fields. One could for instance generalise our LCFT arguments to the case where more logarithmic fields, possibly from Jordan cell with ranks higher than two, are inserted on the flat pants domain. Another generalisation would be to insert logarithmic fields on the periodic pants and the skirt domains, and compare the results with our CFT prediction for primary fields. A parallel challenge would be to define lattice observables whose scaling behaviour reproduces the LCFT predictions for these new settings of logarithmic fields, and compare the new LCFT predictions with these lattice results.

Finally, we believe that the bipartite fidelity is a useful tool to compute the structure constants $\mathcal{C}_{123}$ that arise in the three-point functions (1.23).

Computing a correlation function of a lattice model for a number of arbitrarily located positions in the complex plane is in general a notoriously difficult task, even for two-point functions. In this case, a simple way to measure the conformal dimension Δ_i that appears in a two-point correlator is to consider the problem defined on an infinite cylinder and insert the two fields at infinity at the endpoints of this cylinder. The dimension Δ_i appears in the $1/N$ finite-size correction term of the largest eigenvalue of the transfer matrix. Similarly for the three-point functions, the periodic pants and skirt domains are useful as they have three points at infinity where the three fields can be inserted. This idea has the potential to make the lattice computation of $\mathcal{C}_{123}$ a manageable problem.

Part II

Dynamics of symmetry-resolved entanglement

6

Quantum quenches and symmetry resolution

The nonequilibrium dynamics of isolated quantum systems received considerable attention over the last two decades [42, 45, 59, 178–180]. In particular, the entanglement dynamics plays a fundamental role in our understanding of numerous aspects of quantum many-body systems out of equilibrium, such as the equilibration and thermalisation of isolated many-body systems [42, 180–183], the emergence of thermodynamics in quantum systems [43, 184–186] or the effectiveness of classical computers to simulate quantum dynamics [187–191]. In one-dimensional quantum integrable systems, the entanglement dynamics after a quantum quench [45–47] is well described and understood in terms of the *quasiparticle picture* [43–45, 49, 50]. These theoretical developments benefited from pioneering cold-atom and ion-trap experiments that were able to probe isolated quantum systems at large time-scales with an unprecedented precision [60, 192–197]. Most notably, it has been possible to measure the entanglement of many-body systems out of equilibrium [51–54].

Symmetries and entanglement are two pillars of modern condensed matter physics, and in the following we investigate their interplay in the context of isolated quantum many-body systems out of equilibrium. In the case where the system has a global symmetry, the entanglement splits between the various symmetry sectors, and understanding this symmetry resolution of entanglement [64–66] is a problem that attracted a lot of attention recently. The first surprising result, obtained independently

and with different techniques by Goldstein and Sela [65] and Xavier, Alcaraz and Sierra [66], is the so-called equipartition of the entanglement entropy. It states that the contribution of each symmetry sector to the total entanglement is the same, up to corrections that vanish in the scaling limit. The properties of symmetry-resolved entanglement measures have since been investigated in numerous contexts, such as CFT and critical lattice models [65, 66, 198–204], systems with symmetry-protected topological phases [205–207], integrable systems and field theories [208–214], quantum models in two dimensions [215, 216], disordered systems [217], high-energy physics [218, 219], systems with non-abelian symmetries [220], non-complementary subsystems [221, 222] and quantum many-body systems out of equilibrium [52, 67, 69]. Moreover, symmetry-resolved quantities have already been measured experimentally [68] and play a role in the detection of entanglement in quantum many-body systems [223].

The second part of the thesis is dedicated to the investigation of the nonequilibrium dynamics of symmetry-resolved entanglement measures following a global quantum quench. In this chapter, we review the concepts of quantum quenches in integrable systems and the description of the subsequent entanglement dynamics in terms of the quasiparticle picture. We also define the symmetry-resolved entanglement entropies and discuss useful analytical methods in the context of free-fermion models.

6.1 Entanglement dynamics after a quench

In the following, we discuss chosen aspects of the entanglement dynamics after a quench in integrable systems. For further details, we recommend the pedagogical reviews [43, 44, 180] and references therein.

6.1.1 What is a quantum quench?

Let us consider an isolated quantum many-body system described by a Hamiltonian $H(\lambda)$ that depends on a parameter λ, such as an external magnetic field or a coupling constant. At time $t < 0$ the system is prepared in the groundstate $|\psi_0\rangle$ of $H(\lambda_0)$, that we assume to be

non-degenerate, for simplicity. At $t = 0$, the value of the parameter is modified abruptly from λ_0 to λ, and for times $t > 0$ the system undergoes a unitary evolution governed by the Hamiltonian $H(\lambda)$. The time-dependent state of the system is

$$|\psi(t)\rangle = \mathrm{e}^{-\mathrm{i}tH(\lambda)} |\psi_0\rangle \tag{6.1}$$

in units where $\hbar = 1$. The initial state $|\psi_0\rangle$ is in general not an eigenstate of the Hamiltonian $H(\lambda)$. As a consequence, the quantum expectation values of time-independent observables have a non-trivial dependence on time, and we say that the system is in a nonequilibrium situation. Such a protocol is known as a *quantum quench* [45–47]. In the literature, this denomination often includes situations where the system is prepared in an initial state $|\psi_0\rangle$ that is not an eigenstate of the Hamiltonian H that governs the subsequent unitary time evolution. Indeed, it is always formally possible to construct a Hamiltonian H_0 such that $|\psi_0\rangle$ is its groundstate and interpret the situation as a quench from $\lambda = 0$ to $\lambda = 1$ with the Hamiltonian $H(\lambda) = (1 - \lambda)H_0 + \lambda H$.

In the following, we focus on so-called *global quantum quenches*. In this context, the initial state $|\psi_0\rangle$ has a non-zero overlap with an exponential number of eigenstates of H in the limit of large system size. In particular, $|\psi_0\rangle$ cannot be considered as a small perturbation from the groundstate of H. A defining property of global quantum quenches is that the energy density in the initial state (and hence in the time-dependent state, because the energy is conserved) is larger than the groundstate energy per site. Performing a global quantum quench thus adds an extensive amount of energy in the system. For a one-dimensional system of length L, this translates to [180]

$$\lim_{L\to\infty} \frac{\langle\psi_0|H|\psi_0\rangle}{L} > \lim_{L\to\infty} \frac{E_{\mathrm{GS}}}{L} \tag{6.2}$$

where E_{GS} is the groundstate energy of H.

6.1.2 Relaxation in isolated quantum systems

Relaxation and thermalisation are ubiquitous phenomena in the physics of nonequilibrium many-body systems. A quantum system out of equilibrium is described by a time-dependent density matrix $\rho(t)$, and the

system relaxes if the density matrix reaches a stationary state, namely if the limit

$$\rho(\infty) \equiv \lim_{t\to\infty} \rho(t) \tag{6.3}$$

exists. More precisely, we say that the system relaxes to the statistical ensemble E if $\rho(t)$ converges to the corresponding density matrix ρ_E: $\rho(\infty) = \rho_E$. For example, the canonical (or Gibbs) ensemble is described by the thermal density matrix

$$\rho_{\text{Gibbs}} = \frac{1}{Z}\mathrm{e}^{-\beta H}, \quad Z = \operatorname{Tr} \mathrm{e}^{-\beta H}, \tag{6.4}$$

where Z is the partition function that ensures the normalisation of the density matrix, β is the inverse temperature and H is the Hamiltonian. When the system relaxes to a Gibbs ensemble, we say that it thermalises.

After a quantum quench in an isolated quantum system, the system remains in a pure state $|\psi(t)\rangle$ and is described by the density matrix $\rho(t) = |\psi(t)\rangle\langle\psi(t)|$. Because of the unitary time evolution (6.1), the system does not relax. Numerous experiments [51–54, 60, 192–197] show that, while the system indeed remains in a pure state, the average values of local observables can become stationary and be described by a stationary ensemble. For an isolated quantum system, we extend the definition of relaxation and say that the system relaxes to the ensemble E if, for any finite subsystem A embedded in an infinite system $A\cup B$, the reduced density matrix $\rho_A(t) = \operatorname{Tr}_B \rho(t)$ reaches the stationary state $\rho_A(\infty) = \rho_{A,E} \equiv \operatorname{Tr}_B \rho_E$ [43, 44, 180]. The idea behind the definition of relaxation for isolated quantum systems is that for any finite subsystem A, the infinitely large complementary subsystem B plays the role of the environment.

Conservation laws and integrability. The conservation laws of a quantum system drastically influence the stationary ensemble that describes its stationary behaviour. Since we are dealing with isolated system, energy is always a conserved quantity. In the absence of other conserved quantities, isolated quantum systems are believed to thermalise [180]. In stark contrast, integrable systems are counter examples of systems that never thermalise. Because of their large number of conserved quantities (which diverges in the thermodynamic limit),

the dynamics is constrained and the final stationary state is instead described by a generalised Gibbs ensemble (GGE) [59]. It is important to stress that in a quantum system, it is possible to construct trivial conserved charges that are highly non-local. For instance, a projector onto an eigenstate $|\psi_e\rangle$ of the Hamiltonian is trivially conserved through the time evolution,

$$\langle\psi(t)|\psi_e\rangle\langle\psi_e|\psi(t)\rangle = \langle\psi_0|\mathrm{e}^{\mathrm{i}tH}|\psi_e\rangle\langle\psi_e|\mathrm{e}^{-\mathrm{i}tH}|\psi_0\rangle = \langle\psi_0|\psi_e\rangle\langle\psi_e|\psi_0\rangle, \quad (6.5)$$

but it should not be included as a conserved charge in the GGE description of the stationary state. The notion of quasilocality [224] is a criterion that allows one to select the relevant conserved charges that play a role in the dynamics of the system. If we denote by $\{I_j\}$ the set of quasilocal charges of an integrable system, the associated GGE density matrix is

$$\rho_{\mathrm{GGE}} = \frac{1}{Z}\mathrm{e}^{-\sum_j \beta_j I_j}, \quad Z = \mathrm{Tr}\ \mathrm{e}^{-\sum_j \beta_j I_j}. \quad (6.6)$$

Here, the quantities β_j are the so-called generalised inverse temperatures, which are fixed by the conservation relations

$$\mathrm{Tr}(\rho_{\mathrm{GGE}} I_j) = \langle\psi_0|I_j|\psi_0\rangle. \quad (6.7)$$

Entanglement and thermodynamics. The thermodynamic entropy of a statistical ensemble E is $S_E \equiv -\mathrm{Tr}(\rho_E \log \rho_E)$, and it is extensive in the thermodynamic limit. For a system of volume V, the following limit defines the thermodynamic entropy density s_E:

$$s_E \equiv \lim_{V\to\infty} \frac{S_E}{V}. \quad (6.8)$$

For any subsystem A with volume V_A, we also have

$$\lim_{V_A\to\infty} \frac{\lim_{V\to\infty} S_{A,E}}{V_A} = s_E \quad (6.9)$$

where $S_{A,E} = -\mathrm{Tr}(\rho_{A,E} \log \rho_{A,E})$ is the thermodynamic entropy of subsystem A. With these properties, we conclude that if an isolated quantum system relaxes towards a statistical ensemble E, the stationary value of the entanglement entropy of any subsystem A of volume V_A embedded in a system of volume V satisfies [43, 44]

$$\lim_{V_A\to\infty} \frac{\lim_{V\to\infty} S_1(\infty)}{V_A} = -\lim_{V_A\to\infty} \frac{\lim_{V\to\infty} \mathrm{Tr}(\rho_A(\infty)\log\rho_A(\infty))}{V_A}$$

$$
\begin{aligned}
&= -\lim_{V_A\to\infty} \frac{\lim_{V\to\infty} \mathrm{Tr}(\rho_{A,E}\log\rho_{A,E})}{V_A} \\
&= \lim_{V_A\to\infty} \frac{\lim_{V\to\infty} S_{A,E}}{V_A} \\
&= s_E. \qquad (6.10)
\end{aligned}
$$

The interpretation of this relation is that, in the thermodynamic limit, the thermodynamic entropy density in the stationary state corresponds to the entanglement entropy density accumulated during the unitary time evolution [43]. Understanding how the entanglement entropy grows in time to reach its stationary value is crucial to unveil how thermodynamics and statistical ensemble arise from the unitary quantum dynamics.

6.1.3 The quasiparticle picture

In this section, we discuss a physical picture, known as the *quasiparticle picture* [45, 49, 50], that allows one to predict the time evolution of the entanglement entropy after a global quantum quench from a low-entangled initial state in a one-dimensional quantum integrable model. As we discussed in Section 6.1.1, the initial state has an extensive excess of energy with respect to the groundstate, and it is regarded as a source of quasiparticle excitations. These quasiparticles are assumed to be produced in pairs with opposite momenta k and $-k$ and velocity v_k. For spin chains with local interactions, the Lieb-Robinson bound [225] guarantees that there is a maximum value v_M for the possible velocities of the quasiparticles. Moreover, the quasiparticles are assumed to move ballistically through the system. The key assumption of this description is that the quasiparticles emitted from different points are incoherent, while those emitted from the same point are entangled and spread the entanglement and the correlations through the system. In particular, the entanglement between two parts of the system is proportional to the number of entangled pairs of quasiparticles they share.

In the following, we consider two cases where A is a subsystem of length ℓ embedded in a system of length L. In the first case, A is a single interval of length ℓ, whereas in the second case $A = A_1 \cup A_2$ consists of two subsystems A_1 and A_2 that are intervals of respective lengths ℓ_1 and

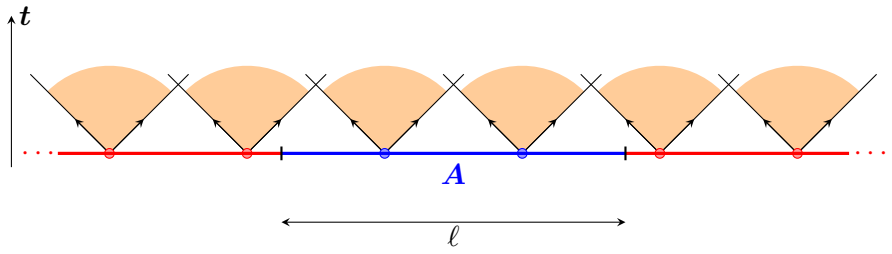

Figure 6.1: Illustration of the quasiparticle picture for the entanglement spreading in a one-dimensional integrable system. The arrows indicate the propagation of the quasiparticles with the largest velocity v_M.

$\ell_2 = \ell - \ell_1$ separated by a distance d. In stark contrast with Part I, here we always take the thermodynamic limit $L \to \infty$ before investigating the limit where the subsystem A becomes large. In that way, the subsystem A can always be seen as embedded in an infinite system, and the ideas developed in the previous sections apply. In that context, the scaling limit corresponds to the limit $L \to \infty$ followed by the limits (i) $\ell, t \to \infty$ where the ratio t/ℓ is kept fixed for the first case, and (ii) $\ell, \ell_1, d, t \to \infty$ with the ratios ℓ_1/ℓ, d/ℓ and t/ℓ fixed for the second case.

Single interval

In the case where A is a single interval of length ℓ, the quasiparticle picture predicts that the entanglement entropy evolves as [45]

$$S_1(t) = 2t \int_{2v_k t<\ell} \mathrm{d}k \; v_k s(k) + \ell \int_{2v_k t>\ell} \mathrm{d}k \; s(k) \tag{6.11}$$

in the scaling limit. Here, the function $s(k)$ depends on the rate of production of the quasiparticles with momentum $\pm k$ and their contribution to the entanglement entropy. This situation is illustrated in Figure 6.1. The two terms of Eq. (6.11) give two different regimes as the entropy evolves in time. For times $t \leqslant \ell/(2v_M)$, the domain of integration of the second integral vanishes, and the entropy grows linearly in time. For larger times, the entanglement entropy growth slows down, and for

$t \gg \ell/2v_M$ the entanglement entropy saturates to a value that is extensive in the subsystem length, namely

$$S_1(\infty) = \ell \int \mathrm{d}k \; s(k). \tag{6.12}$$

To give predictive power to the quasiparticle result (6.11), one needs to compute the function $s(k)$, which depends strongly on the model and on the initial state. For free-fermion models, and Alba and Calabrese [49] derived an exact formula for $s(k)$. The main idea is to compare the stationary value (6.10) with the large-time limit of $S_1(t)$ in (6.12). They find

$$s(k) = \frac{1}{2\pi}(-n_k \log n_k - (1-n_k)\log(1-n_k)) \tag{6.13}$$

where n_k is the probability of occupation of the mode k in the stationary state. The entanglement entropy is thus

$$S_1(t) = \int \frac{\mathrm{d}k}{2\pi}(-n_k \log n_k - (1-n_k)\log(1-n_k)) \min(\ell, 2v_k t) \tag{6.14}$$

where we use the function $\min(\ell, 2v_k t)$ to recast the sum of two integrals in (6.11) in a simpler form. For free-fermion models, the result (6.11) also holds for the Rényi entropies S_n with the replacement [226]

$$s(k) \to s_n(k) = \frac{1}{2\pi}\frac{1}{1-n}\log(n_k^n + (1-n_k)^n). \tag{6.15}$$

We recall that Rényi entropies are entanglement measures defined in (0.6) that reduce to the entanglement entropy in the limit $n \to 1$.

For generic integrable models, there can be different types of quasiparticles m with velocities $v_k^{(m)}$ and kernel $s^{(m)}(k)$. In that case, the quasiparticle result (6.11) generalises to a sum over all the different species [44, 49, 50],

$$S_1(t) = \sum_m \left(2t \int_{2v_k^{(m)} t < \ell} \mathrm{d}k \; v_k^{(m)} s^{(m)}(k) + \ell \int_{2v_k^{(m)} t > \ell} \mathrm{d}k \; s^{(m)}(k)\right). \tag{6.16}$$

In general, it is a daunting task to compute the full entanglement dynamics from exact lattice calculations. In a seminal paper, Fagotti and Calabrese computed the time-dependent entanglement entropy after a

quench in the XY spin chain [48] with ab-initio calculations, and their result matches the quasiparticle prediction (6.11) in the scaling limit. For generic interacting integrable models, the quasiparticle predictions have been tested with numerical results for the XXZ spin chain [49, 50] and the spin-1 Lai–Sutherland model [227]. We also stress that generalising the quasiparticle picture for the Rényi entropies with $n > 1$ in interacting integrable models is still an open problem [226, 228–231].

Disjoint intervals

Let us consider the case in which the subsystem A of length ℓ is formed by two disjoint intervals A_1 and A_2 of respective lengths ℓ_1 and ℓ_2 that are separated by a distance d. Without loss of generality we consider $\ell_1 \leqslant \ell_2$. In this case, we investigate the mutual information (0.7) to quantify the entanglement between A_1 and A_2. In terms of the quasiparticle picture, the total mutual information is related to the number of entangled pairs that, once emitted from the same point, are shared by the two subsystems at subsequent times.

To gain an intuitive understanding of the general quasiparticle result for the dynamics of the mutual information, we first assume that the quasiparticles possess a single velocity v. For short times $t < d/(2v)$, there are no entangled quasiparticles shared by the two intervals and the mutual information is zero. At $t = d/(2v)$, the pair of quasiparticles emitted from the center of the interval of length d reaches the subsystems A_1 and A_2, and the mutual information starts growing linearly in time. For $(d+\ell_1)/(2v) \leqslant t \leqslant (d+\ell_2)/(2v)$, there is a plateau because the rates of pairs that start and stop being shared are the same. The plateau is followed by a linear decrease in time up to $t = (d + \ell)/2v$. For $t \geqslant (d + \ell)/2v$, there are no longer any quasiparticles shared between the subsystems, and the mutual information vanishes. Accordingly, the mutual information is [21, 232]

$$I_1^{A_1:A_2} \propto \max(d, 2vt) + \max(d + \ell, 2vt) - \max(d + \ell_1, 2vt) - \max(d + \ell_2, 2vt). \quad (6.17)$$

We illustrate this behaviour in Figure 6.2.

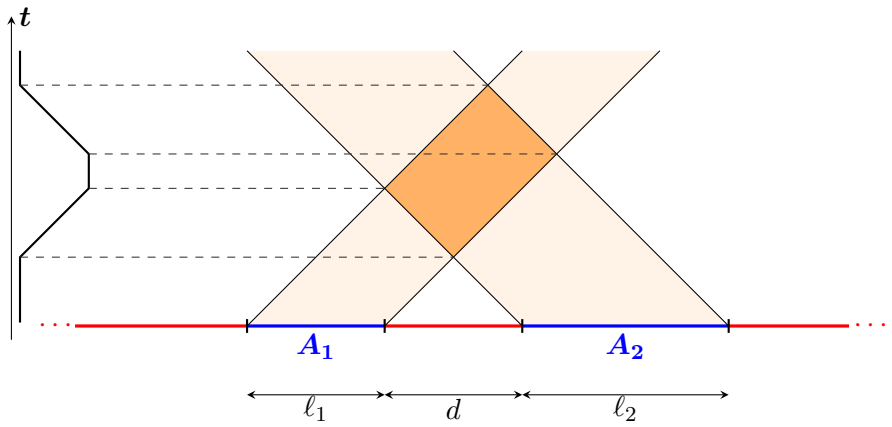

Figure 6.2: Illustration of the mutual information dynamics in the case where there is a single velocity for the quasiparticles. At a given time t, the number of quasiparticles shared between A_1 and A_2 is proportional to the width of the darker orange region. The typical behaviour of the mutual information is reported on the vertical plot on the left. It illustrates the delay before the linear increase, the plateau and the linear decrease discussed in the main text.

In the case of a non-trivial dispersion where the quasiparticles with momenta $\pm k$ have the velocity v_k, the total mutual information reads [21, 49, 50]

$$I_1^{A_1:A_2} = \int \mathrm{d}k\ s(k)(\max(d, 2v_k t) + \max(d+\ell, 2v_k t) - \max(d+\ell_1, 2v_k t) - \max(d+\ell_2, 2v_k t)) \quad (6.18)$$

in the scaling limit, where $s(k)$ is the same kernel as for the entanglement entropy in (6.11). For free fermions, $s(k)$ is given in (6.13). In the case of generic integrable models, (6.18) generalises to a sum over the different species of quasiparticles, similarly to the entanglement entropy.

6.2 Symmetry-resolved entanglement

In this section we give the general definitions of the main quantities of interest for this part of the thesis, namely the symmetry-resolved entanglement entropies. We focus on extended quantum systems with an internal $U(1)$ symmetry. In particular, we show how to express the symmetry-resolved quantities in the context of a free-fermion model. The following discussion is mainly based on the work of Goldstein and Sela [65] and Xavier, Alcaraz and Sierra [66], but we use the conventions of Bonsignori, Ruggiero and Calabrese [198]. For the interested reader, we recommend the latter article for a pedagogical introduction to the subject.

6.2.1 Symmetry resolution

We consider an extended quantum system with an internal $U(1)$ symmetry generated by a global operator Q that is a sum of local operators. In particular, Q splits as a sum of two operators, $Q = Q_A + Q_B$, in the case of a bipartition in two complementary subsystems A and B. Here Q_s, $s = A, B$, acts on the degrees of freedom of the subsystem s. We also assume that the system is in an eigenstate $|\psi_Q\rangle$ of Q. As a consequence, the density matrix $\rho = |\psi_Q\rangle\langle\psi_Q|$ commutes with the charge, $[\rho, Q] = 0$. In the case of a bipartition, the trace over the degrees of freedom of subsystem B in the commutation relation $[\rho, Q] = 0$ yields

$[\rho_A, Q_A] = 0$. This relation implies that the reduced density matrix ρ_A acquires a block diagonal form, where each block corresponds to a given eigenvalue q of Q_A. We thus have

$$\rho_A = \oplus_q \Pi_q \rho_A = \oplus_q [p(q)\rho_A(q)] \tag{6.19}$$

where Π_q is the projector on the eigenspace corresponding to the eigenvalue q, and $p(q) = \mathrm{Tr}\,(\Pi_q \rho_A)$ is the probability that a measurement of Q_A gives q as outcome. The reduced density matrix in the sector q is normalised so that $\mathrm{Tr}\rho_A(q) = 1$. The average value of the charge in subsystem A, denoted $\langle Q_A \rangle$, is

$$\langle Q_A \rangle = \mathrm{Tr}(\rho_A Q_A). \tag{6.20}$$

The block structure of the reduced density matrix induces a decomposition of the entanglement entropy into contributions associated to each charge sector. For example, plugging (6.19) into the definition of the entanglement entropy (0.4), we obtain

$$S_1 = \sum_q p(q) S_1(q) - \sum_q p(q) \log(p(q)) \equiv S^c + S^n \tag{6.21}$$

where $S_1(q)$ is the *symmetry-resolved entanglement entropy* associated to the charge sector q,

$$S_1(q) \equiv -\mathrm{Tr}(\rho_A(q) \log \rho_A(q)). \tag{6.22}$$

The two terms in (6.21) are the so-called *configurational entropy* (S^c) [52, 233–235] and *number entropy* (S^n) [52, 236–241]. The former quantifies the average of the entanglement in each charge sector, whereas the latter measures the entropy caused by the fluctuations of the value of the charge within subsystem A.

Similarly, the *symmetry-resolved Rényi entropies* are defined as

$$S_n(q) \equiv \frac{1}{1-n} \log \mathrm{Tr}\rho_A(q)^n. \tag{6.23}$$

There is an expression similar to (6.21) that expresses the total Rényi entropies in terms of the symmetry-resolved one [199], but we do not use it in the following and do not reproduce it here.

In principle, the evaluation of the symmetry-resolved contributions requires the knowledge of the resolution of the spectrum of ρ_A in Q_A. This is a highly non-trivial problem, mainly because of the non-local nature of the projector Π_q. A different strategy, put forward in [65,66], is based on the evaluation of the *charged moments*

$$Z_n(\alpha) \equiv \mathrm{Tr}(\rho_A^n \mathrm{e}^{\mathrm{i}\alpha Q_A}). \tag{6.24}$$

We mention that the charged moments evaluated at $\alpha = 0$ are proportional to the total entanglement entropies,

$$S_n = \frac{1}{1-n} \log Z_n(0), \qquad S_1 = -(\partial_n Z_n(0))|_{n=1}. \tag{6.25}$$

The symmetry-resolved entanglement entropies are obtained from the Fourier transform of the charged moments,

$$\mathcal{Z}_n(q) = \int_{-\pi}^{\pi} \frac{d\alpha}{2\pi} \mathrm{e}^{-\mathrm{i}q\alpha} Z_n(\alpha) \equiv \mathrm{Tr}(\Pi_q \rho_A^n), \tag{6.26}$$

and read

$$S_n(q) = \frac{1}{1-n} \log\Big(\frac{\mathcal{Z}_n(q)}{\mathcal{Z}_1(q)^n}\Big), \qquad S_1(q) = -\partial_n\Big(\frac{\mathcal{Z}_n(q)}{\mathcal{Z}_1(q)^n}\Big)\Big|_{n=1}. \tag{6.27}$$

Finally, the probability $p(q)$ is

$$p(q) = \mathcal{Z}_1(q). \tag{6.28}$$

6.2.2 Free fermions

The charged moments $Z_n(\alpha)$ are the key ingredients in the definition of the symmetry-resolved entanglement entropies. In this section, we show how to compute $Z_n(\alpha)$ in the tight-binding model, a one-dimensional free-fermion model with a $U(1)$ symmetry. For a chain of size L with periodic boundary conditions, the Hamiltonian is

$$H = \sum_{j=1}^{L} (c_j^\dagger c_{j+1} + c_{j+1}^\dagger c_j). \tag{6.29}$$

Here, c_j and $c_j^\dagger$ are the canonical fermionic annihilation and creation operators on site j, that satisfy the anticommutation relations $\{c_i, c_j^\dagger\} =$

$\delta_{i,j}$ and $\{c_i, c_j\} = \{c_i^\dagger, c_j^\dagger\} = 0$. Up to a sign, (6.29) is the Hamiltonian (1.54) with periodic boundary conditions, and is thus equivalent to the XX spin chain via the Jordan-Wigner transformation (1.52). The conserved charge is the fermion number

$$Q = \sum_{j=1}^{L} c_j^\dagger c_j, \tag{6.30}$$

and it trivially splits as

$$Q = \sum_{j\in A} c_j^\dagger c_j + \sum_{j\in B} c_j^\dagger c_j = Q_A + Q_B \tag{6.31}$$

in the case of a bipartition in two complementary subsystems A and B. We consider the case where A is a subsystem of size ℓ, but the following results are independent of the topology of A.

In the following, we consider states $|\psi_0\rangle$ that satisfy the factorisation property

$$\langle\psi_0|c_{x_1}\cdots c_{x_n} c^\dagger_{x_{n+1}}\cdots c^\dagger_{x_{2n}}|\psi_0\rangle = \det_{i,j=1}^{n} \langle\psi_0|c_{x_i} c^\dagger_{x_{n+j}}|\psi_0\rangle. \tag{6.32}$$

Such states are often denoted *Slater determinants* in the literature [242], and are ubiquitous in free-fermion models. For instance, the eigenstates of free-fermion Hamiltonians satisfy (6.32), and when $|\psi_0\rangle$ is the fermionic vacuum $|0\rangle$, the condition (6.32) is equivalent to Wick's theorem (2.62). Another aspect of free-fermion models is that many operators $\mathcal{G}$ can be expressed as exponentials of quadratic forms of fermion operators,

$$\mathcal{G} = g\ \mathrm{e}^{-\sum_{i,j} G_{i,j} c_i^\dagger c_j}, \tag{6.33}$$

where g is a constant and G is a diagonalisable matrix. Such operators are denoted *Gaussian operators*. In particular, when the whole system is in a state $|\psi_0\rangle$ that satisfies (6.32), the reduced density matrix of A is Gaussian and reads

$$\rho_A = \frac{1}{Z}\mathrm{e}^{-\sum_{i,j} h_{i,j} c_i^\dagger c_j}, \quad Z = \mathrm{Tr}\Big(\mathrm{e}^{-\sum_{i,j} h_{i,j} c_i^\dagger c_j}\Big). \tag{6.34}$$

The matrix h depends on the state $|\psi_0\rangle$, but we do not need its explicit form. Since ρ_A is a Gaussian operator, it is completely determined by

the two-point correlation matrix $C_A = \langle\psi_0|c_x^\dagger c_{x'}|\psi_0\rangle$, with $x, x' \in A$ [125, 242, 243]. By definition, we have

$$[C_A]_{x,x'} = \mathrm{Tr}(\rho_A c_x^\dagger c_{x'}), \quad x, x' \in A \tag{6.35}$$

and the eigenvalues of h and C_A, respectively denoted ϵ_k and ξ_k, satisfy

$$\xi_k = \left(\mathrm{e}^{\epsilon_k} + 1\right)^{-1}. \tag{6.36}$$

Because ρ_A commutes with Q_A, and hence with the Gaussian operator $\mathrm{e}^{\mathrm{i}\alpha Q_A}$, the relation between ρ_A and C_A can be generalised to the charged moments $Z_n(\alpha)$ (6.24) as [65]

$$\log Z_n(\alpha) = \mathrm{Tr}\log\left[(C_A)^n \mathrm{e}^{\mathrm{i}\alpha} + (1 - C_A)^n\right]. \tag{6.37}$$

For later convenience, we define the matrix J_A as

$$J_A = 2C_A - \mathbb{I}_\ell \tag{6.38}$$

where $\mathbb{I}_\ell$ is the $\ell \times \ell$ identity matrix. We denote the eigenvalues of J_A by ν_i, $i = 1, \ldots, \ell$, and write the charged moments as

$$\log Z_n(\alpha) = \sum_{i=1}^{\ell} \log\left[\left(\frac{1+\nu_i}{2}\right)^n \mathrm{e}^{\mathrm{i}\alpha} + \left(\frac{1-\nu_i}{2}\right)^n\right]. \tag{6.39}$$

To perform analytical calculations, it is useful to express the charged moments as a Taylor series in $\mathrm{Tr}J_A^m$. We thus introduce the function $h_{n,\alpha}(x)$ and the coefficients $c_{n,\alpha}(m)$ as

$$h_{n,\alpha}(x) = \log\left[\left(\frac{1+x}{2}\right)^n \mathrm{e}^{\mathrm{i}\alpha} + \left(\frac{1-x}{2}\right)^n\right] \equiv \sum_{m=0}^{\infty} c_{n,\alpha}(m) x^m \tag{6.40}$$

and conclude

$$\log Z_n(\alpha) = \sum_{m=0}^{\infty} c_{n,\alpha}(m) \mathrm{Tr}J_A^m. \tag{6.41}$$

As we shall see in the subsequent chapters, the precise form of the coefficients $c_{n,\alpha}(m)$ is not needed.

6.3 Organisation of Part II

After a quantum quench in the tight binding model (6.29), if the initial state $|\psi_0\rangle$ is a Slater determinant, then time-evolved state

$$|\psi(t)\rangle = \mathrm{e}^{-\mathrm{i}tH}|\psi_0\rangle \tag{6.42}$$

also satisfies (6.32) at all times during the unitary evolution. In the following, we use this property to investigate the quench dynamics of symmetry-resolved entanglement measures in the tight-binding model. We consider quenches from two low-entangled initial states $|\psi_0\rangle$ that (i) are Slater determinants, (ii) are eigenstates of the fermion number operator Q, and (iii) whose time-dependent correlation matrix $C_A(t) = \langle\psi_0|\mathrm{e}^{\mathrm{i}tH}c_x^\dagger c_{x'}\mathrm{e}^{-\mathrm{i}tH}|\psi_0\rangle$, with $x, x' \in A$, is exactly known when H is the tight-binding Hamiltonian. The states we consider are the Néel and the dimer states, written $|N\rangle$ and $|D\rangle$, respectively. For a system of even length L and with the conventions of Section 1.2.2, they read

$$\begin{aligned} |N\rangle &= \bigotimes_{j=1}^{L/2} |{\downarrow\uparrow}\rangle_{2j-1,2j} = \prod_{j=1}^{L/2} c_{2j}^\dagger|0\rangle, \\ |D\rangle &= \bigotimes_{j=1}^{L/2} \frac{[|{\downarrow\uparrow}\rangle - |{\uparrow\downarrow}\rangle]_{2j-1,2j}}{\sqrt{2}} = \prod_{j=1}^{L/2} \frac{c_{2j}^\dagger - c_{2j-1}^\dagger}{\sqrt{2}}|0\rangle. \end{aligned} \tag{6.43}$$

Despite their apparent simplicity, these two states are relevant to investigate realistic quantum many-body systems. In particular, they can be engineered in cold-atom and ion-trap experiments [53, 244].

In Chapter 7, we derive exact expressions for the charged moments $Z_n(\alpha)$ after the quenches from the Néel and the dimer states. We use these results to investigate the symmetry-resolved Rényi entropies in both cases. In particular, we find that the symmetry-resolved entanglement entropies (i) start growing after a time delay that depends on the charge sector, and (ii) exhibit an effective equipartition in the scaling limit. We argue that the behaviour of the charged moments can qualitatively be understood in terms of the quasiparticle picture for free-fermion models, and we conjecture an analogous result for generic integrable models. We also study the dynamics of the number entropy for both quenches, and find that it grows logarithmically in time before saturating to a value proportional to the logarithm of the subsystem size.

We investigate the case where the subsystem consists of two disjoint intervals in Chapter 8. In particular, we define a symmetry-resolved mutual information and express it in terms of doubly-charged moments that depend on two $U(1)$ charges. For free-fermion models, we express these doubly-charged moments in terms of two-point correlation matrices. We use these results to investigate the dynamics of the symmetry-resolved mutual information after the quenches from the Néel and the dimer states, and find an effective equipartition of the mutual information in the scaling limit.

We present concluding remarks and outlooks in Chapter 9.

7

Symmetry-resolved Rényi entropies after a quench

In this chapter, we use the known expression of the time-dependent correlation matrix $C_A(t)$ to derive exact results and approximations for the charged moments, the symmetry-resolved Rényi entropies and the number entropy after the quenches from the Néel state $|N\rangle$ and the dimer state $|D\rangle$ in the tight-binding model.

We also use the expression of $C_A(t)$ to perform numerical checks of our analytical results. To obtain our numerical results, we diagonalise the matrix by brute force and use the formula (6.39) to obtain the charged moments. The numerical Fourier transform yields the symmetry-resolved moments and entropies. In the following, we consider that our analytical and numerical results match convincingly if they exhibit the same qualitative behaviour, and if the difference between the analytical predictions and the numerical data decreases drastically with the system size. Since we use our numerical investigations to support our analytical results but not to draw new conclusions, we do not quantify the numerical precision further.

In the following, we consider the case where the system A is a single interval of ℓ adjacent sites in an infinite chain with periodic boundary conditions. Because of the translation invariance of the model and the structure of the initial states, we choose $A = \{1, \dots, \ell\}$ and work with even ℓ. Since the charge Q_A is a conserved quantity, its average value

$\langle Q_A \rangle$, defined in (6.20), is fixed by the initial conditions $\langle N|Q_A|N\rangle$ and $\langle D|Q_A|D\rangle$. In both cases we have

$$\langle Q_A \rangle = \frac{\ell}{2}. \tag{7.1}$$

The results discussed in this chapter were initially presented in the publications [1, 2].

7.1 Quench from the Néel state

The two-point correlation function after a quench from the Néel state $|N\rangle$, defined in (6.43), in the tight-binding model (6.29) is $[C(t)]_{x,x'} = \langle N|\mathrm{e}^{\mathrm{i}tH} c_x^\dagger c_{x'} \mathrm{e}^{-\mathrm{i}tH}|N\rangle$ and reads [21]

$$[C(t)]_{x,x'} = \frac{\delta_{x,x'}}{2} + \frac{(-1)^{x'}}{2} \int_{-\pi}^{\pi} \frac{\mathrm{d}k}{2\pi} \mathrm{e}^{\mathrm{i}k(x-x')+4\mathrm{i}t\cos k}. \tag{7.2}$$

As explained in Section 6.2.2, the expression of the time-dependent correlation matrix is the starting point to compute the charged moments, and hence the symmetry-resolved entanglement measures. The correlation matrix of subsystem A is $C_A = \frac{1}{2}(\mathbb{I}_\ell + J_A)$ with

$$[J_A(t)]_{x,x'} = (-1)^{x'} \int_{-\pi}^{\pi} \frac{\mathrm{d}k}{2\pi} \mathrm{e}^{\mathrm{i}k(x-x')+4\mathrm{i}t\cos k}, \quad x, x' \in \{1, 2, \dots, \ell\}. \tag{7.3}$$

7.1.1 Charged moments

The first step to compute the charged moments $Z_n(\alpha)$ is the evaluation of the trace of powers of J_A. Using the exact expression (7.3), it is possible to perform this calculation analytically using the multidimentional stationary phase approximation in the scaling limit, where $t, \ell \to \infty$ with a fixed finite ratio t/ℓ. We adapt the calculations of [48], where the authors find an exact expression for the time-dependent entanglement entropy after a quench in the XY spin chain. Their method relies on the following elements: (i) the correlation matrix is a Toeplitz matrix, and (ii) the exact expressions for the two-point correlation functions contain several terms that oscillate and can be neglected in the scaling limit. In

our case, the correlation matrix in (7.3) satisfies the same properties, and we find

$$\mathrm{Tr}J_A(t)^{2j} = \ell - \int_{-\pi}^{\pi} \frac{\mathrm{d}k}{2\pi} \min(\ell, 2v_k t), \quad \mathrm{Tr}J_A(t)^{2j+1} = 0, \tag{7.4}$$

with $v_k = 2|\sin k|$. We note that, with our normalisation, the maximal velocity $v_M = \max_k v_k$ is $v_M = 2$. To compute the charged moments $Z_n(\alpha)$, we evaluate the sum (6.41) with (7.4). We use the fact that $\mathrm{Tr}J_A(t)^m$ only depends on the parity of the exponent for $m > 0$, and $\mathrm{Tr}J_A(t)^0 = \ell$. We find

$$\log Z_n(\alpha) = \ell c_{n,\alpha}(0) + \mathrm{Tr}J_A(t)^2 \sum_{m=1}^{\infty} c_{n,\alpha}(2m), \tag{7.5}$$

where the coefficients $c_{n,\alpha}(m)$ are defined in (6.40). To proceed, we notice that the coefficient $c_{n,\alpha}(0)$ and the sum $\sum_{m=1}^{\infty} c_{n,\alpha}(2m)$ in fact correspond to the function $h_{n,\alpha}(x)$ from (6.40) evaluated in certain points. Indeed, we have

$$\begin{aligned} c_{n,\alpha}(0) &= h_{n,\alpha}(0) \\ &= (1-n)\log 2 + \log\cos\frac{\alpha}{2} + \mathrm{i}\frac{\alpha}{2}, \\ \sum_{m=1}^{\infty} c_{n,\alpha}(2m) &= \left(\frac{h_{n,\alpha}(1) + h_{n,\alpha}(-1)}{2} - c_{n,\alpha}(0)\right) \\ &= (n-1)\log 2 - \log\cos\frac{\alpha}{2}. \end{aligned} \tag{7.6}$$

It immediately follows that

$$\log Z_n(\alpha) = \mathrm{i}\ell\frac{\alpha}{2} + \int_{-\pi}^{\pi} \frac{\mathrm{d}k}{2\pi} \mathrm{Re}[h_{n,\alpha}(0)] \min(\ell, 2v_k t), \tag{7.7}$$

or equivalently

$$Z_n(\alpha) = \left(\frac{\cos\frac{\alpha}{2}}{2^{n-1}}\right)^{\mathcal{J}} \mathrm{e}^{\mathrm{i}\ell\frac{\alpha}{2}} \tag{7.8}$$

where we introduced the quantity

$$\mathcal{J}(t) \equiv \ell - \mathrm{Tr}J_A(t)^2 = \int_{-\pi}^{\pi} \frac{\mathrm{d}k}{2\pi} \min(\ell, 2v_k t). \tag{7.9}$$

The function $\mathcal{J}(t)$ is an increasing function of time, going from $\mathcal{J}(t = 0) = 0$ to $\mathcal{J}(t = \infty) = \ell$. Its time evolution is separated in two distinct

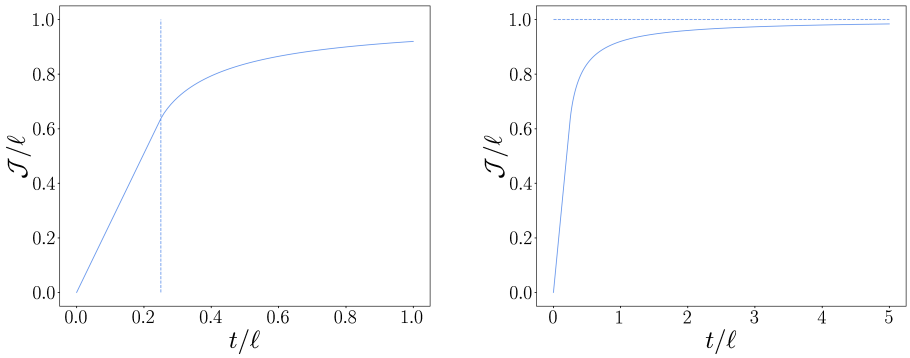

Figure 7.1: Time evolution of $\mathcal{J}(t)/\ell$ from (7.9) as a function of t/ℓ for $\ell = 100$. *Left:* For small times, we observe the cross-over between the linear growth and the saturation. The vertical dashed line indicates the time at which the transition occur and is placed at time $t/\ell = 1/4$. This is in agreement with $t/\ell = 1/(2v_M)$ and $v_M = 2$. *Right:* For large time, $\mathcal{J}(t)/\ell$ saturates to the horizontal dashed line that indicates the value $\mathcal{J}(t = \infty)/\ell = 1$.

regimes. For short times $t < \ell/(2v_M)$, $\mathcal{J}(t) \propto t$ increases linearly with time. On the other hand, for $t > \ell/(2v_M)$ the derivative of $\mathcal{J}(t)$ with respect to t decreases with time, and $\mathcal{J}(t)$ eventually saturates to its asymptotic value ℓ for large time. These behaviours are illustrated in Figure 7.1. From the definition (7.9), it is clear that the ratio $\mathcal{J}(t)/\ell$ is a function of t/ℓ, and in the scaling limit we have $\mathcal{J}(t)/\ell = \mathcal{O}(1)$. In the following, we make repeated use of this property.

In Figure 7.2 we compare the prediction (7.8) for the charged moments $Z_n(\alpha)$ with the numerical results obtained by exact diagonalisation of the correlation matrix. From the top left, top right and bottom left panels, we see that the dependence of $Z_n(\alpha)$ in t and ℓ is convincingly reproduced by the exact result. Concerning the α-dependence, we observe that away from $\alpha = \pi$, the analytic prediction and numerical data match convincingly, even for relatively small ℓ. However, as α gets closer to π, the difference between the numerical results and the exact prediction gets larger. To highlight this phenomenon, we zoom on the region in the vicinity of $\alpha = \pi$ in Figure 7.3. Similar discrepencies close to $\alpha = \pi$ were observed in other contexts [198, 201], and in this case additional terms should be included to correctly describe these large corrections.

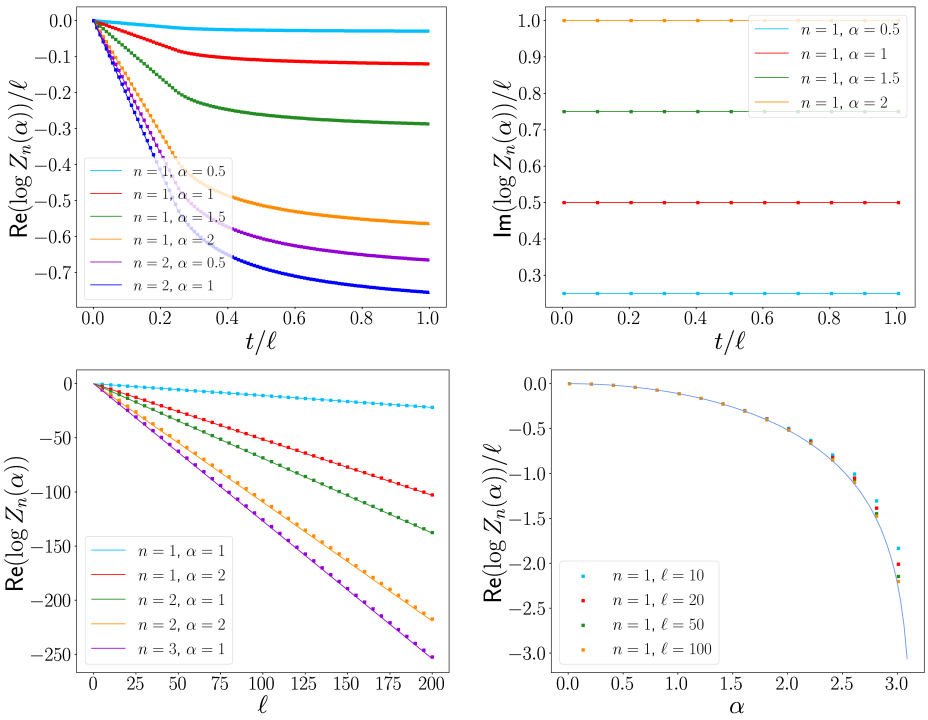

Figure 7.2: Comparison between the exact result (7.8) (solid lines) and numerical results (symbols) for $\log Z_n(\alpha)$ after a quench from the Néel state in the tight-binding model (6.29). *Top left:* Time evolution of the real part of $\log Z_n(\alpha)$ as a function of t/ℓ with $\ell = 120$. *Top right*: Time evolution of the imaginary part of $\log Z_n(\alpha)$ as a function of t/ℓ with $\ell = 20$ and $n = 1$. *Bottom left:* Real part of $\log Z_n(\alpha)$ as a function of ℓ with $t/\ell = 0.5$. *Bottom right:* Real part of $\log Z_n(\alpha)$ as a function of α with $t/\ell = 0.5$ and $n = 1$.

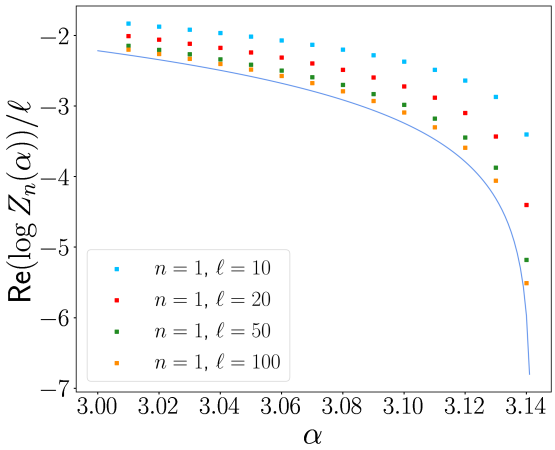

Figure 7.3: Real part of $\log Z_n(\alpha)$ after a quench from the Néel state in the tight-binding model (6.29) as a function of α with $t/\ell = 0.5$ and $n = 1$ near the value $\alpha = \pi$.

However, this issue will not affect our forthcoming investigations, because we strongly rely on saddle-point approximations close to $\alpha = 0$.

7.1.2 Fourier transform

In this section, we compute the symmetry-resolved moments $\mathcal{Z}_n(q)$ defined in (6.26) as the Fourier transform of the charged moments $Z_n(\alpha)$. We express the charge q in terms of the average value of Q_A as $q = \Delta q + \langle Q_A \rangle$. The quantity Δq measures the difference between the charge sector q and the average value of the charge. By definition, we have

$$\mathcal{Z}_n(q) = \int_{-\pi}^{\pi} \frac{d\alpha}{2\pi} \mathrm{e}^{-\mathrm{i}(\Delta q + \frac{\ell}{2})\alpha} Z_n(\alpha) \tag{7.10}$$

where we used $\langle Q_A \rangle = \frac{\ell}{2}$. To proceed, we introduce the function $\zeta_n(q)$ as

$$\zeta_n(q) \equiv 2^{(1-n)\mathcal{J}} \int_{-\pi}^{\pi} \frac{\mathrm{d}\alpha}{2\pi} \left(\cos\frac{\alpha}{2}\right)^{\mathcal{J}} \mathrm{e}^{-\mathrm{i}\alpha\Delta q} \tag{7.11}$$

where the function $\mathcal{J} = \mathcal{J}(t)$ is defined in (7.9). In the scaling limit where $\ell, t \to \infty$ with fixed t/ℓ, we use the asymptotic result (7.8) and find

$$\mathcal{Z}_n(q) = \zeta_n(q). \tag{7.12}$$

In finite size however, the function $\zeta_n(q)$ in (7.11) can be negative, whereas the symmetry-resolved moment $\mathcal{Z}_n(q)$ as defined in (6.26) are positive quantities. In particular, $\mathcal{Z}_1(q)$ is interpreted as a probability, as we discussed in Section 6.2.1. In the following, we investigate the properties of the function $\zeta_n(q)$.

Since the n-dependence in (7.11) is simple, we focus on $n = 1$. The integral $\zeta_1(q)$ can be evaluated in terms of the Euler Beta function $B(x, y) = \frac{\Gamma(x)\Gamma(y)}{\Gamma(x+y)}$, where $\Gamma(z)$ is the Gamma function. With the integral representation

$$B(x, y) = \int_0^1 \mathrm{d}t\; t^{x-1}(1-t)^{y-1}, \tag{7.13}$$

the result reads

$$\zeta_1(q) = 2^{-\mathcal{J}} \frac{\Gamma(\mathcal{J}+1)}{\Gamma\big(\frac{\mathcal{J}+2\Delta q+2}{2}\big)\Gamma\big(\frac{\mathcal{J}-2\Delta q+2}{2}\big)}. \tag{7.14}$$

The function $\zeta_1(q)$ depends on $\mathcal{J} = \mathcal{J}(t)$ and hence implicitly on t. Since $\mathcal{J}(t)$ is a monotonically increasing function of time, we investigate the behaviour of $\zeta_1(q)$ as a function of $\mathcal{J}$ to understand its time evolution. However, we plot $\zeta_1(q)$ as a function of t/ℓ in Figure 7.4 to ease the comparison with forthcoming results.

The function $\Gamma(z)$ has poles when z is a negative integer. Since $\mathcal{J} \geq 0$, it follows that $\zeta_1(q)$ vanishes when $\mathcal{J} - 2|\Delta q|$ is a negative even integer. For other values of $\mathcal{J}$ in the regime $\mathcal{J} < 2|\Delta q|$, the function $\zeta_1(q)$ oscillates in ℓ around zero. We illustrate this behaviour on the top panels of Figure 7.4. The amplitudes of the oscillations quickly decay to zero for increasing ℓ, an in the scaling limit we have $\mathcal{Z}_1(q) = \zeta_1(q) = 0$. The last zero of the function $\zeta_1(q)$ is at position $\mathcal{J} = 2|\Delta q| - 2$, after which it starts growing monotonically with $\mathcal{J}$. At $\mathcal{J} = 2|\Delta q|$, we have $\zeta_1(q) = 2^{-\mathcal{J}}$. This value becomes negligible in the scaling limit, and we conclude that $\mathcal{Z}_1(q) = 0$ in the regime $\mathcal{J} < 2|\Delta q|$, whereas it grows monotonically in $\mathcal{J}$ (en hence in t) for $\mathcal{J} > 2|\Delta q|$. These behaviours are illustrated on the bottom panels of Figure 7.4, where we compare the exact result (7.14) for $\zeta_1(q)$ (solid lines) with numerical computations of $\mathcal{Z}_1(q)$ (symbols). In particular, on the bottom left panel, we indeed observe that $\mathcal{Z}_1(q)$ vanishes for small $\mathcal{J}$, whereas $\zeta_1(q)$ oscillates and can be negative.

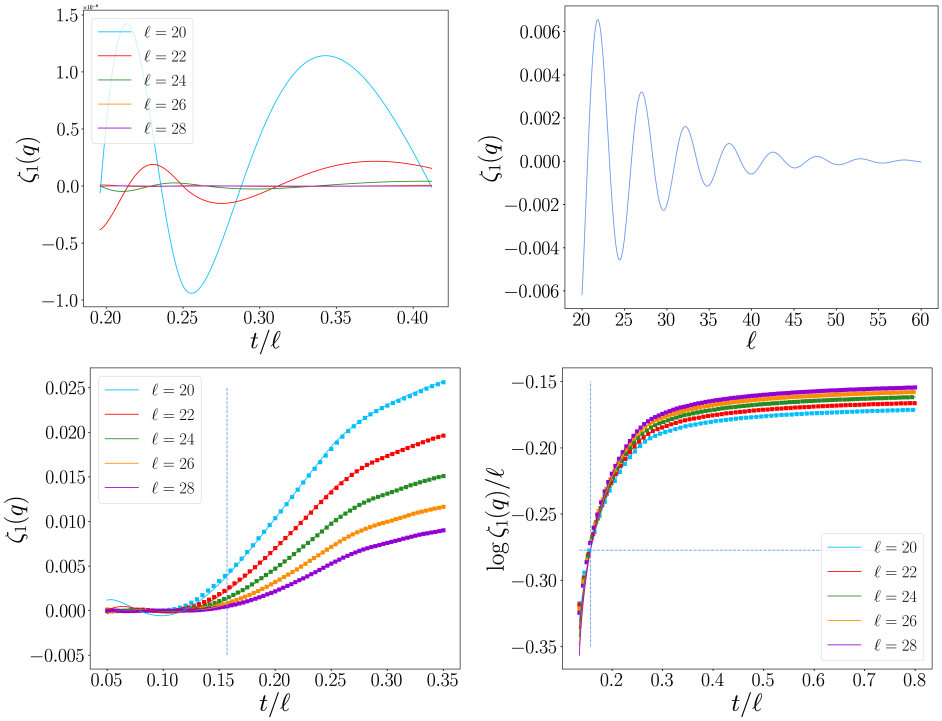

Figure 7.4: The function $\zeta_1(q)$ in (7.14) after a quench from the Néel state in the tight-binding model (6.29). **Top**: Short time regime $\mathcal{J} < 2|\Delta q|$. *Left:* $\zeta_1(q)$ as a function of t/ℓ for $q = \ell$ and various values of ℓ. As ℓ increases, $\zeta_1(q)$ quickly averages to zero. *Right:* $\zeta_1(q)$ as a function of ℓ with $q = 9\ell/10$ and fixed $\mathcal{J} = \ell/100$. **Bottom**: $\zeta_1(q)$ (left) and $\log \zeta_1(q)/\ell$ (right) as a function of t/ℓ with $q = 7\ell/10$. We compare the exact formula (7.14) for $\zeta_1(q)$ (solid lines) with numerical data for $\mathcal{Z}_1(q)$ (symbols). The vertical dashed lines are placed at the value of t/ℓ corresponding to $\mathcal{J}(t)/\ell = 2|\Delta q|/\ell = 2/5$ in both panels. *Left:* $\zeta_1(q)$ starts growing monotonically at the value of t/ℓ corresponding to $\mathcal{J}(t) = 2|\Delta q| - 2$. *Right:* The horizontal dashed line is at position $\log \zeta_1(q) = -2|\Delta q| \log 2$. All the curves collapse on the point $\zeta_1(q) = 2^{-\mathcal{J}}$ at the value of t/ℓ corresponding to $\mathcal{J}(t) = 2|\Delta q|$.

In the following, we only work in the scaling limit. In the regime $\mathcal{J} > 2|\Delta q|$, we use Stirling's formula to derive the asymptotic behaviour of $\mathcal{Z}_1(q)$ and find

$$\log \mathcal{Z}_1(q) = -\Big(\frac{\mathcal{J}}{2}+|\Delta q|\Big)\log\Big(1+\frac{2|\Delta q|}{\mathcal{J}}\Big)-\Big(\frac{\mathcal{J}}{2}-|\Delta q|\Big)\log\Big(1-\frac{2|\Delta q|}{\mathcal{J}}\Big) + \frac{1}{2}\log\Big(\frac{4\mathcal{J}}{(\mathcal{J}+2\Delta q)(\mathcal{J}-2\Delta q)}\Big) - \frac{1}{2}\log 2\pi. \quad (7.15)$$

The first line of (7.15) contains the leading terms, the second one gives the first corrections, and sub-leading terms are omitted.

We have seen that $\mathcal{Z}_1(q)$ is zero for short $\mathcal{J}$ and starts growing at $\mathcal{J} = 2\Delta q$. These relations can be transferred from the auxiliary variable $\mathcal{J}$ to the physical time t. The crossover between the zero-probability regime and the growing one takes place at a time t_D that we dub *delay time*. The latter is defined by the relation $\mathcal{J}(t_D) = 2|\Delta q|$. In general, this relation does not allow us to find an explicit expression for t_D. However, for $2v_M t < \ell$ the definition (7.9) reads

$$\mathcal{J}(t) = 2t\int_{-\pi}^{\pi}\frac{\mathrm{d}k}{2\pi}v_k, \quad 2v_M t < \ell. \quad (7.16)$$

Since $v_k = 2|\sin k|$ and $v_M = 2$, we find

$$4t_D\int_{-\pi}^{\pi}\frac{\mathrm{d}k}{2\pi}|\sin k| = 2|\Delta q|, \quad 4t_D < \ell, \quad (7.17)$$

and conclude

$$t_D = \pi\frac{|\Delta q|}{4}, \quad \text{for} \quad |\Delta q| < \frac{\ell}{\pi}. \quad (7.18)$$

For larger $|\Delta q|$, there is no explicit expression for t_D. In Figure 7.5 we compare the numerical solution of $\mathcal{J}(t_D) = 2|\Delta q|$ (symbols) with the linear result $t_D = \pi\frac{|\Delta q|}{4}$ (solid line). For $|\Delta q| < \frac{\ell}{\pi}$ the match is perfect, but for larger Δq the delay grows faster than linearly in $|\Delta q|$.

Even though the behaviour of $\mathcal{Z}_1(q)$ in the scaling limit is encoded in (7.14), we also analyse it with the saddle-point approximation. The reason is that this method is useful in the cases where there are no analytical formulas for $\mathcal{Z}_1(q)$ comparable to (7.14). We recast (7.12) as

$$\mathcal{Z}_1(q) = \int_{-\pi}^{\pi}\frac{\mathrm{d}\alpha}{2\pi}\mathrm{e}^{\ell h(\alpha)}, \quad h(\alpha) = -\mathrm{i}\alpha\frac{\Delta q}{\ell} + \frac{\mathcal{J}}{\ell}\log\cos\frac{\alpha}{2}, \quad (7.19)$$

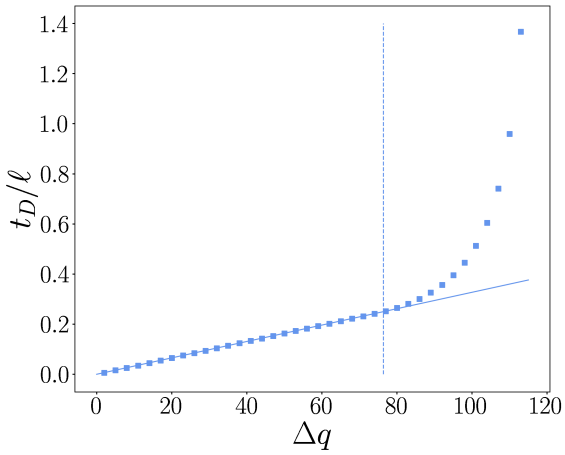

Figure 7.5: Delay t_D obtained from the numerical solution of $\mathcal{J}(t_D) = 2|\Delta q|$ for $\ell = 240$ (symbols) compared with the linear result $t_D = \pi\frac{|\Delta q|}{4}$ (solid line). The dashed vertical line is at position $\Delta q = \frac{\ell}{\pi}$.

so that the saddle point α^*, defined as $h'(\alpha^*) = 0$, is

$$\alpha^* = -2\mathrm{i}\,\mathrm{arctanh}\left(\frac{2\Delta q}{\mathcal{J}}\right) = \mathrm{i}\log\left(\frac{\mathcal{J}-2\Delta q}{\mathcal{J}+2\Delta q}\right). \tag{7.20}$$

We have two regimes, (i) $\mathcal{J} < 2|\Delta q|$, where α^* has a real part, and (ii) $\mathcal{J} > 2|\Delta q|$, where α^* is purely imaginary. In the first regime, the real part of α^* leads to a non-zero imaginary part of $h(\alpha^*)$ and $\mathcal{Z}_1(q)$ oscillates quickly in ℓ around zero. This behaviour is the same as the one we found by analysing the exact formula (7.14). These oscillations average to zero for all the relevant physics.

Conversely, for $\mathcal{J} > 2|\Delta q|$, we deform the integration contour to pass through α^* while remaining in the analyticity region of the integrand. The saddle-point method gives

$$\mathcal{Z}_1(q) = \mathrm{e}^{\ell h(\alpha^*)}\sqrt{\frac{1}{2\pi\ell|h''(\alpha^*)|}}. \tag{7.21}$$

The logarithm of this equation precisely gives (7.15), as expected. In the limit where $\mathcal{J} \gg |\Delta q|$ we have

$$\mathcal{Z}_1(q) = \sqrt{\frac{2}{\mathcal{J}\pi}}\mathrm{e}^{-\frac{2\Delta q^2}{\mathcal{J}}} \tag{7.22}$$

at leading order.

7.1.3 Symmetry-resolved Rényi entropies

We now turn to the evaluation of the symmetry-resolved Rényi entropies in the scaling limit. We insert (7.12) with (7.11) into the definition (6.27) of $S_n(q)$ and find

$$S_n(q) = \mathcal{J} \log 2 + \log \mathcal{Z}_1(q). \tag{7.23}$$

In particular, $S_n(q)$ does not depend on n. In the regime $\mathcal{J} > 2|\Delta q|$, we express $\mathcal{Z}_1(q)$ with (7.14) and obtain an exact result for $S_n(q)$. Following the discussion of the previous section, the entropies start to grow for $t > t_D$. In the top panels of Figure 7.6, we compare the exact prediction (7.23) with numerical results for $S_n(q)$ and find a good agreement. In particular, Figure 7.6 convincingly shows that the numerical results for $S_n(q)$ do not depend on n. We thus focus on $S_1(q)$ for the rest of this subsection. We also compare the prediction (7.18) for the delay with the numerical results in the bottom right panel of Figure 7.6 and again find a very good agreement.

If in the scaling limit we also take $\mathcal{J} \gg |\Delta q|$, we expand (7.23) in powers of $|\Delta q|/\mathcal{J}$ and find

$$S_n(q) = \mathcal{J} \left(\log 2 - 2 \Big(\frac{\Delta q}{\mathcal{J}} \Big)^2 \right). \tag{7.24}$$

This equation implies that for small $|\Delta q|$ there is an effective equipartition of entanglement between the various symmetry sectors, with violations of order $(\Delta q)^2/\ell$. We report this prediction as dashed lines in the bottom left panel of Figure 7.6. There appears to be some discrepancies, close to the delay time, between this approximation and the numerical results, even for small $|\Delta q|$, where one would expect the approximation to be very accurate. The reason for such disagreement is that at the delay time we have $\mathcal{J}(t_D) = 0$, and hence the subleading terms in (7.24) cannot be neglected. Looking at (7.15) (or equivalently (7.21)), we see that the first correction to $S_n(q)/\ell$ in the large-ℓ expansion is proportional to $\ell^{-1} \log \ell$. In the same panel of Figure 7.6, we add this correction to S_n/ℓ and report $\frac{\mathcal{J}}{\ell} \left(\log 2 - 2 \Big(\frac{\Delta q}{\mathcal{J}} \Big)^2 \right) - 1/(2\ell) \log \ell$ as the dotted lines. These curves get closer to the numerical data and fit them convincingly for $t \gg t_D$, namely in the region where $\mathcal{J}$ is significantly

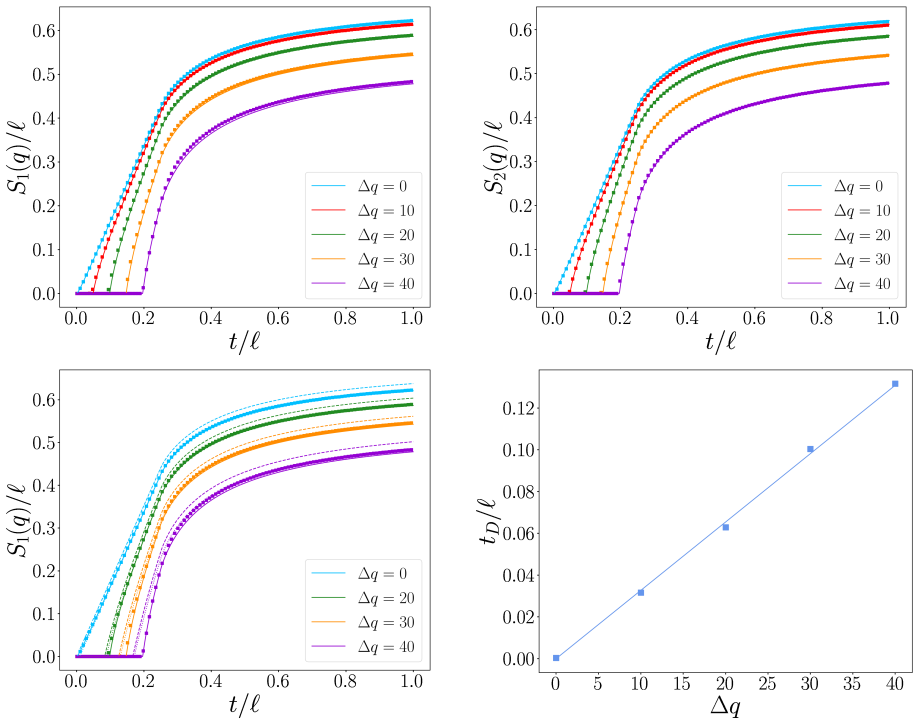

Figure 7.6: *Top left and right:* Time evolution of the symmetry-resolved entanglement entropies $S_n(q)$ after a quench from the Néel state in the tight-binding model (6.29). We compare the exact numerical results for $\ell = 160$ and various Δq (symbols) with our prediction (7.23) (solid line) and find a good agreement. *Bottom left:* The dashed lines are the approximation (7.24) and the dotted ones are the same approximation with the logarithmic correction. *Bottom right:* Delay time t_D for various Δq and $\ell = 240$. The solid line is the analytic prediction (7.18) and the symbols are the numerical results. They are obtained as the time for which $S_1(q)/\ell = 0.007$.

larger than $|\Delta q|$. The correction is of order $\ell^{-1}\log\ell$ and is thus subleading in the scaling limit. We conclude that the prediction (7.24) correctly reproduces the numerical data in the regime $\mathcal{J} \gg |\Delta q|$.

7.1.4 Total and number entropies

A question worth investigating it whether our results for the symmetry-resolved entanglement entropy are coherent with the known results for the dynamics of the total entanglement entropy S_1. We also investigate the contribution of the number entropy S^n to the total entanglement. To proceed, we insert (7.23) into (6.21) and find

$$S_1 = \sum_{q=0}^{\ell} \mathcal{Z}_1(q)\mathcal{J}\log 2, \tag{7.25}$$

where we used the relation $p(q) = \mathcal{Z}_1(q)$, given in (6.28). With the exact formula (7.14) it is direct to show that the sum over the probabilities is $\sum_{q=0}^{\ell}\mathcal{Z}_1(q) = 1$ in the scaling limit, as expected. We thus recover the known result for the total entanglement entropy after a quench from the Néel state [49, 50], namely

$$S_1(t) = \log 2 \int_{-\pi}^{\pi} \frac{\mathrm{d}k}{2\pi} \min(\ell, 2v_k t). \tag{7.26}$$

This result corresponds to the quasiparticle prediction (6.14) with $n_k = 1/2$ and $v_k = 2|\sin k|$. For large times, we have $\lim_{t\to\infty} S_1(t) = \ell\log 2$. We stress that (7.26) immediately follows from the relation between the total entanglement and the charged moments (6.25) and our exact result for $Z_n(\alpha)$ in (7.7). However, the fact that we recover this result from our formula (7.23) for the symmetry-resolved entanglement entropy and (6.21) shows that our calculations are consistent.

To better understand the contribution of the charge fluctuation between the various symmetry sectors to the total entropy, we analyse the number entropy S^n. It is defined in (6.21), providing in our case

$$S^n = -\sum_{q=0}^{\ell} \mathcal{Z}_1(q)\log\mathcal{Z}_1(q). \tag{7.27}$$

With the same asymptotic calculations as in Section 7.1.2 and the Gaussian approximation (7.22) for the symmetry-resolved moments, we find

$$S^n = \sqrt{\frac{2}{\mathcal{J}\pi}} \sum_{\Delta q=-\ell/2}^{\ell/2} \Big(\frac{2\Delta q^2}{\mathcal{J}} + \frac{1}{2}\log\frac{\mathcal{J}\pi}{2}\Big) \mathrm{e}^{-\frac{2\Delta q^2}{\mathcal{J}}}. \tag{7.28}$$

The approximation (7.22) holds for $\mathcal{J} \gg |\Delta q|$, but this condition is not met for the extreme values of $|\Delta q|$ in the sum, where instead we have $\mathcal{J} \sim |\Delta q|$. However, such values of the subsystem charge have a very low probability and hence we nonetheless expect this approximation to give good results. Since we are in the scaling limit, we transform the sum in (7.28) into a Gaussian integral. The evaluation is straightforward and we find

$$S^n = \frac{1}{2}\Big(1 + \log\frac{\mathcal{J}\pi}{2}\Big). \tag{7.29}$$

In particular, (7.29) implies that the number entropy grows logarithmically with time until saturation to a value which is proportional to $\log \ell$. This behaviour for the number entropy was observed in many different contexts [237, 238, 240].

In Figure 7.7, we compare the result (7.29) (solid lines) with numerical evaluations of S^n (symbols), and find a good agreement. The inset in the left panel shows the time evolution of S^n in a log-linear scale and highlights the logarithmic growth in time before the saturation. It directly follows from (7.29) that the large-time limit of the number entropy is

$$\lim_{t\to\infty} S^n(t) = \frac{1}{2}\Big(1 + \log\frac{\ell\pi}{2}\Big). \tag{7.30}$$

This asymptotic value is the ordinate of the dotted horizontal line in the left panel of Figure 7.7. Our analysis shows that the number entropy has a negligible contribution to the total entropy for large times,

$$\lim_{t\to\infty} \frac{S^n(t)}{S_1(t)} = \mathcal{O}(\ell^{-1}\log\ell). \tag{7.31}$$

7.2 Quench from the dimer state

In this section, we adapt the calculations of the previous section in the case of a quench from the dimer state $|D\rangle$, defined in (6.43), in the tight-binding model (6.29). Because of the structure of the initial state, the

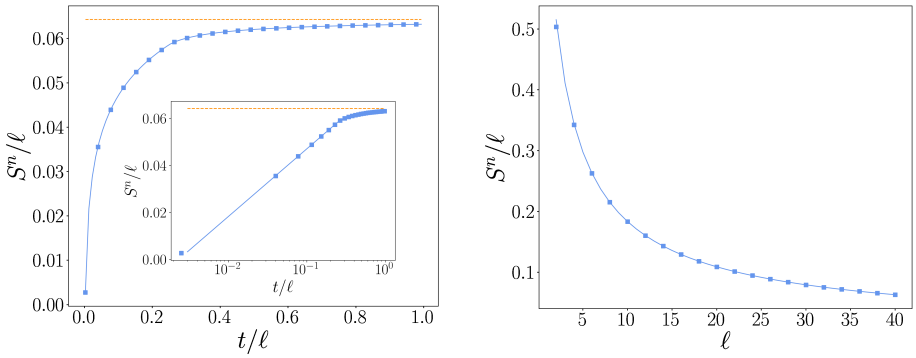

Figure 7.7: Evolution of S^n after a quench from the Néel state in the tight-binding model (6.29) as a function of t/ℓ for $\ell = 40$ (left panel), and as a function of ℓ with $t/\ell = 1$ (right panel). The prediction (7.29) (solid line) convincingly matches the numerical results (symbols). In the left panel, the horizontal dotted line is the asymptotic value $\frac{1}{2\ell}\left(1 + \log\frac{\ell\pi}{2}\right)$ for large times. In the same panel, the inset shows S^n as a function of t/ℓ in a log-linear scale.

two-point correlation functions are organised in 2×2 matrices

$$[C(t)]_{j,k} = \left\langle D \middle| \mathrm{e}^{\mathrm{i}tH} \begin{pmatrix} c^\dagger_{2j-1} \\ c^\dagger_{2j} \end{pmatrix} \cdot \begin{pmatrix} c_{2k-1} & c_{2k} \end{pmatrix} \mathrm{e}^{-\mathrm{i}tH} \middle| D \right\rangle. \tag{7.32}$$

They read [245]

$$[C(t)]_{j,k} = \frac{1}{2}\big(\delta_{j,k}\mathbb{I}_2 + \Pi_{k-j}\big) \tag{7.33}$$

where Π_m is

$$\Pi_m = \mathrm{i}\int_{-\pi}^{\pi} \frac{\mathrm{d}k}{2\pi} \mathrm{e}^{-\mathrm{i}mk} \begin{pmatrix} -f(k,t) & g(k,t) \\ -g(k,t)^* & f(k,t) \end{pmatrix} \tag{7.34}$$

and

$$\begin{aligned} f(k,t) &= \mathrm{i}\sin k \sin(2\epsilon_k t), \\ g(k,t) &= \mathrm{e}^{-\mathrm{i}k}(\cos k + \mathrm{i}\sin k \cos(2\epsilon_k t)), \\ \epsilon_k &= \cos k. \end{aligned} \tag{7.35}$$

The correlation matrix $C_A(t) = \frac{1}{2}(\mathbb{I}_\ell + J_A(t))$ is the $\ell \times \ell$ matrix whose entries are $[C(t)]_{j,k}$ given in (7.33) with $j, k \in \{1, \dots, \ell/2\}$.

7.2.1 Charged moments

We compute the trace of $J_A(t)^m$ in the scaling limit where $t, \ell \to \infty$ with a fixed finite ratio. The computation is exactly the same as in [48] and we find

$$\begin{aligned} \mathrm{Tr} J_A(t)^{2j} &= \ell - \int_{-\pi}^{\pi} \frac{\mathrm{d}k}{2\pi} (1 - (\cos k)^{2j}) \min(\ell, 2v_k t), \\ \mathrm{Tr} J_A(t)^{2j+1} &= 0, \end{aligned} \tag{7.36}$$

with $v_k = 2|\sin k|$. As for the quench from the Néel state, the maximal velocity is $v_M = 2$. We evaluate the sum (6.41) with (7.36) and find

$$\log Z_n(\alpha) = \mathrm{i}\ell\frac{\alpha}{2} + \int_{-\pi}^{\pi} \frac{\mathrm{d}k}{2\pi} \mathrm{Re}[h_{n,\alpha}(\cos k)] \min(\ell, 2v_k t) \tag{7.37}$$

where $h_{n,\alpha}(x)$ is given in (6.40). This result is very similar to the result (7.7) for the Néel quench, with the difference that the function $h_{n,\alpha}(x)$ is now evaluated in $x = \cos k$ and hence cannot be factorised out of the integral. In Figure 7.8 we compare this prediction with numerical results and find a very good agreement.

7.2.2 Fourier transform and symmetry-resolved entropies

We evaluate the symmetry-resoled moments $\mathcal{Z}_n(q)$ with the definition (6.26) and $q = \Delta q + \langle Q_A \rangle$. For a quench from the dimer state, we have $\langle Q_A \rangle = \ell/2$. In the scaling limit, we use the asymptotic result (7.37) and find

$$\mathcal{Z}_n(q) = \int_{-\pi}^{\pi} \frac{\mathrm{d}\alpha}{2\pi} \mathrm{e}^{-\mathrm{i}\alpha\Delta q + \int_{-\pi}^{\pi} \frac{\mathrm{d}k}{2\pi} \mathrm{Re}[h_{n,\alpha}(\cos k)] \min(\ell, 2v_k t)}. \tag{7.38}$$

Contrarily to the quench from the Néel state, there is no closed-form expression similar to (7.14) for this integral. However, we can infer the validity of our two main results, namely the existence of a time delay that grows linearly in $|\Delta q|$ for small values of $|\Delta q|$, and an effective equipartition of entanglement broken at order $(\Delta q)^2/\ell$.

For the delay, we analyse (7.38) with the saddle-point approximation in the regime where $2v_M t < \ell$. The saddle-point equation is

$$-\mathrm{i}\Delta q + \mathrm{i}t \int_{-\pi}^{\pi} \frac{\mathrm{d}k}{2\pi} \partial_{\mathrm{i}\alpha} \big(\mathrm{Re}[h_{n,\alpha}(\cos k)]\big) 2v_k = 0 \tag{7.39}$$

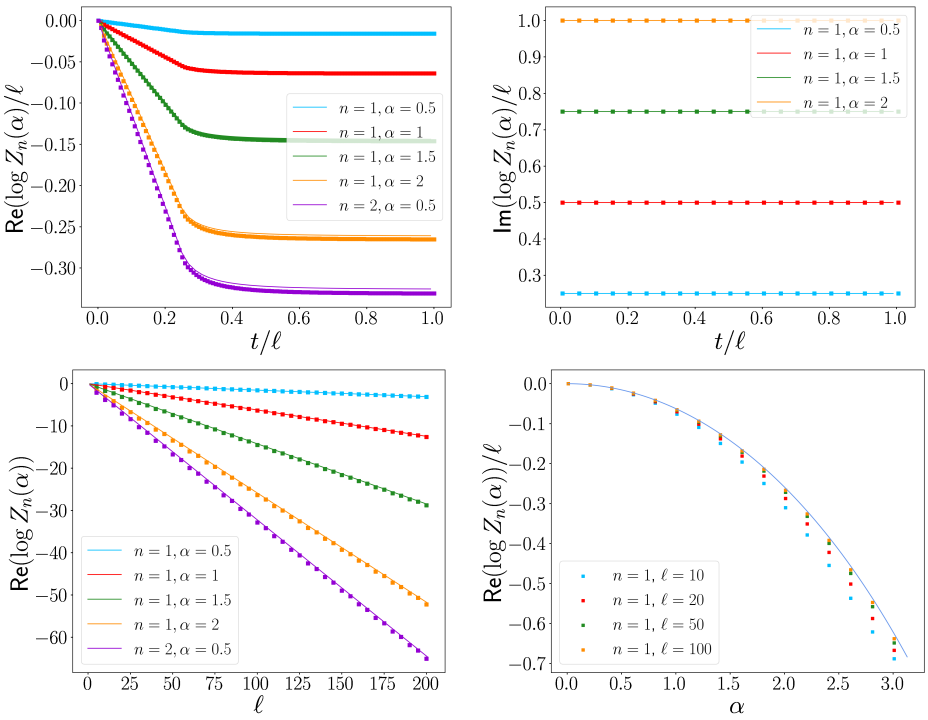

Figure 7.8: Comparison between the exact result (7.37) (solid lines) and numerical results (symbols) for $\log Z_n(\alpha)$ after a quench from the dimer state in the tight-binding model (6.29). *Top left:* Time evolution of the real part of $\log Z_n(\alpha)$ as a function of t/ℓ with $\ell = 120$. *Top right*: Time evolution of the imaginary part of $\log Z_n(\alpha)$ as a function of t/ℓ with $\ell = 20$ and $n = 1$. *Bottom left:* Real part of $\log Z_n(\alpha)$ as a function of ℓ with $t/\ell = 0.5$. *Bottom right:* Real part of $\log Z_n(\alpha)$ as a function of α with $t/\ell = 0.5$ and $n = 1$.

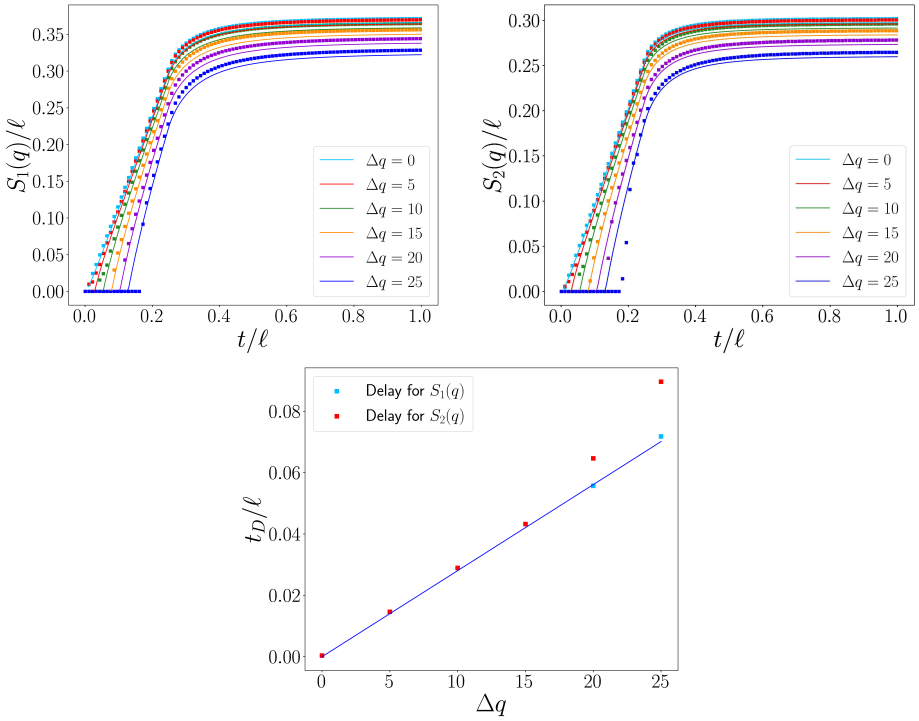

Figure 7.9: *Top:* Time evolution of the symmetry-resolved entropies $S_1(q)$ and $S_2(q)$ after a quench from the dimer state in the tight-binding model (6.29) for $\ell = 140$ and various Δq. We compare the predictions (7.45) and (7.46) (solid lines) with numerical data (symbols). *Bottom:* Delay time t_D for various Δq and $\ell = 280$. The solid line is the analytic prediction $t_D = \frac{\pi|\Delta q|}{4}$ and the symbols are the numerical results. They are obtained as the time for which $S_{1,2}(q)/\ell = 0.011$.

and it admits a solution for imaginary α only. In that case, the integral $\int_{-\pi}^{\pi}\frac{\mathrm{d}k}{2\pi}\partial_{\mathrm{i}\alpha}\big(\mathrm{Re}[h_{n,\alpha}(\cos k)]\big)2v_k$ is a monotonic function of $\mathrm{i}\alpha$, going from $4/\pi$ at $\alpha=-\mathrm{i}\infty$ to $-4/\pi$ at $\alpha=\mathrm{i}\infty$. It thus follows that (7.39) only admits a solution for $t>\frac{\pi|\Delta q|}{4}$. Hence we find precisely the same delay as for the Néel quench, with the same self-consistency relation $|\Delta q|<\ell/\pi$, as given in (7.18).

For the equipartition, we expand the charged moments at quadratic order in α,

$$\log Z_n(\alpha)=\mathrm{i}\ell\frac{\alpha}{2}+\log Z_n(0)-\frac{\alpha^2}{8}\mathcal{J}^{(n)} \tag{7.40}$$

with

$$\mathcal{J}^{(n)}=\int_{-\pi}^{\pi}\frac{\mathrm{d}k}{2\pi}\frac{4\sin^{2n}k}{((1+\cos k)^n+(1-\cos k)^n)^2}\,\min\big(\ell,2v_kt\big). \tag{7.41}$$

These $\mathcal{J}^{(n)}$ integrals generalise the function $\mathcal{J}$ defined in (7.9). In particular, we have $\mathcal{J}^{(0)}=\mathcal{J}$. With the quadratic expansion (7.40), we compute the Fourier transform and find

$$\mathcal{Z}_n(q)=Z_n(0)\mathrm{e}^{-\frac{2\Delta q^2}{\mathcal{J}^{(n)}}}\sqrt{\frac{2}{\pi\mathcal{J}^{(n)}}}. \tag{7.42}$$

We insert this result into the definition of the symmetry-resolved entropies (6.27) and find at leading order

$$S_n(q)=\frac{1}{1-n}\log Z_n(0)-\frac{2\Delta q^2}{(1-n)}\Big\{\frac{1}{\mathcal{J}^{(n)}}-\frac{n}{\mathcal{J}^{(1)}}\Big\} \tag{7.43}$$

where we used $\log Z_1(0)=0$. The symmetry-resolved entanglement entropy is obtained as the limit $n\to1$ of (7.43), and reads

$$S_1(q)=-(\partial_nZ_n(0))|_{n=1}-\frac{2\Delta q^2}{\mathcal{J}^{(1)}}\Big\{\frac{(\partial_n\mathcal{J}^{(n)})|_{n=1}}{\mathcal{J}^{(1)}}+1\Big\}. \tag{7.44}$$

Equations (7.43) and (7.44) are physically equivalent to (7.24). Similarly to the case of a quench from the Néel state, the match with the numerical data is better when we include the sub-leading terms that arise from the square root present in (7.42). The expansion of the entropies with this correction reads

$$S_n(q)=\frac{1}{1-n}\log Z_n(0)-\frac{2\Delta q^2}{(1-n)}\Big\{\frac{1}{\mathcal{J}^{(n)}}-\frac{n}{\mathcal{J}^{(1)}}\Big\}$$

$$+\frac{1}{2}\log\frac{2}{\pi}-\frac{1}{2(1-n)}\log\frac{\mathcal{J}^{(n)}}{(\mathcal{J}^{(1)})^n} \quad (7.45)$$

and the limit $n\to 1$ is

$$S_1(q)=-(\partial_n Z_n(0))|_{n=1}-\frac{2\Delta q^2}{\mathcal{J}^{(1)}}\Big\{\frac{(\partial_n\mathcal{J}^{(n)})|_{n=1}}{\mathcal{J}^{(1)}}+1\Big\}$$
$$+\frac{1}{2}\log\frac{2}{\pi}+\frac{1}{2}\Big(\frac{(\partial_n\mathcal{J}^{(n)})|_{n=1}}{\mathcal{J}^{(1)}}-\log\mathcal{J}^{(1)}\Big). \quad (7.46)$$

We compare these predictions with numerical results in Figure 7.9. As expected, the delay is not well reproduced by the approximation for large $|\Delta q|$, but the asymptotic values match convincingly. In the same figure we report the delays for $S_1(q)$ and $S_2(q)$ and compare them with the prediction $t_D=\frac{\pi|\Delta q|}{4}$. For $S_1(q)$, the match is good. We expect that finite-size effect play an increasing role for larger values of n and $|\Delta q|$, and indeed the match is less precise for $S_2(q)$ at large $|\Delta q|$.

7.2.3 Total and number entropies

As in Section 7.1.4, we verify that our results for the symmetry-resolved entanglement entropy are compatible with previously known results regarding the time evolution of the total entropy. We also investigate the behaviour of the number entropy and its contribution to the total entanglement.

We insert the Gaussian approximations (7.42) and (7.46) in the decomposition (6.21) and find

$$S_1=-(\partial_n Z_n(0))|_{n=1}$$
$$+\frac{(\partial_n\mathcal{J}^{(n)})|_{n=1}}{\mathcal{J}^{(1)}}\Big(\frac{1}{2}-\sqrt{\frac{2}{\pi\mathcal{J}^{(1)}}}\sum_{q=0}^{\ell}\frac{2\Delta q^2}{\mathcal{J}^{(1)}}\mathrm{e}^{-\frac{2\Delta q^2}{\mathcal{J}^{(1)}}}\Big) \quad (7.47)$$

where we also used $\sum_q \mathcal{Z}_1(q)=1$. In the scaling limit, the sum in the right-hand side of (7.47) becomes a Gaussian integral. The expression in the parenthesis on the second line vanishes and we recover

$$S_1=-(\partial_n Z_n(0))|_{n=1} \quad (7.48)$$

as expected from (6.25). Using (7.37), we conclude

$$S_1 = \int_{-\pi}^{\pi} \frac{\mathrm{d}k}{2\pi}(-n_k \log n_k - (1-n_k)\log(1-n_k)) \min(\ell, 2v_k t) \tag{7.49}$$

with $n_k = \frac{1+\cos k}{2}$. This result matches the quasiparticle prediction for the entanglement entropy after a quench from the dimer state [49, 50].

The number entropy is given in (7.27) and only depends on $\mathcal{Z}_1(q)$. We use the quadratic approximation (7.42) and find that the calculations are exactly the same as in Section 7.1.4 where $\mathcal{J}$ is replaced by $\mathcal{J}^{(1)} = \int_{-\pi}^{\pi} \frac{\mathrm{d}k}{2\pi}(1-\cos^2 k)\min(\ell, 2v_k t)$. We thus find

$$S^n = \frac{1}{2}\Big(1 + \log \frac{\mathcal{J}^{(1)}\pi}{2}\Big). \tag{7.50}$$

In Figure 7.10 we compare this result (solid lines) with numerical results for S^n (symbols), and find a good agreement. The inset in the left panel shows the time evolution of S^n in a log-linear scale. We note that $\mathcal{J}^{(1)}$ saturates to the value $\ell/2$ for large times, so that

$$\lim_{t\to\infty} S^n(t) = \frac{1}{2}\Big(1 + \log \frac{\ell\pi}{4}\Big) \tag{7.51}$$

This asymptotic value is the ordinate of the dotted horizontal line in the left panel of Figure 7.10. Similarly to the quench from the Néel state, the number entropy grows logarithmically with time before saturation, and has negligible contribution to the total entropy in the large-time limit,

$$\lim_{t\to\infty} \frac{S^n(t)}{S_1(t)} = \mathcal{O}(\ell^{-1}\log \ell). \tag{7.52}$$

7.3 Quasiparticle picture

From our results of Sections 7.1.1 and 7.2.1 for the charged moments and our discussion of Section 6.1.3 on the quasiparticle picture, we conjecture the following form for the charged moments after a global quench in a free-fermion model:

$$\log Z_n(\alpha) = \mathrm{i}\alpha\langle Q_A\rangle$$

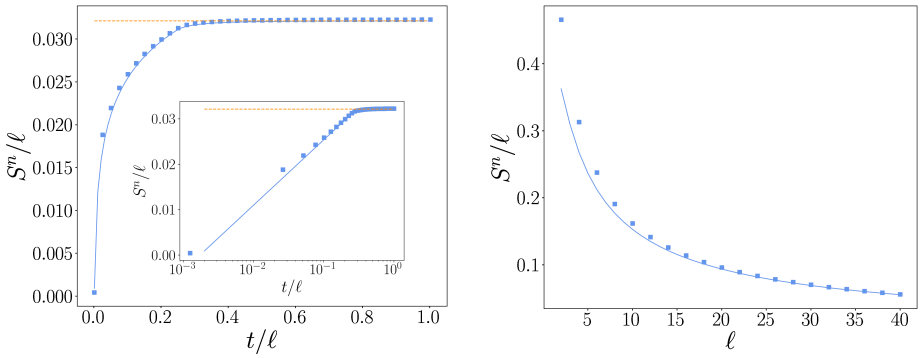

Figure 7.10: Evolution of S^n after a quench from the dimer state in the tight-binding model (6.29) as a function of t/ℓ for $\ell = 80$ (left panel), and as a function of ℓ with $t/\ell = 1$ (right panel). The prediction (7.50) (solid line) convincingly matches the numerical results (symbols). In the left panel, the horizontal dotted line is the asymptotic value $\frac{1}{2\ell}\left(1 + \log\frac{\ell\pi}{4}\right)$ for large times. In the same panel, the inset shows S^n as a function of t/ℓ in a log-linear scale.

$$+ \int_{-\pi}^{\pi} \frac{\mathrm{d}k}{2\pi} \mathrm{Re}[\log(n_k^n \mathrm{e}^{\mathrm{i}\alpha} + (1-n_k)^n)] \min(\ell, 2v_k t). \quad (7.53)$$

This conjecture matches the exact results of (7.7) with $n_k = 1/2$ and (7.37) with $n_k = (1+\cos k)/2$ for the quenches from the Néel and the dimer states, respectively. Similarly to the total entanglement entropy in a generic interacting integrable model (6.16), we conjecture that, in the presence of different species of quasiparticles m, the result (7.53) generalises to a sum over the different species:

$$\log Z_n(\alpha) = \mathrm{i}\alpha\langle Q_A\rangle + \sum_m \int \frac{\mathrm{d}k}{2\pi} s_{n,\alpha}^{(m)}(k) \min(\ell, 2v_k^{(m)} t). \quad (7.54)$$

Here, the functions $s_{n,\alpha}^{(m)}(k)$ and $v_k^{(m)}$ strongly depend on the model and the initial state, and we expect that their evaluation is a highly non-trivial problem.

For free-fermion models, the validity of the quasiparticle conjecture (7.53) can be inferred from the following argument. For the Rényi entropy, the quasiparticle conjecture is

$$\begin{aligned} S_n(t) &= \frac{1}{1-n}\int_{-\pi}^{\pi}\frac{\mathrm{d}k}{2\pi}h_{n,0}(x_k)\min(\ell,2v_kt) \\ &= \frac{1}{1-n}\sum_{j=0}^{\infty}c_{n,0}(2j)\int_{-\pi}^{\pi}\frac{\mathrm{d}k}{2\pi}x_k^{2j}\min(\ell,2v_kt), \end{aligned} \tag{7.55}$$

where x_k is related to the probability of occupation of the mode k by $n_k = (1+x_k)/2$ and the function $h_{n,0}(x)$ is given in (6.40). In terms of the function $s_n(k)$ defined in (6.15), it is just $h_{n,0}(2n_k-1) = 2\pi(1-n)s_n(k)$. Similarly to the charged moments, the total entropies can be expressed in terms of the eigenvalues of the two-point correlation matrix. Combining (6.25) and (6.39), we recover the known result [35]

$$\begin{aligned} S_n(t) &= \frac{1}{1-n}\sum_{i=1}^{\ell}\log\left[\left(\frac{1+\nu_i}{2}\right)^n+\left(\frac{1-\nu_i}{2}\right)^n\right] \\ &= \frac{1}{1-n}\sum_{j=0}^{\infty}c_{n,0}(2j)\mathrm{Tr}J_A(t)^{2j} \end{aligned} \tag{7.56}$$

where ν_i are the eigenvalues of the matrix J_A introduced in (6.38). We compare (7.56) and (7.55), and find

$$\mathrm{Tr}J_A(t)^{2j} = \ell + \int_{-\pi}^{\pi}\frac{\mathrm{d}k}{2\pi}(x_k^{2j}-1)\min(\ell,2v_kt). \tag{7.57}$$

The combination of this expression for the trace of J_A and (6.41) yields the desired result (7.53).

8

Symmetry-resolved mutual information after a quench

In this chapter, we propose a definition for the symmetry-resolved mutual information. In particular, we express this new quantity in terms of two-point correlation matrices in free-fermion models. We use these results to investigate the behaviour of this symmetry-resolved mutual information after the quenches from the Néel and the dimer states in the tight-binding model. As in the previous chapter, we use the exact expressions of the correlation matrices for the two quenches to perform numerical calculations and support our analytical results.

In the following, we consider the case where the system $A = A_1 \cup A_2$ consists on two disjoint intervals of respective lengths ℓ_1 and ℓ_2, with $\ell_1 + \ell_2 = \ell$, separated by d lattice sites. Because of the structure of the initial states, we work with systems of even lengths. The conserved charge for the system A split as a sum over the subsystems, $Q_A = Q_{A_1} + Q_{A_2}$, and the respective time-independent averages are

$$\langle Q_A \rangle = \frac{\ell}{2}, \qquad \langle Q_{A_j} \rangle = \frac{\ell_j}{2}, \quad j = 1, 2. \tag{8.1}$$

The results discussed in this chapter were initially presented in the publication [1].

8.1 The symmetry-resolved mutual information

For the sake of completeness, let us recall the definition (0.7) of the total mutual information,

$$I_1^{A_1:A_2} = S_1^{A_1} + S_1^{A_2} - S_1^{A_1\cup A_2}, \tag{8.2}$$

where the superscripts A_1, A_2 and $A_1 \cup A_2$ indicate which system the entanglement entropies pertain to, where the notation $A_1 \cup A_2$ serves as a remainder that the system A consists on two disjoint intervals. We use this notation for various other objects throughout this chapter. Each of the entanglement entropies in (8.2) admits its own symmetry decomposition with respect to a different charge. It is thus not straightforward to define a symmetry-resolved version of $I_1^{A_1:A_2}$, and in particular there is not a unique way to do so. We propose to define the *symmetry-resolved mutual information* as

$$I_1^{A_1:A_2}(q) = \sum_{q_1=0}^{q} p(q_1, q-q_1)\Big(S_1^{A_1}(q_1)+S_1^{A_2}(q-q_1)\Big) - S_1^{A_1\cup A_2}(q), \tag{8.3}$$

where weight $p(q_1, q-q_1)$ is the probability that a simultaneous measurement of the charges Q_{A_1} and Q_{A_2} yields q_1 and $q-q_1$, respectively, while the charge sector of the system A is fixed to q. The idea behind the definition (8.3) is that for a given charge sector q of the subsystem A, we take a weighted sum over the contributions from charge sectors q_1 and q_2 of A_1 and A_2 such that $q_1 + q_2 = q$.

To express the weight $p(q_1, q-q_1)$ in terms of concrete lattice quantities, we introduce the doubly-charged moment

$$Z_1^{A_1:A_2}(\alpha,\beta) = \mathrm{Tr}\big(\rho_A \mathrm{e}^{\mathrm{i}\alpha Q_{A_1}+\mathrm{i}\beta Q_{A_2}}\big) \tag{8.4}$$

and its double Fourier transform

$$\mathcal{Z}_1^{A_1:A_2}(q_1,q_2) = \int_{-\pi}^{\pi} \frac{d\alpha}{2\pi}\frac{d\beta}{2\pi} \mathrm{e}^{-\mathrm{i}q_1\alpha}\mathrm{e}^{-\mathrm{i}q_2\beta} Z_1^{A_1:A_2}(\alpha,\beta). \tag{8.5}$$

The weight $p(q_1, q-q_1)$ reads

$$p(q_1, q-q_1) = \frac{\mathcal{Z}_1^{A_1:A_2}(q_1, q-q_1)}{\mathcal{Z}_1^{A_1\cup A_2}(q)} \tag{8.6}$$

and satisfies $\sum_{q_1=0}^{q} p(q_1, q-q_1) = 1$. The symmetry-resolved moment $\mathcal{Z}_1^{A_1\cup A_2}(q)$ is defined in (6.26) with $A = A_1 \cup A_2$ and is the probability that a measurement of the charge Q_A yields the value q.

Similarly to the entanglement entropy, it is possible to reconstruct the total mutual information from the symmetry-resolved ones. We have

$$\begin{aligned} I_1^{A_1:A_2} &= \sum_q p(q) I_1^{A_1:A_2}(q) + S^{A_1,n} + S^{A_2,n} - S^{A_1\cup A_2,n} \\ &= \sum_q p(q) I_1^{A_1:A_2}(q) + I^{A_1:A_2,n}, \end{aligned} \tag{8.7}$$

where the notation $S^{s,n}$ stands for the number entropy associated with system s, and $p(q) = \mathcal{Z}_1^{A_1\cup A_2}(q)$. The last equality defines the number mutual information $I^{A_1:A_2,n} \equiv S^{A_1,n} + S^{A_2,n} - S^{A_1\cup A_2,n}$.

8.1.1 Free fermions

In this section, we express the doubly-charged moments $Z_1^{A_1:A_2}(\alpha,\beta)$ in terms of two-point correlation matrices for free-fermion model. As in Section 6.2.2, we consider the case where the whole system is in a pure state that satisfies the condition (6.32) and hence the reduced density matrix ρ_A is a Gaussian operator.

For disjoint intervals, the matrix $J_A = J_{A_1\cup A_2}$ defined in (6.38) has the block structure

$$J_{A_1\cup A_2} = \begin{pmatrix} J_{11} & J_{12} \\ J_{21} & J_{22} \end{pmatrix} \tag{8.8}$$

where the matrices J_{ab}, $a, b = 1, 2$, contain the two-point correlation functions between sites in A_a and A_b. The computation of the charged moments $Z_n(\alpha)$ is not affected by the fact that A is not a connected block. The formula (6.39) still holds, with the eigenvalues of $J_{A_1\cup A_2}$ defined above. To compute the symmetry-resolved mutual information in free-fermion model, it remains to evaluate $Z_1^{A_1:A_2}(\alpha,\beta)$ defined in (8.4). Since the reduced density matrix ρ_A does not commute with the charges Q_{A_1} and Q_{A_2} of the two disjoint subsystems, the method used to compute $Z_n(\alpha)$ in [65] and derive (6.39) does not apply. To circumvent this problem, we adapt a technique devised in [246] to compute the full counting statistics of the magnetisation in the transverse field Ising

chain. The idea is to express $Z_1^{A_1:A_2}(\alpha,\beta)$ in terms of a trace of two non-commuting density matrices. We recast (8.4) as

$$Z_1^{A_1:A_2}(\alpha,\beta) = \tilde{Z}_A \mathrm{Tr}(\rho_A \tilde{\rho}_A) \tag{8.9}$$

were

$$\tilde{\rho}_A = \frac{1}{\tilde{Z}_A} \mathrm{e}^{\mathrm{i}\alpha Q_{A_1} + \mathrm{i}\beta Q_{A_2}}, \quad \tilde{Z}_A = \mathrm{Tr}\Big(\mathrm{e}^{\mathrm{i}\alpha Q_{A_1} + \mathrm{i}\beta Q_{A_2}}\Big) \tag{8.10}$$

and the normalisation $\tilde{Z}_A$ ensures that $\mathrm{Tr}\tilde{\rho}_A = 1$. We use that the charges Q_{A_1} and Q_{A_2} are diagonal in the basis of the canonical fermion operators c_j, and find

$$\tilde{Z}_A = (1+\mathrm{e}^{\mathrm{i}\alpha})^{\ell_1}(1+\mathrm{e}^{\mathrm{i}\beta})^{\ell_2}. \tag{8.11}$$

The matrix $\tilde{\rho}_A$ is not a true density matrix, in the sense that it does not describe the state of a subsystem A. However, it is a very simple Gaussian operator and is completely determined by a two-point correlation matrix $\tilde{C}_A$.

To proceed, we use that the trace of a product of two $\ell \times \ell$ Gaussian operators ρ_1 and ρ_2 is [247, 248]

$$\mathrm{Tr}(\rho_1\rho_2) = \det\Big(\frac{\mathbb{I}_\ell + J_1 J_2}{2}\Big) \tag{8.12}$$

where

$$J_j = 2C_j - \mathbb{I}_\ell, \quad [C_j]_{x,x'} = \mathrm{Tr}(\rho_j c_x^\dagger c_{x'}). \tag{8.13}$$

To ease the comparison with the methods developed in [246], we mention that for free-fermion systems without particle number conservation, one also has to consider correlations of the form $\mathrm{Tr}(\rho_j c_x^\dagger c_{x'}^\dagger)$ and $\mathrm{Tr}(\rho_j c_x c_{x'})$. For that reason, the size of the correlation matrices are 2ℓ instead of ℓ, and the right-hand side of (8.12) is written with an overall square root in [246]. In our case, the two correlation matrices are

$$\begin{aligned} [C_A]_{x,x'} &= \mathrm{Tr}(\rho_A c_x^\dagger c_{x'}), \quad x,x' \in A, \\ [\tilde{C}_A]_{x,x'} &= \mathrm{Tr}(\tilde{\rho}_A c_x^\dagger c_{x'}), \quad x,x' \in A. \end{aligned} \tag{8.14}$$

The matrix C_A is the usual correlation matrix related to $J_{A_1\cup A_2}$, whereas $\tilde{C}_A$ is simply

$$\begin{aligned}\mathrm{Tr}(\tilde{\rho}_A c_x^\dagger c_{x'}) &= \delta_{x,x'}\begin{cases}\frac{1}{\tilde{Z}_A}\mathrm{e}^{\mathrm{i}\alpha}(1+\mathrm{e}^{\mathrm{i}\alpha})^{\ell_1-1}(1+\mathrm{e}^{\mathrm{i}\beta})^{\ell_2} & x\in A_1,\\ \frac{1}{\tilde{Z}_A}\mathrm{e}^{\mathrm{i}\beta}(1+\mathrm{e}^{\mathrm{i}\alpha})^{\ell_1}(1+\mathrm{e}^{\mathrm{i}\beta})^{\ell_2-1} & x\in A_2,\end{cases}\\ &= \delta_{x,x'}\begin{cases}\frac{\mathrm{e}^{\mathrm{i}\alpha}}{1+\mathrm{e}^{\mathrm{i}\alpha}} & x\in A_1,\\ \frac{\mathrm{e}^{\mathrm{i}\beta}}{1+\mathrm{e}^{\mathrm{i}\beta}} & x\in A_2\end{cases}\end{aligned} \tag{8.15}$$

where we used the diagonal form of the charges. Finally, combining (8.9), (8.11), (8.12) and (8.15), we have

$$Z_1^{A_1:A_2}(\alpha,\beta) = (1+\mathrm{e}^{\mathrm{i}\alpha})^{\ell_1}(1+\mathrm{e}^{\mathrm{i}\beta})^{\ell_2}\det\left(\frac{\mathbb{I}_\ell + J_{\alpha\beta}}{2}\right) \tag{8.16}$$

where

$$J_{\alpha\beta} = \begin{pmatrix} J_{11} & J_{12}\\ J_{21} & J_{22}\end{pmatrix}\cdot\begin{pmatrix}\frac{\mathrm{e}^{\mathrm{i}\alpha}-1}{\mathrm{e}^{\mathrm{i}\alpha}+1}\mathbb{I}_{\ell_1} & 0\\ 0 & \frac{\mathrm{e}^{\mathrm{i}\beta}-1}{\mathrm{e}^{\mathrm{i}\beta}+1}\mathbb{I}_{\ell_2}\end{pmatrix}. \tag{8.17}$$

Similarly to the charged moments, we write $Z_1^{A_1:A_2}(\alpha,\beta)$ as an expansion in terms of the traces of the powers of $J_{\alpha\beta}$. We introduce the function $\tilde{h}(x)$ and the coefficients $\tilde{c}(m)$ as

$$\tilde{h}(x) = \log\left(\frac{1+x}{2}\right) \equiv \sum_{m=0}^{\infty}\tilde{c}(m)x^m, \tag{8.18}$$

and find

$$\begin{aligned}\log Z_1^{A_1:A_2}(\alpha,\beta) &= \ell_1\log(1+\mathrm{e}^{\mathrm{i}\alpha})\\ &\quad + \ell_2\log(1+\mathrm{e}^{\mathrm{i}\beta}) + \sum_{m=0}^{\infty}\tilde{c}(m)\mathrm{Tr}J_{\alpha\beta}^m.\end{aligned} \tag{8.19}$$

8.2 Quench from the Néel state

In this section, we investigate the behaviour of the symmetry-resolved mutual information after a quench from the Néel state in the tight binding model. The correlation matrix $C_A = C_{A_1\cup A_2}(t)$ has the form

$$C_{A_1\cup A_2}(t) = \begin{pmatrix} C_{11}(t) & C_{12}(t)\\ C_{21}(t) & C_{22}(t)\end{pmatrix} \tag{8.20}$$

with

$$[C_{11}(t)]_{x,x'} = [C(t)]_{x,x'}, \qquad x, x' \in \{1, \dots \ell_1\}, \tag{8.21}$$
$$[C_{22}(t)]_{x,x'} = [C(t)]_{x+d,x'+d}, \qquad x, x' \in \{1, \dots \ell_2\}, \tag{8.22}$$
$$[C_{12}(t)]_{x,x'} = [C(t)]_{x,x'+d}, \qquad x \in \{1, \dots \ell_1\},\ x' \in \{1, \dots \ell_2\}, \tag{8.23}$$
$$[C_{21}(t)]_{x,x'} = [C(t)]_{x+d,x'}, \qquad x \in \{1, \dots \ell_2\},\ x' \in \{1, \dots \ell_1\}, \tag{8.24}$$

where the matrix elements $[C(t)]_{x,x'}$ are given in (7.2).

8.2.1 Symmetry-resolved moments and entropies

The definition (8.3) of the symmetry-resolved mutual information involves symmetry-resolved moments $\mathcal{Z}_1^{A_1\cup A_2}(q)$ and entropies $S_1^{A_1\cup A_2}(q)$ of disjoint intervals. To investigate these quantities, we start with the charged moments for disjoint intervals and compute the trace of arbitrary powers of the matrix $J_{A_1\cup A_2}(t) = 2C_{A_1\cup A_2}(t) - \mathbb{I}_\ell$. We perform the computation of $\mathrm{Tr} J_{A_1\cup A_2}(t)^m$ in the scaling limit $\ell, \ell_1, d, t \to \infty$ where the various ratios are kept constant. The calculation uses the multidimensional stationary phase approximation, and generalises the methods introduced in [48] to the case of an arbitrary separation d. We find

$$\begin{aligned}\mathrm{Tr} J_{A_1\cup A_2}(t)^{2j} = \ell &- \int_{-\pi}^{\pi} \frac{\mathrm{d}k}{2\pi} (\min(\ell_1, 2v_k t) + \min(\ell_2, 2v_k t)) \\ &+ \int_{-\pi}^{\pi} \frac{\mathrm{d}k}{2\pi} (\max(d, 2v_k t) + \max(d+\ell, 2v_k t) \\ &\qquad - \max(d+\ell_1, 2v_k t) - \max(d+\ell_2, 2v_k t)),\end{aligned} \tag{8.25}$$

with $v_k = 2|\sin k|$ and $\mathrm{Tr} J_{A_1\cup A_2}(t)^{2j+1} = 0$. We note that the case $d = 0$ reduces to the result of (7.4) for a single interval. The computation of the charged moments $Z_n^{A_1\cup A_2}(\alpha)$ proceeds exactly as for the case of a single interval discussed in Section 7.1.1. We thus find

$$Z_n^{A_1\cup A_2}(\alpha) = \left(\frac{\cos\frac{\alpha}{2}}{2^{n-1}}\right)^{\mathcal{J}_d} \mathrm{e}^{\mathrm{i}\ell\frac{\alpha}{2}} \tag{8.26}$$

where we introduced

$$\mathcal{J}_d = \int_{-\pi}^{\pi} \frac{\mathrm{d}k}{2\pi} (\min(\ell_1, 2v_k t) + \min(\ell_2, 2v_k t))$$

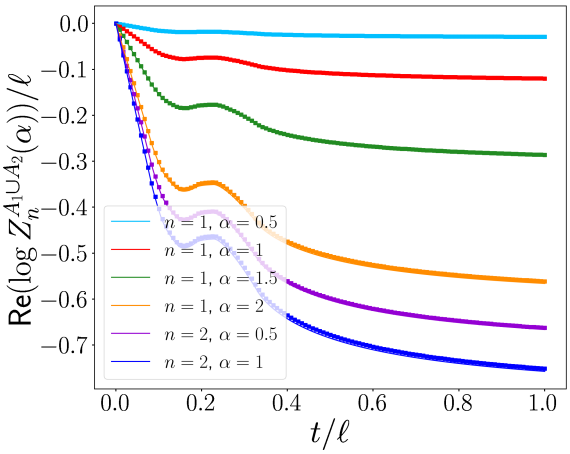

Figure 8.1: Time evolution of the charged moments $Z_n^{A_1\cup A_2}(\alpha)$ after a quench from the Néel state in the tight-binding model (6.29) as a function of t/ℓ with $\ell_1 = 100$, $\ell_2 = 140$ and $d = 80$. The analytical prediction (8.26) (solid lines) convincingly matches the numerical data (symbols).

$$-\int_{-\pi}^{\pi}\frac{\mathrm{d}k}{2\pi}(\max(d,2v_kt)+\max(d+\ell,2v_kt) \\ -\max(d+\ell_1,2v_kt)-\max(d+\ell_2,2v_kt)). \quad (8.27)$$

Similarly to $\mathcal{J}$ defined in (7.9), the integral $\mathcal{J}_d$ is an increasing function of time, going from zero at $t=0$ to ℓ in the limit of large times. In Figure 8.1 we compare the prediction (8.26) for $Z_n^{A_1\cup A_2}(\alpha)$ with numerical results and find a good agreement.

The calculations for the symmetry-resolved moments and Rényi entropies in the scaling limit are exactly the same as the computations of Section 7.1.2 and Section 7.1.3 where $\mathcal{J}$ is systematically replaced by $\mathcal{J}_d$. We thus have

$$\begin{aligned} S_n^{A_1\cup A_2}(q) &= \mathcal{J}_d\log 2+\log\mathcal{Z}_1^{A_1\cup A_2}(q),\\ \mathcal{Z}_1^{A_1\cup A_2}(q) &= 2^{-\mathcal{J}_d}\frac{\Gamma(\mathcal{J}_d+1)}{\Gamma\left(\frac{\mathcal{J}_d+2\Delta q+2}{2}\right)\Gamma\left(\frac{\mathcal{J}_d-2\Delta q+2}{2}\right)}, \end{aligned} \quad (8.28)$$

and

$$S_n^{A_1\cup A_2}(q) = \mathcal{J}_d\left(\log 2 - 2\Big(\frac{|\Delta q|}{\mathcal{J}_d}\Big)^2\right),$$
$$\mathcal{Z}_1^{A_1\cup A_2}(q) = \sqrt{\frac{2}{\mathcal{J}_d\pi}}\mathrm{e}^{-\frac{2\Delta q^2}{\mathcal{J}_d}}, \tag{8.29}$$

in the regime $\mathcal{J}_d \gg |\Delta q|$.

8.2.2 Symmetry-resolved mutual information

We now turn to the computation of the symmetry-resolved mutual information defined in (8.3). The first step is to compute $Z_1^{A_1:A_2}(\alpha,\beta)$. To do so, we evaluate the trace of powers of the matrix $J_{\alpha\beta}$ (8.17) in the scaling limit. We adapt the calculations of Section 8.2.1 for the trace of $J_{A_1\cup A_2}$ and find

$$\begin{aligned}\mathrm{Tr}J_{\alpha\beta}(t)^{2j} = &\Big(\frac{\mathrm{e}^{\mathrm{i}\alpha}-1}{\mathrm{e}^{\mathrm{i}\alpha}+1}\Big)^{2j}\Big[\ell_1 - \int_{-\pi}^{\pi}\frac{\mathrm{d}k}{2\pi}\min(\ell_1, 2v_k t)\Big]\\ &+\Big(\frac{\mathrm{e}^{\mathrm{i}\beta}-1}{\mathrm{e}^{\mathrm{i}\beta}+1}\Big)^{2j}\Big[\ell_2 - \int_{-\pi}^{\pi}\frac{\mathrm{d}k}{2\pi}\min(\ell_2, 2v_k t)\Big]\\ &+(-1)^j\Big(\tan\frac{\alpha}{2}\tan\frac{\beta}{2}\Big)^j\int_{-\pi}^{\pi}\frac{\mathrm{d}k}{2\pi}(\max(d, 2v_k t)\\ &+\max(d+\ell, 2v_k t) - \max(d+\ell_1, 2v_k t) - \max(d+\ell_2, 2v_k t)),\end{aligned} \tag{8.30}$$

whereas the traces of odd-powers vanish, $\mathrm{Tr}J_{\alpha\beta}(t)^{2j+1} = 0$. The resummation in (8.19) is direct and we find

$$\begin{aligned}\log Z_1^{A_1:A_2}(\alpha,\beta) = &\,\mathrm{i}\frac{\ell_1\alpha+\ell_2\beta}{2} + \log\Big(\cos\frac{\alpha}{2}\Big)\mathcal{J}_{A_1}\\ &+\log\Big(\cos\frac{\beta}{2}\Big)\mathcal{J}_{A_2} + \frac{1}{2}\log\Big(1+\tan\frac{\alpha}{2}\tan\frac{\beta}{2}\Big)\mathcal{J}_m\end{aligned} \tag{8.31}$$

with the notations

$$\mathcal{J}_{A_{1,2}} \equiv \mathcal{J}|_{\ell\to\ell_{1,2}} = \int_{-\pi}^{\pi}\frac{\mathrm{d}k}{2\pi}\min(\ell_{1,2}, 2v_k t) \tag{8.32a}$$

and

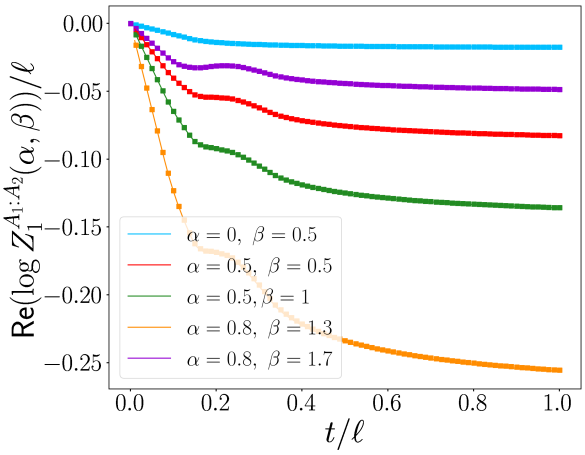

Figure 8.2: Time evolution of $Z_1^{A_1:A_2}(\alpha,\beta)$ after a quench from the Néel state in the tight-binding model (6.29) as a function of t/ℓ with $\ell_1 = 100$, $\ell_2 = 140$ and $d = 80$. The analytical prediction (8.31) (solid lines) convincingly matches the numerical data (symbols).

$$\mathcal{J}_m \equiv \mathcal{J}_{A_1} + \mathcal{J}_{A_2} - \mathcal{J}_d = \int_{-\pi}^{\pi} \frac{\mathrm{d}k}{2\pi} (\max(d, 2v_k t) + \max(d+\ell, 2v_k t) - \max(d+\ell_1, 2v_k t) - \max(d+\ell_2, 2v_k t)) \quad (8.32b)$$

where $\mathcal{J}$ and $\mathcal{J}_d$ are given in (7.9) and (8.27), respectively. As expected, $Z_1^{A_1:A_2}(\alpha,\alpha)$ is equal to the charged moment $Z_1^{A_1\cup A_2}(\alpha)$ given in (8.26). We compare the prediction (8.31) with numerical results in Figure 8.2 and find a good agreement.

To proceed, we investigate $\mathcal{Z}_1^{A_1:A_2}(q_1, q-q_1)$ defined in (8.5). To perform the double Fourier transform, we expend $Z_1^{A_1:A_2}(\alpha,\beta)$ at quadratic order,

$$\log Z_1^{A_1:A_2}(\alpha,\beta) = \mathrm{i}\frac{\ell_1\alpha + \ell_2\beta}{2} - \frac{\alpha^2}{8}\mathcal{J}_{A_1} - \frac{\beta^2}{8}\mathcal{J}_{A_2} + \frac{\alpha\beta}{8}(\mathcal{J}_{A_1} + \mathcal{J}_{A_2} - \mathcal{J}_d), \quad (8.33)$$

and find

$$\mathcal{Z}_1^{A_1:A_2}(q_1, q-q_1) = \frac{2}{\pi\sqrt{\mathcal{J}_{A_1}\mathcal{J}_{A_2} - \frac{\mathcal{J}_m^2}{4}}} \times \mathrm{e}^{-\frac{8}{4\mathcal{J}_{A_1}\mathcal{J}_{A_2}-\mathcal{J}_m^2}\left[\Delta q_1^2 \mathcal{J}_{A_2} + (\Delta q - \Delta q_1)^2 \mathcal{J}_{A_1} + \Delta q_1(\Delta q - \Delta q_1)\mathcal{J}_m\right]} \quad (8.34)$$

where $\Delta q_1 = q_1 - \ell_1/2$. With (8.34) and the equivalent Gaussian approximation (8.29) for $\mathcal{Z}_1^{A_1\cup A_2}(q)$, one can show that the weight defined in (8.6) satisfies $\sum_{q_1=0}^{q} p(q_1, q-q_1) = 1$ in the scaling limit.

Using the Gaussian expressions (7.24), (8.29) and (8.34) for each term involved in the definition of the symmetry-resolved mutual information (8.3), we find

$$I_1^{A_1:A_2}(q) = \mathcal{J}_m \log 2 - \frac{1}{2}\Big(\log \frac{\mathcal{J}_{A_1}\mathcal{J}_{A_2}\pi}{2\mathcal{J}_d}\Big) \\ - \frac{4\mathcal{J}_{A_1}\mathcal{J}_{A_2} - \mathcal{J}_m^2}{8\mathcal{J}_d}\Big(\frac{1}{\mathcal{J}_{A_1}} + \frac{1}{\mathcal{J}_{A_2}}\Big) - 2\Delta q^2 \Big\{ \Big(\frac{-\mathcal{J}_{A_1} + \mathcal{J}_{A_2} - \mathcal{J}_d}{2\mathcal{J}_d}\Big)^2 \frac{1}{\mathcal{J}_{A_1}} \\ + \Big(\frac{\mathcal{J}_{A_1} - \mathcal{J}_{A_2} - \mathcal{J}_d}{2\mathcal{J}_d}\Big)^2 \frac{1}{\mathcal{J}_{A_2}} - \frac{1}{\mathcal{J}_d}\Big\} \quad (8.35)$$

in the scaling limit. The result (8.35) implies that there is equipartition of the symmetry-resolved mutual information at leading order. Here, we computed the corrections to the equipartition up to order $\Delta q^2/\ell$. For $t < d/(2v_M)$ and in the limit $t \to \infty$, the terms of order $\Delta q^2/\ell$ in (8.35) vanish because $\mathcal{J}_d = \mathcal{J}_{A_1} + \mathcal{J}_{A_2}$ in these two regimes, and hence equipartition is broken at higher order. For intermediate times, the equipartition is broken at order $\Delta q^2/\ell$.

In Figure 8.3 we compare the prediction (8.35) (solid lines) with the numerical evaluation of (8.3) where the entropies are given by their exact expressions (7.23) and (8.28), and the weight $p(q_1, q-q_1)$ is obtained from the Gaussian approximations (8.29) and (8.34) (symbols). We find a good agreement. The slight negative values for early times arise from the term $-\frac{1}{2}\log\frac{\mathcal{J}_{A_1}\mathcal{J}_{A_2}\pi}{2\mathcal{J}_d}$ in (8.35). This term is at most of order $\log\ell$ and is negligible in the scaling limit. There is a time delay $t = d/(2v_M) = d/4$, but it is inherent to the disjoint structure of the system A, and independent on the charge sector. We expect that the absence of a sector-dependent delay is related to the fact that, from its definition (8.3), $I_1^{A_1:A_2}(q)$ mixes quantities from different charge sectors.

The leading term $\mathcal{J}_m \log 2$ in (8.35) is the total mutual information,

$$I_1^{A_1:A_2} = \log 2 \int \frac{\mathrm{d}k}{2\pi} (\max(d, 2v_k t) + \max(d+\ell, 2v_k t) \\ - \max(d+\ell_1, 2v_k t) - \max(d+\ell_2, 2v_k t)). \quad (8.36)$$

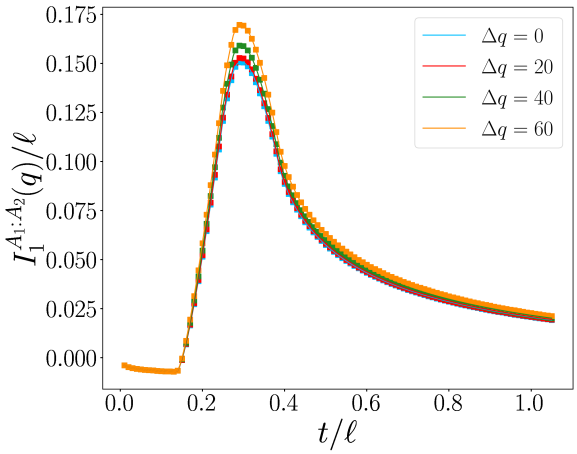

Figure 8.3: Time evolution of $I_1^{A_1:A_2}(q)$ after a quench from the Néel state in the tight-binding model (6.29) as a function of t/ℓ with $\ell_1 = 180$, $\ell_2 = 220$ and $d = 220$ for various values of Δq. We compare the approximation(8.35) (solid lines) with the exact result given by (8.3) where the entropies are replaced by their exact formulas in terms of Gamma functions and the weights are given by their Gaussian approximations (symbols).

This immediately follow from the definition of the mutual information (8.2), the relation (6.25) and the exact results for the charged moments for a single (7.7) and disjoint intervals (8.26). The integral (8.36) is precisely the form predicted by the quasiparticle picture for the spreading of entanglement between two non-complementary subsystems [21]. It is vanishing for times $t < d/(2v_M)$ as well as in the large-time limit. We mention that, to the best of our knowledge, (8.36) is the first ab-initio calculation of the mutual information in a free-fermion model, and hence the first analytical verification of the quasiparticle prediction for the mutual information.

To verify the consistency of our calculations, we must recover the total mutual information from the symmetry-resolved ones with the combination given in (8.7). Using the same Gaussian results as before, (8.35) and the asymptotic result (7.29) for the number entropy, we indeed find

$$\sum_{q=0}^{\ell} \mathcal{Z}_1^{A_1\cup A_2}(q) I_1^{A_1:A_2}(q) + S^{A_1,n} + S^{A_2,n} - S^{A_1\cup A_2,n} = \mathcal{J}_m \log 2 \quad (8.37)$$

in the scaling limit.

8.3 Quench from the dimer state

In this section, we investigate the behaviour of the symmetry-resolved mutual information after a quench from the dimer state in the tight-binding model. The correlation matrix $C_{A_1\cup A_2}(t)$ is obtained from the matrix elements (7.33), and its structure is analogous to the one of the correlation matrix (8.20) that we considered in the previous sections.

8.3.1 Symmetry-resolved moments and entropies

Similarly to the calculations of Section 8.2.1, we compute the trace of arbitrary powers of the matrix $J_{A_1\cup A_2}(t) = 2C_{A_1\cup A_2}(t) - \mathbb{I}_\ell$. We perform the computation of $\mathrm{Tr} J_{A_1\cup A_2}(t)^m$ in the scaling limit $\ell, \ell_1, d, t \to \infty$ where the various ratios are kept constant. We find

$$\begin{aligned}\mathrm{Tr} J_{A_1\cup A_2}(t)^{2j} = \ell &- \int_{-\pi}^{\pi} \frac{\mathrm{d}k}{2\pi}(1-(\cos k)^{2j})(\min(\ell_1, 2v_k t)+\min(\ell_2, 2v_k t)) \\ &+ \int_{-\pi}^{\pi} \frac{\mathrm{d}k}{2\pi}(1-(\cos k)^{2j})(\max(d, 2v_k t) + \max(d+\ell, 2v_k t) \\ &\qquad - \max(d+\ell_1, 2v_k t) - \max(d+\ell_2, 2v_k t)), \end{aligned} \tag{8.38}$$

with $v_k = 2|\sin k|$, and $\mathrm{Tr} J_{A_1\cup A_2}(t)^{2j+1} = 0$. We note that the case $d = 0$ reduces to the result (7.36) for a single interval. The calculation is similar to case of a single interval as presented in Section 7.2.1, and we find

$$\begin{aligned}\log Z_n^{A_1\cup A_2}(\alpha) = \mathrm{i}\ell\frac{\alpha}{2} &\\ + \int_{-\pi}^{\pi} \frac{\mathrm{d}k}{2\pi}&\mathrm{Re}[h_{n,\alpha}(\cos k)](\min(\ell_1, 2v_k t) + \min(\ell_2, 2v_k t)) \\ - \int_{-\pi}^{\pi} \frac{\mathrm{d}k}{2\pi}&\mathrm{Re}[h_{n,\alpha}(\cos k)](\max(d, 2v_k t) + \max(d+\ell, 2v_k t) \\ &- \max(d+\ell_1, 2v_k t) - \max(d+\ell_2, 2v_k t)) \end{aligned} \tag{8.39}$$

where we recall that $h_{n,\alpha}(x)$ is defined in (6.40). We compare the prediction (8.39) for $Z_n^{A_1\cup A_2}(\alpha)$ with numerical results in Figure 8.4 and find a good agreement.

To perform analytical calculations, we approximate $\log Z_n^{A_1\cup A_2}(\alpha)$ at quadratic order in α,

$$\log Z_n^{A_1\cup A_2}(\alpha) = \mathrm{i}\ell\frac{\alpha}{2} + \log Z_n^{A_1\cup A_2}(0) - \frac{\alpha^2}{8}\mathcal{J}_d^{(n)} \tag{8.40}$$

with

$$\begin{aligned}\mathcal{J}_d^{(n)} = &\int_{-\pi}^{\pi}\frac{\mathrm{d}k}{2\pi}\frac{4\sin^{2n}k}{((1+\cos k)^n+(1-\cos k)^n)^2}(\min(\ell_1,2v_kt)+\min(\ell_2,2v_kt))\\ &-\int_{-\pi}^{\pi}\frac{\mathrm{d}k}{2\pi}\frac{4\sin^{2n}k}{((1+\cos k)^n+(1-\cos k)^n)^2}(\max(d,2v_kt)\\ &+\max(d+\ell,2v_kt)-\max(d+\ell_1,2v_kt)-\max(d+\ell_2,2v_kt)).\end{aligned} \tag{8.41}$$

These $\mathcal{J}_d^{(n)}$ integrals generalise $\mathcal{J}_d$ defined in (8.27). In particular, we have $\mathcal{J}_d^{(0)} = \mathcal{J}_d$. We follow the calculations of Section 7.2.2 and find

$$\mathcal{Z}_n^{A_1\cup A_2}(q) = Z_n^{A_1\cup A_2}(0)\ \mathrm{e}^{-\frac{2\Delta q^2}{\mathcal{J}_d^{(n)}}}\sqrt{\frac{2}{\pi\mathcal{J}_d^{(n)}}}, \tag{8.42a}$$

$$\begin{aligned}S_n^{A_1\cup A_2}(q) = S_n^{A_1\cup A_2} &- \frac{2\Delta q^2}{(1-n)}\Big\{\frac{1}{\mathcal{J}_d^{(n)}}-\frac{n}{\mathcal{J}_d^{(1)}}\Big\}\\ &+\frac{1}{2}\log\frac{2}{\pi}-\frac{1}{2(1-n)}\log\frac{\mathcal{J}_d^{(n)}}{(\mathcal{J}_d^{(1)})^n},\end{aligned} \tag{8.42b}$$

$$\begin{aligned}S_1^{A_1\cup A_2}(q) = S_1^{A_1\cup A_2} &- \frac{2\Delta q^2}{\mathcal{J}_d^{(1)}}\Big\{\frac{(\partial_n\mathcal{J}_d^{(n)})|_{n=1}}{\mathcal{J}_d^{(1)}}+1\Big\}\\ &+\frac{1}{2}\log\frac{2}{\pi}+\frac{1}{2}\Big(\frac{(\partial_n\mathcal{J}_d^{(n)})|_{n=1}}{\mathcal{J}_d^{(1)}}-\log\mathcal{J}_d^{(1)}\Big).\end{aligned} \tag{8.42c}$$

8.3.2 Symmetry-resolved mutual information

We now turn to the computation of the symmetry-resolved mutual information. Most of the results and computations are similar to those

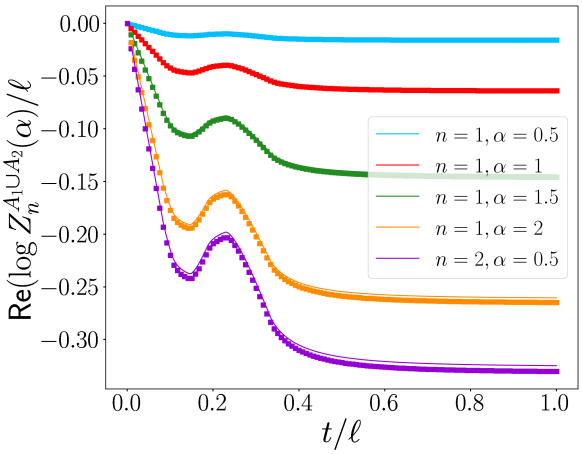

Figure 8.4: Time evolution of the charged moments $Z_n^{A_1\cup A_2}(\alpha)$ after a quench from the dimer state in the tight-binding model (6.29) as a function of t/ℓ with $\ell_1 = 100$, $\ell_2 = 140$ and $d = 80$. The analytical prediction of Eq. (8.39) (solid lines) convincingly matches the numerical data (symbols).

presented in Section 8.2.2 in the case of a quench from the Néel state. The first step is to compute $Z_1^{A_1:A_2}(\alpha,\beta)$ and hence the trace of powers of the matrix $J_{\alpha\beta}$ defined in (8.17). We adapt the calculations of Section 8.3.1 for the trace of $J_{A_1\cup A_2}$ and find $\mathrm{Tr}J_{\alpha\beta}(t)^{2j+1} = 0$, whereas for even powers we have

$$\begin{aligned}\mathrm{Tr}J_{\alpha\beta}(t)^{2j} = &\left(\frac{\mathrm{e}^{\mathrm{i}\alpha}-1}{\mathrm{e}^{\mathrm{i}\alpha}+1}\right)^{2j}\left[\ell_1 - \int_{-\pi}^{\pi}\frac{\mathrm{d}k}{2\pi}(1-(\cos k)^{2j})\min(\ell_1, 2v_k t)\right]\\ &+\left(\frac{\mathrm{e}^{\mathrm{i}\beta}-1}{\mathrm{e}^{\mathrm{i}\beta}+1}\right)^{2j}\left[\ell_2 - \int_{-\pi}^{\pi}\frac{\mathrm{d}k}{2\pi}(1-(\cos k)^{2j})\min(\ell_2, 2v_k t)\right]\\ &+\int_{-\pi}^{\pi}\frac{\mathrm{d}k}{2\pi}\xi(k,j)(\max(d,2v_k t)+\max(d+\ell,2v_k t)\\ &\qquad -\max(d+\ell_1,2v_k t)-\max(d+\ell_2,2v_k t))\end{aligned} \tag{8.43}$$

where

$$\begin{aligned}\xi(k,j) = \sum_{s=1}^{j}\sum_{t=0}^{2j-2s}(-1)^t\left(\frac{\mathrm{e}^{\mathrm{i}\alpha}-1}{\mathrm{e}^{\mathrm{i}\alpha}+1}\right)^{s+t}\left(\frac{\mathrm{e}^{\mathrm{i}\beta}-1}{\mathrm{e}^{\mathrm{i}\beta}+1}\right)^{2j-s-t}\\ \times\gamma_{s,t,j}\cos k^{2j-2s}\sin k^{2s}\end{aligned} \tag{8.44}$$

with

$$\gamma_{s,t,j} = \frac{sj}{(2j-s-t)(s+t)} \binom{2j-s-t}{s} \binom{s+t}{s}. \tag{8.45}$$

The re-summation in (8.19) yields the formal expression

$$\begin{aligned}\log Z_1^{A_1:A_2}(\alpha,\beta) &= \mathrm{i}\frac{\ell_1\alpha+\ell_2\beta}{2} + \int_{-\pi}^{\pi}\frac{\mathrm{d}k}{2\pi}\mathrm{Re}[h_{1,\alpha}(\cos k)]\min(\ell_1, 2v_k t) \\ &+ \int_{-\pi}^{\pi}\frac{\mathrm{d}k}{2\pi}\mathrm{Re}[h_{1,\beta}(\cos k)]\min(\ell_2, 2v_k t) + \int_{-\pi}^{\pi}\frac{\mathrm{d}k}{2\pi}\Xi(k)(\max(d, 2v_k t) \\ &+ \max(d+\ell, 2v_k t) - \max(d+\ell_1, 2v_k t) - \max(d+\ell_2, 2v_k t))\end{aligned} \tag{8.46}$$

with the infinite sum

$$\Xi(k) = \sum_{j=1}^{\infty} \tilde{c}(2j)\xi(k,j), \quad \tilde{c}(2j) = -\frac{1}{2j}, \tag{8.47}$$

where we recall that the coefficients $\tilde{c}(j)$ are the Taylor coefficients of the function $\tilde{h}(x) = \log[(1+x)/2]$. To plot these doubly-charged moments, we use a cut-off Λ for the maximal value of the index j in the infinite sum. Let us stress that the function $\gamma_{s,t,j}$ in (8.45) satisfies the crucial relation

$$\sum_{t=0}^{2j-2s} (-1)^t \gamma_{s,t,j} = \binom{j}{s}. \tag{8.48}$$

With this, it is a simple calculation to show that $Z_1^{A_1:A_2}(\alpha,\alpha)$ indeed reduces to $Z_1^{A_1\cup A_2}(\alpha)$ given in (8.39), as expected. We compare the prediction (8.46) with numerical results in Figure 8.5 and find a good agreement.

Despite the cumbersome form of $Z_1^{A_1:A_2}(\alpha,\beta)$ in terms of an infinite sum, we are able to extract the quadratic orders in α and β and find

$$\log Z_1^{A_1:A_2}(\alpha,\beta) = \mathrm{i}\frac{\ell_1\alpha+\ell_2\beta}{2} - \frac{\alpha^2}{8}\mathcal{J}_{A_1}^{(1)} - \frac{\beta^2}{8}\mathcal{J}_{A_2}^{(1)} + \frac{\alpha\beta}{8}\mathcal{J}_m^{(1)}, \tag{8.49}$$

where we introduced $\mathcal{J}_m^{(1)} = (\mathcal{J}_{A_1}^{(1)} + \mathcal{J}_{A_2}^{(1)} - \mathcal{J}_d^{(1)})$ to lighten the notations. Here, $\mathcal{J}_{A_{1,2}}^{(n)}$ is simply $\mathcal{J}^{(n)}$ from (7.41) where ℓ is replaced by $\ell_{1,2}$, and $\mathcal{J}_d^{(n)}$ is given in (8.41). With (8.49), the double Fourier transform reads

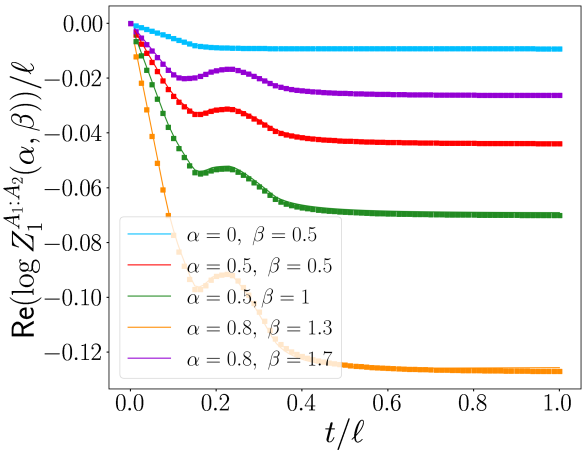

Figure 8.5: Time evolution of $Z_1^{A_1:A_2}(\alpha,\beta)$ after a quench from the dimer state in the tight-binding model (6.29) as a function of t/ℓ with $\ell_1 = 100$, $\ell_2 = 140$ and $d = 80$. The analytical prediction (8.46) with the cut-off $\Lambda = 6$ (solid lines) convincingly matches the numerical data (symbols).

$$\mathcal{Z}_1^{A_1:A_2}(q_1, q-q_1) = \frac{2}{\pi\sqrt{\mathcal{J}_{A_1}^{(1)}\mathcal{J}_{A_2}^{(1)} - \frac{(\mathcal{J}_m^{(1)})^2}{4}}} \times \mathrm{e}^{-\frac{8}{4\mathcal{J}_{A_1}^{(1)}\mathcal{J}_{A_2}^{(1)} - (\mathcal{J}_m^{(1)})^2}\left[\Delta q_1^2 \mathcal{J}_{A_2}^{(1)} + (\Delta q - \Delta q_1)^2 \mathcal{J}_{A_1}^{(1)} + \Delta q_1 (\Delta q - \Delta q_1)\mathcal{J}_m^{(1)}\right]} \tag{8.50}$$

where $\Delta q_1 = q_1 - \ell_1/2$. The two results (8.49) and (8.50) are the same as (8.33) and (8.34) where the $\mathcal{J}_s$ integrals are systematically replaced by $\mathcal{J}_s^{(1)}$. In a similar fashion as for the quench from the Néel state, the weight $p(q_1, q-q_1)$ defined in (8.6) satisfies $\sum_{q_1=0}^{q} p(q_1, q-q_1) = 1$.

To compute the symmetry-resolved mutual information, we replace each quantity in the definition (8.3) by its Gaussian approximation (7.46), (8.42) or (8.50). The calculations are similar to those of Section 8.2.2 and we find

$$I_1^{A_1:A_2}(q) = S_1^{A_1} + S_1^{A_2} - S_1^{A_1\cup A_2} - \frac{1}{2}\Big(\log\frac{\mathcal{J}_{A_1}^{(1)}\mathcal{J}_{A_2}^{(1)}\pi}{2\mathcal{J}_d^{(1)}}\Big)$$

$$+ \frac{1}{2}\Big(\frac{\partial_n(\mathcal{J}_{A_1}^{(n)})|_{n=1}}{\mathcal{J}_{A_1}^{(1)}} + \frac{\partial_n(\mathcal{J}_{A_2}^{(n)})|_{n=1}}{\mathcal{J}_{A_2}^{(1)}} - \frac{\partial_n(\mathcal{J}_d^{(n)})|_{n=1}}{\mathcal{J}_d^{(1)}}\Big)$$

$$
\begin{aligned}
&- \frac{4\mathcal{J}_{A_1}^{(1)}\mathcal{J}_{A_2}^{(1)} - (\mathcal{J}_m^{(1)})^2}{8\mathcal{J}_d^{(1)}}\Big\{\frac{1}{\mathcal{J}_{A_1}^{(1)}}\Big(\frac{\partial_n(\mathcal{J}_{A_1}^{(n)})|_{n=1}}{\mathcal{J}_{A_1}^{(1)}}+1\Big) \\
&\qquad + \frac{1}{\mathcal{J}_{A_2}^{(1)}}\Big(\frac{\partial_n(\mathcal{J}_{A_2}^{(n)})|_{n=1}}{\mathcal{J}_{A_2}^{(1)}}+1\Big)\Big\} \\
&- 2\Delta q^2\Big\{\Big(\frac{-\mathcal{J}_{A_1}^{(1)}+\mathcal{J}_{A_2}^{(1)}-\mathcal{J}_d^{(1)}}{2\mathcal{J}_d^{(1)}}\Big)^2\Big(\frac{\partial_n(\mathcal{J}_{A_1}^{(n)})|_{n=1}}{(\mathcal{J}_{A_1}^{(1)})^2}+\frac{1}{\mathcal{J}_{A_1}^{(1)}}\Big) \\
&\quad + \Big(\frac{\mathcal{J}_{A_1}^{(1)}-\mathcal{J}_{A_2}^{(1)}-\mathcal{J}_d^{(1)}}{2\mathcal{J}_d^{(1)}}\Big)^2\Big(\frac{\partial_n(\mathcal{J}_{A_2}^{(n)})|_{n=1}}{(\mathcal{J}_{A_2}^{(1)})^2}+\frac{1}{\mathcal{J}_{A_2}^{(1)}}\Big) \\
&\qquad - \Big(\frac{\partial_n(\mathcal{J}_d^{(n)})|_{n=1}}{(\mathcal{J}_d^{(1)})^2}+\frac{1}{\mathcal{J}_d^{(1)}}\Big)\Big\}. \qquad (8.51)
\end{aligned}
$$

We compare this prediction with the definition (8.3) where the various quantities are replaced by their Gaussian approximations in Figure 8.6, and find a good match. The result of (8.51) has the same physical interpretation as (8.35), namely the first three terms of the right-hand side correspond to the total mutual information, equipartition is broken at order $\Delta q^2/\ell$ for intermediate times and at higher order for $t < d/(2v_M)$ and $t \to \infty$, since $\mathcal{J}_d^{(n)} = \mathcal{J}_{A_1}^{(n)} + \mathcal{J}_{A_2}^{(n)}$ in those regimes. As for the quench from the Néel state, the combination (8.7) yields the total mutual information, namely

$$
\sum_{q=0}^{\ell} \mathcal{Z}_1^{A_1\cup A_2}(q) I_1^{A_1:A_2}(q) + S^{A_1,n} + S^{A_2,n} - S^{A_1\cup A_2,n} = I_1^{A_1:A_2} \qquad (8.52)
$$

where

$$
\begin{aligned}
I_1^{A_1:A_2} = -\int_{-\pi}^{\pi}\frac{\mathrm{d}k}{2\pi}\partial_n h_{n,0}(\cos k)|_{n=1}(&\max(d,2v_k t)+\max(d+\ell,2v_k t) \\
&-\max(d+\ell_1,2v_k t)-\max(d+\ell_2,2v_k t)) \qquad (8.53)
\end{aligned}
$$

is the quasiparticle prediction for the total mutual information [21]. Similarly to (8.36) and (8.37), it is a good consistency check to obtain the known total mutual information from our definition of the symmetry-resolved ones. Moreover, this result is also a new ab-initio result for the total mutual information after a quench in a free-fermion model.

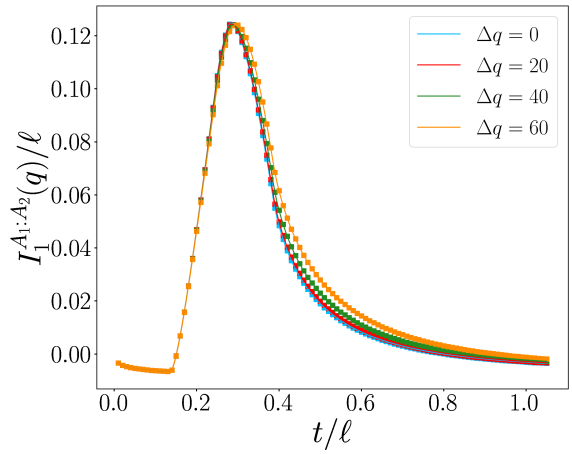

Figure 8.6: Time evolution of $I_1^{A_1:A_2}(q)$ after a quench from the dimer state in the tight-binding model (6.29) as a function of t/ℓ with $\ell_1 = 180$, $\ell_2 = 220$ and $d = 220$ for various values of Δq. We compare the approximation (8.51) (solid lines) with the definition (8.3) where the various quantities are replaced by their Gaussian approximations with the first corrections for the entropies (symbols).

8.4 Quasiparticle picture

In this final section, we interpret our results for disjoint intervals in the framework of the quasiparticle picture. For the charged moment $\log Z_n^{A_1\cup A_2}(\alpha)$, it is straightforward to adapt the argument of Section 7.3 for free-fermion models, and we find

$$\begin{aligned}\log Z_n^{A_1\cup A_2}(\alpha) &= \mathrm{i}\alpha\langle Q_A\rangle \\ &+ \int_{-\pi}^{\pi}\frac{\mathrm{d}k}{2\pi}\mathrm{Re}[h_{n,\alpha}(x_k)](\min(\ell_1,2v_kt)+\min(\ell_2,2v_kt)) \\ &- \int_{-\pi}^{\pi}\frac{\mathrm{d}k}{2\pi}\mathrm{Re}[h_{n,\alpha}(x_k)](\max(d,2v_kt)+\max(d+\ell,2v_kt) \\ &\qquad - \max(d+\ell_1,2v_kt)-\max(d+\ell_2,2v_kt)). \end{aligned} \tag{8.54}$$

This equation precisely matches our analytical results (8.26) with $x_k = 0$ for the quench from the Néel state, and (8.39) with $x_k = \cos k$ in the case of the quench from the dimer state. As in the case of a single interval, we conjecture that in the presence of different species of quasiparticles, the result (8.54) generalises to a sum over the different species.

To investigate the symmetry-resolved mutual information we also need to interpret the doubly-charged moment $Z_n(\alpha, \beta)$ defined in (8.4) in terms of the quasiparticle picture. Unfortunately, this quantity has a more complicated structure than the charged moments, since it requires the manipulation of non-commuting operators. As it was already argued for the full counting statistics of the Ising model [246], the quasiparticle picture fails to capture the complex structure of this kind of objects. The cumbersome function $\Xi(k)$ in (8.46) is a manifestation of this problem.

9

Conclusion and outlooks of Part II

In this second part of the thesis, we investigated the symmetry-resolved entropies and mutual information after a global quantum quench from the Néel and the dimer states in a one-dimensional tight-binding model.

In Chapter 7, we studied the case where the subsystem A is a single interval. With the multidimensional stationary phase approximation developed in [48], we derived exact expressions for the charged moments $Z_n(\alpha)$. The symmetry-resolved entropies are obtained from the Fourier transform of the charged moments, and we found exact results in the case of a quench from the Néel state, whereas we used the saddle-point approximation around $\alpha = 0$ for the quench from the dimer state. In both cases, the structure of the charged moments leads to two main physical results. First, the symmetry-resolved entropies with charge $q = \Delta q + \langle Q_A \rangle$ start evolving after a time delay t_D that depends on $|\Delta q|$. For $|\Delta q| < \ell/\pi$, we were able to compute the delay exactly and found that it grows linearly with $|\Delta q|$. Second, for small $|\Delta q|$ there is an effective equipartition of entanglement broken at order $\Delta q^2/\ell$. We also investigated the number entropy for both quenches. We found that it grows logarithmically with time before saturating to a value proportional to the logarithm of the subsystem size.

We considered the case where A consists of two intervals in Chapter 8. In particular, we defined the symmetry-resolved mutual information in terms of a doubly-charged moment $Z_1^{A_1:A_2}(\alpha, \beta)$ that depends on two

charges. In the context of free-fermion models, we expressed the doubly-charged moments in terms of the two-point correlation matrix and a matrix that contains the dependence in α and β. We generalised the method of [48] in the case of disjoint intervals and obtained exact results for the charged moments $Z_n^{A_1\cup A_2}(\alpha)$ and $Z_1^{A_1:A_2}(\alpha,\beta)$ in the scaling limit for the two quenches we considered. Our analysis reveals that there is also an effective equipartition of the mutual information. For intermediate times, the equipartition is broken at order $\Delta q^2/\ell$, whereas is it broken at higher order for early and infinite times. The leading term of the symmetry-resolved mutual information is the total mutual information. To the best of our knowledge, we provide the first ab-initio computation of the total mutual information after a global quantum quench, and our result matches the quasiparticle prediction [21].

Our investigations of the charged moments for free-fermion models naturally led to the quasiparticle conjecture (7.54) for $Z_n(\alpha)$. To give predictive power to this conjecture, one should devise a way to fix the kernel $s_{n,\alpha}^{(m)}(k)$, but this is a challenging problem for interacting models [226, 228–231]. For the Rényi entropies, which correspond to $\alpha = 0$, the solution is only known in the neighbourhood of $n = 1$, where the kernel is the Yang-Yang entropy [49]. It would already be interesting to generalise this result at $n = 1$ and small $\alpha \neq 0$, and use the saddle-point approximation to investigate the symmetry resolution. Independently from the details of the function $s_{n,\alpha}^{m}(k)$, the form of the conjecture (7.54) is sufficient to infer the two main physical results, namely the existence of a time delay t_D and equipartition for small $|\Delta q|$ in generic integrable models. Moreover, the logarithmic growth of the number entropy follows from the behaviour of $Z_1(\alpha)$ close to $\alpha = 0$ and so follows generically from (7.54) too. In stark contrast, the doubly-charged moments $Z_1^{A_1:A_2}(\alpha,\beta)$ contain information which is not accessible by the quasiparticles picture. This is not surprising, since a similar conclusion was drawn for the generating function of the subsystem magnetisation of the Ising model [246], an object similar to $Z_1^{A_1:A_2}(\alpha,\beta)$. Because of this obstacle, we do not have a quasiparticle conjecture for the symmetry-resolved mutual information.

Our work unveils new features of the symmetry-resolved entanglement dynamics after a global quantum quench, and we conclude with a series of research directions and questions which we believe are worthy of investigation. First, as we already discussed above, it would be important to test the quasiparticle conjecture (7.54) for a variety of generic integrable models. A second question is whether the symmetry-resolved entropies can be obtained in inhomogeneous settings, in a similar fashion as the total entanglement entropy [249–254]. One could also wonder if techniques developed for non-integrable models [255–260] apply to the evaluation of symmetry-resolved quantities, and whether our main physical findings, namely the time delay and equipartition, are robust away from integrability. In the context of disjoint subsystems, it would be interesting to study the symmetry decomposition of the entanglement negativity [221,222] in further detail, and in particular its behaviour out of equilibrium. Finally, we mention that Estienne, Ikhlef and Morin-Duchesne argued in a recent paper [202] that quantum overlaps similar to the bipartite fidelity are useful to compute symmetry-resolved Rényi entropies in integrable models. This result creates a surprising connection between the two parts of this thesis, and we intend to investigate this matter in further details in a near future.

Bibliography

[1] G. Parez, R. Bonsignori and P. Calabrese, *Exact quench dynamics of symmetry resolved entanglement in a free fermion chain*, J. Stat. Mech. (2021) 093102.

[2] G. Parez, R. Bonsignori and P. Calabrese, *Quasiparticle dynamics of symmetry-resolved entanglement after a quench: Examples of conformal field theories and free fermions*, Phys. Rev. B **103** (2021) L041104.

[3] A. Morin-Duchesne, G. Parez and J. Liénardy, *Bipartite fidelity for models with periodic boundary conditions*, J. Stat. Mech. (2021) 023101.

[4] G. Parez, A. Morin-Duchesne and P. Ruelle, *Bipartite fidelity of critical dense polymers*, J. Stat. Mech. (2019) 103101.

[5] C. Hagendorf and G. Parez, *On the logarithmic bipartite fidelity of the open XXZ spin chain at* $\Delta = -1/2$, in preparation (2021).

[6] A. Einstein, B. Podolsky and N. Rosen, *Can quantum-mechanical description of physical reality be considered complete?*, Phys. Rev. **47** (1935) 777.

[7] J.S. Bell, *On the Einstein Podolsky Rosen paradox*, Physics **1** (1964) 195.

[8] A. Aspect, P. Grangier and G. Roger, *Experimental tests of realistic local theories via Bell's theorem*, Phys. Rev. Lett. **47** (1981) 460.

[9] A. Aspect, P. Grangier and G. Roger, *Experimental realization of Einstein-Podolsky-Rosen-Bohm Gedankenexperiment: a new violation of Bell's inequalities*, Phys. Rev. Lett. **49** (1982) 91.

[10] A. Aspect, J. Dalibard and G. Roger, *Experimental test of Bell's inequalities using time-varying analyzers*, Phys. Rev. Lett. **49** (1982) 1804.

[11] E. Schrödinger, *Discussion of probability relations between separated systems*, Proc. Camb. Philos. Soc. **31** (1935) 555.

[12] E. Schmidt, *Zur Theorie der Linearen und Nichtlinearen Integralgleichungen. I. Teil: Entwicklung Willkürlicher Funktionen nach Systemen Vorgeschriebener*, Math. Ann. **63** (1907) 433.

[13] A. Ekert and P.L. Knight, *Entangled quantum systems and the Schmidt decomposition*, Am. J. Phys **63** (1995) 415.

[14] C.H. Bennett, H.J. Bernstein, S. Popescu and B. Schumacher, *Concentrating partial entanglement by local operations*, Phys. Rev. A **53** (1996) 2046.

[15] J. von Neumann, *Mathematische Grundlagen der Quantenmechanik*, Princeton University Press, 1955.

[16] C.E. Shannon, *A mathematical theory of communication*, The Bell system technical journal **27** (1948) 379–423.

[17] A. Rényi, *On measures of entropy and information*, in *Proceedings of the Fourth Berkeley Symposium on Mathematical Statistics and Probability, Volume 1: Contributions to the Theory of Statistics*, page 547, 1961.

[18] M.M. Wolf, F. Verstraete, M.B. Hastings and J.C. Cirac, *Area laws in quantum systems: mutual information and correlations*, Phys. Rev. Lett. **100** (2008) 070502.

[19] V. Vedral, M.B. Plenio, M.A. Rippin and P.L. Knight, *Quantifying entanglement*, Phys. Rev. Lett. **78** (1997) 2275.

[20] G. Vidal and R.F. Werner, *Computable measure of entanglement*, Phys. Rev. A **65** (2002) 032314.

[21] V. Alba and P. Calabrese, *Quantum information dynamics in multipartite integrable systems*, Europhys. Lett. **126** (2019) 60001.

[22] M.A. Nielsen and I. Chuang, *Quantum computation and quantum information*, American Association of Physics Teachers, 2002.

[23] A. Ekert and R. Jozsa, *Quantum computation and Shor's factoring algorithm*, Rev. Mod. Phys. **68** (1996) 733.

[24] C.H. Bennett, G. Brassard, C. Crépeau, R. Jozsa, A. Peres and W.K. Wootters, *Teleporting an unknown quantum state via dual classical and einstein-podolsky-rosen channels*, Phys. Rev. Lett. **70** (1993) 1895.

[25] A.K. Ekert, *Quantum cryptography based on Bell's theorem*, Phys. Rev. Lett. **67** (1991) 661.

[26] C.H. Bennett, D.P. DiVincenzo, J.A. Smolinand and W.K. Wootters, *Mixed-state entanglement and quantum error correction*, Phys. Rev. A **54** (1996) 3824.

[27] D.P. DiVincenzo, *Quantum computation*, Science **270** (1995) 255.

[28] D. Deutsch, *Quantum theory, the church–turing principle and the universal quantum computer*, Proc. R. Soc. Lond. A. **400** (1985) 97.

[29] F. Arute, K. Arya, R. Babbush et al., *Quantum supremacy using a programmable superconducting processor*, Nature **574** (2019) 505.

[30] S.N. Solodukin, *Entanglement entropy of black holes*, Living Rev. Rel. **14** (2011) 1.

[31] L. Amico, R. Fazio, A. Osterloh and V. Vedral, *Entanglement in many-body systems*, Rev. Mod. Phys. **80** (2008) 517.

[32] N. Laflorencie, *Quantum entanglement in condensed matter systems*, Phys. Rep. **646** (2016) 1.

[33] A. Osterloh, L. Amico, G. Falci and R. Fazio, *Scaling of entanglement close to a quantum phase transitions*, Nature **416** (2002) 608.

[34] T.J. Osborne and M.A. Nielsen, *Entanglement in a simple quantum phase transition*, Phys. Rev. A **66** (2002) 032110.

[35] G. Vidal, J.I. Latorre, E. Rico and A. Kitaev, *Entanglement in quantum critical phenomena*, Phys. Rev. Lett. **90** (2003) 227902.

[36] P. Di Francesco, P. Mathieu and D. Sénéchal, *Conformal field theory*, Springer, 1997.

[37] C. Holzhey, F. Larsen and F. Wilczek, *Geometric and renormalized entropy in conformal field theory*, Nucl. Phys. B **424** (1994) 443.

[38] P. Calabrese and J.L. Cardy, *Entanglement entropy and quantum field theory*, J. Stat. Mech. (2004) P06002.

[39] P. Calabrese and J.L. Cardy, *Entanglement entropy and conformal field theory*, J. Phys. A: Math. Theor. **42** (2009) 504005.

[40] J.I. Latorre and A. Riera, *A short review on entanglement in quantum spin systems*, J. Phys. A: Math. Theor. **42** (2009) 504002.

[41] P. Calabrese, J.L. Cardy and B. Doyon, *Special issue: 'Entanglement entropy in extended quantum systems'*, J. Phys. A: Math. Theor. **42** (2009) 500301.

[42] P. Calabrese, F.H.L. Essler and G. Mussardo, *Introduction to 'Quantum Integrability in Out of Equilibrium Systems'*, J. Stat. Mech. (2016) 064001.

[43] P. Calabrese, *Entanglement and thermodynamics in non-equilibrium isolated quantum systems*, Phys. A: Stat. Mech. Appl **504** (2018) 31.

[44] P. Calabrese, *Entanglement spreading in non-equilibrium integrable systems*, SciPost Phys. Lect. Notes (2020) 20.

[45] P. Calabrese and J.L. Cardy, *Evolution of entanglement entropy in one-dimensional systems*, J. Stat. Mech. (2005) P04010.

[46] P. Calabrese and J.L. Cardy, *Time dependence of correlation functions following a quantum quench*, Phys. Rev. Lett. **96** (2006) 136801.

[47] P. Calabrese and J.L. Cardy, *Quantum quenches in extended systems*, J. Stat. Mech. (2007) P06008.

[48] M. Fagotti and P. Calabrese, *Evolution of entanglement entropy following a quantum quench: Analytic results for the XY chain in a transverse magnetic field*, Phys. Rev. A **78** (2008) 010306.

[49] V. Alba and P. Calabrese, *Entanglement and thermodynamics after a quantum quench in integrable systems*, Proc. Natl. Acad. Sci. **114** (2017) 7947.

[50] V. Alba and P. Calabrese, *Entanglement dynamics after quantum quenches in generic integrable systems*, SciPost Phys. **4** (2018) 017.

[51] A.M. Kaufman, M.E. Tai, A. Lukin, M. Rispoli, R. Schittko, P.M. Preiss and M. Greiner, *Quantum thermalization through entanglement in an isolated many-body system*, Science **353** (2016) 794.

[52] A. Lukin, M. Rispoli, R. Schittko, M.E. Tai, A.M. Kaufman, S. Choi, V. Khemani, J. Leonard and M. Greiner, *Probing entanglement in a many-body localized system*, Science **364** (2019) 6437.

[53] T. Brydges, A. Elben, P. Jurcevic, B. Vermersch, C. Maier, B.P. Lanyon, P. Zoller, R. Blatt and C.F. Roos, *Probing Rényi entanglement entropy via randomized measurements*, Science **364** (2019) 260.

[54] A. Elben, R. Kueng, H.-Y. Huang, R. van Bijnen, C. Kokail, M. Dalmonte, P. Calabrese, B. Kraus, J. Preskill, P. Zoller and B. Vermersch, *Mixed-state entanglement from local randomized measurements*, Phys. Rev. Lett. **125** (2020) 200501.

[55] R.J. Baxter, *Exactly Solved Models in Statistical Mechanics*, Academic Press, 1982.

[56] H. Bethe, *Zur Theorie der Metalle*, Z. Phys. **71** (1931) 205.

[57] N. Kitanine, J.M. Maillet and V. Terras, *Form factors of the XXZ Heisenberg spin-1/2 finite chain*, Nucl. Phys. B **554** (1999).

[58] V.E. Korepin, N.M. Bogoliubov and A.G. Izergin, *Quantum inverse scattering method and correlation functions*, Cambridge Cniversity Press, 1997.

[59] M. Rigol, V. Dunjko, V. Yurovsky and M. Olshanii, *Relaxation in a completely integrable many-body quantum system: an ab initio study of the dynamics of the highly excited states of 1D lattice hard-core bosons*, Phys. Rev. Lett. **98** (2007) 050405.

[60] T. Kinoshita, T. Wenger and D.S. Weiss, *A quantum newton's cradle*, Nature **440** (2006) 900.

[61] B. Lake, D.A. Tennant, J.-S. Caux, T. Barthel, U. Schollwöck, S.E. Nagler and C.D. Frost, *Multispinon continua at zero and finite temperature in a near-ideal Heisenberg chain*, Phys. Rev. Lett. **111** (2013) 137205.

[62] J. Dubail and J.-M. Stéphan, *Universal behavior of a bipartite fidelity at quantum criticality*, J. Stat. Mech. (2011) L03002.

[63] J.-M. Stéphan and J. Dubail, *Logarithmic corrections to the free energy from sharp corners with angle* 2π, J. Stat. Mech. (2013) P09002.

[64] N. Laflorencie and S. Rachel, *Spin-resolved entanglement spectroscopy of critical spin chains and Luttinger liquids*, J. Stat. Mech. (2014) P11013.

[65] M. Goldstein and E. Sela, *Symmetry-resolved entanglement in many-body systems*, Phys. Rev. Lett. **120** (2018) 200602.

[66] J.C. Xavier, F.C. Alcaraz and G. Sierra, *Equipartition of the entanglement entropy*, Phys. Rev. B **98** (2018) 041106.

[67] N. Feldman and M. Goldstein, *Dynamics of Charge-Resolved Entanglement after a Local Quench*, Phys. Rev. B **100** (2019) 235146.

[68] V. Vitale, A. Elben, R. Kueng, A. Neven, J. Carrasco, B. Kraus, P. Zoller, P. Calabrese, B. Vermersch and M. Dalmonte,

Symmetry-resolved dynamical purification in synthetic quantum matter, arXiv:2101.07814 (2021).

[69] S. Fraenkel and M. Goldstein, *Entanglement Measures in a Nonequilibrium Steady State: Exact Results in One Dimension*, arXiv:2105.00740 (2021).

[70] J.M. Leger, C. Loriers-Susse and B. Vodar, *Pressure effect on the curie temperatures of transition metals and alloys*, Phys. Rev. B **6** (1972) 4250.

[71] S. Sachdev, *Quantum phase transitions*, Handbook of Magnetism and Advanced Magnetic Materials (2007).

[72] M. Vojta, *Quantum phase transitions*, Rep. Prog. Phys. **66** (2003) 2069.

[73] B.M. McCoy and T.T. Wu, *The two-dimensional Ising model*, Harvard University Press, 1973.

[74] W. Lenz, *Beitrag zum Verständnis der magnetischen Eigenschaften in festen Körpern*, Phys. Zeitschr **21** (1920) 613.

[75] E. Ising, *Beitrag zur Theorie des Ferromagnetismus*, Z. Phys. **31** (1925) 253.

[76] R. Peierls, *On Ising's model of ferromagnetism*, Proc. Camb. Philos. Soc. **32** (1936) 471.

[77] H.A. Kramers and G.H. Wannier, *Statistics of the two-dimensional ferromagnet. Part I*, Phys. Rev. **60** (1941) 252.

[78] L. Onsager, *Crystal statistics. I. A two-dimensional model with an order-disorder transition*, Phys. Rev. **65** (1944) 117.

[79] P. Calabrese, F.H.L. Essler and M. Fagotti, *Quantum quench in the transverse-field Ising chain*, Phys. Rev. Lett. **106** (2011) 227203.

[80] M. Magoni, S.N. Majumdar and G. Schehr, *Ising model with stochastic resetting*, Phys. Rev. B **2** (2020) 033182.

[81] J. Carrasquilla and R.G. Melko, *Machine learning phases of matter*, Nat. Phys. **13** (2017) 431.

[82] D. Stauffer, *Social applications of two-dimensional Ising models*, Am. J. Phys **76** (2008) 470.

[83] P. Heller, *Experimental investigations of critical phenomena*, Rep. Prog. Phys. **30** (1967) 731.

[84] E.H. Lieb, *Residual entropy of square ice*, Phys. Rev. **162** (1967) 162.

[85] B. Sutherland, *Two-dimensional hydrogen bonded crystals without the ice rule*, J. Math. Phys. **11** (1970) 3183.

[86] H. Duminil-Copin and S. Smirnov, *Conformal invariance of lattice models*, Probability and statistical physics in two and more dimensions **15** (2012) 213.

[87] S. Smirnov, *Critical percolation in the plane: conformal invariance, Cardy's formula, scaling limits*, Comptes Rendus de l'Académie des Sciences-Series I-Mathematics **333** (2001) 239.

[88] D. Chelkak and S. Smirnov, *Universality in the 2D Ising model and conformal invariance of fermionic observables*, Inventiones mathematicae **189** (2012) 515.

[89] J. Polchinski, *Scale and conformal invariance in quantum field theory*, Nucl. Phys. B **303** (1988) 226.

[90] V. Riva and J.L. Cardy, *Scale and conformal invariance in field theory: a physical counterexample*, Phys. Rev. B **622** (2005) 339.

[91] C. Itzykson, H. Saleur and J.-B. Zuber, *Conformal invariance and applications to statistical mechanics*, World Scientific, 1998.

[92] J.L. Cardy, *Conformal field theory and statistical mechanics*, Exact Methods in Lowdimensional Statistical Physics and Quantum Computing (Oxford University Press) (2008) 65.

[93] J.L. Cardy, *Conformal invariance and surface critical behavior*, Nucl. Phys. B **240** (1984) 514.

[94] A.A. Belavin, A.M. Polyakov and A.B. Zamolodchikov, *Infinite conformal symmetry in two-dimensional quantum field theory*, Nucl. Phys. B **241** (1984) 333.

[95] H.W.J. Blöte, J.L. Cardy and M.P. Nightingale, *Conformal invariance, the central charge, and universal finite-size amplitudes at criticality*, Phys. Rev. Lett. **56** (1986) 742.

[96] I. Affleck, *Universal term in the free energy at a critical point and the conformal anomaly*, Phys. Rev. Lett. **56** (1986) 746.

[97] D. Friedan, Z. Qiu and S. Shenker, *Conformal invariance, unitarity, and critical exponents in two dimensions*, Phys. Rev. Lett. **52** (1984) 1575.

[98] J.L. Cardy, *Operator content of two-dimensional conformally invariant theories*, Nucl. Phys. B **270** (1986) 186.

[99] P. Goddard, A. Kent and D. Olive, *Unitary representations of the virasoro and super-virasoro algebras*, Commun. Math. Phys. **103** (86) 105.

[100] Z. Maassarani and D. Serban, *Non-unitary conformal field theory and logarithmic operators for disordered systems*, Nucl. Phys. B **489** (1997) 603.

[101] O.A. Castro-Alvaredo, B. Doyon and F. Ravanini, *Irreversibility of the renormalization group flow in non-unitary quantum field theory*, J. Phys. A: Math. Theor. **50** (2017) 424002.

[102] P.A. Pearce, J. Rasmussen and J.-B. Zuber, *Logarithmic minimal models*, J. Stat. Mech. (2006) P11017.

[103] P.A. Pearce and J. Rasmussen, *Solvable critical dense polymers*, J. Stat. Mech. (2007) P02015.

[104] C. Itzykson, H. Saleur and J.-B. Zuber, *Conformal invariance of nonunitary 2d-models*, Europhys. Lett. **2** (1986) 91.

[105] V. Gurarie, *Logarithmic operators in conformal field theory*, Nucl. Phys. B **410** (1993) 535.

[106] M. Flohr, *Bits and pieces in logarithmic conformal field theory*, Int. J. Mod. Phys. A **18** (2003) 4497.

[107] A. Morin-Duchesne and J.L. Jacobsen, *Logarithmic correlation functions for critical dense polymers on the cylinder*, SciPost Phys. **7** (2019) 70.

[108] W. Heisenberg, *Zür Theorie des Ferromagnetismus*, Zeitschrift für Physik A Hadrons and Nuclei **49** (1928) 619.

[109] R. Orbach, *Linear antiferromagnetic chain with anisotropic coupling*, Phys. Rev. **112** (1958) 309.

[110] E.H. Lieb, T. Schultz and D. Mattis, *Two soluble models of an antiferromagnetic chain*, Ann. Phys. **16** (1961) 407.

[111] E. Barouch and B.M. McCoy, *Statistical mechanics of the XY model. II. Spin-correlation functions*, Phys. Rev. A **3** (1971) 786.

[112] A. Morin-Duchesne, J. Rasmussen and P. Ruelle, *Integrability and conformal data of the dimer model*, J. Phys. A: Math. Theor. **49** (2016) 174002.

[113] M. Srednicki, *Entropy and area*, Phys. Rev. Lett. **71** (1993) 666.

[114] M.B. Hastings, *An area law for one-dimensional quantum systems*, J. Stat. Mech. (2007) P08024.

[115] J. Eisert, M. Cramer and M.B. Plenio, *Area laws for the entanglement entropy – a review*, Rev. Mod. Phys. **832** (2010) 277.

[116] J. D. Bekenstein, *Black holes and entropy*, Phys. Rev. D **7** (1973) 2333.

[117] J. D. Bekenstein, *Generalized second law of thermodynamics*, Phys. Rev. D **9** (1974) 3292.

[118] S.W. Hawking, *Particle creation by black holes*, Commun. Math. Phys. **43** (1975) 199.

[119] R. Orús, *A practical introduction to tensor networks: Matrix product states and projected entangled pair states*, Ann. Phys. **349** (2014) 117.

[120] R. Islam, R. Ma, P.M. Preiss, M.E. Tai, A. Lukin M. Rispoli and M. Greiner, *Measuring entanglement entropy in a quantum many-body system*, Nature **528** (2015) 77.

[121] T. Nishioka, S. Ryu and T. Takayanagi, *Holographic entanglement entropy: an overview*, J. Phys. A: Math. Theor. **42** (2009) 504008.

[122] P. Calabrese, J.L. Cardy and R. Tonni, *Entanglement negativity in quantum field theory*, Phys. Rev. Lett. **109** (2012) 130502.

[123] J.I. Latorre, E. Rico and G. Vidal, *Ground state entanglement in quantum spin chains*, Quant. Inf. and Comp. **4** (2004) 048.

[124] A.R. Its, B.-Q. Jin and V.E. Korepin, *Entanglement in the XY spin chain*, J. Phys. A: Math. Gen. **38** (2005) 2975.

[125] I. Peschel and V. Eisler, *Reduced density matrices and entanglement entropy in free lattice models*, J. Phys. A: Math. Theor. **42** (2009) 504003.

[126] N. Crampé, R.I. Nepomechie and L. Vinet, *Free-fermion entanglement and orthogonal polynomials*, J. Stat. Mech. (2019) 093101.

[127] D. Bianchini, O.A. Castro-Alvaredo, B. Doyon, E. Levi and F. Ravanini, *Entanglement entropy of non unitary conformal field theory*, J. Phys. A: Math. Theor. **48** (2014) 04FT01.

[128] R. Couvreur, J.L. Jacobsen and H. Saleur, *Entanglement in non-unitary quantum critical spin chains*, Phys. Rev. Lett. **119** (2017) 040601.

[129] A. Uhlmann, *The "transition probability" in the state space of $A*$ algebra*, Rep. Math. Phys. **9** (1976) 273.

[130] R. Jozsa, *Fidelity for Mixed Quantum States*, J. Mod. Opt. **41** (1994) 2315.

[131] P. Zanardi and N. Paunkovič, *Ground state overlap and quantum phase transitions*, Phys. Rev. E **74** (2006) 031123.

[132] H.-Q. Zhou and J.P. Barjaktarevič, *Fidelity and quantum phase transitions*, J. Phys. A: Math. Theor. **41** (2008) 412001.

[133] J. Sirker, *Finite temperature fidelity susceptibility for one-dimensional quantum systems*, Phys. Rev. Lett. **105** (2010) 117203.

[134] S.-J. Gu, *Fidelity approach to quantum phase transitions*, Int. J. Mod. Phys. B **24** (2010) 4371.

[135] J.L. Cardy and I. Peschel, *Finite-size dependence of the free energy in two-dimensional critical systems*, Nucl. Phys. B **300** (1988) 377.

[136] H.W. Diehl, *The theory of boundary critical phenomena*, Int. J. Mod. Phys. B **11** (1997) 3503.

[137] C. Hagendorf and J. Liénardy, *Open spin chains with dynamic lattice supersymmetry*, J. Phys. A: Math. Theor. **50** (2017) 185202.

[138] R. Weston, *Correlation functions and the boundary qKZ equation in a fractured XXZ chain*, J. Stat. Mech. (2011) P12002.

[139] R. Weston, *Exact and scaling form of the bipartite fidelity of the infinite XXZ chain*, J. Stat. Mech. (2012) L04001.

[140] V. Pasquier and H. Saleur, *Common structures between finite systems and conformal field theories through quantum groups*, Nucl. Phys. B **330** (1990) 523.

[141] A. Morin-Duchesne and J.L. Jacobsen, *Two-point boundary correlation functions of dense loop models*, Scipost **4** (2018) 034.

[142] H. Temperley and E.H. Lieb, *Relations between the "percolation" and "colouring" problem and other graph-theoretical problems associated with regular planar lattices: Some exact results for the "percolation" problem*, Proc. Roy. Soc. Lond. A **322** (1971) 251.

[143] V.F.R. Jones, *Index for subfactors*, Invent. Math. **72** (1983) 1.

[144] P. Martin, *Potts models and related problems in statistical mechanics*, World Scientific, 1991.

[145] F. Goodman and H. Wenzl, *The Temperley-Lieb algebra at roots of unity*, Pacific J. Math. **161** (1993) 307.

[146] B.W. Westbury, *The representation theory of the Temperley-Lieb algebras*, Math. Zeit. **219** (1995) 539.

[147] D. Ridout and Y. Saint-Aubin, *Standard modules, induction and the Temperley-Lieb algebra*, Adv. Theor. Math. Phys. **18** (2014) 957.

[148] A. Morin-Duchesne, *A proof of selection rules for critical dense polymers*, J. Phys. A: Math. Theor. **44** (2011) 495003.

[149] A.M. Gainutdinov, H. Saleur and I.Y. Tipunin, *Lattice W-algebras and logarithmic CFTs*, J. Phys. A: Math. Theor. **47** (2014) 495401.

[150] H. Saleur and M. Bauer, *On some relations between local height probabilities and conformal invariance*, Nucl. Phys. B **320** (1989) 591.

[151] I.S. Gradshteyn and I.M. Ryzhik, *Table of Integrals, Series, and Products*, Elsevier, 2007.

[152] D. Levy, *Algebraic structure of translation-invariant spin-$\frac{1}{2}$ XXZ and q-Potts quantum chains*, Phys. Rev. Lett. **67** (1991) 1971.

[153] P. Martin and H. Saleur, *On an algebraic approach to higher dimensional statistical mechanics*, Commun. Math. Phys. **158** (1993) 155.

[154] J.J. Graham and G.I. Lehrer, *The representation theory of affine Temperley-Lieb algebras*, Enseign. Math. **44** (1998) 173.

[155] R.M. Green, *On representations of affine Temperley-Lieb algebras*, J. Algebra **60** (1997) 498–517.

[156] K. Erdmann and R.M. Green, *On representations of affine Temperley-Lieb algebras, II*, Pac. J. Math. **191** (1999) 243.

[157] P.A. Pearce, J. Rasmussen and S.P. Villani, *Solvable critical dense polymers on the cylinder*, J. Stat. Mech. (2010) P02010.

[158] A. Morin-Duchesne and Y. Saint-Aubin, *A homomorphism between link and XXZ modules over the periodic Temperley-Lieb algebra*, J. Phys. A: Math. Theor. **46** (2013) 285207.

[159] A. Morin-Duchesne, P.A. Pearce and J. Rasmussen., *Modular invariant partition function of critical dense polymers*, Nucl. Phys. B **874** (2013) 312.

[160] P. Di Francesco, H. Saleur and J.B. Zuber, *Relations between the Coulomb gas picture and conformal invariance of two-dimensional critical models*, J. Stat. Phys. **49** (1987) 57.

[161] C.J. Hamer, G.R.W. Quispel and M.T. Batchelor, *Conformal anomaly and surface energy for Potts and Ashkin-Teller quantum chains*, J. Phys. A: Math. Gen. **20** (1987) 5677.

[162] A. Klümper, M.T. Batchelor and P.A. Pearce, *Central charges of the* 6- *and* 19-*vertex models with twisted boundary conditions*, J. Phys. A: Math. Gen. **24** (1991) 3111.

[163] B. Nienhuis, *Critical behavior of two-dimensional spin models and charge asymmetry in the Coulomb gas*, J. Stat. Phys. **34** (1984) 731.

[164] C. Hagendorf and J. Liénardy, *The open XXZ chain at* $\Delta = -1/2$ *and the boundary quantum Knizhnik–Zamolodchikov equations*, J. Stat. Mech. (2021) 013104.

[165] P. Zinn-Justin, *Six-vertex, loop and tiling models: integrability and combinatorics*, Lambert Academic Publishing (2010).

[166] Y. Stroganov, *The importance of being odd*, J. Phys. A : Math. Gen. **34** (2001) L179.

[167] A.V. Razumov and Y.G. Stroganov, *Spin chains and combinatorics*, J. Phys. A : Math. Gen. **34** (2001) 3185.

[168] A.V. Razumov and Y.G. Stroganov, *Spin chains and combinatorics: twisted boundary conditions*, J. Phys. A : Math. Gen. **34** (2001) 5335.

[169] M.T. Batchelor, J. de Gier and B. Nienhuis, *The quantum symmetric XXZ chain at* $\Delta = -1/2$*, alternating-sign matrices and plane partitions*, J. Phys. A : Math. Gen. **34** (2001) L265.

[170] J. de Gier, M.T. Batchelor, B. Nienhuis and S. Mitra, *The XXZ spin chain at $\Delta = -1/2$: Bethe roots, symmetric functions, and determinants*, J. Math. Phys. **43** (2002) 4135–4146.

[171] P. Di Francesco, P. Zinn-Justin and J.B. Zuber, *Sum rules for the ground states of the O(1) loop model on a cylinder and the XXZ spin chain*, J. Stat. Mech. (2006) P08011.

[172] L. Cantini, *Finite size emptiness formation probability of the XXZ spin chain at $\Delta = -1/2$*, J. Phys. A : Math. Theor. **45** (2012) 135207.

[173] A. Morin-Duchesne, C. Hagendorf and L. Cantini, *Boundary emptiness formation probabilities in the six-vertex model at $\Delta = -1/2$*, J. Phys. A : Math. Theor. **53** (2020) 255202.

[174] N.A. Slavnov, *Calculation of scalar products of wave functions and form factors in the framework of the algebraic Bethe ansatz*, Theor. Math. Phys. **79** (1989) 232.

[175] E.K. Sklyanin, *Separation of Variables. New Trends.*, Prog. Theor. Phys. Suppl. **118** (1995) 35.

[176] J.M. Maillet and G. Niccoli, *On quantum separation of variables*, J. Math. Phys. **59** (2018) 091417.

[177] J. Liénardy, *Integrable lattice models and supersymmetry*, PhD Thesis, Université catholique de Louvain (2020).

[178] O.A. Castro-Alvaredo, B. Doyon and T. Yoshimura, *Emergent hydrodynamics in integrable quantum systems out of equilibrium*, Phys. Rev. X **6** (2016) 041065.

[179] B. Bertini, M. Collura, J. De Nardis and M. Fagotti, *Transport in out-of-equilibrium XXZ chains: Exact profiles of charges and currents*, Phys. Rev. Lett. **117** (2016) 207201.

[180] F.H.L. Essler and M. Fagotti, *Quench dynamics and relaxation in isolated integrable quantum spin chains*, J. Stat. Mech. (2016) 064002.

[181] A. Polkovnikov, K. Senguptaa, A. Silva and M. Vengalattore, *Colloquium: Nonequilibrium dynamics of closed interacting quantum systems*, Rev. Mod. Phys. **83** (2011) 863.

[182] C. Gogolin and J. Eisert, *Equilibration, thermalisation, and the emergence of statistical mechanics in closed quantum systems*, Rep. Prog. Phys. **79** (2016) 056001.

[183] L. D'Alessio, Y. Kafri, A. Polkovnikov and M. Rigol, *From Quantum Chaos and Eigenstate Thermalization to Statistical Mechanics and Thermodynamics*, Adv. Phys. **65** (2016) 239.

[184] L.F. Santos, A. Polkovnikov and M. Rigol, *Entropy of Isolated Quantum Systems after a Quench*, Phys. Rev. Lett. **107** (2011) 040601.

[185] J.M. Deutsch, H. Li and A. Sharma, *Microscopic origin of thermodynamic entropy in isolated systems*, Phys. Rev. E **87** (2013) 042135.

[186] M. Collura, M. Kormos and P. Calabrese, *Stationary entanglement entropies following an interaction quench in* $1D$ *Bose gas*, J. Stat. Mech. (2014) P01009.

[187] N. Schuch, M.M. Wolf, F. Verstraete and J.I. Cirac, *Entropy Scaling and Simulability by Matrix Product States*, Phys. Rev. Lett. **100** (2008) 030504.

[188] N. Schuch, M.M. Wolf, K.G.H. Vollbrecht and J.I. Cirac, *On entropy growth and the hardness of simulating time evolution*, New J. Phys. **10** (2008) 033032.

[189] A. Perales and G. Vidal, *Entanglement growth and simulation efficiency in one-dimensional quantum lattice systems*, Phys. Rev. A **78** (2008) 042337.

[190] P. Hauke, F.M. Cucchietti, L. Tagliacozzo, I. Deutsch and M. Lewenstein, *Can one trust quantum simulators?*, Prog. Phys. **75** (2012) 082401.

[191] J. Dubail, *Entanglement scaling of operators: a conformal field theory approach, with a glimpse of simulability of long-time dynamics in 1+1d*, J. Phys. A: Math. Theor. **50** (2017) 234001.

[192] S. Trotzky, Y.-A. Chen, A. Flesch, I.P. McCulloch, U.Schollwöck, J. Eisert and I. Bloch, *Probing the relaxation towards equilibrium in an isolated strongly correlated one-dimensional Bose gas*, Nat. Phys. **8** (2012) 325.

[193] M. Gring, M. Kuhnert, T. Langen, T. Kitagawa, B. Rauer, M. Schreitl, I.E. Mazets, D.A. Smith, E. Demler and J. Schmiedmayer, *Relaxation and prethermalization in an isolated quantum system*, Science **337** (2012) 1318.

[194] M. Cheneau, P. Barmettler, D. Poletti, M. Endres, P. Schauß, T. Fukuhara, C. Gross, I. Bloch, C. Kollath and S. Kuhr, *Light-cone-like spreading of correlations in a quantum many-body system*, Nature **481** (2012) 484.

[195] U. Schneider, L. Hackermüller, J.P. Ronzheimer, S. Will, S. Braun, T. Best, I. Bloch, E. Demler, S. Mandt, D. Rasch and A. Rosch, *Fermionic transport and out-of-equilibrium dynamics in a homogeneous Hubbard model with ultracold atoms*, Nat. Phys. **8** (2012) 213.

[196] T. Langen, R. Geiger, M. Kuhnert, B. Rauer and J. Schmiedmayer, *Local emergence of thermal correlations in an isolated quantum many-body system*, Nat. Phys. **9** (2013) 640.

[197] T. Langen, S. Erne, R. Geiger, B. Rauer, T. Schweigler, M. Kuhnert, W. Rohringer, I.E. Mazets, T. Gasenzer and J. Schmiedmayer, *Experimental observation of a generalized Gibbs ensemble*, Science **348** (2015) 207.

[198] R. Bonsignori, P. Ruggiero and P. Calabrese, *Symmetry resolved entanglement in free fermionic systems*, J. Phys. A: Math. Theor. **52** (2019) 475302.

[199] L. Capizzi, P. Ruggiero and P. Calabrese, *Symmetry resolved entanglement entropy of excited states in a CFT*, J. Stat. Mech. (2020) 073101.

[200] R. Bonsignori and P. Calabrese, *Boundary effects on symmetry resolved entanglement*, J. Phys. A: Math. Theor. **54** (2020) 015005.

[201] S. Fraenkel and M. Goldstein, *Symmetry resolved entanglement: Exact results in 1d and beyond*, J. Stat. Mech. (2020) 033106.

[202] B. Estienne, Y. Ikhlef and A. Morin-Duchesne, *Finite-size corrections in critical symmetry-resolved entanglement*, SciPost Phys. **10** (2021) 54.

[203] H.-H. Chen, *Symmetry decomposition of relative entropies in conformal field theory*, arXiv:2104.03102 (2021).

[204] L. Capizzi and P. Calabrese, *Symmetry resolved relative entropies and distances in conformal field theory*, arXiv:2105.08596 (2021).

[205] E. Cornfeld, L.A. Landau, K. Shtengel and E. Sela, *Entanglement spectroscopy of non-Abelian anyons: Reading off quantum dimensions of individual anyons*, Phys. Rev. B **99** (2019) 115429.

[206] K. Monkman and J. Sirker, *Operational Entanglement of Symmetry-Protected Topological Edge States*, Phys. Rev. Research **2** (2020) 043191.

[207] D. Azses and E. Sela, *Symmetry-resolved entanglement in symmetry-protected topological phases*, Phys. Rev. B **102** (2020) 235157.

[208] S. Murciano, G. Di Giulio and P. Calabrese, *Symmetry resolved entanglement in gapped integrable systems: a corner transfer matrix approach*, SciPost Phys. **8** (2020) 046.

[209] S. Murciano, G. Di Giulio and P. Calabrese, *Entanglement and symmetry resolution in two dimensional free quantum field theories*, J. High Energ. Phys. (2020) 73.

[210] P. Calabrese, M. Collura, G. Di Giulio and S. Murciano, *Full counting statistics in the gapped XXZ spin chain*, Europhys. Lett. **129** (2020) 60007.

[211] D.X. Horváth and P. Calabrese, *Symmetry resolved entanglement in integrable field theories via form factor bootstrap*, J. High Energ. Phys. (2020) 131.

[212] D.X. Horváth, L. Capizzi and P. Calabrese, *U(1) symmetry resolved entanglement in free 1+1 dimensional field theories via form factor bootstrap*, J. High Energ. Phys. (2021) 197.

[213] D.X. Horváth, P. Calabrese and O.A. Castro-Alvaredo, *Branch Point Twist Field Form Factors in the sine-Gordon Model II: Composite Twist Fields and Symmetry Resolved Entanglement*, arXiv:2105.13982 (2021).

[214] L. Capizzi, D.X. Horváth, P. Calabrese and O.A. Castro-Alvaredo, *Entanglement of the 3-State Potts Model via Form Factor Bootstrap: Total and Symmetry Resolved Entropies*, arXiv:2108.10935 (2021).

[215] M.T. Tan and S. Ryu, *Particle number fluctuations, Rényi and symmetry-resolved entanglement entropy in two-dimensional Fermi gas from multi-dimensional bosonisation*, Phys. Rev. B **101** (2020) 235169.

[216] S. Murciano, P. Ruggiero and P. Calabrese, *Symmetry resolved entanglement in two-dimensional systems via dimensional reduction*, J. Stat. Mech. (2020) 083102.

[217] X. Turkeshi, P. Ruggiero, V. Alba and P. Calabrese, *Entanglement equipartition in critical random spin chains*, Phys. Rev. B **102** (2020) 014455.

[218] S. Zhao, C. Northe and R. Meyer, *Symmetry-Resolved Entanglement in AdS_3/CFT_2 coupled to $U(1)$ Chern-Simons Theory*, J. High Energ. Phys. (2020) 30.

[219] K. Weisenberger, S. Zhao, C. Northe and R. Meyer, *Symmetry-resolved entanglement for excited states and two entangling intervals in AdS_3/CFT_2*, arXiv:2108.09210 (2021).

[220] P. Calabrese, J. Dubail and S. Murciano, *Symmetry-resolved entanglement entropy in Wess-Zumino-Witten models*, arXiv:2106.15946 (2021).

[221] E. Cornfeld, M. Goldstein and E. Sela, *Imbalance Entanglement: Symmetry Decomposition of Negativity*, Phys. Rev. A **98** (2018) 032302.

[222] S. Murciano, R. Bonsignori and P. Calabrese, *Symmetry decomposition of negativity of massless free fermions*, SciPost Phys. **10** (2021) 111.

[223] A. Neven, J. Carrasco, V. Vitale, C. Kokail, A. Elben, M. Dalmonte, P. Calabrese, P. Zoller, B. Vermersch, R. Kueng and B. Kraus, *Symmetry-resolved entanglement detection using partial transpose moments*, arXiv:2103.07443 (2021).

[224] E. Ilievski, M. Medenjak, T. Prosen and L. Zadnik, *Quasilocal charges in integrable lattice systems*, J. Stat. Mech. (2016) 064008.

[225] E.H. Lieb and D.W. Robinson, *The finite group velocity of quantum spin systems*, Commun. Math. Phys. **28** (1972) 251.

[226] V. Alba and P. Calabrese, *Quench action and Rényi entropies in integrable systems*, Phys. Rev. B **96** (2017) 115421.

[227] R. Modak, L. Piroli and P. Calabrese, *Correlation and entanglement spreading in nested spin chains*, J. Stat. Mech. (2019) 093106.

[228] V. Alba and P. Calabrese, *Rényi entropies after releasing the Néel state in the XXZ spin-chain*, J. Stat. Mech. (2017) 113105.

[229] M. Mestyán, V. Alba and P. Calabrese, *Rényi entropies of generic thermodynamic macrostates in integrable systems*, J. Stat. Mech. (2018) 083104.

[230] O.A. Castro-Alvaredo, M. Lencses, I.M. Szecsenyi and J. Viti, *Entanglement dynamics after a quench in Ising field theory: a branch point twist field approach*, J. High Energ. Phys. (2019) 79.

[231] K. Klobas and B. Bertini, *Entanglement dynamics in Rule 54: exact results and quasiparticle picture*, arXiv:2104.04513 (2021).

[232] A. Coser, E. Tonni and P. Calabrese, *Entanglement negativity after a global quantum quench*, J. Stat. Mech. (2014) P12017.

[233] H.M. Wiseman and J.A. Vaccaro, *Entanglement of Indistinguishable Particles Shared between Two Parties*, Phys. Rev. Lett. **91** (2003) 097902.

[234] H. Barghathi, C.M. Herdman and A. Del Maestro, *Rényi Generalization of the Accessible Entanglement Entropy*, Phys. Rev. Lett. (2018) 150501.

[235] H. Barghathi, E. Casiano-Diaz and A. Del Maestro, *Operationally accessible entanglement of one dimensional spinless fermions*, Phys. Rev. A **100** (2019) 022324.

[236] X. Cao, A. Tilloy and A. De Luca, *Entanglement in a fermion chain under continuous monitoring*, SciPost Phys. **7** (2019) 024.

[237] M. Kiefer-Emmanouilidis, R. Unanyan, J. Sirker and M. Fleischhauer, *Bounds on the entanglement entropy by the number entropy in non-interacting fermionic systems*, SciPost Phys. **8** (2020) 083.

[238] M. Kiefer-Emmanouilidis, R. Unanyan, J. Sirker and M. Fleischhauer, *Evidence for unbounded growth of the number entropy in many-body localized phases*, Phys. Rev. Lett. **124** (2020) 243601.

[239] Y. Zhao, D. Feng, Y. Hu, S. Guo and J. Sirker, *Entanglement dynamics in the three-dimensional Anderson model*, Phys. Rev. B **102** (2020) 195132.

[240] M. Kiefer-Emmanouilidis, R. Unanyan, M. Fleischhauer and J. Sirker, *Unlimited growth of particle fluctuations in many-body localized phases*, Ann. Phys. (2021) 168481.

[241] M. Kiefer-Emmanouilidis, R. Unanyan, M. Fleischhauer and J. Sirker, *Slow delocalization of particles in many-body localized phases*, Phys. Rev. B **103** (2021) 024203.

[242] I. Peschel, *Calculation of reduced density matrices from correlation functions*, J. Phys. A: Math. Gen. **36** (2003) L205.

[243] M.C. Chung and I. Peschel, *Density-matrix spectra of solvable fermionic systems*, Phys. Rev. B **64** (2001) 064412.

[244] S.K. Yip, *Dimer state of spin-1 bosons in an optical lattice*, Phys. Rev. Lett. **90** (2003) 250402.

[245] M. Fagotti, *On conservation laws, relaxation and pre-relaxation after a quantum quench*, J. Stat. Mech. (2014) P03016.

[246] S. Groha, F.H.L. Essler and P. Calabrese, *Full counting statistics in the transverse field Ising chain*, SciPost Phys. **4** (2018) 043.

[247] M. Fagotti and P. Calabrese, *Entanglement entropy of two disjoint blocks in XY chains*, J. Stat. Mech. (2010) P04016.

[248] R. Balian and E. Brezin, *Nonunitary Bogoliubov transformations and extension of Wick's theorem*, Il Nuovo Cimento B **64** (1969) 37.

[249] J. Dubail, J.-M. Stéphan, J. Viti and P. Calabrese, *Conformal field theory for inhomogeneous one-dimensional quantum systems: the example of non-interacting Fermi gases*, SciPost Phys. **2** (2017) 002.

[250] V. Alba, *Entanglement and quantum transport in integrable systems*, Phys. Rev. B **97** (2018) 245135.

[251] B. Bertini, M. Fagotti, L. Piroli and P. Calabrese, *Entanglement evolution and generalised hydrodynamics: noninteracting systems*, J. Phys. A: Math. Theor. **51** (2018) 39LT01.

[252] V. Alba, B. Bertini and M. Fagotti, *Entanglement evolution and generalised hydrodynamics: interacting integrable systems*, SciPost Phys. **7** (2019) 005.

[253] V. Alba, *Towards a generalized hydrodynamics description of Rényi entropies in integrable systems*, Phys. Rev. B **99** (2019) 045150.

[254] P. Ruggiero, P. Calabrese, B. Doyon and J. Dubail, *Quantum Generalized Hydrodynamics*, Phys. Rev. Lett. **124** (2020) 140603.

[255] A. Nahum, J. Ruhman, S. Vijay and J. Haah, *Quantum Entanglement Growth under Random Unitary Dynamics*, Phys. Rev. X **7** (2017) 031016.

[256] B. Bertini, P. Kos and T. Prosen, *Entanglement Spreading in a Minimal Model of Maximal Many-Body Quantum Chaos*, Phys. Rev. X **9** (2019) 021033.

[257] T. Rakovszky, F. Pollmann and C.W. von Keyserlingk, *Sub-ballistic Growth of Rényi Entropies due to Diffusion*, Phys. Rev. Lett. **122** (2019) 250602.

[258] B. Bertini and P. Calabrese, *Prethermalisation and Thermalisation in the Entanglement Dynamics*, Phys. Rev. B **102** (2020) 094303.

[259] L. Piroli, B. Bertini, J.I. Cirac and T. Prosen, *Exact dynamics in dual-unitary quantum circuits*, Phys. Rev. B **101** (2020) 094304.

[260] R. Modak, V. Alba and P. Calabrese, *Entanglement revivals as a probe of scrambling in finite quantum systems*, J. Stat. Mech. (2020) 083110.